Communauté
UNIVERSITÉ Grenoble Alpes

THÈSE

Pour obtenir le grade de

DOCTEUR DE LA COMMUNAUTE UNIVERSITE GRENOBLE ALPES

Spécialité : **Physique des matériaux**

Arrêté ministériel : 25 mai 2016

Présentée par

Jérôme FLIEGANS

Thèse dirigée par **Nora DEMPSEY**

préparée au sein du **Laboratoire LMCM au CEA-LITEN**
dans **l'École Doctorale de Physique**

Coercivity of NdFeB-based sintered permanent magnets – Experimental and numerical approaches

Thèse soutenue publiquement le **« 16 Décembre 2019 »**,
devant le jury composé de :

M. Viorel POP
Professeur, Babes-Bolyai University, Cluj-Napoca, Roumanie, Rapporteur
Mme Spomenka KOBE
Professeur, Jozef Stefan Institute, Ljubljana, Slovénie, Rapporteur
M. Thomas SCHREFL
Professeur, Danube University Krems, Vienne, Autriche, Examinateur
Mme Sophie RIVOIRARD
Ingénieur de recherche, Institut Néel-CNRS, Grenoble, Examinatrice
M. Olivier ISNARD
Professeur, Institut Néel-CNRS, Grenoble, Président du jury
Mme Nora DEMPSEY
Directrice de recherche, Institut Néel-CNRS, Grenoble, Directrice de thèse
M. Gérard DELETTE
Ingénieur de recherche, CEA-LITEN, Grenoble, Encadrant de thèse

Acknowledgements

First of all, I want to thank Viorel Pop, Spomenka Kobe, Thomas Schrefl, Sophie Rivoirard and Olivier Isnard for accepting to serve in my jury.

I also want to thank my thesis director Nora Dempsey and supervisor Gérard Delette for giving me the opportunity to do a PhD thesis. During these 3 years, their support, assistance and scientific expertise were invaluable to my work.

Special thanks go to Dominique Givord who helped me a lot during the first 2 years. He was the driving force behind the study of demagnetizing field effects in closed- and open-circuit. I hope that he is proud of the simulation results obtained during the last year.

I thank all the people from LMCM: the head of laboratory Céline Delafosse, the engineers and the technicians without whom experiments would not be possible. Specials thanks go to Cyril Rado and Olivier Tosoni for their help and fruitful discussions. I also want to thank all the people from LFM and L2EV laboratories at CEA-LITEN, and from the MNM group at Institut Néel. During these years, many of you became more than colleagues and were part of the wonderful time I had in Grenoble.

I thank Romain Soulas and Laure Guetaz from PFNC at CEA-LITEN for their help in microstructural characterization. I also want to thank Yves Deschanels from Institut Néel for his support concerning magnetic characterization.

Special thanks go to all the people that were/are part of the office of PhD students. This latter is the perfect example of how colleagues can become really good friends.

Last but not least, I am grateful to my family for their amazing support during my very long university studies. And thank you Blandine for your daily support during this last year.

Content

Introduction 1
I. From context to coercivity 4
I.1. History of rare earth permanent magnets 4
I.2. Intrinsic and extrinsic properties of permanent magnets 5
I.2.1. Intrinsic magnetic properties 5
I.2.2. Extrinsic magnetic properties 7
I.3. Magnetization reversal mechanisms 8
I.3.1. Coherent rotation: the Stoner-Wohlfarth model 8
I.3.2. Nucleation vs pinning controlled magnetization reversal 9
I.4. Nd-Fe-B sintered magnets: fabrication and microstructure 10
I.4.1. Microstructure of a Nd-Fe-B sintered magnet 10
I.4.2. Industrial production process: sintering 12
I.4.3. Application fields and limitations 13
I.4.4. State of the art: current strategies to improve coercivity 14
I.5. Micromagnetic simulations and models 17
I.5.1. Micromagnetic simulations (Landau-Lifshitz-Gilbert formalism) 17
I.5.2. Micromagnetic and global models 18
I.5.3. Main results of micromagnetic simulations 22
I.6. The grain boundary diffusion process (GBDP) in Nd-Fe-B sintered magnets 31
I.6.1. Benefits of core-shell microstructure 31
I.6.2. State of the art 32
I.6.3. Micromagnetic simulations on core-shell structures 36
I.7. Problematic of the thesis 38
II. Fabrication of Nd-Fe-B sintered magnets, characterization and numerical methods 40
II.1. From ribbon to green compact 40
II.1.1. Strip-casting 40
II.1.2. Hydrogen decrepitation to coarse powder 42
II.1.3. Jet milling 42
II.1.4. From powder to green compact 43
II.2. Sintering furnace 44
II.2.1. Sintering heat treatment 45
II.2.2. Post-sinter annealing (PSA) heat treatment 45
II.3. GBDP on Nd-Fe-B sintered magnets 46
II.3.1. Sample preparation for GBDP 46

II.3.2. Diffusion heat treatment 47
II.4. Characterization methods 48
II.4.1. Magnetic characterization 48
II.4.2. Metallography 52
II.4.3. Microstructural characterization 52
II.5. Numerical methods 53
II.5.1. FEMME software package 53
II.5.2. Flux 3D software 57
III. Coercivity of polycrystalline hard magnets 64
III.1. Introduction 64
III.2. Study of collective magnetostatic effects: experimental approach 64
III.2.1. Model for the demagnetization field correction 64
III.2.2. Experimental protocol and results 67
III.2.3. Analysis and model improvement 69
III.3. Study of collective magnetostatic effects: numerical approach 71
III.3.1. Closed-circuit configuration simulation 71
III.3.2. Open-circuit configuration simulation 74
III.3.3. Discussion about collective effects 76
III.3.4. Experimental validation 79
III.4. Magnetostatic coupling in heterogeneous magnets 82
III.4.1. J-H curve of a two-grain-population magnet 82
III.4.2. J-H curve of duplex magnets 85
III.5. Conclusions 91
IV. Experimental and computational study of magnetization reversal in Dy-Co diffused Nd-Fe-B sintered magnets 92
IV.1. Magnetic properties in the as-sintered state and after post-sinter annealing (PSA) 92
IV.1.1. Experimental results 92
IV.1.2. FEMME simulations: sintering vs PSA 96
IV.2. Magnetic properties after GBDP and post-diffusion annealing (PDA) 98
IV.2.1. GBDP using intermetallic compound vs eutectic alloy 98
IV.2.2. Influence of diffusion time on magnetic properties 99
IV.2.3. Influence of diffusion temperature on magnetic properties 100
IV.2.4. Influence of PDA on magnetic properties 101
IV.2.5. M(T) measurements 103
IV.2.6. Characterization of microstructure and coercivity profiles 104
IV.2.7. FEMME simulations: core-shell model 113

IV.3. Conclusions 117
V. Discussion: coercivity of graded magnets 119
V.1. Modelling of diffusion profiles 119
V.1.1. Diffusion model hypothesis 119
V.1.2. Results 122
V.1.3. Impact on coercivity profile 127
V.1.4. Diffusion of Co 128
V.2. Polycrystalline model applied to Dy-diffused thick magnets 129
V.2.1. Description of the geometrical model 129
V.2.2. Results: grain reversal patterns in a graded sample 131
V.2.3. Results for other diffusion conditions 137
V.3. Conclusions 139
Conclusions and prospects 140
References 142

List of figures

Fig. 1: Maximum energy product $(BH)_{max}$ and coercivity of commercial Nd-Fe-B sintered magnets according to their composition. [5] 1
Fig. 2: Evolution of $(BH)_{max}$ at room temperature for permanent magnets during the 20th century and their relative volume for the same energy density. [4] 4
Fig. 3: Hysteresis loop for a permanent magnet with intrinsic and extrinsic magnetic properties, and with the $(BH)_{max}$ rectangle in the second quadrant. Adapted from [15], [16] 8
Fig. 4: Coherent rotation of magnetization vectors described by the Stoner-Wohlfarth model. [18] ... 8
Fig. 5: Magnetization configuration in the case of nucleation-pinning reversal. [18] 9
Fig. 6: BSE-SEM image of the typical microstructure of Nd-Fe-B sintered magnets. [6] 10
Fig. 7: Unit cell crystallographic structure of the $Nd_2Fe_{14}B$ phase. [21] 11
Fig. 8: Industrial production route of Nd-Fe-B sintered magnets and pseudo-binary phase diagram (Nd/B = 2) of the Nd-Fe-B ternary system. [11] 13
Fig. 9: Evolution of coercivity with grain size for sintered magnets (triangle symbols). [20] 14
Fig. 10: Demagnetization curves of as-sintered (dashed curves) and post-sinter annealed (solid curves) Nd-Fe-B sintered magnets containing 0.1 at.% (red) and 0.5 at.% Ga (black). [46], [48] 16
Fig. 11: Thermal variation of the ratio v_A/δ_W^3 in Nd-Fe-B sintered magnets. [59] 22
Fig. 12: Thermal dependence of coercivity for modeled Nd-Fe-B magnets with average grain sizes of 30, 50 and 130 nm. [68] 23
Fig. 13: Dependence of H_C/M_S with H_A/M_S for Nd-Fe-B magnets with average grain sizes of 30, 50 and 130 nm. [68] 24
Fig. 14: Modeled geometries with platelet-, cubic- and columnar cuboid-shaped $Nd_2Fe_{14}B$ grains that are partially exchange-coupled. [50] 25
Fig. 15: Simulated demagnetization curves for the models with different grain shapes. [50] 26
Fig. 16: Simulated demagnetization curves for hot-deformed Nd-Fe-B magnets with different grain sizes and GB phase saturation magnetizations. [70] 27
Fig. 17: Magnetization configuration during domain wall propagation of modeled hot-deformed magnets with 60-nm-sized-grains and various GB phase saturation magnetizations. [70] 28
Fig. 18: Micromagnetic models for (a) the exchange-coupled case (0.1 at.% of Ga), (b) the exchange-decoupled case (0.5 at.% of Ga). [48] 29
Fig. 19: (a) Simulated demagnetization curves for the exchange-coupled case. (b) Same for the exchange-decoupled case. (c) Magnetization reversal process for the exchange-coupled case. (d) Same for the exchange-decoupled case. [48] 30
Fig. 20: BSE-SEM image of a Dy-coated Nd-Fe-B sintered magnet from [79]. 31
Fig. 21: Demagnetization curves after diffusion at 900°C for different times. Shaded bars correspond to coercivity and remanence range for reference samples heat-treated without RE diffusion. [94] ... 33
Fig. 22: Finite element model consisting of 8 $Nd_2Fe_{14}B$ grains separated by a 4 nm-thick GB phase and separated from the GB phase by an 8-nm-thick $HRE_2Fe_{14}B$ shell. [105] 37
Fig. 23: Structure of the polycrystalline model created by Voronoi tessellation of a cube. [106] 38
Fig. 24: (Left) Schematic representation of the strip-casting method [108]. (Right) Fabrication of Nd-Fe-B ribbons by the strip-casting process at CEA-LITEN 41
Fig. 25: Microstructure of Nd-Fe-B strip-casted ribbons fabricated at CEA-LITEN. 41
Fig. 26: (Left) Nitrogen jet milling device used at CEA-LITEN. (Right) Typical grain distribution obtained after nitrogen jet milling at CEA-LITEN. 43
Fig. 27: Furnace used at CEA-LITEN for sintering, annealing and diffusion heat treatments. 45
Fig. 28: Thermal cycle used for sintering. 45
Fig. 29: Thermal cycle used for PSA. 46

Fig. 30: Dy-Co binary phase diagram. 46
Fig. 31: Sketch of GBDP direction. Diffusion is performed along the easy-axis. 47
Fig. 32: Thermal cycle used for GBDP. 48
Fig. 33: (Left) Hysteresigraph system used at CEA-LITEN for magnetic characterization in closed-circuit conditions. (Right) Sketch of the magnetic circuit in the hysteresigraph system. [115] 49
Fig. 34: (Left) Pick-up probe for calculation of H and J [115]. (Right) LJT-10 coil used for magnetic characterization in closed-circuit. 49
Fig. 35: Schematic representation of the rectangularity of a demagnetization curve. 50
Fig. 36: Extraction magnetometer used at Institut Néel for magnetic characterization in open-circuit conditions. 51
Fig. 37: Finite element model consisting of 8 $Nd_2Fe_{14}B$ grains separated by a 4-nm-thick GB phase. [119] 55
Fig. 38: Simulated demagnetization curve obtained for the 8-g model with a non-magnetic GB phase. 56
Fig. 39: Image of the magnetization configuration during magnetization reversal for a non-magnetic GB phase. 57
Fig. 40: (Left) Example of a 9x9x9 array of cubic grains. (Right) Detail of a cubic grain meshed with 64 cubic quadratic elements. 59
Fig. 41: (a) FE simulation of the demagnetization of a polycrystalline array (10 x 10 x 5 cubic grains) with inputs indicated in the insert. Each point (open red circle) corresponds to a sub-iteration performed into the principal steps defined by the increment value of ΔH. (b) For some principal steps (labelled by their number), evolution of the ratio W_{iter}/W_0 (current energy/energy at the beginning of the step) during the stabilization loop. 60
Fig. 42: Comparison of the demagnetizing curves obtained numerically by the dipolar approximation (dotted line) and by the FE method implemented in this work (open red circles). 61
Fig. 43: 3D geometrical model used for the simulation in closed-circuit configuration (hysteresigraph measurement system). 62
Fig. 44: Details on the mesh at the contact area between the polycrystalline magnet and the pole piece of the hysteresigraph system. 62
Fig. 45: Simulation of the demagnetization of a polycrystalline sample in closed-circuit (hysteresigraph system) with linear and non-linear magnetic behavior assumptions for the pole pieces. The simulated curves have been fitted to the experimental one by an appropriate choice of the grain coercivity distribution parameters. 63
Fig. 46: Map of demagnetization factors N_z in XY planes at different heights (z) obtained by FE computation for a parallelepiped (a = b = 1 and h = 0.5). The values given below each map correspond to an average value in the plane. 65
Fig. 47: Schematic representation of a heterogeneous granular hard magnet (cavity field concept). 66
Fig. 48: Schematic representation of the demagnetizing field contributions to magnetization reversal. Black line: reversal in the absence of any demagnetizing field effects. (Left graph) Dashed green line: usual demagnetizing field correction (α = 1 and β^{hom} = 1). (Middle graph) Dashed red line: so-called hard demag correction applicable in the absence of collective effects (α = 0 and β^{hom} = 1). (Right graph) Dashed blue line: intermediate correction when collective effects are considered (both α and β^{hom} ≠ 0). [124] 67
Fig. 49: (a) Second and third quadrants of the hysteresis loop for sample S1 of thickness 3 mm. Solid black curve: raw open-circuit measurement without demagnetizing field correction (slope: $1/Nexpop$). Dashed blue curve: open-circuit measurement with the usual demagnetizing field correction (slope: 1/N). Green solid curve: raw open-circuit measurement corrected to be parallel to the closed-circuit one (slope: 1/N'). Red solid curve: closed-circuit measurement (slope: $1/Nexpcl$). Short dotted lines:

tangents at H=H_c for the closed-circuit measurement and for the open-circuit measurement corrected with N'. Inset: complete hysteresis loop for sample S1. (b) Same data for the sample S2 of thickness 4 mm. (c) Same data for the sample S3 of thickness 5 mm. [124]..... 68
Fig. 50: Repartition of the grain coercivity in gray scale in the numerical sample used for the simulation of the closed-circuit configuration (arbitrary units: black = lower value, white = higher value), the 2D maps are given for each XZ plane starting from the mid-plane of the complete grain array (the numbers indicate the position of the XZ plane starting from the mid-plane towards the back)..... 72
Fig. 51: Experimental (black solid line) and simulated (red dots) demagnetization curves in the closed-circuit configuration compared to the grain coercivity distribution (blue solid line). 72
Fig. 52 : (Left) Grain reversal patterns for the first reversal cascade indexed in Fig. 51 (XZ plane labelled #7 in Fig. 50), the filled and non-filled squares in the grids refer to reversed and non-reversed grains, respectively. (Right) Grain reversal patterns for the final reversal cascade indexed in Fig. 51 (XZ plane labelled #1 in Fig. 50)..... 73
Fig. 53: Schematic representation of the cascade grain reversal in closed-circuit. 73
Fig. 54: Repartition of the reduced grain coercivity [$H_c/M_s - N_z$] in gray scale in the numerical sample used for the simulation in the open-circuit configuration (arbitrary units: black = lower value, white = higher value), the 2D maps are given for each XZ plane starting from the mid-plane of the complete grain array (the numbers indicate the position of the XZ plane starting from the mid-plane towards the back). 74
Fig. 55: Experimental (solid lines) and simulated (dots) demagnetization curves in the closed-circuit (red) and open-circuit (black) configurations, grain coercivity distribution (dotted blue line), the magnetic fields at the curve knees and at the coercive field are indicated on each curve as labels for the maps plotted in Fig. 56..... 75
Fig. 56: Grain reversal patterns for selected field values indicated in Fig. 55: the filled and non-filled squares in the grids refer to reversed and non-reversed grains, respectively (XZ planes ranked from the y=0 to higher y positions incremented from left to right). Simulation of a 10x10x5 grains array (symmetry duplicated) with σ_{Hc} = 0.1 T. Patterns at coercive field in closed-circuit (red border) and patterns at coercive field in open-circuit (black border)..... 75
Fig. 57: Comparison of simulated and experimentally measured demagnetization curves in open-circuit for two different aspect ratios (h/D = 0.5 and 1). 78
Fig. 58: (Top) Demagnetizing curves in the closed-circuit (red solid line) and open-circuit (black solid line) configurations obtained by simulation of 10x10x5 grains array and σ_{Hc} = 0.2 T. (Bottom) Grain reversed patterns at the coercive field in open-circuit, the filled and non-filled squares in the grids refer to reversed and non-reversed grains, respectively (XZ planes ranked from the y=0 to higher y positions incremented from left to right, duplicated symmetries). 79
Fig. 59: Induction field map (B_Z component, scale in mT) measured with the Hall probe over the sample in the remanent state after saturation. The value of B_Z indicated in the insert is the spatially averaged value performed inside a 10 mm circle (dotted line) corresponding to the sample dimension. The values on axes correspond to the scanning position in mm. 80
Fig. 60: (Left) Residual induction field maps (B_Z component, scale in mT) measured with the Hall probe over the sample in the demagnetized state achieved in closed-circuit (top) and in open-circuit via the Bitter coil (down). The values of B_Z indicated in the insert are the spatially averaged values performed inside a 10 mm circle (dotted line) corresponding to the sample dimension. The values on axes correspond to the scanning position in mm. (Right) Grids correspond to the grain reversal patterns simulated on the highest XY plane at J=0..... 81
Fig. 61: (Left) Residual induction field maps (B_Z component, scale in mT) measured with the Hall probe over the sample in the demagnetized state achieved in closed-circuit. (Right) Same measurement in open-circuit using the extraction magnetometer. The values of B_Z indicated in the insert are the

spatially averaged values performed inside a 6 mm circle (dotted line) corresponding to the sample dimension. The values on axes correspond to the scanning position in mm. 82
Fig. 62: Repartition of the grain coercivity in gray scale in the numerical sample used for the simulation of the bimodal grain population magnet (arbitrary units: black = lower value, white = higher value), the 2D maps are drawn for each XZ plane starting from the mid-plane of the complete grain array (the numbers indicate the position of the XZ plane starting from the mid-plane towards the back). 83
Fig. 63: Simulated demagnetization curve of the bimodal grain population magnet (red open symbols with following inputs for low coercive grains: $<\mu_0 H_c> = 1.1$ T, $\sigma_{Hc} = 0.1$ T and for high coercive grains: $<\mu_0 H_c> = 1.6$ T, $\sigma_{Hc} = 0.1$ T). The coercivity distribution is indicated by the blue solid line for the whole magnet and by the black solid line for the population 1 alone. The dotted line corresponds to the experimental curve of an annealed sample chosen as reference..... 84
Fig. 64: Grain reversal patterns for the four selected field values indicated in Fig. 63. 84
Fig. 65: Repartition of the grain coercivity in gray scale in the numerical sample used for the simulation of the duplex magnet (arbitrary units: black = lower value, white = higher value). The 2D maps are drawn for each XZ plane starting from the mid-plane of the complete grain array. 85
Fig. 66: Simulated demagnetizing curve of the duplex magnet (in red open symbols, low coercive grains: $<\mu_0 H_C> = 1.6$ T and $\sigma_{Hc} = 0.2$ T, high coercive grains: $<\mu_0 H_C> = 2.35$ T and $\sigma_{Hc} = 0.1$ T). The grain coercivity distribution in the duplex magnet is indicated by the black dotted line. The blue dotted lines correspond to the experimental curve of each magnet measured separately..... 86
Fig. 67: Grain reversal patterns for the 6 selected field values indicated in Fig. 66 (A-F): the filled and non-filled squares in the grids refer to reversed and non-reversed grains, respectively (XZ planes ranked from the y=0 to higher y positions incremented from left to right). 87
Fig. 68: (Left) Residual induction field maps (B_Z component, scale in mT) measured with the Hall probe over the low coercivity sample of the duplex magnet taken in two demagnetized states achieved in closed-circuit (hysteresigraph) corresponding to the points D (up) and F (down) indexed on the J-H curve plotted in Fig. 66. The values of B_Z indicated are the spatially averaged values measured in the 10 mm circle (dotted line) corresponding to the sample dimension. The values on the axes correspond to the scanning position in mm. (Right) Grids correspond to the grain reversal patterns in the XY plane located at the top of the high coercivity magnet and at the top of the low coercivity magnet. 89
Fig. 69: Experimental J-H curves measured on the duplex magnet (central low coercivity magnet with h=5mm, high coercive magnets with h=10mm, diameter 10 mm). The measuring coil is positioned in the middle plane (solid red curve) and then shifted upward by regular steps (t=1.5 mm). 90
Fig. 70: Simulation of the influence of the shift of the measuring coil obtained with the polycrystalline model applied to the duplex magnet configuration. J and H values are averaged over a height equivalent to half of the thickness of the central magnet. Sensors are located at the mid-plane (open red circles) and at the top end of the stack (open black circles)..... 90
Fig. 71: Demagnetization curves measured after PSA at 470, 500, 530, 550 and 600°C. The black curve represents the demagnetization curve of the as-sintered state..... 93
Fig. 72: Evolution of coercivity with the PSA temperature. The black solid line represents the average coercivity of the as-sintered state..... 94
Fig. 73: Pseudo-binary phase diagram (30 at.% Cu) extracted from the ternary Nd-Cu-Fe phase diagram (δ denotes $Nd_6Fe_{13}Cu$ phase). [129] 95
Fig. 74: Cubic model used for preliminary FEMME simulations..... 96
Fig. 75: Simulated demagnetization curves corresponding to a soft ferromagnetic (solid red curve) and to a non-magnetic (solid blue curve) GB phase. 97
Fig. 76: (Left) Demagnetization curves measured for the magnet diffused with the eutectic alloy: after sintering (black solid curve), after optimal PSA (green solid curve), after GBDP (blue solid curve) and

after PDA (red solid curve). (Right) Same measurements for the magnet diffused with the intermetallic compound. 98
Fig. 77: (Left) Image of the surface state of a magnet diffused with the eutectic alloy $Dy_{66}Co_{34}$. (Right) Same for a magnet diffused with the intermetallic compound $Dy_{63}Co_{37}$. 99
Fig. 78: Influence of diffusion time on coercivity for GBDP using $Dy_{63}Co_{37}$ intermetallic compound. 100
Fig. 79: Influence of diffusion temperature on coercivity for GBDP using $Dy_{63}Co_{37}$ intermetallic compound. 101
Fig. 80: Evolution of coercivity with the PDA temperature (compared to the one with the PSA temperature). 102
Fig. 81: Evolution of the second derivative of magnetization (with respect to temperature) with temperature for the magnets diffused in three different experimental conditions and for a reference magnet. (Inset) Corresponding evolution of magnetization with temperature. 103
Fig. 82: BSE-SEM images taken at various distances from the coated surface for the magnets diffused in three different conditions. 104
Fig. 83: EDX maps of Dy at various distances of the coated surface for all samples. 105
Fig. 84: EDX maps of Dy and Nd at a distance of 100 µm for each sample with the corresponding BSE-SEM image and concentration profiles along a line. 106
Fig. 85: EDX maps of Dy and Nd at various distances for a similar microstructural state between all diffused magnets, with the corresponding BSE-SEM image and concentration profiles along a line. 107
Fig. 86: Coercivity improvements after GBDP performed at 920°C for 3h and after PDA compared to the ones from the work of Kim et al. [96]. 108
Fig. 87: Schematic illustration of the microstructures changes after PDA performed on Dy-free and Dy-containing Nd-Fe-B sintered magnets. [96] 109
Fig. 88: Measurement of the demagnetization curve after polishing on a reference magnet. 110
Fig. 89: Measurements of the demagnetization curve after successive polishing on the 920°C-3h diffused magnet. 110
Fig. 90: Measurements of the demagnetization curve after successive polishing on the 920°C-12h diffused magnet. 111
Fig. 91: Evolution of the ratio $H_{cj}/H_{cj,0}$ with the removed thickness for the 920°C-3h and 920°C-12h diffused magnets and respective EDX maps of Dy. 112
Fig. 92: Cubic model representative of a core-shell structure. 113
Fig. 93: Simulated demagnetization curves showing the influence of the Dy-rich shell thickness and content in Dy on magnetization reversal. The red numbers correspond to the screenshots in Fig. 94. 115
Fig. 94: Magnetization configuration during reversal for the case with a $(Nd_{53}Dy_{47})_2Fe_{14}B$ shell of thickness 5 nm and a non-magnetic GB phase (dark blue solid curve in Fig. 93). 115
Fig. 95: Simulated demagnetization curves showing the influence of the GB phase nature on magnetization reversal. The red numbers correspond to the screenshots in Fig. 96. 116
Fig. 96: Magnetization configuration during reversal for the case with a $(Nd_{53}Dy_{47})_2Fe_{14}B$ shell of thickness 5 nm and a soft ferromagnetic GB phase (red solid curve in Fig. 95). 117
Fig. 97: Bi-crystal model for the calculation of the Dy profile in a polycrystalline sample by mixed diffusion (volume/grain boundary) of elements from the surface. The red line illustrates the shape of iso-concentration lines (from [138]). 120
Fig. 98: Dy concentration profile (relative to the surface) obtained with the Fisher model for the three experimental diffusion conditions. 123
Fig. 99: Schematic representation of the possible mechanism for the replacement of Nd by Dy. [98] 125

Fig. 100: Dy/Nd depletion in grain volume at 100 µm and 400 µm for the sample diffused at 920°C-3h. (Left) Measured (open symbols) and calculated (solid line) concentration profiles. (Right) SEM-EDX maps of Nd and Dy with the localization of the profile line..... 125
Fig. 101: Dy/Nd depletion in grain volume at 100 µm and 200 µm for the sample diffused at 870°C-3h. (Left) Measured (open symbols) and calculated (solid line) concentration profiles. (Right) SEM-EDX maps of Nd and Dy with the localization of the profile line..... 126
Fig. 102: Dy/Nd depletion in grain volume at 100 µm and 800 µm for the sample diffused at 920°C-12h. (Left) Measured (open symbols) and calculated (solid line) concentration profiles. (Right) SEM-EDX maps of Nd and Dy with the localization of the profile line..... 126
Fig. 103: Evolution of the Dy enrichment calculated at 10 nm from the grain boundary with the distance from the sample surface with the Fisher model for the three diffusion conditions..... 128
Fig. 104: Evolution of the Co enrichment calculated at 2.5 µm from the grain boundary (grain center) with the distance from the sample surface with the Fisher model for the 920°C-3h diffusion condition. (Insert) Grain concentration profile at 400 µm. 129
Fig. 105: Computation time as a function of the number of grains considered in the simulation. 130
Fig. 106: Demagnetization curves simulated for the four stacks with magnetic properties given in Table 43 (configuration #1). The distribution of grain coercivity is illustrated by the XZ patterns in gray scale (black = lower values, white = higher values) for each stack. 132
Fig. 107: Demagnetization curves simulated for stack #4 with magnetics properties given in Table 43 and for two positions of the pick-up coil relative to the sample. The dashed line represents the expected J-H curve with no magnetostatic interactions. 132
Fig. 108: Grain reversal patterns for the four selected points of the J-H curve labelled in Fig. 107... 133
Fig. 109: Demagnetization curves simulated for the four stacks with magnetics properties given in Table 43 (configuration #2). The distribution of grain coercivity is illustrated by the XZ patterns in gray scale (black = lower values, white = higher values). The grain reversal patterns at selected points of the J-H curve are also given. 134
Fig. 110: Residual induction map at the top of a Dy-diffused sample at three selected stages (1-remanent state, 2-partial demagnetization before recoil, 3-coercivity state) .$B_{z,moy}$ denotes the averaged value of the residual induction measured in the scanned plane (400 µm over the sample). 136
Fig. 111: Grain reversal patterns simulated for stack #4 and for two selected points of the J-H curve from Fig. 110 (XY planes at the top surface and at the interface with the non-enhanced coercivity zone). 136
Fig. 112: Demagnetization curves obtained by simulation for the input data reported in Table 45.. 138

List of tables

Table 1: Intrinsic magnetic properties at 295 K for $RE_2Fe_{14}B$ compounds. [21] 11
Table 2: Micromagnetic parameters and characteristic length scales for $Nd_2Fe_{14}B$ phase. [24] 11
Table 3: Strategies to improve coercivity. 14
Table 4: Simulation parameters used in [68]. 23
Table 5: Simulation parameters for [50]. 25
Table 6: Simulation parameters for [76] and [70]. 26
Table 7: Simulation parameters for [48]. 29
Table 8: Experimental parameters for GBDP using Dy/Tb-containing powders. 32
Table 9: Experimental parameters for GBDP using Dy/Tb-containing powders. 32
Table 10: Experimental parameters for GBDP using metallic vapor. 34
Table 11: Experimental parameters for GBDP using eutectic compounds. 35
Table 12: Experimental parameters for GBDP using eutectic compounds. 35
Table 13: Intrinsic magnetic properties for the $Nd_2Fe_{14}B$ grain and the $(Dy_{47}Nd_{53})_2Fe_{14}B$ hard shell at T = 300 K and T = 450 K. [81] 36
Table 14: Intrinsic magnetic properties for the $Nd_2Fe_{14}B$ grains, the Dy- and Tb- enriched shells and the GB phase. [105] 37
Table 15: Chemical composition of the strip-casted ribbons used in the thesis. Amounts are given in wt.%. 42
Table 16: Median diameters D50 of the six jet-milled powders used in this work. 43
Table 17: Alternating pulses used for magnetic alignment of the powder. 44
Table 18: Polishing steps before microstructural characterization. 52
Table 19: Columns of magnetic properties in the material parameter input file. 54
Table 20: Columns of the initial magnetization input file. 54
Table 21: Intrinsic magnetic properties used in [119] 55
Table 22: Simulated coercivities compared to the ones of the literature case. 56
Table 23: Experimental magnetic characteristics of samples S1, S2 and S3 (same diameter ϕ = 6 mm). 69
Table 24: Calculated magnetic characteristics of samples S1, S2 and S3. 70
Table 25: Influence of the sample aspect ratio on collective effects. 78
Table 26: Magnetic properties of base magnets in the as-sintered state. 92
Table 27: Coercivity reversibility for successive PSA at 530°C. 92
Table 28: Magnetic properties after PSA at 470, 500, 530, 550 and 600°C. The ± values between parentheses correspond to the standard deviation. 94
Table 29: Intrinsic magnetic properties at 300 K of the different phases of the model. 96
Table 30: Coercivity measured after each fabrication step for the magnets diffused with the eutectic alloy and the intermetallic compound. 99
Table 31: Magnetic properties after GBDP at 920°C for 3 and 12 h, and after PDA at 530°C for 2h. 100
Table 32: Magnetic properties after GBDP at 870°C and 920°C for 3 h, and after PDA at 530°C for 2h. 101
Table 33: Magnetic properties after PDA at 500, 530, 550 and 600°C for 2h. 101
Table 34: Average grain size and thickness of the Dy-rich shells determined from Fig. 82 by image analysis. 105
Table 35: Values of $H_{k,1}$, $H_{k,2}$ and coercivity after each polishing step for the 920°C-3h diffused and reference magnets. 111
Table 36: Values of $H_{k,1}$, $H_{k,2}$ and coercivity after each polishing step for the 920°C-12h diffused and reference magnets. 112

Table 37: Intrinsic magnetic properties at 300 K of the Dy-rich shells. 114
Table 38: Geometrical data for the computation of the Dy concentration profile with the Fisher model. 121
Table 39: Dy volumetric concentration (normalized to Dy surface concentration) averaged over 1-µm-thick shell from the Fisher model. Corresponding Dy elemental maps obtained by SEM-EDX. 124
Table 40: Distance from the grain boundary in µm below which the Dy/Nd-init ratio exceeds the threshold value of 0.1 considered as an indicator of the width of the Dy-rich shell visible on SEM-EDX elemental maps. 124
Table 41: Dy/Nd-init ratio averaged over 1-µm-thick grain shell of Dy diffused sample estimated with the Fisher model. The values between parentheses reflect the estimation of the coercivity increase due to the local Dy enrichment. 127
Table 42: Fraction of the total Dy atoms initially available at the free surface and diffused in successive slices distributed from the sample surface. 128
Table 43: Polycrystalline model configurations for simulated magnetization reversal in Dy-diffused samples. 130
Table 44: Coercivity values for the different stacks. 137
Table 45: Polycrystalline model configurations for simulated magnetization reversal in Dy-diffused samples corresponding to the three experimental diffusion conditions (n_x x n_y = 10 x 10). 138

Glossary

BSE: back-scattered electrons

EDX: energy-dispersive X-ray spectroscopy

FE: finite element

FEMME software: Finite Element MicroMagnEtics software

GBDP: grain boundary diffusion process

GB phase: grain boundary phase

GBs: grain boundaries

GM: global model

HRE: heavy rare earths

LLG equation: Landau-Lifshitz-Gilbert equation

LRE: light rare earths

MM: micromagnetic model

MOKE: magneto-optical Kerr effect

OOMMF: Object Oriented MicroMagnetic Framework

PDA: post-diffusion annealing

PSA: post-sinter annealing

SC: strip-casting

S(T)EM: scanning (transmission) electron microscopy

Introduction

The discovery of Nd-Fe-B magnets in 1984 [1]–[3] constituted an important step in the history of permanent magnets. At that time, the Sm-Co based permanent magnets had to be replaced because Co was a strategic and expensive material. Nd-Fe-B magnets had strong advantages compared to Sm-Co: they had larger saturation magnetization, Nd was much less expensive than Sm and Fe is one of the most abundant elements on Earth. Nd-Fe-B permanent magnets were first used in hard disk drives and speakers. More recently, these magnets play a pivotal part in energy efficient technologies. Since they produce the highest energy density among all commercially available magnets, they play a significant role in motors of electric vehicles and generators of windmills. For instance, higher energy density means lighter and less energy consuming machines. [4]

The outstanding properties of Nd-Fe-B permanent magnets come from the intrinsic magnetic properties of the $Nd_2Fe_{14}B$ phase (magnetocrystalline anisotropy, saturation magnetization) and from their microstructure. Nevertheless, electrical machines operate at about 120-180°C and magnetic properties decrease rapidly with temperature. At 180°C, the anisotropy field of the $Nd_2Fe_{14}B$ phase is reduced to unaccepted values. This impacts directly the coercivity of the magnet which represents its resistance to demagnetization. To maximize coercivity at the operating temperature, a fraction of Nd is substituted with heavy rare earth elements such as Dy with a content depending on the application (see Fig. 1 from [5]). The demand for Dy is particularly high for electrical motors, especially for those of hybrid electric vehicles which can contain more than 5 wt.% of Dy.

However, the Dy magnetic moments couple antiparallel to the Fe ones, leading to a decrease in remanence and thus in the maximum energy density provided by the magnet. In addition, Dy is a strategic element classified as a critical raw material by EU. The supply risk is high since China has a quasi-monopolistic position in the extraction of Dy (more than 98 % of the total world production). Moreover, the price of Dy has been particularly volatile in the last decade. Considered separately, the cost of Dy in magnets could represent more than 50 % of the cost of all other materials. For these reasons, end-users of magnets are very reluctant to use magnets containing Dy.

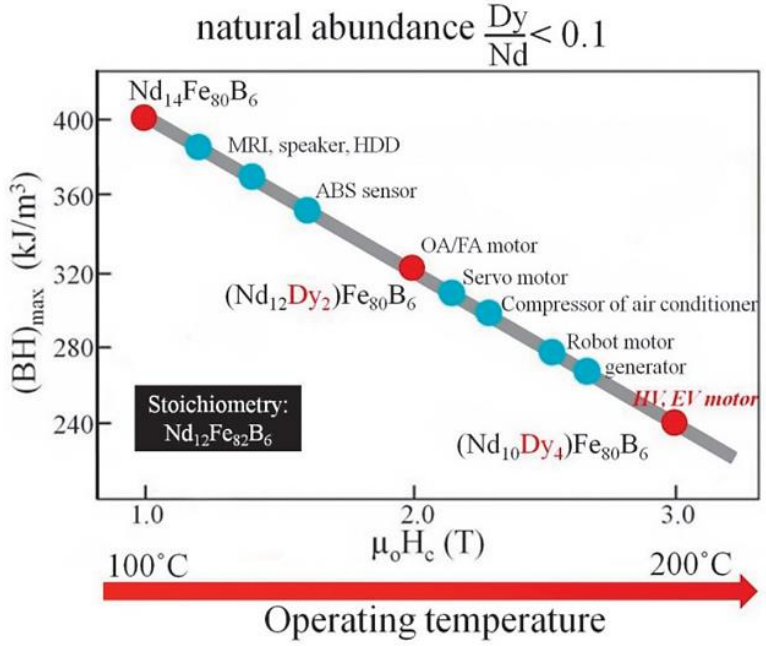


Fig. 1: Maximum energy product $(BH)_{max}$ and coercivity of commercial Nd-Fe-B sintered magnets according to their composition. [5]

Consequently, the major driving force for research and development of Nd-Fe-B permanent magnets is to develop magnets that possess excellent magnetic properties with a reduced content of Dy [4]. This requires a better understanding of the link between microstructure and coercivity in these materials. The key point is the control of the grain size and the distribution of secondary phases at grain boundaries to prevent magnetization reversal and magnetic coupling [6]. Many efforts have been undertaken in the last decade by research groups and the magnet industry to reduce the Dy content in magnets. During this period, significant progresses have also been obtained in the characterization of the local chemistry of grain boundaries at the nanoscale. This allowed a better understanding of coercivity mechanisms in Nd-Fe-B sintered magnets. Furthermore, micromagnetic simulations have shown to be efficient in the description of magnetization reversal in realistic polycrystalline models, taking into account the fundamental role of grain boundaries.

The work presented in this thesis has been developed in the framework of a collaborative action between CEA-LITEN and Institut Néel. The global objective of the thesis is the better understanding of coercivity of Nd-Fe-B sintered magnets by experimental and numerical approaches. The magnets studied here are fabricated on the pilot line at CEA-LITEN by powder metallurgy route. The fundamental activity included preparation of model systems, microstructural and magnetic characterization and numerical modelling.

Nd-Fe-B hard magnets are obtained by liquid phase sintering of an oriented monocrystalline powder. Post-sinter annealing at low temperature enables the optimal distribution of thin Nd-rich phases at grain boundaries [7], [8]. Consequently, grains are mostly exchange-decoupled and it is widely accepted that magnetization reversal occurs via switching of individual grains. However, magnetostatic or dipolar interactions between grains play also an important role in magnetization reversal in such materials. In this work, a first study investigates the demagnetizing field effects in Nd-Fe-B sintered grain-decoupled magnets that can lead to some misinterpretation of the demagnetization curves usually measured on magnets. Two different experimental configurations (open- and closed-circuit) widely used for coercivity measurement are compared experimentally and numerically.

One of the strategies to improve coercivity is the grain boundary diffusion process developed in 2000 [9] and which is now an industrially established technique. It consists in the development of core-shell grains with Dy-rich phases in the outer regions of $Nd_2Fe_{14}B$ grains. In this work, a second study deals with the grain boundary diffusion process performed on Nd-Fe-B sintered magnets using Dy-Co alloys. The coercive properties are progressively improved after Dy diffusion but the rectangularity of the measured demagnetization curves is also deteriorated. Microstructural observations and further magnetic measurements are carried out to establish the link between microstructure and coercivity and also explain the shape of the experimental demagnetization curves. The latter is reproduced via micromagnetic simulations. Moreover, one of the drawbacks of the grain boundary diffusion process is its limitation to thin magnets. It can thus lead to Dy-diffused magnets with coercivity gradient. In the last part, coercivity in graded magnets is discussed with the help of a diffusion model and further micromagnetic simulations.

The present manuscript is organized in five chapters.

Chapter I gives a general introduction on the history and properties of permanent magnets. Then, the microstructure, the fabrication process and the coercivity mechanisms of Nd-Fe-B sintered magnets are presented. Finally, bibliographic researches about micromagnetism and the grain boundary diffusion process are detailed.

Chapter II describes the fabrication process of Nd-Fe-B sintered magnets at CEA-LITEN. The grain boundary diffusion process using Dy-Co alloys is also detailed. Furthermore, the characterization (microstructural and magnetic) and numerical methods used in the thesis are described.

Chapter III deals with the demagnetizing field effects in Nd-Fe-B sintered magnets. The experimental and numerical comparison of demagnetization curves measured in open- and closed-circuit is presented.

Chapter IV concerns the experimental and computational parametric study of the grain boundary diffusion process using Dy-Co alloys performed on Nd-Fe-B sintered magnets. An important aspect is the understanding of the shape of the demagnetization curves measured after Dy diffusion with the help of numerical modelling.

Chapter V constitutes a discussion about coercivity in graded magnets and the reported results are strongly related to those of Chapter IV.

The main results of this work are recalled in the conclusion. The perspectives of research to further progress in the understanding of magnetization reversal processes in Nd-Fe-B sintered magnets are also suggested.

I. From context to coercivity

I.1. History of rare earth permanent magnets

The first discovered permanent magnets were the lodestones that provided a stable magnetic field. Until the turn of the 19th century, magnets were weak, unstable and made of carbon steel. Some improvements were made with the discovery of cobalt magnet steels in Japan in 1917. Then, the performances of permanent magnets have been continuously improved since the discovery of the alnicos (Al/Ni/Co alloys) in the 30's [10]. This evolution is represented by the increase in the maximum energy product $(BH)_{max}$. This latter is a figure of merit for permanent magnets and represents the maximum energy density that, for a magnet of given volume, can be transformed into work in a machine that uses the magnet. Fig. 2 shows the rapid improvement in the performances of magnets encountered in the middle of the 60's when the first generation of transition metals and rare-earth alloys, such as Sm-Co systems, was developed. However, in the late 70's, the price of Co increased drastically due to an unstable supply situation in the Democratic Republic of Congo. At that time, Sm-Co permanent magnets showed the highest $(BH)_{max}$ and the research community was then forced to replace these magnets. A few years later, in 1984, Nd-Fe-B based permanent magnets were developed for the first time by Sagawa *et al.* [1] using powder metallurgy techniques at Sumitomo Special Metals, and in parallel by Croat *et al.* [2], [3] using melt-spinning technique at General Motors. As shown by the below graph, in almost a century, $(BH)_{max}$ has been enhanced, starting from ≈1 MGOe for steels at the early part of the century, to ≈56 MGOe for Nd-Fe-B magnets during the past twenty years [4], [11].

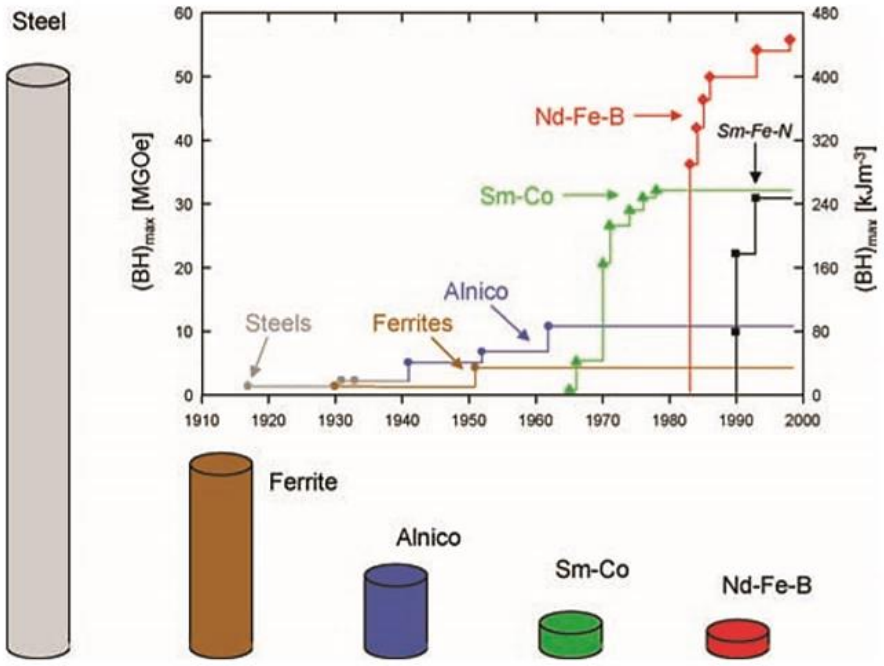


Fig. 2: Evolution of $(BH)_{max}$ at room temperature for permanent magnets during the 20th century and their relative volume for the same energy density. [4]

Moreover, for the same energy density, newly developed Nd-Fe-B magnets enable an important reduction in volume for their applications, compared to former systems. Today, more than 80% of rare earth permanent magnets implemented by end users are Nd-Fe-B magnets. [4]

While the maximum energy product represents the strength of a magnet, the resistance to demagnetization is crucial for the design of electrical machines, regarding the operating temperature.

This second characteristic, named coercivity, will be introduced in more details in the following since large efforts in magnet industry and research groups have been engaged in the three last decades to improve this property. To further optimize magnetic properties of Nd-Fe-B magnets, emphasis of research is nowadays to better understand the link between magnetization reversal (coercivity) mechanisms and microstructure in these materials. [6]

I.2. Intrinsic and extrinsic properties of permanent magnets

Rare earth permanent magnets are mainly constituted by ferromagnetic materials that exhibit remarkable basic properties. These magnetic properties are generally seen as "intrinsic" since they are completely determined by the atomic composition and the structure of the ferromagnetic phases. It is important to keep in mind that standard magnet characteristics, widely considered for design purposes, are rather "extrinsic" since the magnet performances are strongly affected by the process parameters [12]. In this section, the basic properties of hard ferromagnetic materials are briefly recalled in order to point out the influence of the microstructure on them.

I.2.1. Intrinsic magnetic properties

I.2.1.1. Definition of the macroscopic magnetization

The macroscopic magnetization of a magnetic material is denoted M and corresponds to the volume density of internal magnetic moments. This amount is therefore given in $A.m^2/m^3$, thus in A/m, while the polarization of the material is given by $J = \mu_0 M$, with J in Tesla and $\mu_0 = 4\pi \times 10^{-7}$ T.m/A the permeability of free space. When an external magnetic field H (in A/m or Oe) is applied on the material, the magnetic induction B is expressed as $B = \mu_0(H+M)$, with B in Tesla [13]. The macroscopic characterization of magnetic materials generally consists in the measurement of the evolution of B (or J) as a function of H. This reveals how magnetization develops in the material and helps determining the most energy-favorable configurations of the magnetization distribution. In this frame, permanent magnets display specific features that are introduced below.

I.2.1.2. Hard ferromagnetism

A ferromagnetic material displays a spontaneous macroscopic magnetization that comes from the ordering of individual microscopic magnetic moments. These latter are carried by atoms and result from the summation of spin and orbital moments of electrons. Transition metals (Fe, Co…) display the largest magnetic moment per atom (at room temperature). The ordering is related to the exchange interaction occurring between the magnetic moments.

A material is hard ferromagnetic when the microscopic magnetic moments are preferentially oriented along a specific crystallographic direction. This property depends on the magnetocrystalline anisotropy of the atomic lattice. These three features (high magnetic moment, ordering and anisotropy) are required for hard magnets and are fulfilled with the magnetic phase that constitutes them.

In these materials, neighboring magnetic moments are strongly coupled through exchange interactions. Exchange occurs between electronic orbitals and induces an internal energy minimization when the moments are aligned in parallel directions (ferromagnetism) or in antiparallel directions (ferrimagnetism). Basically, the exchange energy is given by $W_{ex} = \sum_{i,j} A m_i m_j$ for which the summation is extended to all couples of microscopic magnetic moments. However, exchange interactions are a short range effect that develops at a distance roughly equal to the lattice parameter. The amount A characterizes the microscopic exchange stiffness and is related to the shape of electronic orbitals and the crystal structure.

This trend towards parallel or antiparallel distribution of the magnetic moments gives rise to magnetic ordering at finite temperature and zero field. This results in the occurrence of the macroscopic spontaneous magnetization M_S. Furthermore, ferromagnetic ordering is limited by the thermal agitation and disappears above the Curie temperature T_C (in K). As expected, the Curie temperature is proportional to the exchange stiffness:

$$A \approx \frac{K_B T_C}{2a_0} \qquad \text{[Eq. 1]}$$

with a_0 the lattice parameter of the considered structure. The exchange stiffness is expressed in J/m and determines also the exchange length L_{ex} (in nm). This quantity is the length below which atomic exchange interactions dominate dipolar interactions. It is given by:

$$L_{ex} = \sqrt{\frac{2A}{\mu_0 M_S^2}} \quad \text{[Eq. 2]}$$

Magnetic anisotropy corresponds to the existence of energetically favorable directions for magnetization, related to the crystalline axes (magnetocrystalline anisotropy). In a uniaxial crystallographic system, the anisotropy energy E_a is defined as:

$$E_a(\theta) = K_1 sin^2(\theta) + K_2 sin^4(\theta) + K_3 sin^6(\theta) + \cdots \qquad \text{[Eq. 3]}$$

K_i is the i-th order anisotropy constant in MJ/m^3 and θ is the angle between the magnetization direction and the easy axis. Only the first term is generally considered for Nd-Fe-B systems. In the absence of external magnetic field, magnetization will preferentially lie along the z-easy axis, with either the positive or negative orientation. The energy needed to align magnetization along any direction perpendicular to the easy axis is the anisotropy energy.

I.2.1.3. Magnetic domains

Magnetic domains form in a magnetic material as a result of the magnetostatic energy reduction. They are regions in which magnetization is uniform, while its direction may vary from one domain to another. Magnetic domains are also called Weiss domains. Between two magnetic domains of opposite magnetization, the magnetization vector has to change its direction. The transition area is called a domain wall. A particular type is the Bloch domain wall for which magnetization rotates in the plane of the domain wall. [13]

The transition length of magnetization reversal is called domain wall width and noted δ_W (in nm). In the particular case of a Bloch domain wall, it can be approximated by:

$$\delta_W \approx \sqrt{\frac{A}{K_1}} \qquad \text{[Eq. 4]}$$

Moreover, the associated domain wall energy γ_W (in J/m^2) can be expressed as:

$$\gamma_W \approx \sqrt{AK_1} \qquad \text{[Eq. 5]}$$

The hysteresis loop is the most common characterization of a magnetic material, underlying many processes that imply magnetic domains. Extrinsic magnetic properties that can be determined from the hysteresis loop depend strongly on the above introduced parameters.

I.2.2. Extrinsic magnetic properties

I.2.2.1. Hysteresis loop of a permanent magnet: remanence and coercivity

When an external magnetic field H is applied to a permanent magnet which is originally in a demagnetized state, the magnetization M follows the initial magnetization curve that increases rapidly and then approaches an asymptotic value called the saturation magnetization M_S. When the magnetic field is decreased from the saturated state, the magnetization gradually decreases and at zero field strength, it reaches a non-zero value called the remanent magnetization or remanence M_R. Further increase of the magnetic field in the negative sense results in a continued decrease of magnetization, which finally falls to zero. The absolute value of the field at this point is called the coercive field or coercivity H_C. It represents the resistance to demagnetization of the permanent magnet. Another definition says that the magnetic susceptibility (*i.e.* the quantity dM/dH) is maximal at the coercivity point. The curve in the second quadrant from M_R to the zero magnetization state is referred as the demagnetization curve. Further increase of H in the negative sense results in a decrease of M until reaching the $-M_S$ value. When H is then reversed again to the positive sense, M increases again and the loop is closed (see Fig. 3). [14]

This dependence of the magnetization as a function of the applied magnetic field constitutes the hysteresis loop of a permanent magnet. The evolution of the magnetic induction B or of the polarization J with H are also hysteresis loops. Hard magnets are difficult to demagnetize: they exhibit a larger coercive field and thus a broader hysteresis loop than soft magnets.

I.2.2.2. Microstructure related magnetic properties

Extrinsic magnetic properties depend on intrinsic properties and on microstructure. The remanence M_R is directly proportional to M_S, depends on the porosity of the material and on the degree of alignment of magnetic easy axes of the hard magnetic phase. The coercive field H_C depends on the magnetocrystalline anisotropy, on the presence of defects in the microstructure and on other microstructural features such as the grain size, determined by the fabrication process. [6], [12]

H_C determines if the magnet is hard and M_R directly impacts the maximum energy product $(BH)_{max}$ (in kJ/m^3 or MGOe). This latter is a figure of merit for permanent magnets. On the hysteresis loop (see Fig. 3), $(BH)_{max}$ is the area of the largest rectangle that can be inserted under the demagnetization curve. Its maximum possible value for an ideal system is $\mu_0 M_S^2/4$. [12]

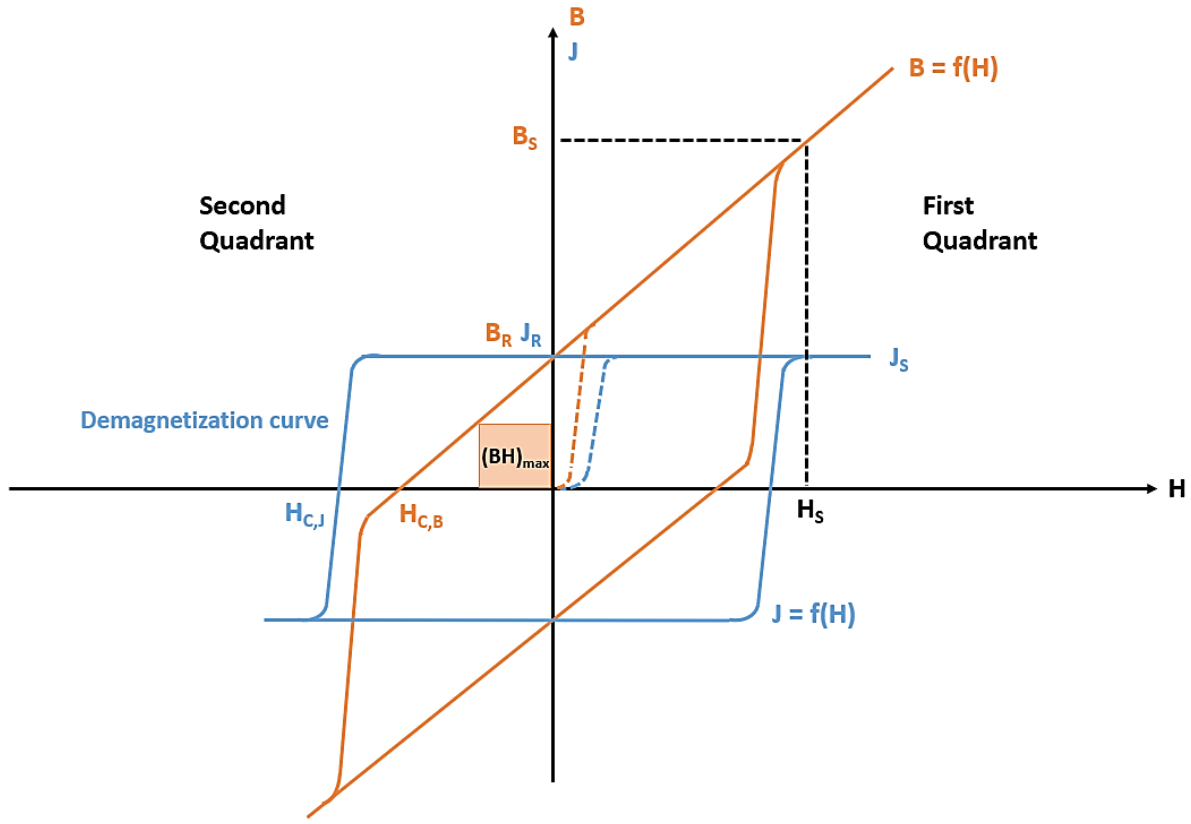


Fig. 3: Hysteresis loop for a permanent magnet with intrinsic and extrinsic magnetic properties, and with the $(BH)_{max}$ rectangle in the second quadrant. Adapted from [15], [16]

I.3. Magnetization reversal mechanisms

I.3.1. Coherent rotation: the Stoner-Wohlfarth model

The Stoner-Wohlfarth model [17] describes magnetization reversal in a ferromagnetic crystal by coherent rotation involving all magnetic moments (*i.e.* without formation of domains). In such system, the magnetic moments are considered to remain parallel. As a result, the exchange interaction is neglected in the model and the total energy of the system is the summation of the Zeeman energy (coming from the interaction with the external field H_{ext} and that tends to align the moments along H_{ext}), and the magnetocrystalline energy that prevents the moments from deviation from the easy axes. Magnetization is considered to be homogeneous and the applied field is along the easy axis direction, as shown in Fig. 4.

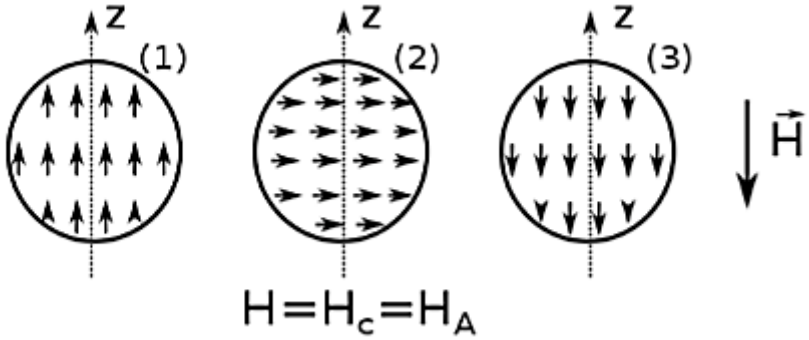


Fig. 4: Coherent rotation of magnetization vectors described by the Stoner-Wohlfarth model. [18]

In the case of uniaxial systems with strong magnetocrystalline anisotropy, there is only one easy axis for magnetization. During reversal, magnetization changes its direction, but not its magnitude. Cases (1) and (3) correspond to two energy minima, whereas case (2) is the hard axis magnetization configuration. The external field required to reverse the magnetic moment and defined as the anisotropy field H_A is given by:

$$H_A = \frac{2K_1}{\mu_0 M_S} \qquad \text{[Eq. 6]}$$

The anisotropy field in Nd-Fe-B magnets, calculated from K_1 and M_S intrinsic properties, is around 8 T at room temperature. In practice for Nd-Fe-B magnets, the measured coercivity is only about 20-30 % of the theoretical anisotropy field given by the Stoner-Wohlfarth model. This discrepancy is known as Brown's paradox [19] and is attributed to the presence of defects in the microstructure that exhibit locally reduced magnetocrystalline anisotropy [6]. This has been understood by introducing the concept of the activation volume that represents the smallest volume in which magnetization reversal begins before macroscopic propagation.

I.3.2. Nucleation vs pinning controlled magnetization reversal

Magnetization reversal consists of two steps: it begins at defects, corresponding to the nucleation of reversed domains, and then propagation of these reversed domains within the entire microstructure occurs. Depending on their respective field values, either nucleation or propagation could be the process that triggers magnetization reversal and limits coercivity.

After nucleation, reversal may propagate in the entire system for a given magnetic field value: it is in this case controlled by nucleation. Alternatively, the reversed domain may be pinned at magnetic heterogeneities: reversal is, in this case, controlled by pinning (*i.e.* propagation-driven reversal). Fig. 5 depicts magnetization configuration in the case of nucleation-pinning reversal:

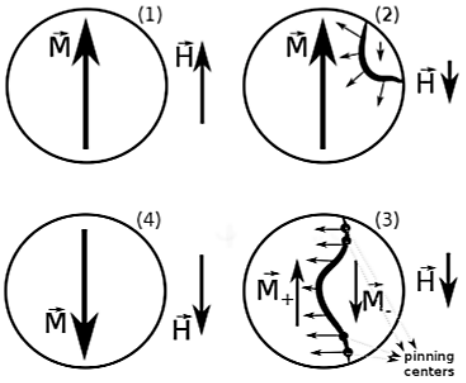


Fig. 5: Magnetization configuration in the case of nucleation-pinning reversal. [18]

Case (1) corresponds to saturation. The direction of the applied field is then reversed and nucleation starts at (2) with the formation of a small domain with reversed magnetization and its respective domain wall. At (3), this latter starts to move and then encounters defect points that act as pinning centers for the domain wall. At (4), a bigger field value is applied for the depinning of the domain wall, to finally achieve saturation in the opposite direction.

Two models based on the micromagnetic approach have been proposed to describe coercivity in Nd-Fe-B permanent magnets and to determine the mechanism controlling magnetization reversal. They will be presented in Section I.5.2.

It is worth noting that microstructural heterogeneities in Nd-Fe-B magnets have a negative effect on coercivity since they act as nucleation points for reversal. However, in other systems such as Sm-Co magnets, heterogeneities may also act as pinning sites, preventing the propagation of reversed domains, and may therefore be crucial for coercivity enhancement. This underlines the need to control the microstructure to obtain excellent magnetic properties for permanent magnets.

I.4. Nd-Fe-B sintered magnets: fabrication and microstructure

I.4.1. Microstructure of a Nd-Fe-B sintered magnet

The microstructure of Nd-Fe-B sintered magnets typically consists of single crystalline $Nd_2Fe_{14}B$ (at.%) hard magnetic grains with a size between 3 and 10 µm. These grains are surrounded by a continuous layer of an amorphous Nd-rich phase with a thickness of a few nm. Larger Nd-rich phases are located at grain triple junctions. [6], [20]

On the below BSE-SEM image (Fig. 6), taken from [6], the $Nd_2Fe_{14}B$ single crystalline grains are in grey. The white regions correspond to Nd-rich phases. The bright contrast between grains is the continuous nm-thick grain boundary (GB) phase.

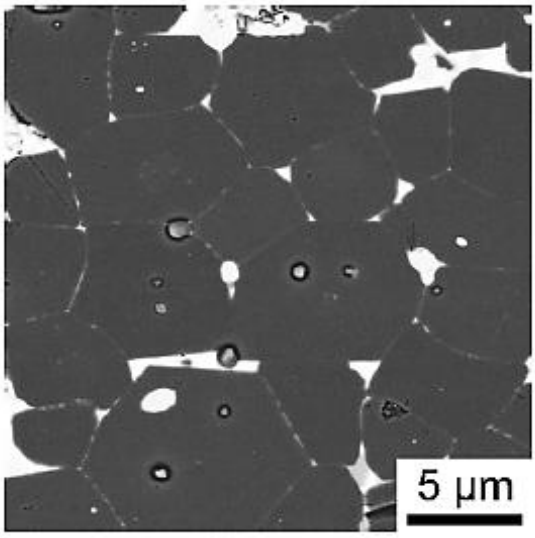


Fig. 6: BSE-SEM image of the typical microstructure of Nd-Fe-B sintered magnets. [6]

I.4.1.1. The $Nd_2Fe_{14}B$ hard magnetic phase

The $Nd_2Fe_{14}B$ phase (also called T_1 or ϕ-phase) crystallizes in the *$P4_2/mnm$* space group and has a tetragonal symmetry. The unit cell parameters are a = 8.8 Å and c = 12.2 Å (see Fig. 7) [21]. The magnetization easy axis is along c-axis above 135 K but it starts to tilt away from the c-axis below this temperature (known in the literature as the spin reorientation temperature) [22].

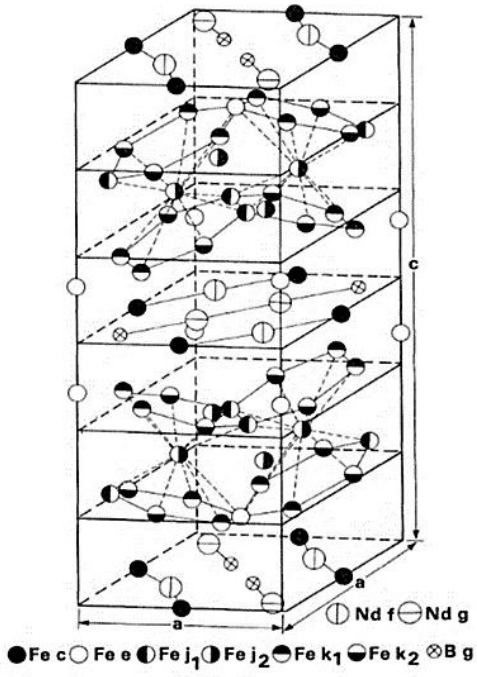


Fig. 7: Unit cell crystallographic structure of the $Nd_2Fe_{14}B$ phase. [21]

In the unit cell, Nd atoms with their 4f electron states are responsible for the strong magnetocrystalline anisotropy. Fe atoms with their 3d electron bands are responsible for the high magnetic moment. The Fe magnetic lattice couples parallel with the light rare earths (LRE) magnetic lattice [23]. B atoms contribute to the thermodynamic stability of the entire structure [21].

The substitution of Nd with other RE elements leads to an important modification of the intrinsic magnetic properties of the phase. For example, the replacement of Nd by heavy rare earths (HRE) such as Dy and Tb increases the anisotropy field, whereas this latter is reduced when Nd is substituted with Ce and Gd. Moreover, the saturation magnetization of $HRE_2Fe_{14}B$ phases is decreased compared to the one of $LRE_2Fe_{14}B$, because of the antiferromagnetic coupling of magnetic moments. Table 1 gives intrinsic magnetic properties at 295 K for some $RE_2Fe_{14}B$ compounds: the saturation polarization μ_0M_S, the anisotropy field μ_0H_A and the Curie temperature T_C.

Phase	μ_0M_S (T)	μ_0H_A (T)	T_C (K)
$Ce_2Fe_{14}B$	1.17	2.60	424
$Pr_2Fe_{14}B$	1.56	7.50	565
$Nd_2Fe_{14}B$	1.60	7.30	585
$Gd_2Fe_{14}B$	0.89	2.4	661
$Tb_2Fe_{14}B$	0.70	≈22	620
$Dy_2Fe_{14}B$	0.71	≈15	598

Table 1: Intrinsic magnetic properties at 295 K for $RE_2Fe_{14}B$ compounds. [21]

In addition, important micromagnetic parameters and characteristic length scales are given in Table 2 for the $Nd_2Fe_{14}B$ phase: the exchange stiffness A, the magnetocrystalline anisotropy constant K_1, the exchange length L_{ex}, the domain wall width δ_W and the domain wall energy γ_W.

A (pJ/m)	K_1 (MJ/m^3)	L_{ex} (nm)	δ_W (nm)	γ_W (mJ/m^2)
8.0	4.9	1.9	3.9	25

Table 2: Micromagnetic parameters and characteristic length scales for $Nd_2Fe_{14}B$ phase. [24]

I.4.1.2. Nd-rich secondary phases

In Nd-Fe-B sintered magnets, there are several different Nd-rich phases, including metallic and oxide phases. The larger and more rounded Nd-rich regions are usually oxides, whereas the thin layers in the $Nd_2Fe_{14}B$ grain boundaries are metallic in character. [25]–[27]

These secondary phases play a major role on magnetic properties. The remanence is reduced in proportion to the volume fraction of secondary phases [6]. Furthermore, the amorphous metallic Nd-rich phases reduce or remove defects at the surface of $Nd_2Fe_{14}B$ grains. It has also been generally accepted that these phases do not contain a significant amount of Fe and therefore are paramagnetic, thus guaranteeing exchange decoupling of the $Nd_2Fe_{14}B$ grains, leading to high coercivity [7], [28]. More recently, Sepehri-Amin *et al.* [27] used atom probe elemental analysis to estimate the chemical composition of Nd-rich intergranular layers and claimed that the phase is rich in Fe. They prepared then a 50 nm-thick layer of the same composition and measured a saturation magnetization of about 400 emu/cm^3 (≈ 0.5 T). They concluded that the GB phase is soft ferromagnetic and the $Nd_2Fe_{14}B$ grains are most likely to be exchange-coupled. In this case, magnetization reversal is controlled by the pinning of domain walls at this GB phase. But this conclusion is still not generally accepted by the research community, because measuring the chemical composition of nm-thick layers between µm-sized $Nd_2Fe_{14}B$ grains is experimentally non-trivial [6].

As said before, it has been shown that Nd-rich phases at multijunction sites in Nd-Fe-B sintered magnets consist of both metallic and oxide compounds [25], [26]: face-centered cubic (fcc) metallic Nd, double hexagonal close packed (dhcp) metallic Nd, a-type Nd_2O_3 (at.%), c-type Nd_2O_3 and NdO (at.%). Hrkac *et al.* [29], [30] studied the coercivity dependence on the interfaces between $Nd_2Fe_{14}B$ grains and these Nd-rich phases, using EBSD, finite element micromagnetics and atomistic models. Indeed, such interfaces can distort the crystal structure, resulting in distorted layers with lower magnetocrystalline anisotropy that act as nucleation sites for magnetization reversal, being detrimental for coercivity. The metallic dhcp Nd produces the largest distortions in $Nd_2Fe_{14}B$, followed by a-type Nd_2O_3, and then by metallic fcc Nd, c-type Nd_2O_3 and NdO, which all produce similar distortion. As a result, the removal of metallic dhcp Nd phases from the microstructure is crucial to improve coercivity.

Sasaki *et al.* [31] reported quite recently that there are two types of GB phases in a standard sintered Nd-Fe-B magnet: one is the crystalline GB phase perpendicular to the easy-axis of $Nd_2Fe_{14}B$ grains with a Nd content higher than 60 at.% and the other is the amorphous GB phase parallel to the c-axis of $Nd_2Fe_{14}B$ grains with a lower content of Nd (about 35 at.%). This latter GB phase is assumed to be ferromagnetic and the intergrain exchange coupling in Nd-Fe-B sintered magnets is therefore anisotropic. This anisotropic nature in the chemical composition of the grain boundaries was also investigated by Zickler *et al.* [32].

For Nd-Fe-B sintered magnets, magnetic properties such as coercivity and remanence depend strongly on the magnet microstructure. This latter must be controlled during the fabrication process.

I.4.2. Industrial production process: sintering

The industrial sintering process of Nd-Fe-B permanent magnets is schematically shown in Fig. 8:

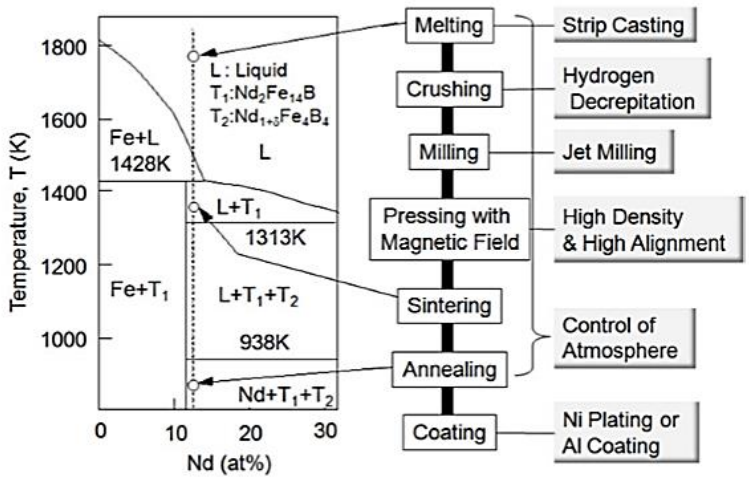


Fig. 8: Industrial production route of Nd-Fe-B sintered magnets and pseudo-binary phase diagram (Nd/B = 2) of the Nd-Fe-B ternary system. [11]

The alloy with a typical composition $Nd_{15}Fe_{77}B_8$ (at.%) is produced via a rapid solidification technique, called "strip-casting". The next step is the powder production from the base ingot. This latter is hydrogen-decrepitated and further milled into a fine single crystalline powder, the particle size of which lies between 3 and 10 µm. This powder is then filled in a mold, aligned in a magnetic field and compacted. The obtained green compact is finally sintered and annealed afterwards at lower temperature. The magnet is coated to be protected against oxidation.

The individual steps of the industrial sintering process will be described in more detail in Section II.1 and II.2. Other production routes exist for Nd-Fe-B permanent magnets, such as the HDDR process and hot-deformation [28], that will not be covered in this work.

I.4.3. Application fields and limitations

Nd-Fe-B permanent magnets have the highest $(BH)_{max}$ at room temperature. They play a significant role in energy applications, such as in the motors of hybrid electric vehicles and in the generators of windmills. They contribute to both the saving of electric power and the reduction of CO_2 emissions in these devices [4]. However, these devices have operating temperatures of about 120-180°C and magnetic properties such as remanence and coercivity decrease rapidly with temperature. As a result, coercivity is reduced to unacceptable values at maximum operating temperatures. An increase in coercivity at room temperature is therefore needed.

One way of improving coercivity of Nd-Fe-B magnets is to substitute some Nd atoms with HRE such as Dy or Tb. This leads to an increase of the anisotropy field and to coercivity enhancement. Nevertheless, the substitution of Nd with Dy has also some major drawbacks. For instance, Dy addition leads to a decrease of the remanence, because of the antiferromagnetic coupling (see Section I.4.1.1), and it directly impacts the $(BH)_{max}$ value. Furthermore, Dy is a critical and strategic element whose price is high and fluctuating. Most of the known Dy resources are in China and this monopolistic market situation led to the "rare earth crisis" in 2011. At that time, the price of Dy rose considerably to 3400 $/kg (2018: 200 $/kg).

One major objective of the research community is now to develop Nd-Fe-B permanent magnets that possess excellent magnetic properties at room temperature with a reduced content of HRE. A good control of the microstructure during the fabrication process is therefore needed.

I.4.4. State of the art: current strategies to improve coercivity

Since the discovery of Nd-Fe-B magnets, coercivity has gradually been improved thanks to a better control of the fabrication process. Furthermore, in the last two decades, description of coercivity in Nd-Fe-B magnets has also been improved, particularly thanks to developments in microstructural characterization. The better understanding of magnetization reversal processes led to recent coercivity enhancement in Nd-Fe-B magnets. [4], [20].

Current strategies to improve coercivity are given in Table 3 and will be further detailed in the following:

Strategies	Mechanism	Assessment
Grain size reduction	Reduced stray field in the vicinity of GB	Numerical modelling: the stray field decreases with grain size
Defect reduction at GB	Amorphous phase formed during annealing	SEM/TEM characterization
Exchange decoupling of grains	Formation of a thin and continuous non-magnetic GB phase during annealing	SEM/TEM characterization Numerical modelling
HRE diffusion at GB	Enhanced anisotropy in the vicinity of GB	SEM/TEM characterization Numerical modelling

Table 3: Strategies to improve coercivity.

I.4.4.1. Grain size reduction

Coercivity is known to be improved with the reduction of grain size (see Fig. 9). The limit grain size, below which oxidation occurs, is 2.5 µm for the conventional fabrication process (jet milling under nitrogen atmosphere and pressing) and 1 µm for the "pressless" process (jet milling under helium atmosphere and without pressing), developed by the research team of Sagawa. Sepehri-Amin *et al.* [33] fabricated high-coercivity and Dy-free Nd-Fe-B sintered magnets with a grain size of about 1 µm, using this "pressless" sintering process. The coercivity of the as-sintered state was 1362 kA/m, far better than the value for conventional magnets with a grain size of 5 µm (around 950 kA/m). More recently, Sagawa *et al.* [34] developed the "new pressless" process to achieve better efficiency, alignment degree and homogeneity of magnets.

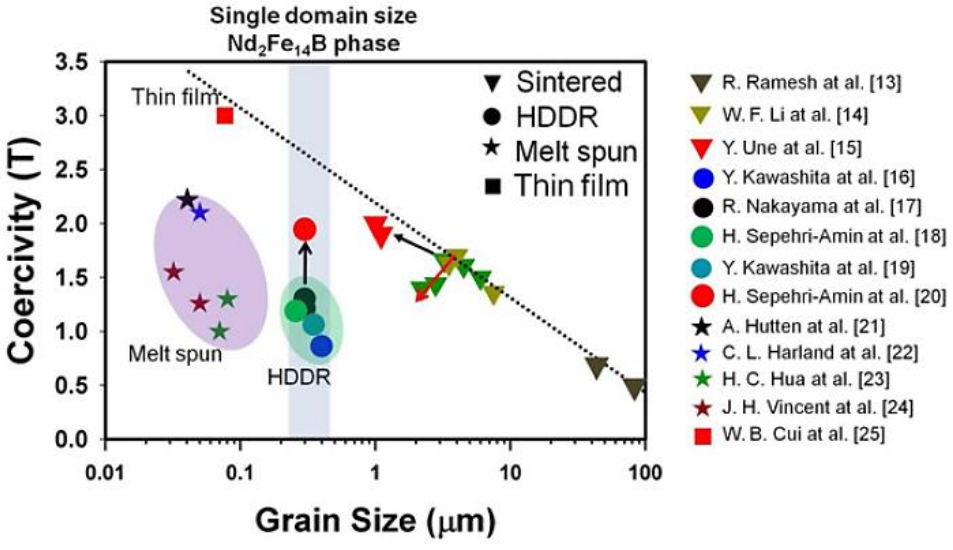


Fig. 9: Evolution of coercivity with grain size for sintered magnets (triangle symbols). [20]

Coercivity enhancement caused by the reduction of grain size can be interpreted in two ways. Ramesh *et al.* [35] calculated hysteresis loops of polycrystalline Nd-Fe-B sintered magnets and suggested that the coercivity increase with the reduction of the grain size, following a logarithmic dependence, is explained by the smaller defect density on the grain surface. Smaller grains are therefore less likely to act as nucleation points for magnetization reversal. More recently, Bance *et al.* [36] used numerical modelling to show that the logarithmic decay of coercivity with increasing grain size comes from the logarithmic increase in the demagnetizing field near the edges of a grain. Magnetostatic interactions are thus less important for smaller grain size.

I.4.4.2. Defect reduction at GB

Post-sinter annealing (PSA) at relatively low temperatures (< 900K) leads to a tremendous increase in coercivity. PSA depends strongly on the magnet composition and the coercivity optimum is reached for a given PSA temperature. In the original work of Sagawa *et al.* [1], optimal magnetic properties for Nd-Fe-B sintered magnets were obtained after annealing at 883K (610°C). Moreover, Shinba *et al.* [8] performed two-stage PSA: at 1073K (800°C) followed by 773K (500°C). They suggested that PSA at temperatures above the Nd-Fe-B eutectic point at 938K (665°C) leads to the formation of a small amount of liquid phase and to an uniform distribution of the Nd-rich phase, forming the nm-thick GB phase. The second PSA, performed below the eutectic point, smoothes grain boundaries and decreases defect density, thus preventing nucleation of reversal domains. After PSA, continuous thin layers of amorphous Nd-rich phase are found along the grain boundaries.

I.4.4.3. Exchange decoupling of grains

- Cu, Al and Co

The addition of some elements in the base magnet composition has also an important impact on magnetic properties. This combined with an optimized PSA increases magnetic properties.

The addition of Cu leads to coercivity enhancement, even in very small proportion (0.2 at.%). Cu doesn't penetrate the hard magnetic phase and forms a eutectic compound with Nd with a melting temperature of 508°C [37]. Cu decreases significantly the melting temperature of the Nd-rich phase leading to a better wettability of the intergranular phase, when PSA is done at a temperature near the eutectic point [7], [27], [38], [39]. After PSA, Cu has been shown to segregate at grain boundaries: this was observed by Kim *et al.* [40] using STEM-EDX technique and by Sepehri-Amin *et al.* [27] by means of 3D atom probe tomography. The formation of such a Cu-rich layer leads to exchange decoupling between $Nd_2Fe_{14}B$ grains which is beneficial to coercivity.

According to Strzeszewski *et al.* [41] and Knoch *et al.* [42], the addition of Al promotes wettability of the intergranular phase. Moreover, Mottram *et al.* [43] and Sadullahoglu *et al.* [44] showed that Al penetrates the hard magnetic grains and hence decreases remanence. Nevertheless, Al leads also to coercivity improvement by the formation of the paramagnetic $Nd(Fe,Al)_2$ phase that reduces magnetic coupling between grains.

In addition, Mottram *et al.* [45] studied the role of Co as addition element in Nd-Fe-B sintered magnets. Co substitutes Fe of the hard magnetic phase and increases the Curie temperature. However, it also contributes to the formation of the intergranular and ferromagnetic $Nd(Fe,Co)_2$ phase that is detrimental for coercivity.

Al, Cu and Co can be added at the same time in the base composition to combine their effects and finely tune magnetic properties (see Chapter IV).

- Ga

In 2016, Sasaki *et al.* [46] characterized the microstructure of Ga-doped Nd-Fe-B sintered magnets of composition $Nd_{11.6}Pr_{3.7}Fe_{77.1}B_{5.1}Cu_{0.1}Co_{1.0}Al_{0.9}Ga_{0.5}$ (at.%). GB chemistry after PSA was studied using SEM-EDX and aberration-corrected STEM. Ga has been shown to enhance wettability of grain boundaries, because of the formed $Nd_6(Fe,Ga)_{14}$ (at.%) phase located at triple junctions. The GB phase has the composition $(Nd,Pr)_{90.4}Fe_{3.4}Cu_{5.4}Ga_{0.8}$ (at.%), with a small amount of Fe, and has a thickness of 10 nm. This phase is then assumed to be non-ferromagnetic and decouples hard magnetic grains, explaining the 1.8 T (1432 kA/m) coercivity obtained after PSA. This value is achieved for an average grain size of 6 µm and further grain size refinement could lead to even higher coercivity values.

In 2017, Soderznik *et al.* [47] observed magnetization reversal of the above exchange-decoupled Ga-doped and of conventional Nd-Fe-B sintered magnets, by magneto-optical Kerr effect (MOKE) microscopy. In the standard magnet (with exchange-coupled grains), reversed domains suddenly propagate throughout many neighboring grains along the easy axis. Such a cascade type of magnetic domain propagation is only observed in the standard magnet. On the contrary, the Ga-doped Nd-Fe-B magnet (with exchange-decoupled grains) reveals switching of individual grains. The cascade propagation of magnetization reversal is, in this case, suppressed by the thick non-magnetic GB phase. The hypothesis of exchange-decoupled grains seems to be valid.

In 2018, Xu *et al.* [48] investigated the microstructure of Dy-free Nd-Fe-B sintered magnets that contain 0.1 at.% of Ga. These magnets show a less important gain in coercivity after PSA but a better rectangularity of the demagnetization curve, compared to magnets containing 0.5 at.% of Ga, as shown on the below demagnetization curves in Fig. 10. Note that the magnets containing 0.1 at.% of Ga have finer $Nd_2Fe_{14}B$ grains and a higher Al concentration in their base composition.

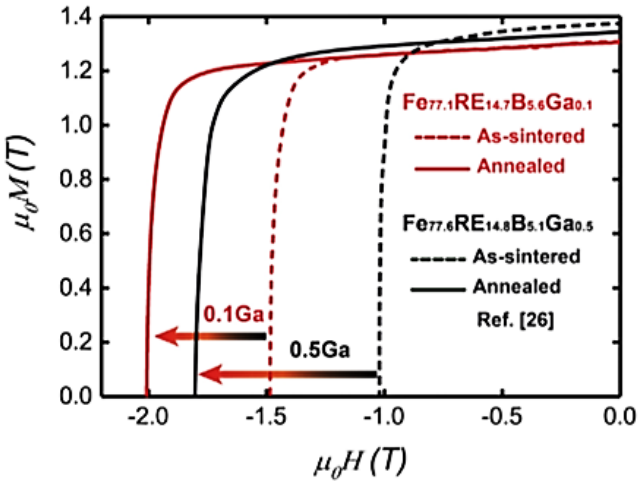


Fig. 10: Demagnetization curves of as-sintered (dashed curves) and post-sinter annealed (solid curves) Nd-Fe-B sintered magnets containing 0.1 at.% (red) and 0.5 at.% Ga (black). [46], [48]

Xu *et al.* found a high Fe concentration in the GB phase of magnets containing 0.1 at.% Ga: the intergranular phase is assumed to be ferromagnetic and grains are thus thought to be exchange-coupled. This explains the better rectangularity of the demagnetization curves. In this case, coercivity is governed by the pinning of reversed magnetic domains at this ferromagnetic GB phase, accounting for the observed coercivity increase, even with a smaller Ga addition. In conclusion, Ga-doped Nd-Fe-B sintered magnets are good candidates to achieve very high coercivity at room temperature and without the use of HRE.

I.4.4.4. HRE diffusion at GB

HRE can be incorporated into Nd-Fe-B sintered magnets by the grain boundary diffusion process. The latter enables the diffusion of HRE mainly along grain boundaries, as well as the formation of HRE-rich shells with enhanced anisotropy field in the outer regions of $Nd_2Fe_{14}B$ grains. This process will be described in further detail in Section I.6.

In addition to the development of microstructural characterization in the past years, micromagnetic simulations plays now an important role in a quantitative understanding of magnetization reversal processes in Nd-Fe-B permanent magnets, in relation with some microstructural features.

I.5. Micromagnetic simulations and models

I.5.1. Micromagnetic simulations (Landau-Lifshitz-Gilbert formalism)

Micromagnetic simulations treat a ferromagnetic material as an assembly of small magnetization vectors and predicts the magnetization states and dynamics by solving a time-evolution equation [49]. They are generally based on two assumptions:

- The magnetization M and all other quantities are continuous functions of the space variable **r**.
- The norm M_S of the magnetization vector is constant and uniform in any homogeneous material, and at zero or finite temperature. [13]

Based on these two assumptions, constant magnetization modulus equation $\boldsymbol{M_S}(\boldsymbol{r}) = M_S\boldsymbol{m}(\boldsymbol{r})$ can be written, for which **m**(**r**) is the unit vector to describe magnetization distributions.

I.5.1.1. Landau-Lifshitz-Gilbert (LLG) equation for ferromagnetic materials

The time evolution of magnetization is computed at different applied magnetic fields by solving the Landau-Lifshitz-Gilbert (LLG) differential equation:

$$\frac{d\boldsymbol{m}}{dt} = \gamma\boldsymbol{m} \times \boldsymbol{H_{eff}} + \alpha(\boldsymbol{m} \times \frac{d\boldsymbol{m}}{dt}) \qquad \text{[Eq. 7]}$$

γ is the gyromagnetic ratio and α is a damping factor. The first right-hand side term describes the magnetization precession around the effective magnetic field $\mathbf{H_{eff}}$. The second right-hand side term describes the damping process that leads magnetization to the minimum energy state, parallel to the effective field. This latter is also the negative derivative of the total Gibb's free energy with respect to the magnetization [50]:

$$\mu_0\boldsymbol{H_{eff}} = -\frac{\delta E_{TOT}}{\delta \mathbf{m}} \qquad \text{[Eq. 8]}$$

The total magnetic Gibbs' free energy E_{TOT} is the sum of several energy terms:

$$E_{TOT} = E_Z + E_{MC} + E_{EX} + E_D \qquad \text{[Eq. 9]}$$

E_Z is the Zeeman energy and corresponds to the energy of magnetic moments in an external applied magnetic field. This energy tends to align the magnetization along the external applied field. E_{MC} is the magnetocrystalline anisotropy energy and arises from the combination of crystal-field effects (coupling between electronic orbitals and the lattice) and of spin-orbit effects (coupling between orbital and spin moments). It leads to the tendency for the magnetization to align along some preferential axes, called easy directions, in a solid. E_{EX} is the exchange energy between neighboring sites. E_D is called the magnetostatic or dipolar energy and is the mutual Zeeman-type energy that arises between all moments of a magnetic material through their stray field. [13]

The total magnetic Gibbs' free energy as a function of magnetization **M** and the external applied magnetic field $\mathbf{H_{ext}}$ can be expressed as:

$$E_{TOT}(\boldsymbol{M}, \boldsymbol{H_{ext}}) = \iiint [- \mu_0 \boldsymbol{H_{ext}}.\boldsymbol{M} + f_k(\boldsymbol{M}) + \frac{A}{M_S^2}\sum_{k=1}^{3}(\nabla M_k)^2 - \frac{\mu_0}{2}\boldsymbol{H}_D.\boldsymbol{M}]dV \qquad \text{[Eq. 10]}$$

In this equation, f_k is the magnetocrystalline energy density, A is the exchange stiffness, M_S is the saturation magnetization, M_k is the k-th component of the magnetization vector **M** and $\mathbf{H_D}$ is the dipolar field.

I.5.1.2. Application of micromagnetic simulations for ferromagnetic materials

Micromagnetism allows the competition between the above energy terms to be investigated, giving rise to characteristic magnetic length scales, and is at the origin of the complexity of magnetization distributions in hard magnets [13]. The equations [Eq. 7-10] pave the way for micromagnetic simulations liable to describe the dynamic behavior and complex magnetization patterns in ferromagnetic materials.

However, the numerical resolution is based on time and geometrical discretization schemes that require very fine time steps and meshing compatible with the exchange length in hard magnets (around 1 nm), leading to a considerable limitation of the size of studied systems. An approximation, based on an energy minimization scheme in which dynamic aspects are not considered, could be helpful but the implementation of these micromagnetic simulations remains restricted to small volumes of several regular grains. Typically and providing that a defect is pre-determined in the meshed geometry, the simulation could naturally describe the nucleation phase as the onset of magnetization reversal in this zone, as well as the accurate domain wall structure separating the nucleus and the rest of the magnet. The propagation of the domain wall in the meshed volume could also be explicitly described with an account for the effect of non-homogeneous properties. Some geometrical and microscopic details such as sharp edges and corners of grains can be explicitly described.

I.5.2. Micromagnetic and global models

Some models have been proposed to describe quantitatively how the external field could trigger the magnetization reversal in a ferromagnet in which some nucleus is assumed to be present, without consideration on the time evolution or the spatial variation of magnetization. Combined and/or fitted to experimental results, these models have brought a better understanding of the magnetization reversal processes in Nd-Fe-B magnets and shed light on the link between coercivity and microstructural features.

As for micromagnetic simulations, the physical basis of these models lies on the Gibbs energy minimization, combined with further simplifications made on the calculation of the dipolar energy. In the simplest cases, some analytical solutions were derived. Chronologically, these models have been designated as micromagnetic and global models. The micromagnetic model was developed by Aharoni [51], [52], and more recently by Kronmüller *et al.* [53]–[55], while the global model has been proposed by Givord *et al.* [56].

I.5.2.1. Micromagnetic model (MM) based on nucleation

- Assumptions of the MM

The MM aims at describing how the external conditions of field and temperature produce magnetization reversal starting in a critical region of a grain where nucleation occurs by coherent

rotation [10]. The MM assumes that the critical field in this region is proportional to the anisotropy field H_A of the hard magnetic phase (like in the Stoner-Wohlfarth model, see Section I.3.1) and thus the coercive field H_C is expressed as:

$$H_C = \alpha H_A - N_{eff} M_S = \alpha \frac{2K_1}{\mu_0 M_S} - N_{eff} M_S \qquad \text{[Eq. 11]}$$

M_S is the spontaneous magnetization. α describes the reduction in coercivity due to defects and misorientation. N_{eff} is the effective demagnetization constant accounting for the dipolar field resulting from local magnetostatic interactions near sharp edges and corners of the microstructure [53]. The parameters α and N_{eff} are determined from the temperature dependent values of $H_c(T)$, $H_A(T)$ and $M_S(T)$ by plotting $H_C(T)/M_S(T)$ versus $H_A(T)/M_S(T)$ and fitting a straight line [36]. In the literature, α and N_{eff} are assumed to be temperature independent, even if theoretically they are not. In this model, nucleation is considered to be the determining mechanism for magnetization reversal. For instance, values of $\alpha > 0.3$ are compatible with a nucleation mechanism, whereas values of $\alpha < 0.3$ may include both pinning and nucleation mechanisms for magnetization reversal [57].

Kronmüller *et al.* assume that uniform coherent rotation of the magnetization vectors occurs during magnetization reversal in the defect region: the Stoner-Wohlfarth model [17] is used as a reference in the MM. In the case of Stoner-Wohlfarth systems, the angular dependence of coercivity (θ_{cH} being the angle between the applied field and the easy axis) is expressed as:

$$\frac{H_C(\theta_{cH})}{H_C(0)} = \frac{1}{(sin\theta_{cH}^{2/3} + cos\theta_{cH}^{2/3})^{3/2}} \qquad \text{[Eq. 12]}$$

The above equation refers to magnetization reversal process starting from a defect undergoing coherent rotation. However, the exact nature of defects is not described into details. Several improvements have been achieved by considering that the defect can be represented by a shell around the grain, in which the anisotropy is reduced to zero. Moreover, the link with the non-degraded inner phase is depicted by different profiles: step-like, linear and quasi-harmonic anisotropy perturbations [10]. Hence, nucleation and propagation of reversal can be described.

- <u>Micromagnetic model based on nucleation and propagation</u>

Aharoni [52] assumed a step-like anisotropy profile with $K_1(z) = 0$ for $z < d$ and $K_1(z) = K_1$ for $z > d$, where d is the defect size and K_1 is the anisotropy constant of the main phase. The minimization of the total Gibbs' free energy with such an anisotropy profile was calculated for the two regions, and both nucleation field H_N and passage field H_P (corresponding to the passage of the nucleated domain wall from the soft to the hard magnetic phase) were compared. For $d < \delta_W/4$, H_N is higher than H_P, indicating that nucleation determines magnetization reversal. Both fields are approximatively equal for $d = \delta_W/4$. For $d > \delta_W/4$, magnetization reversal is rather governed by the propagation of the domain wall.

Abraham and Aharoni [51] then considered a linear variation of K_1: this latter was taken as zero in a part of the defect region and was assumed to increase linearly to its constant value in the remaining part. The nucleation field H_N doesn't change a lot compared with the case of a step function for K_1.

Fukunaga *et al.* [58] used a numerical approach to study the effect of magnetic inhomogeneity on the magnetization reversal in a sintered Nd-Fe-B magnet, according to the model in which the anisotropy and exchange constants decrease linearly on the surface of $Nd_2Fe_{14}B$ grains. A local decrease of the exchange constant has no significant effect on H_N, whereas a decrease of the anisotropy constant causes a remarkable reduction of H_N. The H_N values are smaller compared with those reported by

Aharoni [52]. Finally, the simulated angular dependence of coercivity is in good agreement with the experimental results for a reduced anisotropy constant in the 30-50 Å surface region of the grain.

Kronmüller [53] considered another profile for the anisotropy in a planar defect region of halfwidth r_0:

$$K(z) = K(\infty) - \frac{\Delta K}{ch(z/r_0)^2} \qquad \text{[Eq. 13]}$$

K(∞) corresponds to the anisotropy within the ideal matrix and ΔK denotes the reduction of anisotropy at the center of the inhomogeneous region. Assuming this type of anisotropy profile, the passage field H_P is found to be:

$$H_P = H_A \frac{2\delta_W}{3\pi r_0} \quad \text{[Eq. 14]}$$

The passage field H_P decreases with increasing defect width.

Conclusion: For small defect (soft) regions ($d < \delta_W/4$), coercivity is limited by nucleation. For larger soft regions, it is rather limited by propagation.

I.5.2.2. Global model (GM) based on activation volume

- Assumptions of the GM

The GM was proposed by Givord *et al.*. Unlike the MM, it doesn't relate directly coercivity to the anisotropy of the main phase. Whatever the involved coercivity mechanism, magnetization reversal develops through thermal activation of a critical volume of reversed magnetization [59]. Therefore, the GM is based on the formation of a magnetization heterogeneity, which is typically a domain wall.

The energy barrier that must be overcome for magnetization reversal is noted Δ_0. It must be proportional to the increase in the domain wall energy of the critical nucleus: Δ_0 α $\gamma_W's$, where γ_W' is the domain wall energy within the nucleus and s is the surface area of the nucleus [10]. Furthermore, the domain wall energy can be written as $\gamma_W's = \alpha\gamma_W v^{2/3}$, where α is a geometrical parameter that takes into account the relation between the surface and the volume v of the critical nucleus [59], [60]. Note here that the domain wall energy within the nucleus is assumed to be proportional to the domain wall energy in the main phase γ_W [59].

- Expression of the energy barrier Δ_0

When an external field equal to the coercive field H_C is applied, the energy barrier Δ_0 can be written as follows [10]:

$$\Delta_0 = \mu_0 v M_S . H_C + \mu_0 v N_{eff} {M_S}^2 + \Delta_{act} \text{ [Eq. 15]}$$

The first two terms on the right-hand side of the above equation correspond to the interaction energy with the external applied field and to the interaction energy with the dipolar field, respectively. The third term Δ_{act} expresses the thermal activation energy and is equal to 25 kT [61].

- Expression of coercivity H_C as a function of temperature

Combining the above expression of the energy barrier Δ_0 with the dimensional considerations of the first paragraph, one obtains:

$$\alpha\gamma_W v^{2/3} = \mu_0 v M_S . H_C + \mu_0 v N_{eff} {M_S}^2 + 25kT \qquad \text{[Eq. 16.1]}$$

$$\mu_0 v M_S . H_C = \alpha\gamma_W v^{2/3} - \mu_0 v N_{eff} {M_S}^2 - 25kT \qquad \text{[Eq. 16.2]}$$

$$H_C = \frac{\alpha\gamma_W}{\mu_0 M_S v_A^{1/3}} - N_{eff} M_S - 25 S_V \qquad \text{[Eq. 16.3]}$$

where $S_V = {kT}/{\mu_0 v M_S}$ is the magnetic viscosity coefficient, experimentally accessible from magnetic after-effect measurements. In addition, the critical volume v is assumed to be equal to the experimentally derived activation volume v_A. [10], [56]

So, from the above equation, it is obvious that the GM relates coercivity to intrinsic magnetic properties (domain wall energy γ_W and saturation magnetization M_S) of the main hard phase through α and N_{eff} coefficients. The coercivity is also related to the activation volume v_A which can be experimentally determined from M=f(t) measurements. [60]

- Determination of the activation volume as a function of temperature

Using the relation $v_A = {kT}/{\mu_0 S_V M_S}$, $v_A(T)$ can be determined if $S_V(T)$ is known. Moreover, the magnetic viscosity coefficient S_V is defined as $S_V = {S}/{\chi_{irr}}$, where S is the magnetic viscosity and χ_{irr} is the irreversible magnetic susceptibility [62]. The coefficient S_V has the dimension of a fluctuation field [10]. It is experimentally observed that the magnetization decreases linearly with the natural logarithm of time. This is mathematically expressed as $M(t) = M_0 - S ln(t)$. Hence, the magnetic viscosity S can be calculated by determining the slope of the magnetization time variation ($S = -{dM}/{dln(t)}$). Time effects are more obvious when the applied field is close to the coercive field [18]. In addition, the irreversible magnetic susceptibility χ_{irr} is determined by dM/dH measurements. For instance, χ_{irr} is the difference $\chi_{irr} = \chi_{tot} - \chi_{rev}$ between the total experimental susceptibility and the reversible susceptibility that represents the slopes of the recoil loops [18]. Consequently, $S_V(T)$ can be deduced at each temperature from after-effect measurements at several applied fields near H_C. $v_A(T)$ is then calculated using appropriate M_S values for $Nd_2Fe_{14}B$ and the experimental values of $S_V(T)$. [60]

- Analysis of the temperature dependence of H_C

The equation giving the temperature dependence of H_C is equivalent to:

$$H_0 = H_C + 25 S_V = \frac{\alpha\gamma_W}{\mu_0 M_S v_A^{1/3}} - N_{eff} M_S \qquad \text{[Eq. 17.1]}$$

$$\frac{H_0}{M_S} = \frac{\alpha\gamma_W}{\mu_0 M_S^2 v_A^{1/3}} - N_{eff} \quad \text{[Eq. 17.2]}$$

H_0 represents the field needed to reverse the magnetization if thermal activation isn't involved. By plotting the reduced parameter H_0/M_S as a function of $\gamma_W/\mu_0 M_S^2 v_A^{1/3}$ (appropriate values for $M_S(T)$ and $\gamma_W(T)$ must be taken), a linear dependence is obtained. This indicates that α (slope of this line) is temperature independent for a given magnet and that N_{eff} (the negative of the intercept with the vertical axis) takes only a mean value characterizing the effective dipolar interactions during magnetization reversal. [59], [60]

- Magnetic properties of the activation volume v_A

In the GM, the activation volume corresponds to a non-uniform state of magnetization. In a ferromagnetic material, the length that characterizes such non-uniform magnetization state is the domain wall width δ_W. Hence, the experimentally obtained activation volume v_A can be compared with the value of δ_W^3 calculated for the $Nd_2Fe_{14}B$ phase. The ratio v_A/δ_W^3 can be plotted as a function of temperature (see Fig. 11). This gives information about the differences between the intrinsic magnetic properties of the activation volume and those of the main phase. [59]

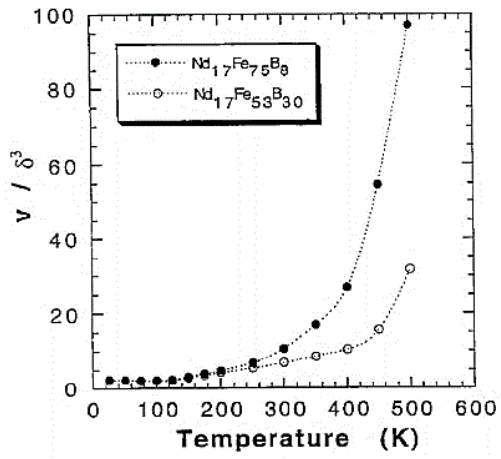


Fig. 11: Thermal variation of the ratio v_A/δ_W^3 in Nd-Fe-B sintered magnets. [59]

For Nd-Fe-B sintered magnets, the ratio v_A/δ_W^3 is roughly constant up to room temperature and increases dramatically at higher temperatures. The proportionality between v_A and δ_W^3 at low temperature shows that the magnetic properties of the activation volume are not very different from those of the bulk [59]. If nucleation was the determinant coercivity mechanism, the anisotropy of the activation volume would differ strongly from the main phase anisotropy. As a result, magnetization reversal is not limited by nucleation. On the contrary, magnetization reversal is believed to be rather governed by passage and expansion mechanisms. [63]

Conclusion: The MM and GM approaches show that, except for small defect zones (with reduced K_1), coercivity is controlled by the passage/propagation of reversal into the non-affected zone (with non-reduced K_1). This has been recently confirmed by Bance *et al.* [64].

I.5.3. Main results of micromagnetic simulations

Unlike micromagnetic and global models, micromagnetic simulations aim at describing magnetization patterns without simplifications on the dipolar field and exchange interactions. Consequently, this approach helps to understand the role of the grain size and shape, and of coupling/decoupling phases at GB.

Most of the micromagnetic simulations presented here are performed with the software package FEMME (Finite Element MicroMagnEtics), which is a hybrid finite element / boundary element method code [65].

I.5.3.1. Influence of grain size on coercivity

As explained in Section I.4.4.1, the size of $Nd_2Fe_{14}B$ grains has been shown to have an influence on the coercive field and its thermal stability. In addition to the already described works of Ramesh *et al.* [35] and of Bance *et al.* [36], Schrefl *et al.* [66] showed that a decrease of the grain size increases coercivity because the magnetostatic interactions between the grains are less effective and therefore lead to a decrease of the demagnetizing field. Kronmüller *et al.* [67] also showed that dipolar long-range magnetic stray fields reduce coercivity mainly for large grain sizes.

Sepehri-Amin *et al.* [50], [68] used finite-element micromagnetic simulations to understand the link between grain size and coercivity for exchange-coupled polycrystalline anisotropic Nd-Fe-B sintered magnets. Table 4 gives the simulation parameters used in [68].

Simulation parameters	Simulation 1	Simulation 2
Model dimensions	8 x 8 x 8 μm^3	400 x 400 x 400 nm^3
Grain shape	Polyhedral	Polyhedral
Grain size	0.7 µm / 2.7 µm	30 nm / 50 nm / 130 nm
Intrinsic magnetic properties of $Nd_2Fe_{14}B$ grains	$\mu_0 M_S$ = 1.61 T K = 4.5 MJ/m^3 [69] A = 12.5 pJ/m	Determined between 300 and 400 K
Nature of the GB phase	Exchange-coupling	/

Table 4: Simulation parameters used in [68].

For the simulation 1, tetrahedral meshes were generated and the LLG equation was solved at each node using the FEMME software [65]. The results showed that coercivity increases by 0.4 T when the grain size is decreased from 2.7 to 0.7 µm. Moreover, the magnetization curves demonstrate a decrease in the maximum susceptibility as the grain size is reduced. For instance, for grain sizes ≤ 1 µm, a two-step initial magnetization curve can be observed. On the one hand, the initial high susceptibility observed for large-sized grains comes from the easy displacement of the domain walls within the multidomain grains. On the other hand, small-sized single-domain grains require higher magnetic fields to reach saturation because of the pinning of the domain walls at the GB phase.

Furthermore, Sepehri-Amin *et al.* calculated the stray field generated from the reversed surface grains for different grain sizes (1, 2 and 2.7 µm) and showed that the maximum stray field decreases as the grain size decreases. Larger stray fields induced by a larger grain size lead to magnetization reversal of the neighboring grains at a lower external magnetic field, being detrimental for coercivity.

A second model (see parameters of simulation 2 in Table 4) was used by Sepehri-Amin *et al.* to study the influence of grain size on the temperature coefficient of coercivity β:

$$\beta = \frac{\Delta H_C}{H_C \Delta T} \times 100 \qquad \text{[Eq. 18]}$$

Demagnetization curves were calculated as a function of temperature from 300 K to 400 K (increments of 20 K). Fig. 12 shows the temperature dependence of the simulated coercive field for 30, 50 and 130 nm-sized grains.

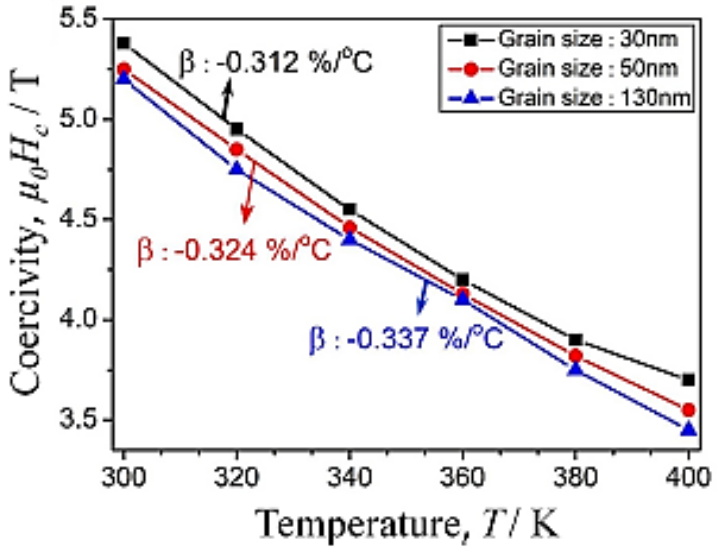


Fig. 12: Thermal dependence of coercivity for modeled Nd-Fe-B magnets with average grain sizes of 30, 50 and 130 nm. [68]

To enable a permanent magnet to be used in motors, the lowest absolute value of β is desirable. The simulation showed that β is the highest for a grain size of 130 nm. This result indicates that the temperature coefficient of coercivity deteriorates with increasing grain size. It is in good agreement with the experimental observations made by Liu *et al.* [70] on hot-deformed Nd-Fe-B anisotropic magnets.

In addition, Sepehri-Amin *et al.* also determined the values of α and N_{eff} for Nd-Fe-B sintered magnets by plotting the $H_C(T)/M_S(T)$ versus $H_A(T)/M_S(T)$ and further fitting (see Fig. 13), based on the MM. The slope and the intercept of the fitted lines give α and N_{eff}, respectively.

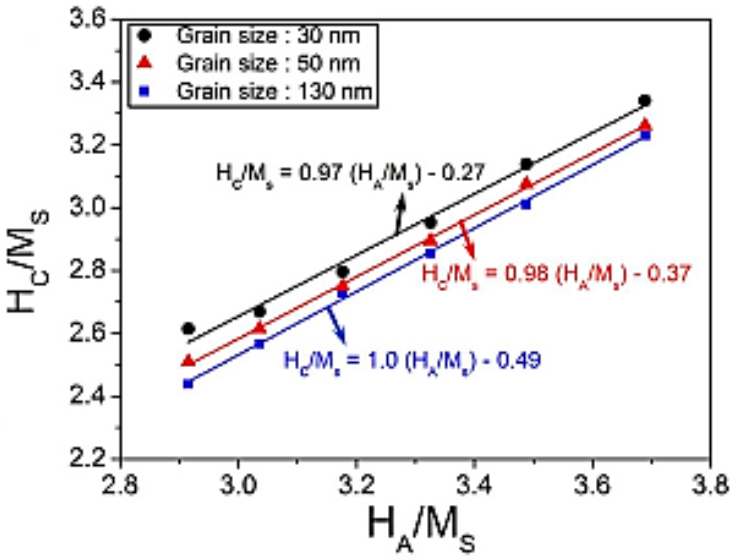


Fig. 13: Dependence of H_C/M_S with H_A/M_S for Nd-Fe-B magnets with average grain sizes of 30, 50 and 130 nm. [68]

The effective demagnetization constant N_{eff} was shown to increase with the grain size, being consistent with the grain size dependence of the stray field. Liu *et al.* [70] also found that a decrease in the grain size leads to a lower N_{eff} for hot-deformed magnets.

To conclude, the increase in coercivity with decreasing grain size is attributed to the reduction in the stray field arising from neighboring grains. The temperature coefficient of coercivity β is improved with decreasing grain size because of the lower effective demagnetization constant N_{eff}.

I.5.3.2. Influence of grain shape on coercivity

The grain shape (especially the edges or corners of a grain), which is one critical microstructural parameter of permanent magnets, can affect the local demagnetization field distribution and thus have a significant contribution to the magnetization reversal. Forster *et al.* [71] calculated energy barriers on a columnar-shaped ferromagnetic grain and showed that the energy barrier required for magnetization reversal (*i.e.* coercivity) increases with the column length. Fukada *et al.* [72] evaluated the effective demagnetization factor N_{eff} for Nd-Fe-B sintered magnets with different grain sizes and shapes: they reported higher demagnetization factors for platelet-shaped ferromagnetic grains. Bance *et al*. [73] reported that by changing the shape of soft magnetic particles from spheres to long wires, the nucleation field and thus coercivity can be enhanced. Yi *et al.* [74] performed micromagnetic simulations to study the effect of grain shape in Nd-Fe-B magnets and showed that the coercivity can be almost doubled by changing the grain shape from the triangular prism to the spheroid.

Sepehri-Amin *et al.* [50] calculated demagnetization curves of single $Nd_2Fe_{14}B$ grains with the same volume, but with different aspect ratios. The smallest coercive field was obtained for single platelet-shaped grains and the highest coercivity was for elongated grains. These results are in agreement with those of Bance *et al.* [73]. Moreover, they calculated the demagnetization field (prior to the nucleation of a reversed domain) for grains of different shapes: plateled-shaped, cuboidal, tetragonal-shaped and spherical. The value of the demagnetization field decreases by increasing the aspect ratio from the platelet-shaped to the elongated-cuboidal grain, and the minimum demagnetization field was found for the spherical grain.

Further calculations were performed by Sepehri-Amin *et al.* on the influence of the demagnetizing field on coercivity, but this time for exchange-coupled models with different grain shapes. The volume of all models is the same. Table 5 gives the simulation parameters used in [50]:

Simulation parameters	**Simulation 1**
Model dimensions	Cubic: 128 x 128 x 128 nm^3
Grain shape	Platelet – Cubic – Columnar cuboid
Grain size	/
Intrinsic magnetic properties of $Nd_2Fe_{14}B$ grains	/
Nature of the GB phase	Thickness: 2 nm $\mu_0 M_S$ = 0.5 T K = 0 MJ/m^3 A = 4 pJ/m

Table 5: Simulation parameters for [50].

By introducing this type of GB phase in the simulation, the $Nd_2Fe_{14}B$ grains are assumed to be partially exchange-coupled. The modeled geometries with different grain shapes are presented in Fig. 14:

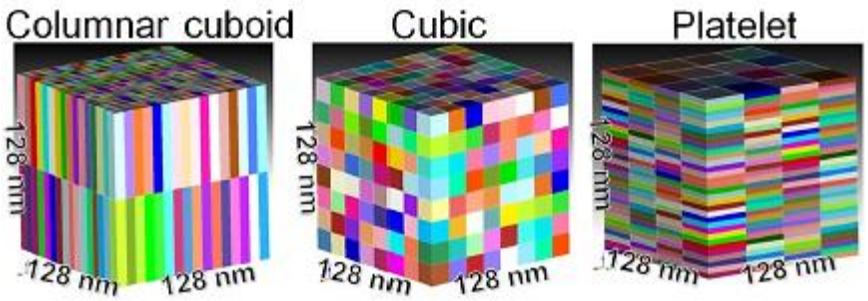


Fig. 14: Modeled geometries with platelet-, cubic- and columnar cuboid-shaped $Nd_2Fe_{14}B$ grains that are partially exchange-coupled. [50]

Simulated demagnetization curves of the three above models are shown in Fig. 15:

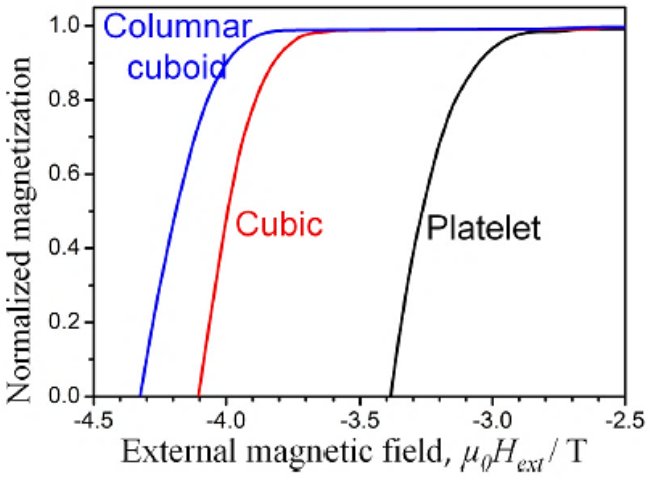


Fig. 15: Simulated demagnetization curves for the models with different grain shapes. [50]

The model with platelet-shaped grains shows lower coercivity and by changing the grain shape to cubic and columnar cuboid, coercivity increases. As determined previously, coercivity can be improved by increasing the aspect ratio of $Nd_2Fe_{14}B$ grains in order to reduce the stray field.

To conclude, the largest coercive field value is obtained for grains with highest aspect ratios (*i.e.* columnar-shaped grains). This result is independent of the considered model (either single-grain or coupled multi-grain) in the micromagnetic simulations. The grain shape dependence of coercivity is explained by the grain shape dependence of the demagnetization field. This latter is reduced for columnar- or spherical-shaped grains.

I.5.3.3. Influence of GB phase on coercivity

Micromagnetic simulations can also give an insight into the influence of the chemical composition and the structure of the GB phase on coercivity of Nd-Fe-B based permanent magnets. [49], [50], [75]–[77]

Liu *et al.* [76] found a clear correlation between the Nd concentration in the GB phase and the coercive field for hot-deformed Nd-Fe-B permanent magnets. The same research team [70] studied the influence of saturation magnetization of the GB phase on the demagnetization process in these magnets. Simulation parameters for [76] and [70] are given in Table 6:

Simulation parameters	**Liu *et al.* [76]**	**Liu *et al.* [70]**
Model dimensions	Cubic: 400 x 400 x 400 nm^3	Cubic: 300 x 300 x 300 nm^3
Grain shape	Cuboid	Platelet
Grain size	(125±25) x (200±25) x (100±25) nm^3	Lateral direction: 60 and 150 nm Longitudinal direction : 30 and 75 nm
Intrinsic magnetic properties of $Nd_2Fe_{14}B$ grains	$\mu_0 M_S$ = 1.61 T K = 4.5 MJ/m^3 A = 12 pJ/m	$\mu_0 M_S$ = 1.61 T K = 4.3 MJ/m^3 A = 12 pJ/m
Nature of the GB phase	Thickness : 4 nm $\mu_0 M_S$ = [0-1.2] T K = 0 MJ/m^3 A = [0-8] pJ/m	Thickness : 3 nm $\mu_0 M_S$ = [0.03-1.2] T K = 0 MJ/m^3 A = [1-12] pJ/m

Table 6: Simulation parameters for [76] and [70].

In [76], tetrahedron meshes were applied with a size of 2 nm at grain boundaries and 7 nm at the center of $Nd_2Fe_{14}B$ grains. The LLG equation was solved at each node using the FEMME software and

demagnetization curves were then simulated: coercivity is enhanced by the reduction of the saturation magnetization of GB phase (caused by its increasing Nd content). For the model containing a ferromagnetic GB phase ($\mu_0 M_S$ = 1.2 T), nucleation starts at a much lower magnetic field than for the sample containing a non-magnetic GB phase ($\mu_0 M_S$ = 0 T). In the case of a ferromagnetic GB phase, reversed magnetic domains can easily propagate into neighboring grains. For a non-ferromagnetic GB phase, the pinning strength increases and the propagation of reversed magnetic domains is prevented. The improvement of the pinning force of the GB phase is caused by the increase in Nd content.

In [70], tetrahedral meshes of 3 nm were applied for the GB phase and the LLG equation was solved at each node with the FEMME software. Simulated demagnetization curves for the models with grain sizes of 60 and 150 nm are shown in Fig. 16:

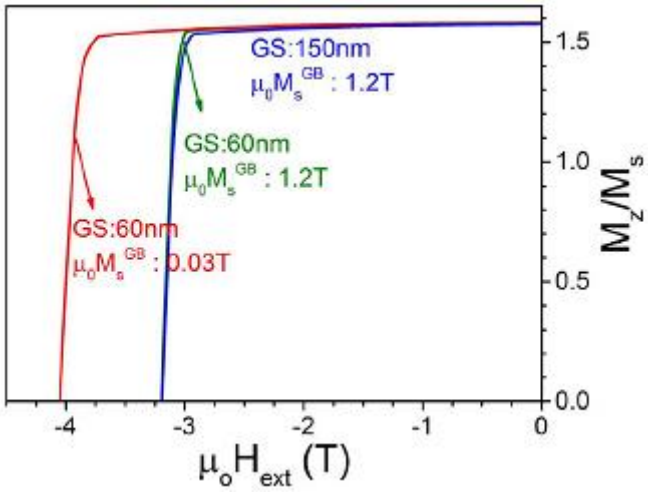


Fig. 16: Simulated demagnetization curves for hot-deformed Nd-Fe-B magnets with different grain sizes and GB phase saturation magnetizations. [70]

The two exchange-coupled models ($\mu_0 M_S$ = 1.2 T and A = 12 pJ/m) show the same coercivity of 3.19 T, independent of the grain size. The weakly exchange-coupled model ($\mu_0 M_S$ = 0.03 T and A = 1 pJ/m) shows a larger coercivity of 4.05 T. The decrease in saturation magnetization and the minimization of the ferromagnetic exchange coupling between $Nd_2Fe_{14}B$ grains leads to higher coercivity values. In addition, the magnetization configuration during domain wall propagation (see Fig. 17) was studied in the 60-nm-grain-sized model with various GB phase saturation magnetizations (0.03 and 1.2 T). Red and blue colors correspond to M_z/M_S = +1 and -1 states, respectively.

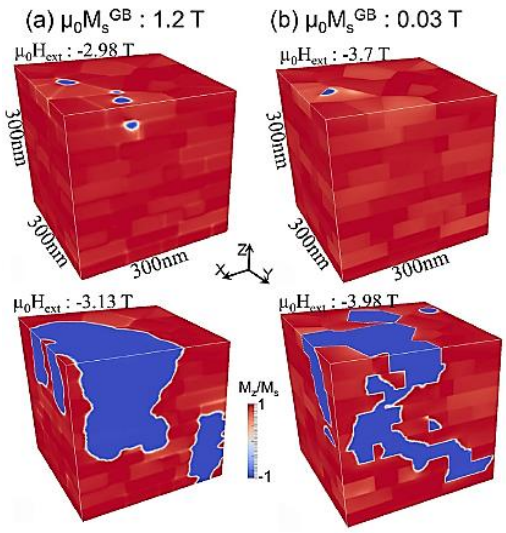


Fig. 17: Magnetization configuration during domain wall propagation of modeled hot-deformed magnets with 60-nm-sized-grains and various GB phase saturation magnetizations. [70]

On the one hand, when applying an external magnetic field, several nucleation domains of reversed magnetization can be observed in the GB phase in the exchange-coupled model ($\mu_0 M_S$ = 1.2 T) and they propagate easily into neighboring grains. So, no domain wall pinning occurs in the exchange-coupled model. On the other hand, for the weakly exchange-coupled model ($\mu_0 M_S$ = 0.03 T), a "zigzag" domain wall configuration is observed at the GB phase, typical of a strong pinning strength, leading to higher coercivity.

Zickler *et al.* [32] performed micromagnetic simulations to study the influence of the anisotropic magnetic properties of the GBs on coercivity of anisotropic sintered heavy rare-earth free Nd-Fe-B magnets. The grain boundaries parallel to the c-axis with a large Fe content are called y-GBs. The grain boundaries perpendicular to the c-axis with a low Fe content are called x-GBs. According to the simulation results, the coercive field related to the x-GBs is higher by 12% compared to the coercivity related to the y-GBs. For instance, the y-GBs switch earlier than the x-GBs. Fujisaki *et al.* [49] also studied the orientation dependence of GB properties on coercivity, using large scale parallel computation. They reported that a reduction of the exchange stiffness and the spontaneous magnetization of the GB phase parallel to the c-axis enhances coercivity of Nd-Fe-B sintered magnets more efficiently than that perpendicular to the c-axis.

Micromagnetic simulations explaining the squareness of demagnetization curves were also performed by Xu *et al.* [48]. Models with ferromagnetic and non-ferromagnetic GB phases were constructed and correspond to Nd-Fe-B sintered magnets containing 0.1 at.% and 0.5 at.% of Ga, respectively. Simulation parameters for the exchange-coupled case (magnets with 0.1 at.% of Ga) and for the exchange-decoupled case (magnets with 0.5 at.% of Ga) are given in Table 7. For the exchange-coupled case, the intrinsic parameters of the GB phase were determined by experimental microstructure analysis and *ab initio* calculations. These parameters depend on the orientation of the GB phase with respect to the easy-axis (c-axis).

Simulation parameters	Exchange-coupled case	Exchange-decoupled case
Model dimensions	Cubic: 250 x 250 x 250 nm^3	Cubic: 250 x 250 x 250 nm^3
Grain shape	Polyhedral	Polyhedral
Grain size	64 equiaxed grains	64 equiaxed grains
Intrinsic magnetic properties of $Nd_2Fe_{14}B$ grains	$\mu_0 M_S$ = 1.61 T K = 4.4 MJ/m^3 A = 8 pJ/m	$\mu_0 M_S$ = 1.61 T K = 4.4 MJ/m^3 A = 8 pJ/m
Nature of the GB phase	**Side-plane GB phase** Thickness : 2.2 nm $\mu_0 M_S$ = 0.60 T K = 0 MJ/m^3 A = 7.14 pJ/m **c-plane GB phase** Thickness : 3 nm $\mu_0 M_S$ = 0.22 T K = 0 MJ/m^3 A = 3.98 pJ/m	Thickness : 6 nm $\mu_0 M_S$ = 0 T K = 0 MJ/m^3 A = 0 pJ/m

Table 7: Simulation parameters for [48].

The models used in [48] are shown in Fig. 18:

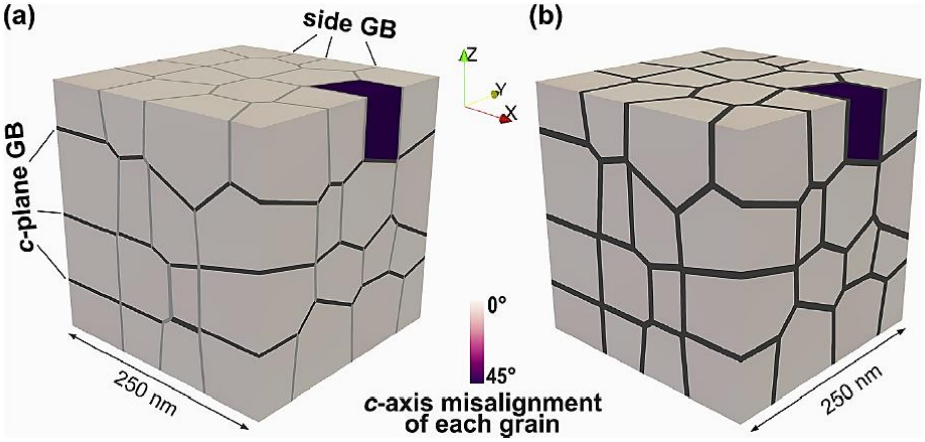


Fig. 18: Micromagnetic models for (a) the exchange-coupled case (0.1 at.% of Ga), (b) the exchange-decoupled case (0.5 at.% of Ga). [48]

In both models, a grain at the surface having a misalignment angle of 45° and of reduced anisotropy energy acts as nucleation point for magnetization reversal. The models were meshed with tetrahedrons ranging from 1.3 to 2.5 nm in size. The demagnetization curves were calculated by minimizing the free energy of the systems in a decreasing magnetic field. The simulated demagnetization processes and their respective magnetization configuration are shown in Fig. 19:

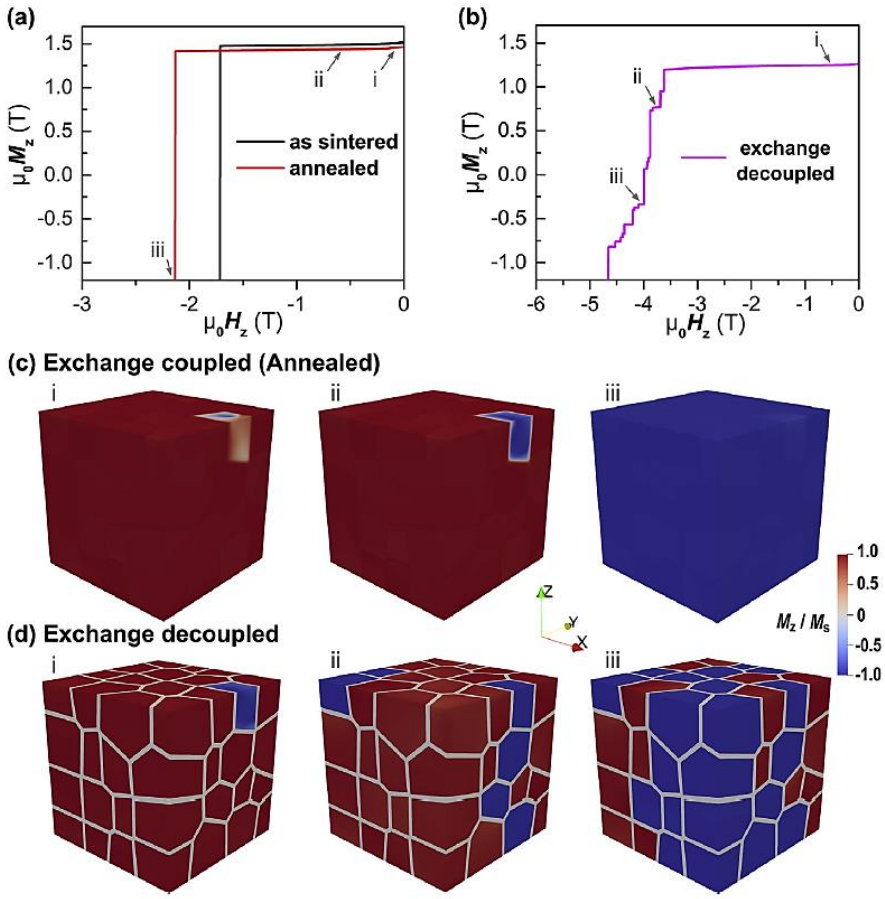


Fig. 19: (a) Simulated demagnetization curves for the exchange-coupled case. (b) Same for the exchange-decoupled case. (c) Magnetization reversal process for the exchange-coupled case. (d) Same for the exchange-decoupled case. [48]

For the exchange-coupled case, good squareness of the demagnetization curve is observed, whereas squareness is deteriorated when the grains are exchange-decoupled. Moreover, in the case of exchange-coupling, magnetization reversal starts from the nucleation grain and then cascade-type reversal of neighboring grains happens. This is in agreement with the brutal reduction in magnetization in the demagnetization curve and leads to its good squareness. On the contrary, for the exchange-decoupled case, magnetization reversal starts from the nucleation grain and then individual reversal of neighboring grains occurs. This explains the higher coercivity but also the deteriorated squareness of the demagnetization curve.

To conclude, micromagnetic simulations can give additional information and interpretation to microstructural effects on coercivity in Nd-Fe-B magnets. Coercivity depends strongly on the chemical composition of the GB phase and therefore on its intrinsic properties. The shape of experimental demagnetization curves can also be explained by simulations and is mainly determined by the ferromagnetic (or not) nature of the GB phase. Recently, more realistic models have been developed and take into account the change in properties of the GB phase depending on its orientation with respect to the easy axis. However, models in micromagnetic simulations have often two orders of magnitude smaller grain size than real Nd-Fe-B sintered magnets, owing to the limitations of computation power.

I.6. The grain boundary diffusion process (GBDP) in Nd-Fe-B sintered magnets

I.6.1. Benefits of core-shell microstructure

The grain boundary diffusion process (GBDP) is a way to incorporate HRE into Nd-Fe-B sintered magnets. This method was proposed in 2000 by Park *et al.* [9]. In this process, Nd-Fe-B sintered magnets are coated with HRE in different forms and undergo a subsequent heat treatment [78]. The latter enables the diffusion of HRE from the surface into the magnet, mainly along grain boundaries [78]. Core-shell structures can be obtained by GBDP: $(Nd,HRE)_2Fe_{14}B$ phases are formed in the outer region of $Nd_2Fe_{14}B$ hard magnetic grains. On the below BSE-SEM image (Fig. 20), the $Nd_2Fe_{14}B$ cores appear dark and the HRE-rich shells are brighter.

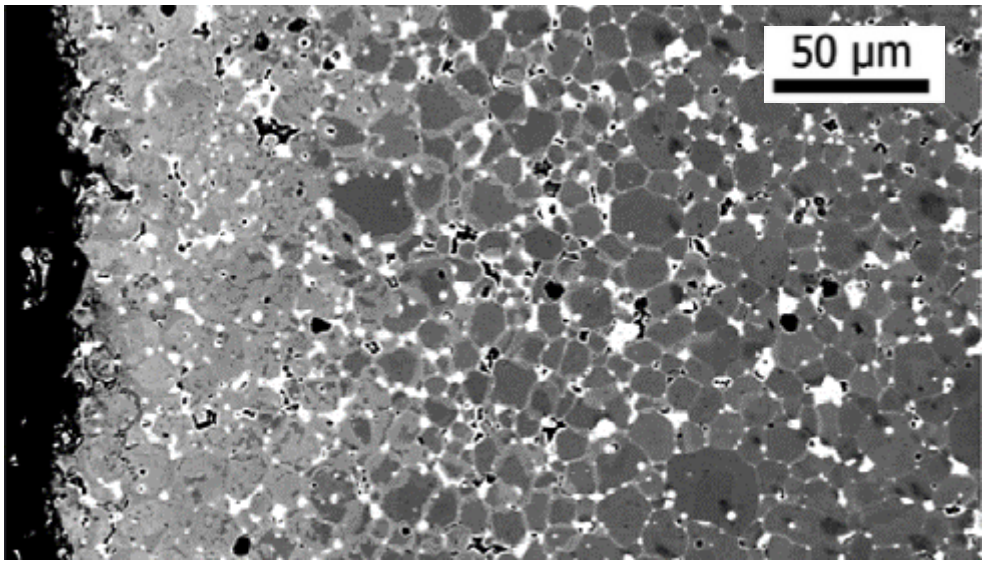


Fig. 20: BSE-SEM image of a Dy-coated Nd-Fe-B sintered magnet from [79].

The HRE diffuses from the grain boundaries into the $Nd_2Fe_{14}B$ phase because of the concentration gradient. Moreover, the rejection of Nd from the $(Nd,HRE)_2Fe_{14}B$ shells results in a thickening of the GB phase [80].

For Nd-Fe-B sintered magnets, it is generally accepted that magnetization reversal is initiated by the nucleation of reversed magnetic domains in a locally reduced magnetocrystalline anisotropy region, *e.g.* at grain boundaries [6], [53], [81]. This lower anisotropy can be compensated by the addition of HRE elements using GBDP. Indeed, the latter enables the selective deposition of HRE in the vicinity of grain boundaries, forming HRE-rich shells with an enhanced anisotropy field and thus increasing coercivity [78], [80]. Another reason for the coercivity enhancement after GBDP is the increase of the grain boundary phase thickness, leading to the improvement of the magnetic isolation of hard magnetic grains [80]. In addition, the use of HRE can be minimized by GBDP, as well as the sacrifice of remanence (see Section I.4.1.1), since the substitution of Nd by HRE is limited to the region near grain boundaries. However, the diffusion length has a limitation of a few millimeters and it is therefore challenging to upscale this process to magnets with larger sizes [82].

The GBDP has been studied extensively in the last years. A lot of works have been performed with GBDP on Nd-Fe-B sintered magnets using Dy/Tb-containing powders, metallic vapor and eutectic

alloys, which will be further detailed here. The HRE diffusion in hot-deformed Nd-Fe-B magnets has also received a lot of attention in the past years [77], [83]–[86].

I.6.2. State of the art

I.6.2.1. GBDP using Dy/Tb-containing powders

Dy/Tb-containing coatings have been used as diffusion sources for GBDP on Nd-Fe-B sintered magnets. Table 8 and Table 9 give experimental parameters used in some works for different coating techniques:

Reference	**Kim *et al.* [87]**	**Nakamura *et al.* [88]**	**Soderznik *et al.* [89]**	**Samardzija *et al.* [90]**
Base material	Commercial 48 M Nd-Fe-B sintered magnets	N52 Nd-Fe-B sintered magnets	Nd-Fe-B sintered magnets (1.2 wt.% Dy + Tb)	Anisotropic sintered $Nd_2Fe_{14}B$ magnets
Magnet dimensions (mm^3)	12 x 12 x 5	40 x 10 x 14.5	14 x 8 x 3.5	16 x 16 x 2
Diffusion source	TbH powder-ethanol slurry	TbF powder slurry	TbF_3 powder-ethanol slurry	Tb_4O_7 powder-ethanol slurry
Coating technique	Dip-coating	Dip-coating	Electrophoretic deposition	Dip-coating
GBDP	900-960°C, 6h, vacuum	800-900°C, 10-110h	875°C, 10h, vacuum	850°C, 10h
Post-diffusion annealing	860-960°C, 10h, argon and 440-520°C, 2h, argon	500°C, 1h	500°C, 1h	500°C, 1h, argon

Table 8: Experimental parameters for GBDP using Dy/Tb-containing powders.

Reference	**Bae *et al.* [91]**	**Ma *et al.* [92]**	**Kim *et al.* [93]**	**Löwe *et al.* [94]**
Base material	$Nd_{32}Fe_{bal}B_{0.97}M_{2.4}$ (wt.%, M=Cu, Al, Co, Nb) sintered magnets	$Nd_{21.84}Pr_{7.03}Ho_2(Fe,M)_{bal}B_{0.95}$ (wt.%, M=Co, Al, Ga, Cu) sintered magnets	$Nd_{28}Dy_{3.0}Fe_{bal}B_{1.0}M_{2.5}$ (wt.%, M=Cu, Al, Co, Nb) sintered magnets	$Nd_{29.0}Dy_{2.6}Fe_{bal}B_{1.0}Co_{1.0}Cu_{0.1}$ (wt.%)
Magnet dimensions (mm^3)	10 x 10 x 5	10 x 10 x 5	10 x 12 x 3.6 10 x 10 x 5 3.6 x 12 x 10	8 x 5 x 5
Diffusion source	DyF_3/DyH_x-ethanol slurry	DyH_x (DyH_3 and few DyH_2) powder-ethanol-polyvinyl pyrrolidone slurry	DyH_2 powder-ethanol solution	Rare-earth foils (Dy, Tb, Ce and Gd) with 25 µm thickness
Coating technique	Dip-coating	Coating	Dip-coating	Foils attached to magnets
GBDP	900°C, 2h	850°C, 6h	900°C, 2h	900°C (1.5, 6, 10h)
Post-diffusion annealing	500°C, 2h	465°C, 4h	500°C, 2h	500°C, 2h

Table 9: Experimental parameters for GBDP using Dy/Tb-containing powders.

In these studies, core-shell microstructures have been obtained after GBDP. The thickness of the shells decreases from the magnet surface to its center part. For example, in [90], they are 1- µm-thick near the magnet surface and their thickness is reduced to a few tens of nm in the center of the magnet. These structures suppress the nucleation of reversed domains at the interfaces between the main and Nd-rich phases: coercivity is therefore enhanced. For example, in [87], coercivity of the base magnet is 15.28 kOe (1216 kA/m), increases to 21.04 kOe (1674 kA/m) after GBDP and is further increased to 24.86 kOe (1978 kA/m) after post-diffusion annealing.

In addition, the research teams in [92] and [93] investigated the anisotropic diffusion mechanism of Dy. GBDP was performed along and perpendicular to the easy axis. Results of both works are in good agreement: coercivity enhancement (compared to coercivity of the as-sintered state) is more important when GBDP is done in the direction parallel to the easy-axis. This is attributed to the anisotropic distribution of the Nd-rich phase that acts as a diffusion channel. These works thus show that diffusing HRE along the easy-axis is the best way to enhance coercivity of Nd-Fe-B sintered magnets.

In [94], the diffusion of different RE (Dy, Tb, Ce and Gd) was studied in Dy-containing Nd-Fe-B sintered magnets. Demagnetization curves after GBDP for different times are shown in Fig. 21 for each diffused element:

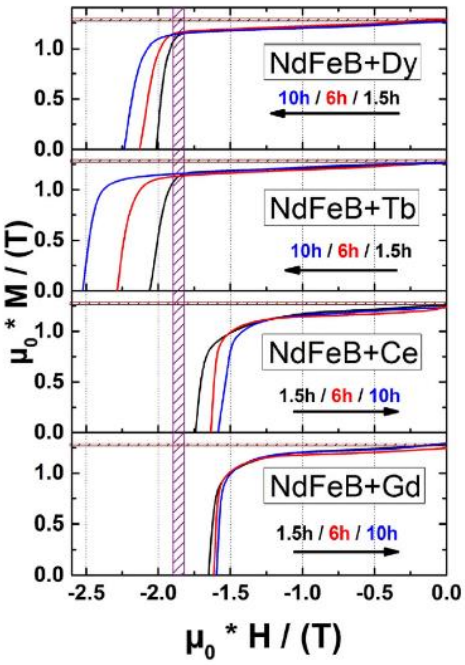


Fig. 21: Demagnetization curves after diffusion at 900°C for different times. Shaded bars correspond to coercivity and remanence range for reference samples heat-treated without RE diffusion. [94]

Both Dy and Tb lead to an increase in coercivity compared to the reference samples, while Ce and Gd decrease it. Unlike for HRE, Ce shows no shell formation. Moreover, the evaluation of diffusion speeds highlights that Tb diffuses significantly faster than Dy in these magnets.

I.6.2.2. GBDP using metallic vapor

GBDP using metallic vapor as the diffusion source was also studied in some works detailed in the below Table 10:

Reference	Watanabe *et al.* [95]	Sepehri-Amin *et al.* [78]	Kim *et al.* [96]
Base material	Nd-Fe-B sintered magnets	$Nd_{24.0}Pr_{6.6}Fe_{66}Co_{2.2}B_{1.0}Ga_{0.1}Cu_{0.1}$ (wt.%) sintered magnet	$Nd_{31.8}Fe_{66}B_{1.0}Cu_{0.1}Al_{0.15}Co_{0.9}Ga_{0.05}$ and $Nd_{24.3}Dy_{7.5}Fe_{66}B_{1.0}Cu_{0.1}Al_{0.15}Co_{0.9}Ga_{0.05}$ (wt.%) sintered magnets
Magnet dimensions (mm^3)	3 x 3 x 2.8	5 x 5 x 5.5	6.5 x 6.5 x 6.5
Diffusion source	Tb vapor	Dy vapor	Dy vapor
Coating technique	3D-sputtering	Vapor deposition	Vapor deposition
GBDP	900°C, 12h, argon	800-1000°C	950°C, 4h
Post-diffusion annealing	/	500-600°C, 1-3h, argon	520°C, 1h

Table 10: Experimental parameters for GBDP using metallic vapor.

In [95], the Tb-treated magnet showed an important gain in coercivity (from 950 kA/m for the as-sintered state to 1980 kA/m after GBDP) and no significant decrease in remanence (from 1.44 T to 1.43 T). In [78], SEM analysis showed that the thickness of the formed shells decreases from the surface to the center of the magnet, in good agreement with the above mentioned works. Furthermore, atom probe tomography determined that the Dy content in the shells near the surface and in the center of the bulk are 3.3 and 1.4 at.%, respectively. In [96], very high coercivity of 3 T (2387 kA/m) was achieved in Dy-containing Nd-Fe-B sintered magnets after GBDP and subsequent post-diffusion annealing. This is attributed to the formation of a secondary Dy-rich shell after post-diffusion annealing. During the latter, a large amount of Dy atoms diffuse from the GB phase to the primary Dy-rich shell. A higher Dy concentration is therefore achieved at the interface between the GB phase and the secondary Dy-rich shell.

I.6.2.3. GBDP using eutectic compositions

Compared to hydrides, fluorides and oxides, GBDP using eutectic alloys with low melting points has a much higher diffusing efficiency. Indeed, these alloys melt into liquid and infiltrate faster into the sample at elevated temperatures [97]. Table 11 and Table 12 give experimental parameters for works using eutectic compositions as diffusion source:

Reference	Oono *et al.* [98]	Tang *et al.* [99]	Lu *et al.* [97]
Base material	$Nd_{26.6}Dy_{0.03}Pr_{4.7}Fe_{bal}Co_{0.92}B_{1.01}Al_{0.27}Cu_{0.09}$ (wt.%) sintered magnet	Nd-Ce-Fe-B sintered magnets with 22 wt.% of Ce	Commercial N50 Nd-Fe-B sintered magnets
Magnet dimensions (mm^3)	7 x 7 x 5 7 x 7 x 6	ϕ8 x 4	ϕ8 x 5
Diffusion source	$Dy_{73}Ni_{9.5}Al_{17.5}$ eutectic alloy mixed with paraffin	$Nd_{80-x}Dy_XAl_{20}$ (at.%) alloy ribbons	$Tb_{70}Cu_{30}$ $Pr_{52.5}Tb_{17.5}Cu_{30}$ $Pr_{60}Tb_{20}Al_{20}$ $Pr_{60}Tb_{10}Cu_{15}Al_{15}$ (at.%) alloy ribbons
Coating technique	Painting	/	/
GBDP	900°C, 3h, vacuum	900°C, 4-13h	900°C, 4h
Post-diffusion annealing	500°C, 3h	470°C, 2h, argon	500°C, 2h

Table 11: Experimental parameters for GBDP using eutectic compounds.

Reference	Lu *et al.* [100]	Chen *et al.* [101]	Lee *et al.* [102]
Base material	Commercial 38 M Nd-Fe-B sintered magnets	Commercial $Nd_{10.36}Pr_{3.53}Fe_{bal}B_{5.92}Co_{0.89}Cu_{0.1}$ (at.%) sintered magnet	$Nd_{29}Dy_{3.00}Fe_{bal}B_{0.97}M_{2.39}$ (wt.%, M=Cu, Al, Co, Nb) sintered magnets
Magnet dimensions (mm^3)	ϕ8 x 5	15 x 15 x 4	12.5 x 12.5 x 5
Diffusion source	$Pr_{68}Cu_{32}$ $Dy_{70}Cu_{30}$ $Pr_{35}Dy_{35}Cu_{30}$ (at.%) alloy ribbons	$Dy_{60}Co_{40}$ (at.%) eutectic alloy	Ethanol solution of DyCo, DyCo + Cu and DyCo + Al powders
Coating technique	/	/	Dip-coating
GBDP	900°C, 4h	865°C, 3h, vacuum	880°C, 8h, vacuum
Post-diffusion annealing	500°C, 2h	/	530°C, 2h and 500°C, 2h, vacuum

Table 12: Experimental parameters for GBDP using eutectic compounds.

In those works, the role of low melting point elements such as Cu and Al on the Dy diffusion behavior was studied. It has been shown that both Cu and Al act as carriers for Dy atoms owing to their solubility in the Nd-rich GB phase, which leads to the enhancement of Dy diffusivity during GBDP. Moreover, the Al addition also promotes wettability of diffusion alloys. The presence of Co in diffusion alloys improves the temperature coefficient of remanence. For example, in [101], the latter is improved from -0.140 %/°C to -0.095 %/°C after GBDP. Finally, the anisotropic diffusion mechanism of Dy was also studied by Chen *et al.* [103] using $Dy_{70}Cu_{30}$ (at.%) eutectic alloy for GBDP. The magnet diffused parallel to the easy axis showed much higher squareness factor (0.92) than that diffused perpendicular (0.83).

To conclude, the coercivity enhancement by GBDP can be explained by two microstructural features: the Dy-rich shells that increase the anisotropy field and the continuous and thin GB phase formed after

post-diffusion annealing that isolates $Nd_2Fe_{14}B$ grains. Other works using powder-blending methods or concerning intergranular addition of alloy powders will not be covered here.

I.6.3. Micromagnetic simulations on core-shell structures

Micromagnetic simulations have been performed to simulate core-shell structures obtained in GB diffused Nd-Fe-B magnets. The two main codes used for these simulations are FEMME [65] and OOMMF (Object Oriented MicroMagnetic Framework) [104].

Bance *et al.* [81] calculated the temperature-dependent magnetic properties of a single $Nd_2Fe_{14}B$ grain to study the influence of a hard $(Nd,Dy)_2Fe_{14}B$ shell on its magnetization reversal. The geometry of the studied grain was dodecahedral and its diameter was 50 nm. 3 single grain models were introduced: 1) the pure $Nd_2Fe_{14}B$ grain, 2) the $Nd_2Fe_{14}B$ core with a soft outer 2-nm-thick defect, 3) the $Nd_2Fe_{14}B$ core with a hard 4-nm-thick $(Nd,Dy)_2Fe_{14}B$ shell and soft outer 2-nm-thick defect. Intrinsic magnetic properties for the $Nd_2Fe_{14}B$ and $(Nd,Dy)_2Fe_{14}B$ phases at 300 and 450 K are given in Table 13:

Phase	T (K)	Magnetocrystalline anisotropy constant K_1 (MJ/m^3)	Saturation polarization J_S (T)	Exchange stiffness A (pJ/m)
$Nd_2Fe_{14}B$	300	4.30	1.613	7.70
$Nd_2Fe_{14}B$	450	2.90	1.285	4.89
$(Dy_{47}Nd_{53})_2Fe_{14}B$	300	5.17	1.151	8.70
$(Dy_{47}Nd_{53})_2Fe_{14}B$	450	2.70	0.990	6.44

Table 13: Intrinsic magnetic properties for the $Nd_2Fe_{14}B$ grain and the $(Dy_{47}Nd_{53})_2Fe_{14}B$ hard shell at T = 300 K and T = 450 K. [81]

Demagnetization curves were computed by minimizing the micromagnetic energy for decreasing external field. At both studied temperatures, the reduction in coercivity caused by the soft defect is canceled out by the hard shell. Moreover, the soft surface defect doubles the size of the activation volume (see Section I.5.2.2), whereas the hard $(Dy_{47}Nd_{53})_2Fe_{14}B$ shell reduces it by about one third.

Zickler *et al.* [105] carried out micromagnetic simulations on core-shell structures observed in Dy-F treated Nd-Fe-B sintered magnets. This work studied the influence of the GB phase and its intrinsic magnetic properties on magnetization reversal. The LLG equation is solved at each node of the mesh using the FEMME software. The original model structure consists of 8 $Nd_2Fe_{14}B$ grains of dimensions 100 x 100 x 100 nm^3, separated by a 4-nm-thick GB phase. To simulate the core-shell structure, an 8-nm-thick $HRE_2Fe_{14}B$ (HRE = Dy, Tb) shell is put between the GB phase and the $Nd_2Fe_{14}B$ grains, as shown in Fig. 22:

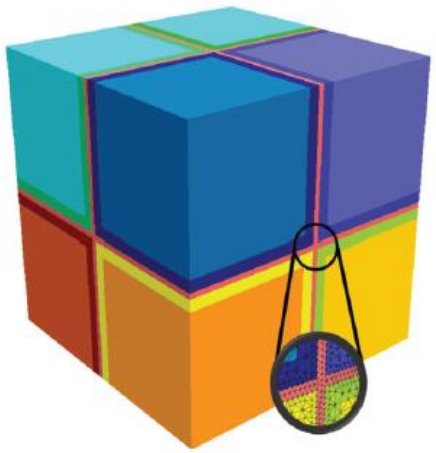


Fig. 22: Finite element model consisting of 8 $Nd_2Fe_{14}B$ grains separated by a 4 nm-thick GB phase and separated from the GB phase by an 8-nm-thick $HRE_2Fe_{14}B$ shell. [105]

The input parameters for the simulations are given in Table 14:

Phase	Magnetocrystalline anisotropy constant K_1 (MJ/m³)	Saturation polarization J_S (T)	Exchange stiffness A (pJ/m)
$Nd_2Fe_{14}B$	4.9	1.61	7.7
$Dy_2Fe_{14}B$	4.5	0.67	7.7
$Tb_2Fe_{14}B$	6.13	0.7	7.7
Non-magnetic GB	0	0.001	0.077
Paramagnetic GB	0	0.75	0.077
Soft-ferromagnetic GB	0	0.75	2.5

Table 14: Intrinsic magnetic properties for the $Nd_2Fe_{14}B$ grains, the Dy- and Tb- enriched shells and the GB phase. [105]

The simulated coercivity is 4.65 T when the GB phase is non-magnetic or paramagnetic in the case of Dy-rich shells, and 4.66 T in the case of Tb-rich shells. The coercivity is reduced to 3.58 T when the GB phase is soft-ferromagnetic in the case of Dy-rich shells, but it has a more important value of 4.34 T for Tb-rich shells in that case. The presence of HRE elements between the GB phase and the $Nd_2Fe_{14}B$ grains acts as a protective shield against nucleation of reversed magnetic domains and as a pinning layer preventing their propagation.

Oikawa *et al.* [106] simulated magnetization reversal processes for (Nd,Dy)-Fe-B sintered magnets with core-shell structures having different Dy concentrations in their shells and cores, using the energy minimization method. The purpose of this work was to understand whether the alloying of $Nd_2Fe_{14}B$ with Dy prior to GBDP is essential to achieve high coercivity or not. Simulations were performed using a supercomputer (1728 cores). In the model, each of the 125 Nd-Fe-B grains has a core-shell structure and is separated from its neighbors by a GB phase. The shape of each grain is polyhedral and is generated from the Voronoi tessellation of a cube. The model size is 300 x 300 x 300 nm^3 and consists of about 20 million tetrahedral elements (mesh size of 2.5 nm). The thicknesses of both GB phase and shells are set to 5 nm (see Fig. 23).

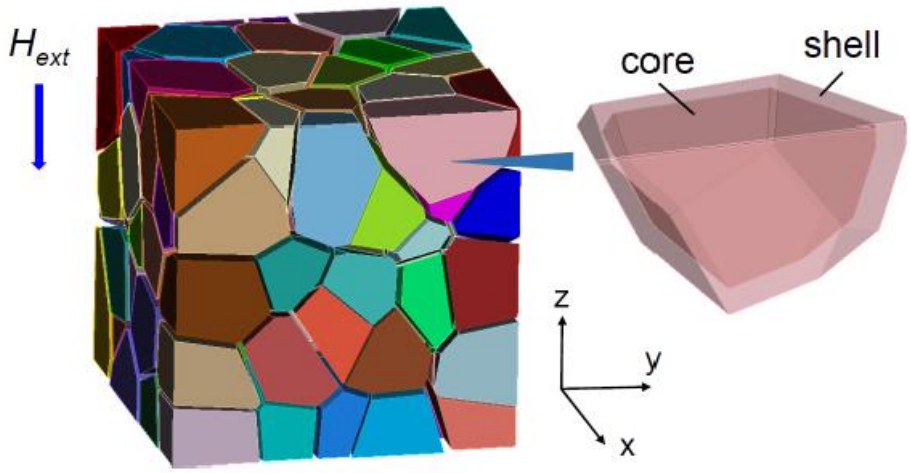


Fig. 23: Structure of the polycrystalline model created by Voronoi tessellation of a cube. [106]

The GB phase is set to be an amorphous soft magnetic layer, leading to exchange coupling between the hard magnetic grains. To start a simulation, the K_1 value of a given grain located at the edge of the model is set to 1/10 of the K_1 value of $Nd_2Fe_{14}B$ to act as a nucleation point for magnetization reversal and as a source of domain wall propagation. Calculated magnetization reversal patterns showed that the origin of coercivity is the pinning of reversed domains at grain boundaries and the anisotropy field of the shell influences the domain wall pinning strength. In addition, Dy alloying in the initial sintered magnets is not essential to achieve high coercivity after GBDP since coercivity has been shown to be independent of the Dy composition of the core (if the shell thickness is greater than 15 nm). The challenge is to increase the Dy concentration in the shell to achieve a high value of anisotropy field, necessary for high coercivity.

Helbig *et al.* [82] carried out micromagnetic simulations to identify the specific nucleation site for magnetization reversal in (Nd,Dy)-Fe-B core-shell model magnets prepared by co-sintering Nd-Fe-B and (Nd,Dy)-Fe-B powders. The model was constructed and discretized in 1-nm-sized cubic meshes, according to the real microstructure, derived from SEM and Kerr microscopy analyses. In the model, the GB phase is non-magnetic and the grains are thus magnetically decoupled. It is also assumed that the boundary of each grain is covered by a 10-nm-thick defect edge layer of magnetocrystalline anisotropy K^{edge}. The LLG equation was solved at each node by the OOMMF software. Simulation results revealed a strong dependency of the coercivity of the analyzed grain on K^{edge}. When K^{edge} is small, nucleation of magnetization reversal occurs at the shell surface and the increase of K^{edge} leads to an increased grain coercivity. Finally, higher values for K^{edge} cause a shift of the nucleation site from the shell surface to the grain core.

The OOMMF software was also used by Chen *et al.* [103] and Li *et al.* [107] to investigate the anisotropic diffusion mechanism during GBDP on sintered Nd-Fe-B magnets. Both works concluded that GBDP along the direction parallel to the easy axis is more effective to improve coercivity than that along any other direction. For instance, in the direction parallel to the easy axis, the initial demagnetization needs to overcome a much higher energy barrier.

I.7. Problematic of the thesis

Coercivity in Nd-Fe-B sintered magnets has been extensively studied with the purpose of HRE reduction (critical materials) and the last two decades have brought decisive advances in microstructural characterization, as well as in realistic micromagnetic modelling. Among others, the crucial role of the

magnetocrystalline anisotropy in the vicinity of grain boundaries combined with dipolar field effects has been assessed. Among the different strategies to improve coercivity, the addition of some elements (Cu, Ga) that form eutectic compounds with RE showing good wettability at grain boundaries, is now widely adopted. It is generally accepted that these intergranular phases are non-magnetic and the adjacent grains are thus believed to be exchange-decoupled. As a result, high performance magnets are assumed to be made of assemblies of grains in which magnetization reverses uniformly by switching. However, while exchange interactions between grains are negligible, magnetostatic or dipolar interactions in such a granular ferromagnetic material play a distinct role from other ferromagnets. This aspect has not been fully investigated yet, both experimentally and numerically. The first part of the thesis aims at investigating some features of the demagnetizing field in Nd-Fe-B sintered magnets and at bringing some quantitative understanding on how they can affect the magnet coercivity (see Chapter III).

Moreover, one of the strategies to improve coercivity consists in developing core-shell grains with Dy-rich phases in the outer regions of the grains. This approach is now used in the magnet industry but still requires optimization to improve the thickness of the fabricated magnet and the process efficiency. Furthermore, the choice of a precursor alloy that contains Co (also considered as a critical material) is of interest since Co is used in magnets for improving their resistance to corrosion and the thermal stability of magnetic properties. Moreover, the solid state diffusion process requires a homogeneous distribution of the Dy-Co diffusion source at the sample surface. It has been experimentally observed that an intermetallic compound can be more homogeneously deposited at the magnet surface than an eutectic alloy. These considerations have led to the study of the grain boundary diffusion process in Nd-Fe-B sintered magnets using a Dy-Co intermetallic compound. This work constitutes the second part of the thesis (see Chapter IV and V).

II. Fabrication of Nd-Fe-B sintered magnets, characterization and numerical methods

In order to answer the questions related to the coercivity of Nd-Fe-B magnets and raised at the end of the previous chapter, different magnet samples have been specifically fabricated and characterized on the pilot line at CEA-LITEN. The equipment and processes available on the platform are fully representative of the magnet industry even if, for research purposes, smaller amounts of material are produced for each batch. This brings the advantage of a fine selection and a better control of the composition and microstructure of the sintered magnets (compared to commercial magnets). This work also takes benefit from a previous investigation performed during the thesis of B. Hugonnet who studied the role of different alloying elements (Al, Co and Cu) and annealing conditions on the magnetic performances.

This chapter firstly recalls the fabrication process of sintered and Dy-diffused Nd-Fe-B magnets implemented in this thesis. For the reference sintered magnets, the experimental work covers operations from the milling of the starting alloy ribbons to the sintering of green compacts, followed by post-sinter annealing heat treatments for further coercivity enhancement.

Specific attention has been paid to sample preparation for the grain boundary diffusion process (GBDP) performed on sintered magnets. Both sintered and diffused magnets have been analyzed by the combination of magnetic measurements, microstructural characterization and numerical modelling to support our interpretations. The different methods (characterization, simulation) used for the interpretation of results are described in the last part of this chapter.

II.1. From ribbon to green compact

In this work, Nd-Fe-B magnets are fabricated by the powder metallurgy route. In the obtained magnets, a maximum amount of the hard magnetic $Nd_2Fe_{14}B$ phase is desirable, as well as a certain amount of Nd-rich phase during the sintering process for rapid densification, limited grain growth and coercivity development. Moreover, oxidation during the fabrication process has to be limited since it implies a composition shift in the Nd-Fe-B ternary phase diagram and can therefore lead to the formation of secondary phases ($Nd_{1.1}Fe_4B_4$, γ-Fe, Fe_2B and Nd_2Fe_{17}) that are detrimental for both remanence (paramagnetic $Nd_{1.1}Fe_4B_4$ phase) and coercivity (ferromagnetic γ-Fe, Fe_2B and Nd_2Fe_{17} phases).

II.1.1. Strip-casting

For conventional casting techniques, slow cooling rates can lead to the formation of the above mentioned γ-Fe phase. The Nd concentration dependence of the critical velocity of solidification front above which the formation of $Nd_2Fe_{14}B$ is kinetically favored over that of γ-Fe has been reported in [5]. During cooling, γ-Fe transforms into α-Fe: the latter is ferromagnetic and therefore couples to hard magnetic grains, implying coercivity degradation. The amount of α-Fe can be reduced by post-casting annealing, but the process is thus costly. A way to get rid of this problem is to use the strip-casting (SC) process with rapid cooling rates. This technique is implemented at CEA-LITEN and is similar to melt-spinning, but with lower wheel speed (see Fig. 24). Nd-Fe-B is obtained in the form of platelet-like flakes/ribbons with a thickness of hundreds of μm.

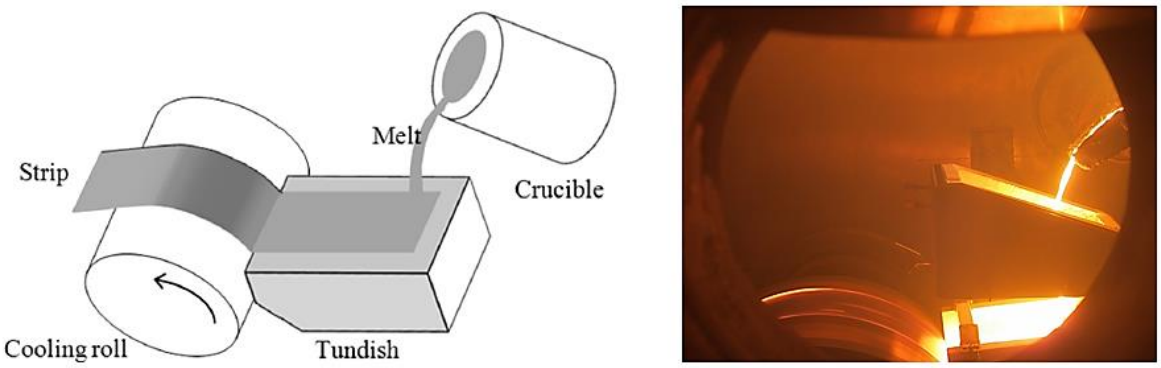


Fig. 24: (Left) Schematic representation of the strip-casting method [108]. (Right) Fabrication of Nd-Fe-B ribbons by the strip-casting process at CEA-LITEN.

The typical microstructure of Nd-Fe-B ribbons obtained by SC consists of columns of $Nd_2Fe_{14}B$ phase separated by Nd-rich lamellar phases (see Fig. 25). The interlamellar spacing between the Nd-rich phases is about a few micrometers and determines the grain size after milling of the strip-casted ribbons. This characteristic length depends mainly on the cooling rate and on the composition of the starting melt [109]. To conclude, the microstructure obtained by SC has three main advantages compared to conventional casting methods: the distribution of Nd-rich phases is fine and thus less sensitive to oxidation, the absence of α-Fe and the fine obtained grain size after milling; all lead to coercivity improvement.

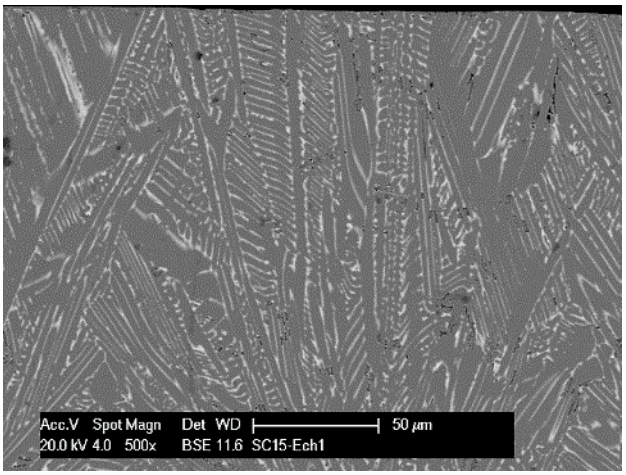


Fig. 25: Microstructure of Nd-Fe-B strip-casted ribbons fabricated at CEA-LITEN.

The chemical composition of the strip-casted ribbons used in this work are given in Table 15. The first ribbons are used in Chapter III about magnetic characterization. The model alloy ribbons are used in Chapter IV/V about GBDP. The denomination TR in the ribbons' names refers to the amount of RE in the ribbon.

	Ribbons	(Nd+Pr)	Dy	Fe	B	Al	Co	Cu	(Ti+Zr)
Chapter III	/	30.8	0.5	Bal.	0.99	0.25	1	0.15	0.07
Chapter IV/V	TR30	29.5	0.5	Bal.	1	0	0	0	0
	TR32	31.5	0.5	Bal.	1	0	0	0	0
	TR31+Al	30.5	0.5	Bal.	1	2	0	0	0
	TR31+Co	30.5	0.5	Bal.	1	0	4	0	0
	TR31+Cu	30.5	0.5	Bal.	1	0	0	0.4	0

Table 15: Chemical composition of the strip-casted ribbons used in the thesis. Amounts are given in wt.%.

II.1.2. Hydrogen decrepitation to coarse powder

After SC, hydrogen decrepitation is performed on the strip-casted ribbons to obtain coarse powder. The different phases pick up hydrogen and as an example, the Nd-rich phase reacts with hydrogen to form mainly NdH_3. Decrepitation leads to the formation of micro-cracks in the ribbon and it is attributed to the volume increase of the phases during hydrogenation.

Decrepitation of the ribbons has been performed with the device available at CEA-LITEN. This equipment works at room temperature and decrepitation takes a few minutes. The hydrogen picked-up by the hard magnetic phase reduces its anisotropy field and has to be removed by a heat treatment at 200°C under vacuum after decrepitation [110]. Further heat treatment is performed at 550°C under vacuum to enable the transformation of NdH_3 into NdH_2, which is crucial for the next step of milling. The complete decomposition of NdH_2 into Nd and H_2 is performed during sintering. After decrepitation and desorption, the obtained coarse powder can be easily milled.

II.1.3. Jet milling

Jet milling has some advantages compared to conventional milling techniques. First, it is a faster process. Secondly, the powder is not in contact with machine components and the milling gas is inert, avoiding contamination of the powder.

The jet mill used at CEA-LITEN is of the fluidized-bed type (see Fig. 26). The coarse powder is put into the jet mill. In the milling vessel, the powder is picked up by high velocity nitrogen gas jets. Interparticle collisions in the nitrogen jets result in the diminution of powder size. This low-energy milling enables to maintain the Nd-rich phase at the surface of hard magnetic grains, which is important to achieve homogeneous sintering. Furthermore, Hattori *et al.* [111] showed that the grain size after jet milling is of the same order of magnitude as the interlamellar spacing between the Nd-rich phases in the SC ribbon, guaranteeing an optimal distribution of Nd-rich phase and monocrystalline grains.

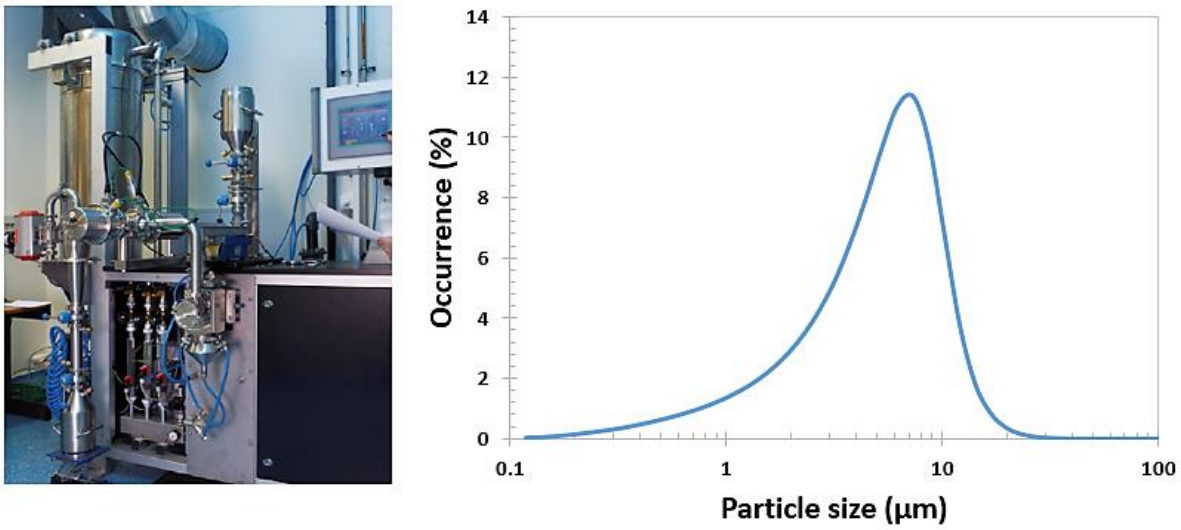


Fig. 26: (Left) Nitrogen jet milling device used at CEA-LITEN. (Right) Typical grain distribution obtained after nitrogen jet milling at CEA-LITEN.

A grain size of about 5 µm is common in industry after nitrogen jet milling. As already mentioned in Section I.4.4.1, ultrafine grain size of around 1 µm can nowadays be obtained after helium jet milling, because of the higher energy of helium jets.

In this work, six jet-milled powders are used for the next fabrication steps. The first one (powder 1) comes from the ribbons $(Nd,Pr)_{30.8}Dy_{0.5}Fe_{bal}B_{0.99}Al_{0.25}Co_1Cu_{0.15}(Ti,Zr)_{0.07}$ (wt.%) and is used in Chapter III (see the associated grain distribution in Fig. 26). The five other powders (powders 2 to 6) come from the ribbons TR30, TR32, TR31 + Al, TR31 + Co and TR31 + Cu, respectively (see Table 15 and Table 16). These five powders are then mixed to obtain the desired composition studied in Chapter IV and V. The median diameters D50 of these six jet-milled powders are given in Table 16.

Jet-milled powder	Starting ribbons	D50 (µm)
1	$(Nd,Pr)_{30.8}Dy_{0.5}Fe_{bal}B_{0.99}Al_{0.25}Co_1Cu_{0.15}(Ti,Zr)_{0.07}$	4.95
2	TR30	5.24
3	TR32	5.14
4	TR31 + Al	4.93
5	TR31 + Co	5.19
6	TR31 + Cu	4.90

Table 16: Median diameters D50 of the six jet-milled powders used in this work.

II.1.4. From powder to green compact

The jet milled powder is transferred into a glove box under nitrogen atmosphere and is afterwards put into a cylindrical silicon mold of diameter 14 mm and of height 25 mm. In the glove box, the risk of pyrophoricity and oxidation of the powder is minimized. The silicon mold with the powder is then put into a plastic packet that is sealed under vacuum since further magnetic alignment and pressing steps are performed outside of the glove box.

II.1.4.1. Magnetic alignment

Magnetic alignment of the powder is performed in a Bitter coil. The alignment cycle is composed of consecutive magnetic pulses of opposite directions and of decreasing intensity. For each pulse, the magnetic field intensity and pulse duration are given in Table 17. This enables optimal orientation of

the powder, as well as its demagnetization (pulse 5). Indeed, if the powder remains magnetized, isostatic pressing will be less effective and the green compact will be too brittle.

Pulse	Mag/Demag	Direction	Magnetic field intensity (T)	Pulse duration (ms)
1	Mag	+	7	5
2	Mag	-	6	5
3	Mag	+	4	5
4	Mag	-	0.5	5
5	Demag	+	6	5

Table 17: Alternating pulses used for magnetic alignment of the powder.

The grains of the powder are mainly monocrystalline. When a magnetic field is applied to monocrystalline grains, the easy axes are along the field direction. In the case of cylindrical green compacts, the easy axes are aligned along the revolution axis of the cylinder.

II.1.4.2. Cold isostatic pressing

The last fabrication step before sintering is the cold isostatic pressing of the aligned powder. The pressing pressure is mediated through a liquid medium (in our case, water) and is applied homogeneously from all directions. Such a pressing technique does not disturb the powder alignment. In our case, powder is compacted at a pressure of 1500 bars.

After magnetic alignment and pressing, the green compact has a high degree of texture: grains are aligned with their easy axis of magnetization in the same direction. Moreover, the powder is consolidated into a mechanically stable green body.

II.2. Sintering furnace

The oriented and pressed green body is then further consolidated by liquid phase sintering. The latter consists in the melting of the Nd-rich phase to form a fully dense magnet. The optimal sintering temperature depends on several parameters: the composition of the green body, the powder grain size and the amount of impurities. This temperature should be high enough to enable the formation of enough liquid Nd-rich phase, as well as low enough to prevent abnormal grain growth. For instance, low density and larger grain size are both detrimental for the coercivity of the final magnet.

The sintering furnace used in this work is the Lilliput from ECM Technologies (see Fig. 27). The sintering atmosphere is secondary vacuum: heat treatment starts when a vacuum of $9x10^{-5}$ mbar is reached. Moreover, quenching with argon can be performed to freeze the magnet microstructure into a thermodynamic metastable state. The furnace is also equipped with an integrated glove box, so that oxygen and water vapor contamination is minimized during the experiments. However, this contamination still needs to be better prevented during the displacement of the green body from the glove box of the lab to the one of the furnace. Moreover, the precise control of a homogeneous furnace temperature is also challenging during operations.



Fig. 27: Furnace used at CEA-LITEN for sintering, annealing and diffusion heat treatments.

This furnace is also used to perform the annealing and the diffusion heat treatments. Both sintering and post-sinter annealing heat treatments are described in further detail in the following section.

II.2.1. Sintering heat treatment

Sintering is composed of two consecutive heat treatments. The first heat treatment is performed at 750°C to remove the residual H_2 from NdH_2. The second one constitutes the real sintering and is done at 1050 and 1032°C for the magnets studied in Chapter III and IV/V, respectively. The thermal cycle used for sintering is detailed in Fig. 28.

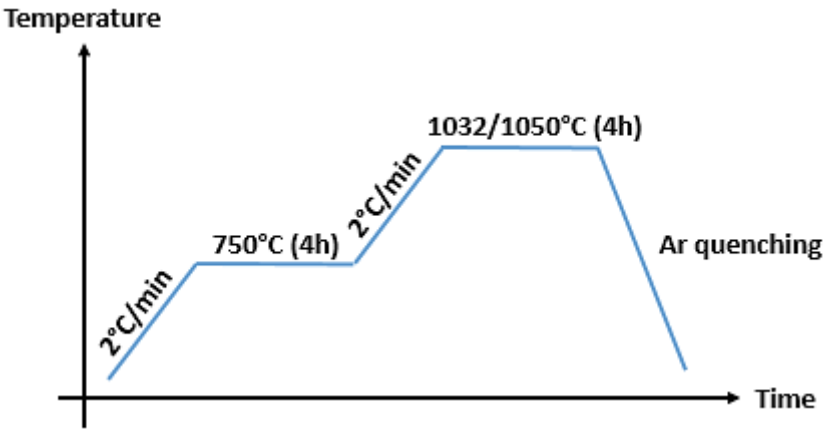


Fig. 28: Thermal cycle used for sintering.

II.2.2. Post-sinter annealing (PSA) heat treatment

After sintering, annealing is performed to enhance coercivity. This PSA consists in two distinct heat treatments. The first one is performed at 800°C such that the Nd-rich phase is in the liquid state. The second heat treatment is carried out between 470 and 600°C. The thermal cycle used for PSA is detailed in Fig. 29. The influence of PSA on magnetic properties is reported in Chapter IV.

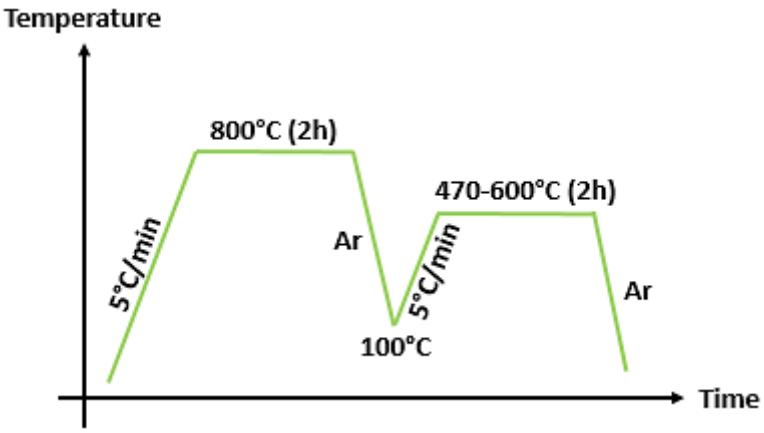


Fig. 29: Thermal cycle used for PSA.

Note also that different annealing heat treatments at low temperatures (470-600°C) can be tested on the same magnet. For instance, a heat treatment at higher temperatures (≈ 900-920°C) after PSA enables the recovery of the magnetic properties obtained in the as-sintered state (see Section IV.1.1).

II.3. GBDP on Nd-Fe-B sintered magnets

II.3.1. Sample preparation for GBDP

GBDP on Nd-Fe-B sintered magnets is performed in this work using Dy-Co eutectic and congruent melting compounds. Dy-Co binary alloys exhibit low melting points which is crucial to achieve efficient diffusion. Furthermore, the presence of Co in these alloys makes them less sensitive to oxidation and Co is also known to improve the thermal stability of magnetic properties and the Curie temperature of the diffused Nd-Fe-B magnets [112], [113]. The Dy-Co binary phase diagram is given in Fig. 30:

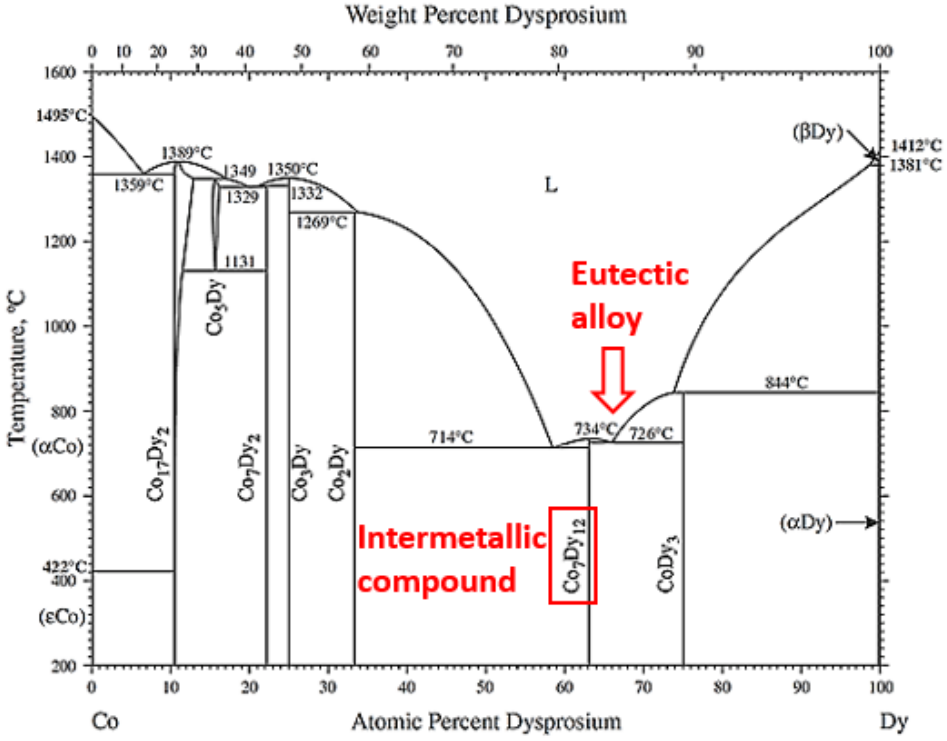


Fig. 30: Dy-Co binary phase diagram.

Dy-Co alloys used for GBDP are the $Dy_{66}Co_{34}$ (at.%) eutectic alloy (T_M=726°C) and the $Dy_{63}Co_{37}$ (at.%) congruent melting or intermetallic compound (T_M=734°C). Both alloys are prepared by mixing Dy and Co in proper ratios and the ingots are obtained after melting at 850°C for 20 minutes. In a glove box, the ingots are then cut into flakes and further ground in a mortar. Experimentally, it has been observed that the grinding of the $Dy_{63}Co_{37}$ intermetallic compound was easier than that of the $Dy_{66}Co_{34}$ eutectic alloy. On the one hand, $Dy_{63}Co_{37}$ can be ground to a powder size of about 50 µm. On the other hand, mm-sized particles are obtained after challenging grinding of $Dy_{66}Co_{34}$.

The diffused Nd-Fe-B sintered magnets are cylindrical, with a thickness of about 5 mm and a diameter of about 10 mm. Before diffusion experiments, the magnets undergo chemical cleaning in a diluted nitric acid solution to remove oxidation layers at their surface. The diffusion source used for GBDP is an ink fabricated by mixing the Dy-Co powder with Terpineol. Mixing is performed so that the ink is composed of about 65 wt.% of Dy-Co powder for optimal viscosity. The ink is then painted on the two magnet faces that are perpendicular to the easy-axis (revolution axis) so that the magnet is diffused with 0.8 wt.% of Dy (see Fig. 31).

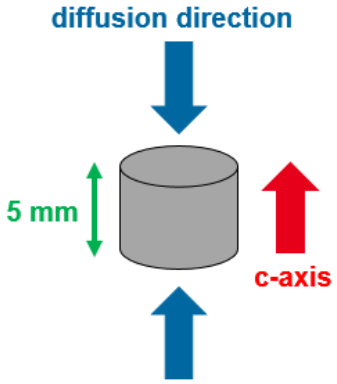


Fig. 31: Sketch of GBDP direction. Diffusion is performed along the easy-axis.

Since the intermetallic compound $Dy_{63}Co_{37}$ can be more easily ground, the deposition of the ink at the magnet surfaces is more homogeneous and diffusion is therefore more efficient than for the eutectic alloy $Dy_{66}Co_{34}$. As a consequence, the results presented in Chapter IV are mainly obtained for GBDP using the intermetallic $Dy_{63}Co_{37}$ compound as the diffusion source.

II.3.2. Diffusion heat treatment

The thermal cycle used for GBDP of Dy-Co is composed of two distinct heat treatments. The first one is performed at 250°C to remove the residual Terpineol at the diffused surfaces of the magnet. The second one is the real diffusion heat treatment and is done either at 870°C for 3h or at 920°C for 3 and 12h. The temperature range and duration for GBDP are taken from literature [114] (good diffusion kinetics). The thermal cycle used for GBDP is detailed in Fig. 32.

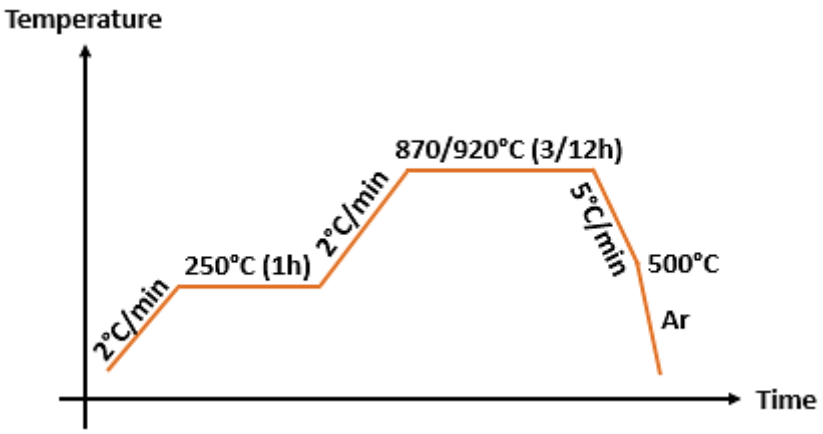


Fig. 32: Thermal cycle used for GBDP.

Further annealing heat treatment is required after GBDP of Dy-Co. In fact, a heat treatment around 900°C leads to a microstructural state equivalent to the as-sintered one (see Section IV.2.1). The influence of this post-diffusion annealing (PDA) on magnetic properties is also studied in Chapter IV.

II.4. Characterization methods

II.4.1. Magnetic characterization

Magnetic properties can be measured using a hysteresigraph system or an extraction magnetometer in closed- or open-circuit conditions, respectively. The differences between both types of measurement will be discussed in Chapter III.

II.4.1.1. Closed-circuit measurement: hysteresigraph system

- Principle of hysteresigraph

Magnetic properties are measured in closed-circuit with a hysteresigraph AMH-300-P of Laboratorio Elettrofisico (see Fig. 33). The sample is inserted within the airgap of a magnetic circuit (see Fig. 33) situated between two poles made of Fe-Co (J_S = 2.3 T). The sample surfaces have to be machined in order to obtain plane surfaces and to avoid undesired air gap and mechanical stress between the sample and the poles. In fact, air gap or irregularities at the sample surface reduce the measured remanence. For example, in the case of our magnet compositions, an air gap of about 100 µm leads to a drop in remanence of 0.04 T, compared to the same measurement with no air gap.

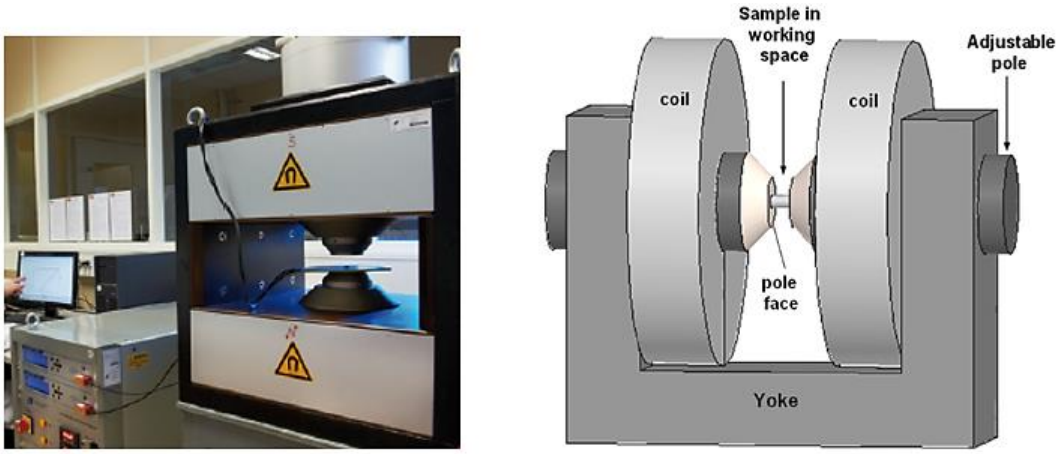


Fig. 33: (Left) Hysteresigraph system used at CEA-LITEN for magnetic characterization in closed-circuit conditions. (Right) Sketch of the magnetic circuit in the hysteresigraph system. [115]

The magnetic field H is generated by an electric current circulating in the winding coils. The yoke structure is large enough to avoid saturation and the distribution of the magnetic field H is assumed to be homogeneous between the Fe-Co poles. The magnetic field H and the polarization J are measured thanks to a planar drilled probe equipped with pick-up coils that allows accurate flux measurements. The sample is inserted inside the circular hole of the probe (see Fig. 34). It is not mandatory that the probe exactly fits the sample (which is cylindrical in our case).

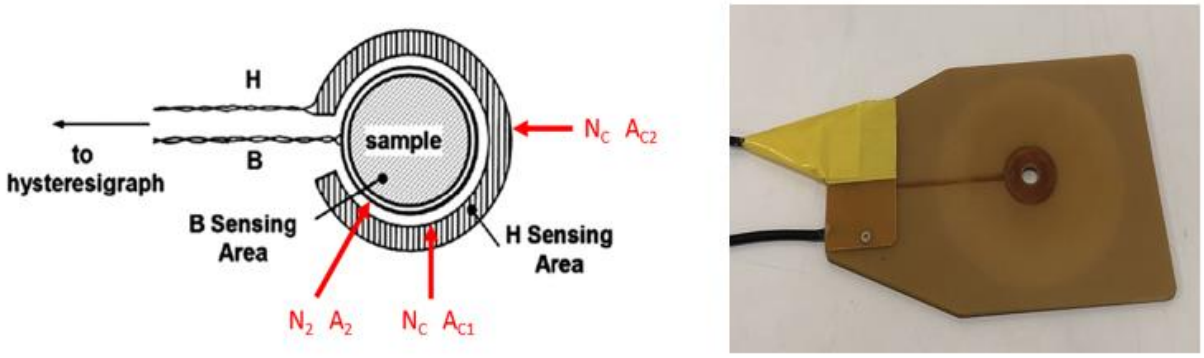


Fig. 34: (Left) Pick-up probe for calculation of H and J [115]. (Right) LJT-10 coil used for magnetic characterization in closed-circuit.

As shown in Fig. 34, the probe is composed of three concentric coils. Two of them are designed for compensation purpose. The magnetic flux ϕ crossing the inner coil with N_2 turns (denoted as "B sensing area") and delimiting an area A_2 surrounding the sample is given by the summation of two terms:

$$\Phi = N_2 A J + N_2 A_2 \mu_0 H \qquad \text{[Eq. 19]}$$

The first right-hand term represents the contribution of the sample magnetization which exhibits a polarization J and a geometrical section A. The second right-hand term comes from the magnetic field generated by the winding coils. In addition, the magnetic flux ϕ_C crossing the dashed area in Fig. 34 between the two external coils of the probe is given by:

$$\Phi_C = N_C (A_{C2} - A_{C1}) \mu_0 H \qquad \text{[Eq. 20]}$$

Thus, the magnetic field H is determined by the measurement of the flux ϕ_C. The turn numbers N_C and N_2, as well as the areas A_2, A_{C1} and A_{C2} can be fitted in such a way that the contribution of the external field H is exactly compensated:

$$N_2 A_2 = N_C (A_{C2} - A_{C1}) \qquad \text{[Eq. 21]}$$

The above condition is fulfilled during the probe building and the flux ϕ_T resulting from the difference of the two previously defined fluxes is then:

$$\Phi_T = \Phi - \Phi_C = N_2 A J \qquad \text{[Eq.22]}$$

Taking into account the section A of the sample, the measurement of the flux ϕ_T gives the value of the sample polarization J. The flux values are obtained from the time-integration of the voltage measured at the coil ends (according to Faraday's law).

The hysteresigraph is considered to supply an absolute measurement of the polarization J. No correction is performed after the measurement of J. The sample section A is the only required parameter. The length of the sample is considered for calibration purpose (in order to adjust the current or voltage increment between two points of the J-H curve).

In practice, the measuring coils have a non-zero thickness which corresponds to the minimal sample thickness. For non-homogeneous samples, it also leads to experimental values of J averaged over few millimeters along the sample height. For the LJT-10 coil used in this work (see Fig. 34), the minimal thickness is 2.5 mm.

- Magnetic properties determined using hysteresigraph

The hysteresigraph system characterizes the demagnetization curve of the measured magnet. Magnetic properties such as the remanence B_R, the coercive field H_{cj} and $(BH)_{max}$ can be determined, as well as H_{knee} (the value of the field for which magnetization value is $0.9M_R$). The ratio H_{knee}/H_{cj} is called the squareness or rectangularity. This ratio can be determined qualitatively by looking at the shape of the demagnetization curve (see Fig. 35).

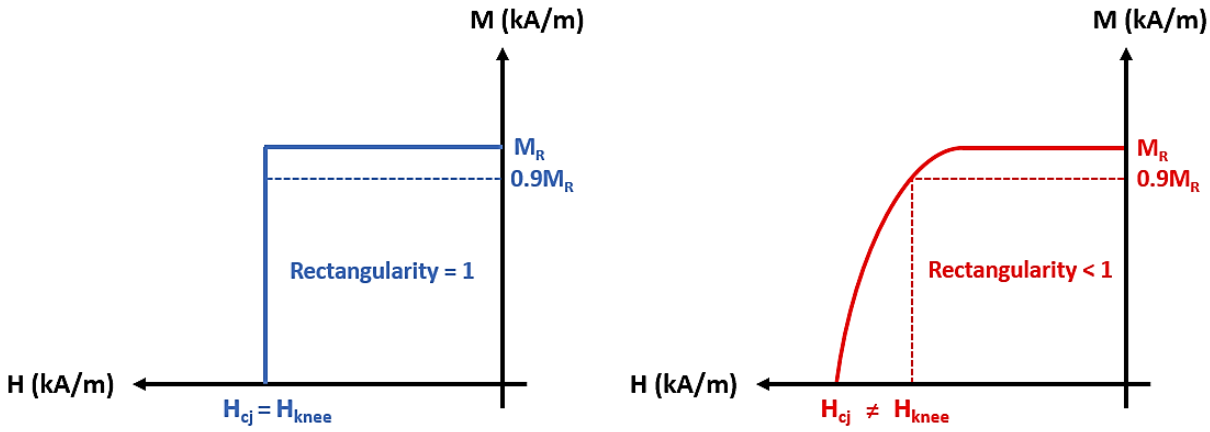


Fig. 35: Schematic representation of the rectangularity of a demagnetization curve.

The more rectangularity is close to 1, the better it is for the magnet application. For instance, a deteriorated rectangularity can lead to irreversible magnetic flux losses, generally for applied field values higher than H_{knee}.

In this work, the sample size is generally around 5 mm (height) and 10 mm (diameter) after post-sintering rectification. The input parameters are the sample thickness, diameter, weight and density, and measurements are performed at room temperature. Preliminary saturation under a pulsed magnetic field of 6 T is required and performed in the laboratory with a Bitter coil prior to each measurement.

II.4.1.2. Open-circuit measurement: extraction magnetometer

Magnetic properties are measured in open-circuit using a custom-built extraction magnetometer available at Institut Néel (CNRS) (see Fig. 36). Magnetization measurements can be performed in a magnetic field range from -10.5 to 10.5 T and at temperatures between 2 to 330 K. The required dimensions for the sample is a cylinder of maximum diameter 6 mm and of maximum height 6 mm to avoid signal saturation.

A supraconducting coil generates the external magnetic field. The measurement of the voltage in the resistor determines the current value in the coil and thus the magnetic field value. The magnetization is determined from the flux variation caused by the sample displacement. When both desired temperature and magnetic field values are reached, the sample is moved between two detection coils in a homogeneous field area. The displacement causes a variation of the magnetic flux that induces an electromotive force ($e = -\frac{d\Phi}{dt}$) at the terminals of the detection coils. The flux variation integrated on the sample displacement is proportional to the sample magnetization. The sensitivity of the extraction magnetometer is 5.10^{-6} A/m^2.



Fig. 36: Extraction magnetometer used at Institut Néel for magnetic characterization in open-circuit conditions.

Magnetic characterization in open-circuit conditions suffers from the inconvenience that the internal field sensed by the sample is the applied external field reduced by the geometry dependent demagnetizing field. Consequently, a field correction must be applied to determine the internal field in open-circuit. In closed-circuit measurements, the sample is part of the magnetic circuit and there is therefore no demagnetizing field contribution to the internal field. A comparison of both techniques constitutes the basis of the work described in Chapter III.

II.4.1.3. Measurement of the Curie temperature

The Curie temperature is determined by measuring magnetization as a function of temperature. This measurement is done in open-circuit on another extraction magnetometer available at Institut Néel with a magnetic field range from -7 to 7 T and a temperature range from 200 to 800 K. The required dimensions for the sample is a cylinder of maximum diameter 4.4 mm and of maximum height 7 mm.

In this work, the samples are rectangular cuboids. Prior to each measurement, saturation of the sample at 6 T is performed. Then, magnetization is measured under an applied magnetic field of 1 T from 300 K to 520 K by increments of 10 K and from 520 K to 720 K by increments of 5 K. The Curie temperature for each sample is determined at the inflexion point when plotting the second derivative of magnetization with respect to temperature as a function of temperature.

II.4.2. Metallography

For microstructural characterization, the samples first have to be embedded and properly polished. The embedding resin is prepared from a mixture of epoxy resin and hardener. Polishing steps are detailed in Table 18:

Polishing step	Polishing disk	Solution	Duration (min)	Rotation speed (rpm)	Applied force (N)
1	SiC #1200	Water	2	250	15
2	Diamond paste 9 µm	Water	8	300	20
3	Diamond paste 6 µm	Ethanol	4	300	10
4	Diamond paste 3 µm	Ethanol	4	250	10
5	Diamond paste 1 µm	Ethanol	2	200	10
6	Diamond paste 0.25 µm	Ethanol	1	200	10

Table 18: Polishing steps before microstructural characterization.

II.4.3. Microstructural characterization

II.4.3.1. Scanning electron microscopy (SEM)

In SEM, a focused beam of high-energy electrons is directed towards the surface of a solid sample. The incident electrons are then decelerated in the sample by electron-sample interactions and their kinetic energy is dissipated as a variety of signals. These latter reveal information about the morphology, the chemical composition and the crystalline structure or orientation of the sample. SEM analysis is carried out under vacuum conditions to avoid collisions between the electron beam and air molecules. [116]

Typical signals used for imaging include secondary electrons, backscattered electrons, cathodoluminescence, Auger electrons and characteristic X-rays. Each signal depends on the electron-sample interaction volume and has its own imaging resolution. For example, signals due to secondary and Auger electrons show the best imaging resolution because they are generated in the smallest volume near the sample surface. Backscattered electrons are generated over a larger volume and thus result in images of intermediate resolution. Cathodoluminescence is generated over the largest volume and implies images with the poorest resolution. [116]

In this work, investigations were carried out using a Gemini MERLIN from Zeiss. Samples were coated with silver paste to make them conductive. Two types of detectors were used during microstructure analysis. The first one is the backscattering spectrometry detector for which heavy elements appear brighter than light elements (atomic number contrast). The second one is the energy-dispersive X-ray spectroscopy detector which enables quantitative analysis of the chemical composition.

II.4.3.2. Energy-dispersive X-ray spectroscopy (EDX)

EDX is an analytical technique that can be coupled with SEM. The EDX spectroscopy detects X-rays emitted from the sample when it is bombarded by an electron beam. During the bombardment, electrons are ejected from the sample surface. This leads to electron vacancies which are then filled by electrons from a higher energy state. An X-ray is emitted to balance the energy difference between the two states of the electron. [116]

In addition to elemental characteristic X-ray peaks, an EDX spectrum also consists of a continuous Bremsstrahlung X-ray background. Bremsstrahlung (*i.e.* braking radiation) refers to the electromagnetic radiation produced by the deceleration of an electron when it is scattered by an atom. The kinetic energy of the incident electron beam is slowed down and its excitation energy is transformed into the energy of a Bremsstrahlung photon, satisfying the law of energy conservation. [117]

The EDX technique enables qualitative analysis of the sample since each X-ray energy peak is characteristic of the element from which it was emitted. Elements from beryllium to uranium can be theoretically detected and the detection limit varies from 0.1 to a few atomic percent. Moreover, it allows quantitative analysis because the EDX detector measures the relative abundance of emitted X-rays as a function of their energy. [116]

II.5. Numerical methods

In this work, micromagnetic simulations have been performed at the sub-grain scale on core-shell models using the FEMME software [65]. Furthermore, magnetization reversal has been simulated using the Flux 3D software in multigrain systems in either closed- or open-circuit conditions and with coercivity gradient. The two approaches are described in more detail in the following sections.

II.5.1. FEMME software package

FEMME is a commercial software supplied by the SUESSCO company and developed by T. Schrefl from Danube University Krems (Vienna, Austria) [65]. Basically, this code solves the LLG equation (see I.5.1.1) and gives, by an energy minimization procedure, the magnetization map in a ferromagnetic material for a given external field.

Finite element micromagnetic simulations performed with FEMME consist of the following steps:

- Creation of the model geometry and finite element mesh generation (Salome software)
- Creation of input files (intrinsic magnetic properties, initial state for magnetization vectors and setting of simulation parameters like the external field direction and the field sweep time)
- Computation of magnetization reversal (FEMME code)
- Plotting of the simulated demagnetization curve
- Visualization of magnetization reversal in the model (ParaView software)

II.5.1.1. Mesh generation

The Salome program [118] is used to draw and mesh the model geometry. It has to be remembered that the maximum mesh size should not exceed the exchange length of the considered material. In this work, tetrahedral meshes are used with a size ranging from 2 nm near grain boundaries to 10 nm in the grain core, respectively. Moreover, the model surfaces are meshed with 2-nm-sized triangles. After generation of the mesh, this latter is exported and further converted into FEMME input files.

II.5.1.2. Input files for FEMME and computation of magnetization reversal

There are three other input files necessary to run a FEMME simulation. The first one defines the material parameters, the second one determines the initial state of magnetization in each grain and the third one gives the control parameters for the simulation.

The material parameter file contains one line per material group, and 7 columns that correspond to the magnetic properties of the material. These latter are detailed in Table 19:

Column	Name	Symbol	Unit
1	Azimuthal angle of the uniaxial anisotropy axis with respect to z axis	θ	radians
2	Polar angle of the uniaxial anisotropy axis with respect to x axis	ϕ	radians
3	Uniaxial anisotropy constant	K_1	J/m^3
4	Second anisotropy constant (unused)	K_2	J/m^3
5	Saturation polarization	J_S	T
6	Exchange constant	A	J/m
7	Gilbert damping constant	α	/

Table 19: Columns of magnetic properties in the material parameter input file.

Similarly, the initial magnetization file has one line per material group, and 4 columns that are given in Table 20:

Column	Name	Symbol	Unit
1	Line number	l	/
2	Unit vector of magnetization in x direction	m_X	/
3	Unit vector of magnetization in y direction	m_Y	/
4	Unit vector of magnetization in z direction	m_Z	/

Table 20: Columns of the initial magnetization input file.

The third input file contains all necessary parameters for the finite element calculation. A first section gives the problem name, the initial time and the final time of the simulation. An additional parameter specifies the amount of output files (time interval after which an output file is created). These intermediate output files are useful to follow the dynamics of the system. In addition, a second section gives the finite element model specific data (mesh size …). The last section details the external field direction and value range.

When all input files are set, calculation of magnetization reversal is performed using the FEMME code. The LLG equation is resolved at each node of the mesh. The calculation gives a log-file with the time, the total magnetization in x, y and z direction and the external field along the x, y and z direction. The evolution of magnetization in the z direction as a function of the external field along the z direction can be plotted as the simulated demagnetization curve.

II.5.1.3. Visualization of magnetization reversal

Post-processing is performed using the ParaView software to observe magnetization reversal within the model. Images of the magnetization direction distribution can be represented for different external applied fields. The objective is to obtain a solid that is colored corresponding to the value of magnetization in z direction. In fact, magnetization vectors aligned along the +z direction and the -z direction correspond to red and blue domains, respectively (see Section II.5.1.4).

II.5.1.4. Application case

A simulation case of the demagnetization in a cubic grain system taken from the literature [119] has been reproduced using the FEMME software. The model consists of 8 $Nd_2Fe_{14}B$ grains of dimensions 100 x 100 x 100 nm^3 that are separated by a GB phase of thickness 4 nm and of various nature (non-magnetic and paramagnetic) and is represented in Fig. 37:

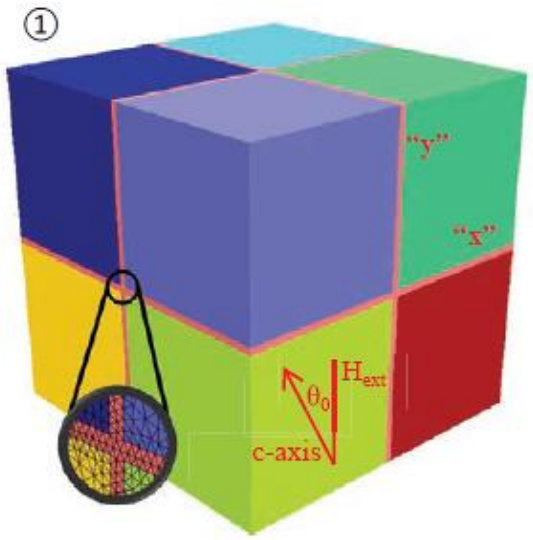


Fig. 37: Finite element model consisting of 8 $Nd_2Fe_{14}B$ grains separated by a 4-nm-thick GB phase. [119]

The intrinsic magnetic properties for the hard magnetic phase and for the GB phase are given in Table 21:

Phase	K_1 (MJ/m^3)	J_S (T)	A (pJ/m)	H_A (T)	L_{ex} (nm)
$Nd_2Fe_{14}B$	4.9	1.61	7.7	7.65	2.7
Non-magnetic GB	0	0.001	0.077	0	440
Paramagnetic GB	0	0.75	0.077	0	0.6

Table 21: Intrinsic magnetic properties used in [119].

The simulations are performed with the influence of the demagnetizing field and without misalignment of the easy axes with respect to the external field. Tetrahedral meshes of 2 nm are used in the entire model. The coercivities obtained by our simulations are compared to the ones obtained in [119] in Table 22:

GB phase	H_{cj} (T) - Simulation	H_{cj} (T) - [119]
Non-magnetic	5.6 (0°)	5.54 (0°)
Paramagnetic	5.1 (0°)	4.79 (0°)

Table 22: Simulated coercivities compared to the ones of the literature case.

For the case with a paramagnetic GB phase, coercivity is overestimated in our simulation by about 0.3 T. This comes from the fact that the meshing is not fine enough to take into account exchange interactions in this paramagnetic GB phase (exchange length smaller than 1 nm). The computation with 1-nm-sized mesh elements is not possible with our informatic system.

For the case with a non-magnetic GB phase, the simulated demagnetization curve exhibits one step and coercivity reaches about 5.6 T (see Fig. 38). The shape of the demagnetization curve and the calculated coercivity are both in good agreement with those from [119]. In this case, the mesh elements are largely smaller than the exchange length of the non-magnetic GB phase.

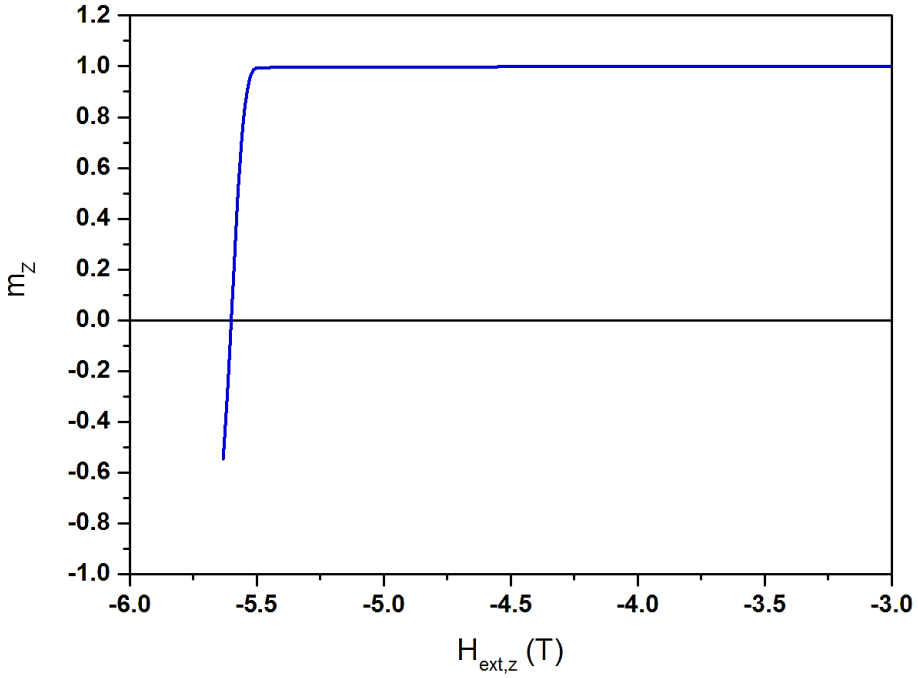


Fig. 38: Simulated demagnetization curve obtained for the 8-g model with a non-magnetic GB phase.

Furthermore, an image of the magnetization configuration is taken during magnetization reversal (see Fig. 39):

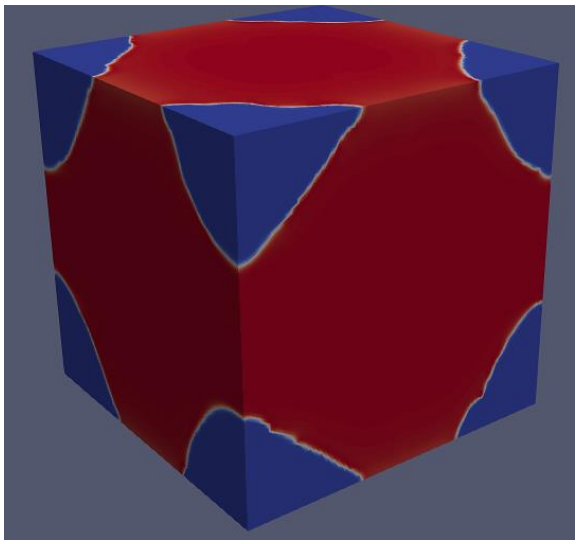


Fig. 39: Image of the magnetization configuration during magnetization reversal for a non-magnetic GB phase.

The nucleation of reversed domains in the model with a non-magnetic GB phase occurs at the outer corners of the model. This is also in good agreement with the observations made in [119].

Bance *et al.* [36] provided an interesting assessment of the fact that reversal should occur near the edges in a cubic grain. They took into account that near the edge, the direction of the self-demagnetizing field H_D of the cube departs largely from the axial direction (*i.e.* the direction of magnetization). Combined with the axially oriented external field H_{ext}, this gives rise to a total field that forms at a distance of 2.5 L_{ext} from the cube border with a small angle (ψ = 4-20°) with respect to the axial direction (depending on the cube size). Considering that nucleation starts at this distance and can be locally depicted by the Stoner-Wohlfarth model, they argued that the switching field H_{sw} is reduced with respect to the anisotropy field. As a consequence, the dependence of H_{sw} as a function of this angle is given by:

$$H_{sw} = f H_A \qquad \text{[Eq. 23.1]}$$

$$\text{with } f = \left[\cos\psi^{2/3} + \sin\psi^{2/3}\right]^{-3/2} \qquad \text{[Eq. 23.2]}$$

For a cube of 100 nm, they determined a value of ψ close to 8° and a value of *f* around 0.7. Applied to the case simulated here for which H_A = 7.65 T, this simple consideration leads to an expected switching field of 5.4 T. Although this result stands for an isolated cubic grain, the value obtained with the above model (5.54 T) is consistent. It is worth noting that the reduction of the grain coercivity with respect to the anisotropy field is, in this case, only correlated to the demagnetizing field and not to a possible degradation of the intrinsic properties (K_1).

This preliminary study made with the micromagnetic model indicates that the description of nanoscale grain boundaries requires very low mesh size and also that reversal of hard ferromagnetic grains should be simulated with very refined elements that are smaller than the exchange length (typically 3 nm) near grain boundaries. Such calibration of the meshing and FEMME set up is relevant for further simulations of Dy-diffused grains performed in Chapter IV.

II.5.2. Flux 3D software

While the FEMME code allows solving the LLG equation taking into account exchange interactions at the nanometric length scale, the simulation using FEMME of large systems consisting of several

thousand of micrometric grains is still beyond the capacity (memory) of current computers. Nevertheless, magnetostatic interactions are of some importance in polycrystalline systems made of hard ferromagnetic grains and should also be described for a better understanding of coercivity in hard magnets. Actually, in high-performance sintered Nd-Fe-B magnets, grains are mostly exchange-decoupled and magnetization reversal spreads over the whole polycrystalline material by switching of individual grains. Basically, the polarization of a given grain is reversed when the local magnetic field exceeds the grain coercivity [120]–[122]. As a consequence, a pattern of reversed and non-reversed grains that are magnetostatically coupled develops as long as demagnetization proceeds. The spatial homogeneity of this discrete pattern, governed by the minimization of the magnetostatic energy, is investigated in Chapter III with simulations performed using a standard finite element software and according to an original set-up described below.

II.5.2.1. Polycrystalline model

In this approach, the polycrystalline magnet material is depicted as a regular array of identical cubic grains of 10 µm width. Each grain is assumed to be homogeneously polarized along the axial direction and can switch from the initial positive value M_S to the negative value $-M_S$. The magnetostatic problem is solved by a finite element (FE) commercial software (Flux 3D, Altair) monitored by a specific Python script. Each grain is meshed with 64 quadratic cubic elements refined near the edges and corners (see Fig. 40). In order to reduce the model size, three symmetry planes (x=0, y=0 and z=0) are considered, allowing only 1/8 of the total volume to be actually simulated. In the following, the simulations are labelled with the number of grains used in each direction of the reduced model, *i.e.* n_x x n_y x n_z.

The Flux 3D code is used to solve the partial differential equation system for standard magnetostatic problems in which the induction B and the magnetic field H are the unknowns:

$$div\ \vec{B} = 0 \qquad \text{and} \qquad rot\ \vec{H} = \vec{J} \qquad \text{[Eq. 24 and 25]}$$

The relation between the two vectors depends on the material. Inside the volume of ferromagnetic grains, the relation takes into account the contribution of the polarization J while this term disappears in non-magnetic materials (air):

$$\vec{B} = \mu_0 \vec{H} + \vec{J} \quad \text{[Eq. 26]}$$

In the polycrystalline model, the polarization J of hard grains is only allowed to switch and should be considered as an input data for each sub-iteration. The problem is solved into a domain comprising the magnet, and in some cases the structure surrounding the magnet (closed-circuit configuration) and a containing “box” of air bonded by some specific elements that take into account the possible long range extension of the magnetic field in the magnet environment (so-called “infinite box”). When a ferromagnetic structure is present, the polarization inside the material is given by:

$$\vec{J} = \mu_0 . \chi(\vec{H}) . \vec{H} \qquad \text{[Eq. 27]}$$

The magnetic susceptibility χ may be a function of the magnetic field, tabulated for the selected materials.

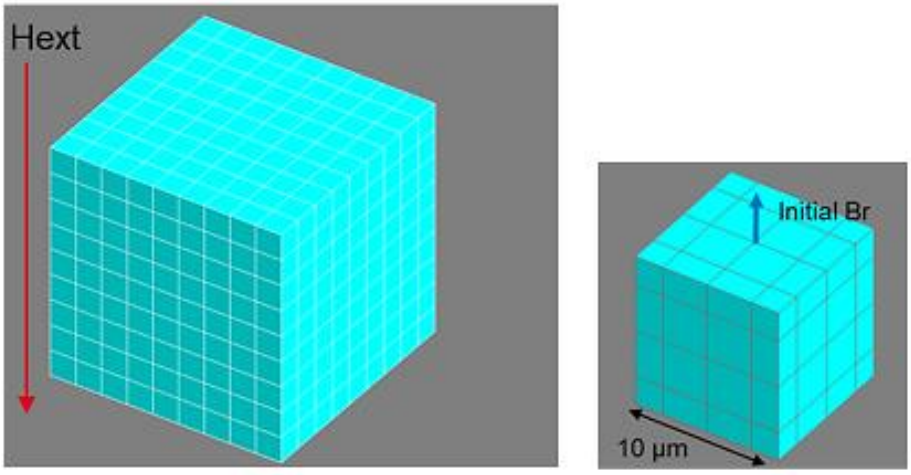


Fig. 40: (Left) Example of a 9x9x9 array of cubic grains. (Right) Detail of a cubic grain meshed with 64 cubic quadratic elements.

Magnetization reversal occurs in a given grain when the projection of the local magnetic field H along the z-axis, averaged on the grain volume, exceeds the coercive field H_C assigned to the grain. A Gaussian distribution of coercivity is ascribed to the individual grains of the array. The mean value $<H_C>$ and the standard deviation σ_{Hc} are fitted to the experimental demagnetization curves. At the beginning of the simulation, all the grains are polarized along the +z direction yielding the remanent state reached after saturation. An external magnetic field is progressively applied on the magnet by small increments ΔH in the opposite direction. For each increment, the reversal condition is tested on all grains and, when fulfilled, the polarization of the grains is switched. Since each grain reversal changes the overall magnetostatic field, the test is repeated until achieving a stable magnetization pattern. Then, the next step with a new field increment is performed considering the updated grain magnetization pattern. Fig. 41(a) is an example of a demagnetizing curve simulated for an array composed of 10 x 10 x 5 grains. Increments of about 10 kA/m are used and some of them have been labelled in Fig. 41(a) according to their step number. Fig. 41(b) shows the evolution of the magnetostatic energy computed during the stabilization loop W_{iter} for these selected steps. The results are normalized by the value of the magnetostatic energy calculated at the beginning of the loop W_0. It can be observed that the magnetization always converges to a steady value corresponding to an energy minimization.

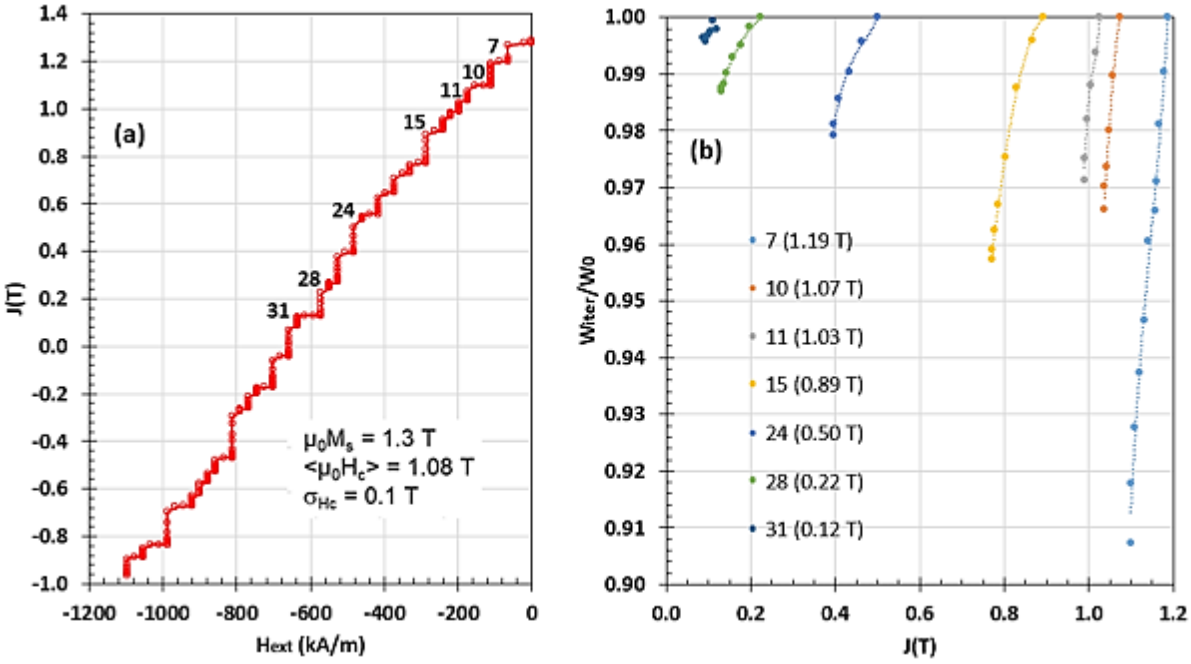


Fig. 41: (a) FE simulation of the demagnetization of a polycrystalline array (10 x 10 x 5 cubic grains) with inputs indicated in the insert. Each point (open red circle) corresponds to a sub-iteration performed into the principal steps defined by the increment value of ΔH. (b) For some principal steps (labelled by their number), evolution of the ratio W_{iter}/W_0 (current energy/energy at the beginning of the step) during the stabilization loop.

II.5.2.2. Comparison with results obtained by an analytical method

The accuracy of FE simulation can be checked by comparing the results with those obtained by the analytical method based on the dipolar approximation [120] (see Fig. 42). An open-circuit configuration (*i.e.* an isolated magnet) should be considered in this case since the dipolar approximation is strictly valid when the flux lines coming from the grain assembly is not influenced by any other neighboring magnetic material. In the dipolar approximation, each grain is considered to be a point dipole creating a magnetic field in free space that is a function of the position *r* and of the moment carried by the dipole *m*:

$$\vec{H} = \frac{3(\vec{m}.\vec{r})-r^2\vec{m}}{4\pi r^5} \qquad \text{[Eq. 28]}$$

The magnetic field produced at any point of the array is then computed by the summation of each dipolar field. The two methods (FE and analytical) give very consistent results for the open-circuit configuration as shown in Fig. 42 (the case corresponds to the data published in [120]).

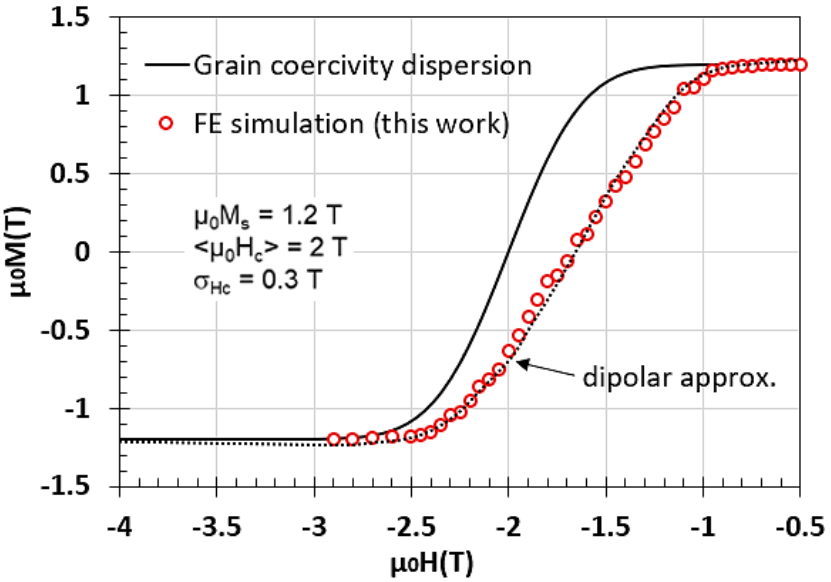


Fig. 42: Comparison of the demagnetizing curves obtained numerically by the dipolar approximation (dotted line) and by the FE method implemented in this work (open red circles).

II.5.2.3. Closed-circuit configuration model

Closed-circuit configurations refer to cases where the magnet is working in a "solid" magnetic circuit. The hysteresigraph system used for magnet characterization forms a particular closed-circuit. The flux lines coming from the sample are channeled by the hysteresigraph yoke and by the pole pieces that are made of a non-linear magnetic material. For these reasons, a FE method has been implemented in this work for the closed-circuit simulation considering the following hysteresigraph features: (i) the external field is created by a coil excited by an electric current and wound around a ferromagnetic armature positioned laterally from the sample, (ii) the flux is channeled towards the sample thanks to vertical arms and planar poles having a large area compared to the sample and (iii) the magnetic field is determined in the mid-plane of the sample by a measuring coil. Although simple, this geometrical model gives a sufficient description of the hysteresigraph system (compare Fig. 43 with Fig. 33).

Fig. 43 illustrates the 3D geometrical model simulated by FE. The sample is located between two symmetrical prismatic-shaped pole pieces. The yoke is roughly represented by a rectangular armature. Two electrical coils are wound around the external arms of the yoke. The external field applied on the sample is proportional to the electrical current. The current amplitude is selected in order to cover the range of demagnetizing field. Some details regarding the mesh are visible in Fig. 44. The size of the mesh elements in the parts surrounding the magnet are gradually growing from the grain dimension to a millimetric length scale. Eventually, the model comprises about 100 000 elements. The computation time is of the order of 10 hours on a standard 6-core-workstation (DELL Windows 10).

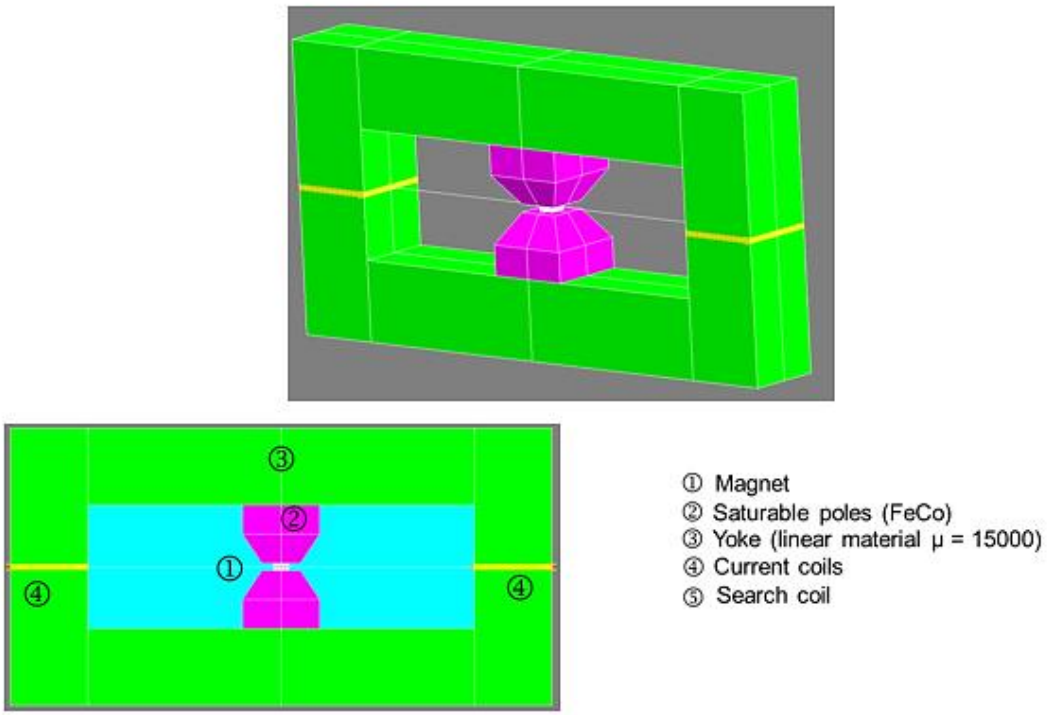


Fig. 43: 3D geometrical model used for the simulation in closed-circuit configuration (hysteresigraph measurement system).

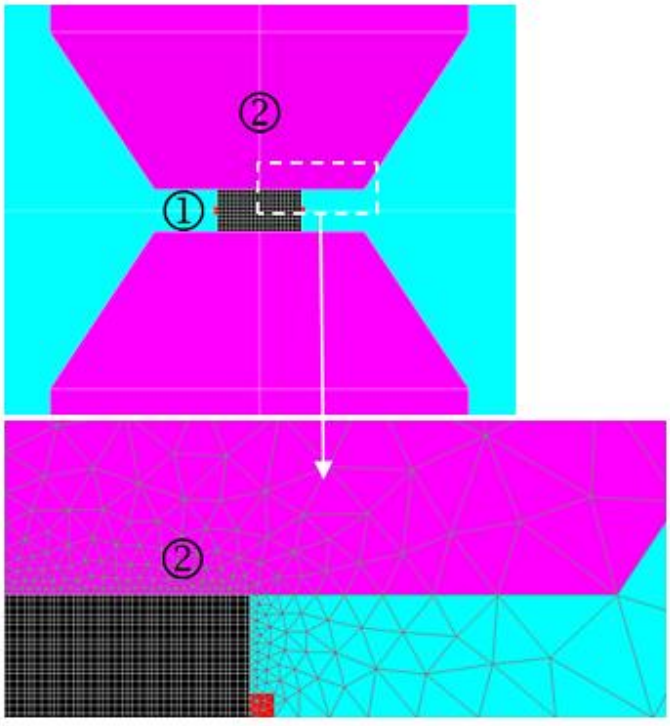


Fig. 44: Details on the mesh at the contact area between the polycrystalline magnet and the pole piece of the hysteresigraph system.

All materials considered in the following simulation are assumed to follow a linear magnetic behavior (*i.e.* they exhibit a constant susceptibility and no saturation). However, it has been reported that localized saturation of the pole piece may occur for elevated applied field values and, in some cases, can affect the results [115]. A simulation run has been performed with a non-linear model applied to

the pole piece (the magnetization curve of Fe-Co 17% is available in the material database of Flux 3D). The demagnetizing curves are shown in Fig. 45. It has been found that linear and non-linear models give similar results. Due to the large increase in the computation time for the non-linear model, further simulations have been performed with the linear approximation. The small difference doesn't affect the main conclusions of the analysis. It can also be noticed that the simulated demagnetizing curve in closed-circuit configuration is more "rectangular" than the distribution of grain coercivities. Basically, the demagnetization starts when the applied field reaches the lowest grain coercivity and magnetization reversal abruptly propagates within the whole sample. This result points out the fact that the coercivity of the polycrystalline sample is much lower than the average value of the grain coercivity. This finding will be analyzed in more detail in Chapter III.

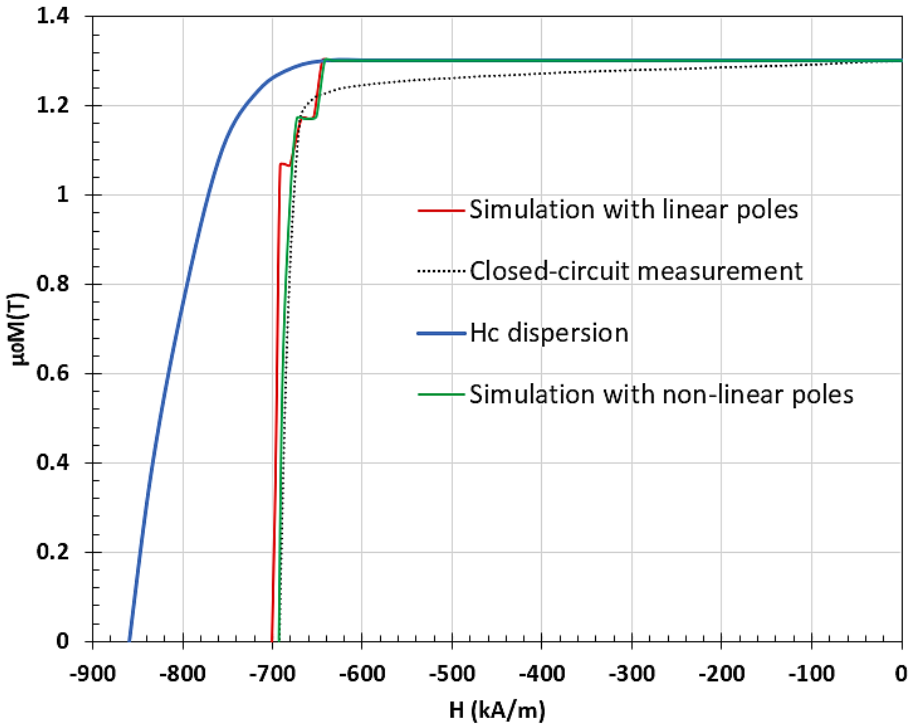


Fig. 45: Simulation of the demagnetization of a polycrystalline sample in closed-circuit (hysteresigraph system) with linear and non-linear magnetic behavior assumptions for the pole pieces. The simulated curves have been fitted to the experimental one by an appropriate choice of the grain coercivity distribution parameters.

II.5.2.4. Limitation of the polycrystalline model

The polycrystalline model should be seen as a very simplified representation of sintered magnets. First, the spatial discretization of the cubic grains is not fine enough to capture the demagnetizing field details near grain boundaries, at a distance for which nucleation occurs. The switching field of grains is therefore considered as an input data disregarding details such as local orientation effects pointed out in the Stoner-Wohlfarth model. The second model limitation comes from the number of grains that can be simulated (up to 4000). However, in this approach, the grain size is not really a relevant factor since dipolar effects are averaged over the grain volume, making the results identical whatever the cube dimension. Consequently, macroscopic magnets are simulated by 3D arrays of arbitrary sized grains, the aspect ratio of the array being the same as the magnet. This allows the self-demagnetizing field to be correctly described at both magnet and grain size. Obviously, the weight of a cubic grain reversal in the simulation is considerably higher than the one of a real grain, making highly stepped J-H curves (see Fig. 45).

III. Coercivity of polycrystalline hard magnets

III.1. Introduction

As pointed out in Chapter I, the demagnetization of hard ferromagnets is intricately dependent on their microstructure. In high-performance sintered Nd-Fe-B magnets, grains are mostly exchange-decoupled and it is widely accepted that magnetization reversal spreads over the whole polycrystalline material by switching of individual grains. At the grain scale, the polarization of a given grain is considered to reverse abruptly when the local magnetic field exceeds the grain coercivity. This latter implies nucleation of reversal at nano-sized defects localized near grain boundaries. The coercive field also depends on the chemical composition and phase distribution of the magnet. The relationship between coercivity and the anisotropy field is thus strongly microstructure-dependent and can be partially clarified thanks to micromagnetic models. Within this scope, Chapter IV will present numerical simulations of magnetization reversal in Dy-diffused magnets performed with the FEMME software.

However, at the micrometric scale, the spatial homogeneity of the grain reversal pattern is mainly governed by the minimization of the magnetostatic energy and cannot be, in practice, studied with the micromagnetic approach due to the limitation in the model size. These magnetostatic effects are of importance since they could lead to some misinterpretation of the demagnetization curves usually measured on magnets for design purposes [121], [122]. More precisely, attention has to be paid to the correction applied to open-circuit measurements to extract the intrinsic demagnetization curve. A difficulty rises from the demagnetizing field shift that is inherent to this kind of experimental technique and has to be removed from raw data. The first part of this chapter investigates the demagnetizing field in hard ferromagnets and its link with the grain reversal pattern in order to propose an updated protocol for the treatment of open-circuit measurements. To assess the demagnetizing field correction, the polycrystalline model introduced in Section II.5.2.1 is implemented. This original approach helps the quantitative understanding of the effects of grain reversal pattern in two different experimental configurations (open- and closed-circuit) widely used for coercivity measurement. Then, in a last part, the polycrystalline model is used to analyze the reversal patterns in non-homogeneous magnets, represented in that case by a duplex magnet. The objective is to anticipate the analysis of magnets with coercivity gradient that are obtained after Dy diffusion and detailed in Chapter IV and V.

III.2. Study of collective magnetostatic effects: experimental approach

III.2.1. Model for the demagnetization field correction

III.2.1.1. The usual demagnetizing field correction and validity

For ferromagnetic and ferrimagnetic materials, the internal field felt by the material is the summation of the external applied field and of the demagnetizing field ($H_{int} = H_{app} + H_D$). The magnetization M is the source of the demagnetizing field, usually given by:

$$H_D = -NM \qquad \text{[Eq. 29]}$$

N is a geometrical demagnetization factor and the slope of the magnetization variation with H_{app} is 1/N. Apart from the special case of a sphere for which the demagnetization factors are constant and identical along all directions ($N_x = N_y = N_z = 1/3$), the values of N evolve spatially in the volume for a general shaped body. For parallelepipeds, analytical expressions and tables are available to supply

accurate values of N for a wide range of shape ratios (for instance, Aharoni [123] gave analytical expressions for a = b ≠ h). For a regular solid with a square section (a = b = 1) and a height h equal to 0.5, the spatial distribution of N_z is plotted in Fig. 46. These values have been computed by the finite element method presented in Chapter II. The values of N_z lie within a range having a minimum of 0.23 and a maximum of 0.70. The averaged values of N_z are also reported in Fig. 46 for five XY planes located at different heights. In the mid-plane, the averaged value is 0.47, lower than the value averaged over the whole body (0.5). The averaged value of N_z in the mid-plane is generally used for fluxmetric corrections ([Eq. 29]) in the case of a magnetization oriented along the axial direction.

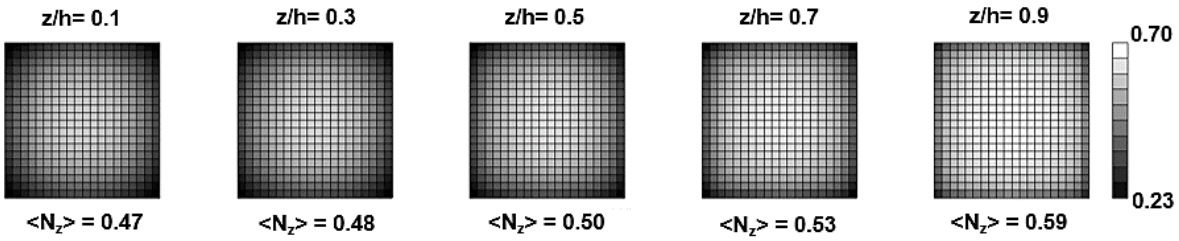


Fig. 46: Map of demagnetization factors N_z in XY planes at different heights (z) obtained by FE computation for a parallelepiped (a = b = 1 and h = 0.5). The values given below each map correspond to an average value in the plane.

The equation [Eq. 29] constitutes the usual demagnetizing field correction that must be applied to open-circuit measurements to obtain the real demagnetization curve. For closed-circuit measurements, no correction is needed since the sample is part of the magnetic circuit and there is no demagnetizing field contribution (N=0).

One of the assumptions for the validity of the above equation is that the magnetization generates surface magnetic charges (and no volume charges) that give a homogeneous contribution to H_D inside the considered material. In soft magnetic materials, the magnetization state is homogeneous at a higher scale than that of magnetic domains and only surface charges contribute to H_D: the usual demagnetizing field correction is valid. However, in hard magnets, the magnetization state is heterogeneous owing to the discrete switching of exchange-decoupled grains. Both surface and volume charges contribute to H_D and the usual demagnetizing field correction is therefore not applicable to hard magnetic materials.

As a consequence, another demagnetizing field evaluation is required for hard magnets. This is important in the perspective of defining experimental protocols to compare the properties of magnets measured in open-circuit to those of other magnets measured in closed-circuit.

III.2.1.2. The demagnetizing field model (cavity field concept)

With the help of the cavity field concept, the demagnetizing field in hard magnets can be expressed in terms of three contributions [53]:

$$H_D = H_D^{surf} + H_D^{cav} + H_D^{grain} \quad \text{[Eq. 30]}$$

The first contribution is the usual one coming from surface magnetic charges. The second and third contributions are due to volume charges. They are understood by considering that individual grains are virtually removed from inside matter, as schematized below in Fig. 47:

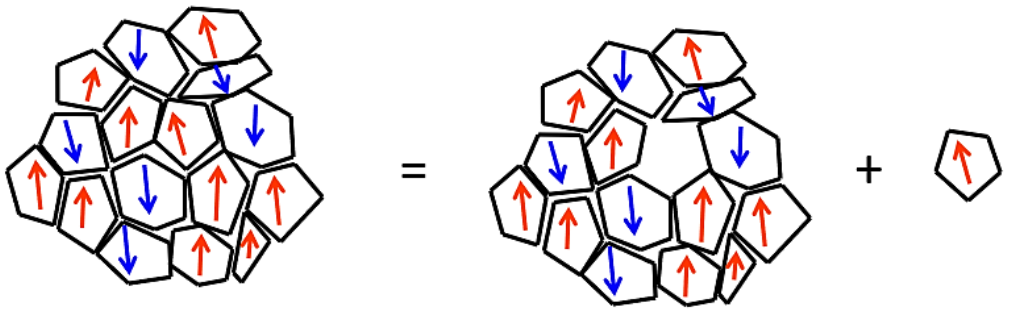


Fig. 47: Schematic representation of a heterogeneous granular hard magnet (cavity field concept).

The second contribution represents the field created in the thus-created cavity. The third contribution represents the grain's self-demagnetizing field.

The first term is expressed as $H_D^{surf} = -NM$. The second term is given by $H_D^{cav} = N_g M$, where N_g is the individual grain demagnetizing factor (taken as 1/3 for spherical grains). The third term is expressed as $H_D^{grain} = -N_g M_S$ and depends on the spontaneous magnetization M_S and not on the mean magnetization M, because reversal proceeds by successive discrete switching of individual grains. Note that H_D^{surf} and H_D^{cav} do not cancel out, the slope of the magnetization variation is therefore affected and amounts to $1/(N-N_g)$. This constitutes the so-called "hard demag" correction. It is worth noting that this is true when H_D^{surf} dominates H_D^{cav}, leading principally to homogeneous reversal.

Alternatively, when H_D^{cav} dominates H_D^{surf}, magnetization reversal occurs mainly via collective processes. Considering that reversal may have intermediate character between fully homogeneous (dependence on M) and fully collective (dependence on M_S), a new general expression for the cavity field may be defined as follows [124]:

$$H_D^{cav} = (1-\alpha)\beta^{hom} N_g M + \alpha\beta^{col} N_g M_S \qquad \text{[Eq. 31]}$$

The parameter α gives the weight of collective effects in the cavity field (α=1 when fully collective, α=0 when fully homogeneous). The parameters β^{hom} and β^{col} are phenomenological and represent the strength of the cavity field for homogeneous and collective reversal, respectively. The total demagnetizing field becomes:

$$H_D = -NM + (1-\alpha)\beta^{hom} N_g M + \alpha\beta^{col} N_g M_S - N_g M_S \qquad \text{[Eq. 32]}$$

The slope of the magnetization variation is also affected and is now 1/N' with:

$$N' = N - (1-\alpha)\beta^{hom} N_g \qquad \text{[Eq. 33]}$$

If the parameter β^{hom} is taken equal to 1, for α=1, the 1/N slope of the usual demagnetizing field correction is recovered. For α=0, the $1/(N-N_g)$ slope of the "hard demag" correction is recovered.

The reduction in coercivity due to the demagnetizing field (compared to the ideal case for which coercivity corresponds to the nucleation field H_N of the grain, H_N being identical for all grains), by taking M=0 in [Eq. 32]), amounts to:

$$\Delta H_c = \left(\alpha\beta^{col} - 1\right) N_g M_S \qquad \text{[Eq. 34]}$$

The three mentioned demagnetizing field corrections (usual, "hard demag" and with collective effects) are schematically represented in Fig. 48:

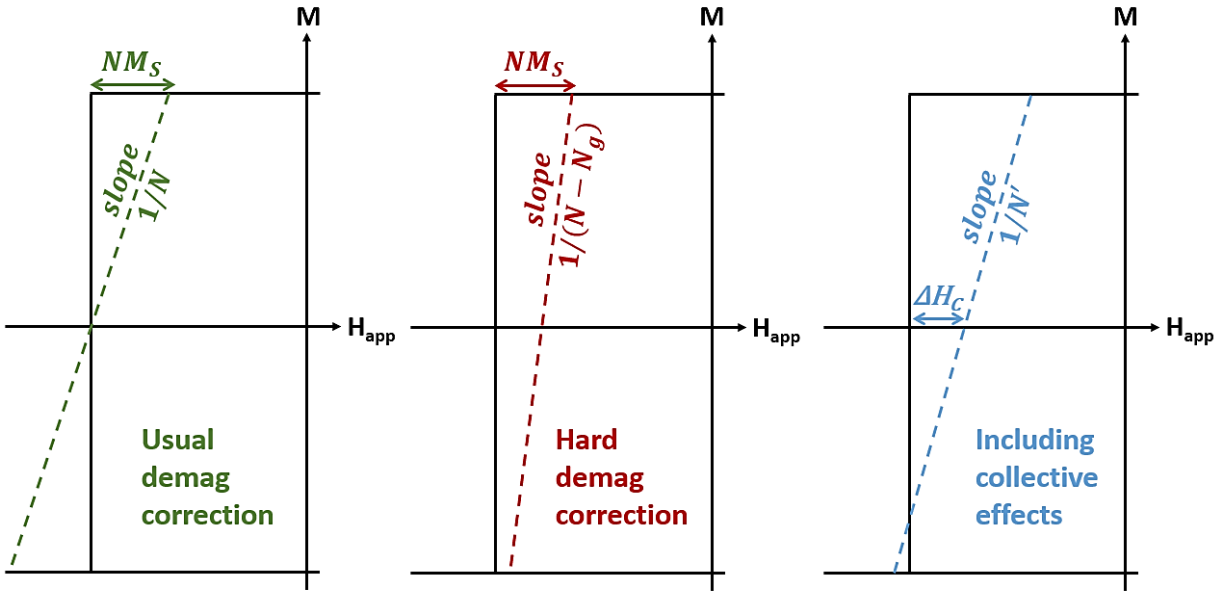


Fig. 48: Schematic representation of the demagnetizing field contributions to magnetization reversal. Black line: reversal in the absence of any demagnetizing field effects. (Left graph) Dashed green line: usual demagnetizing field correction (α = 1 and β^{hom} = 1). (Middle graph) Dashed red line: so-called hard demag correction applicable in the absence of collective effects (α = 0 and β^{hom} = 1). (Right graph) Dashed blue line: intermediate correction when collective effects are considered (both α and β^{hom} ≠ 0). [124]

The above model that takes into account collective effects in the demagnetizing field expression will be used in the following sections for the interpretation of demagnetization curves measured in both closed- and open-circuit conditions.

III.2.2. Experimental protocol and results

The magnets studied here are prepared by the powder metallurgy route described in Chapter II. The green compacts of composition $(Nd,Pr)_{30.8}Dy_{0.5}Fe_{bal}B_{0.99}Al_{0.25}Co_1Cu_{0.15}(Ti,Zr)_{0.07}$ (wt.%) are sintered at 1050°C for 4 h to produce the final magnets. No post-sinter annealing is performed, so that coercivity is limited to the order of 1 T to allow measurements in both closed- and open-circuit conditions. However, even if the grain boundary phase is not optimally distributed around grains since annealing has not been performed, grains are still assumed to be mainly exchange-decoupled thanks to the presence of alloying elements that form non-magnetic phases.

After sintering, the obtained magnets have the shape of cylinders, 10 mm in diameter and 15 mm in height. From these magnets, three cylinders of diameter ϕ = 6 mm are cut with different thicknesses: t = 3, 4 and 5 mm. Hereafter, the samples will be referred to as S1, S2 and S3, respectively. Note that the dimensions of the three samples are chosen such that they could be measured in both closed- and open-circuit devices. The open-circuit measurements are performed on the custom-built extraction magnetometer under a maximum applied of 6 T. The closed-circuit measurements are carried out on the hysteresigraph system following saturation under a pulsed magnetic field of 6 T. The measurements are performed at 292 K on samples S1 and S2 and at 300 K on sample S3.

The hysteresis curves measured for the three samples using both the hysteresigraph system (red solid curve, slope: $1/N_{exp}^{cl}$) and the extraction magnetometer (black solid curve, slope: $1/N_{exp}^{op}$) are shown in Fig. 49. Furthermore, the open-circuit measurement with the usual demagnetizing field correction

(dashed blue curve, slope: 1/N) and the open-circuit measurement corrected to be parallel to the closed-circuit curve (green solid curve, slope: 1/N') are also represented.

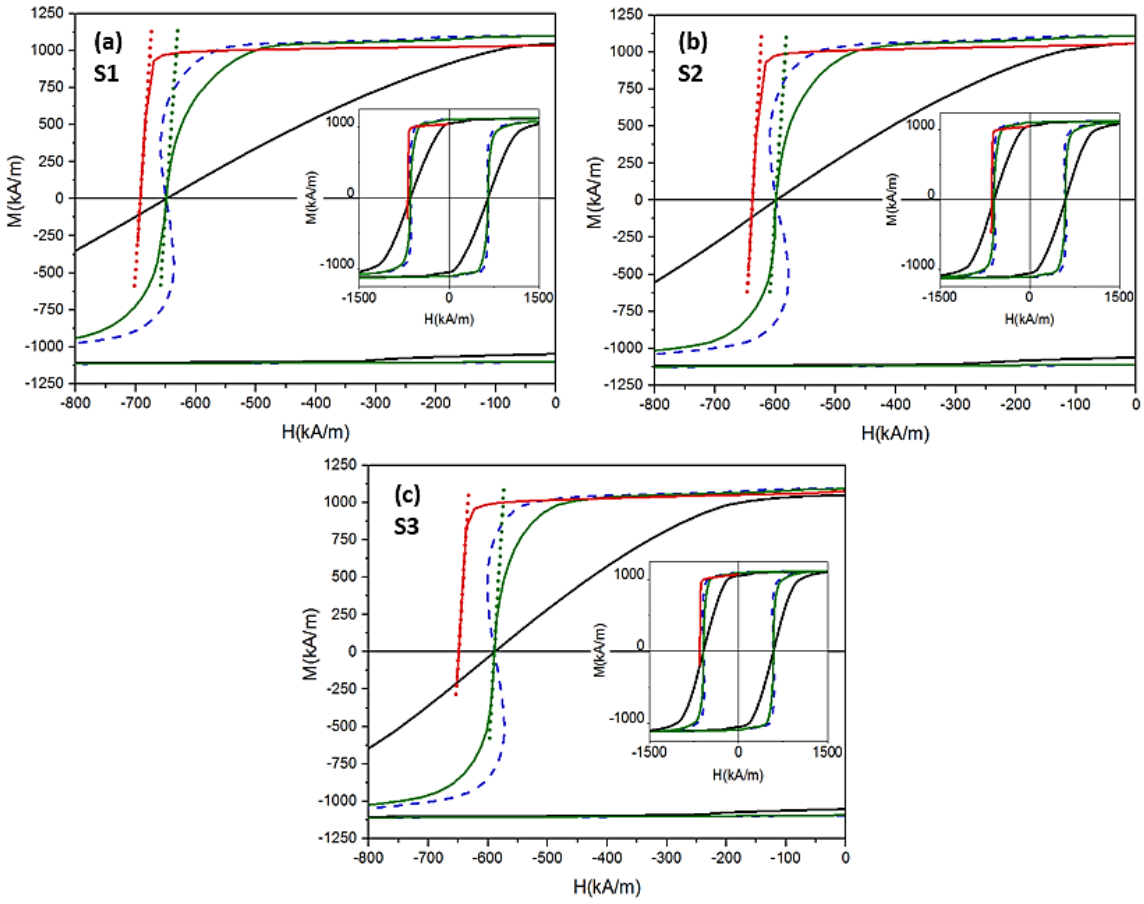


Fig. 49: (a) Second and third quadrants of the hysteresis loop for sample S1 of thickness 3 mm. Solid black curve: raw open-circuit measurement without demagnetizing field correction (slope: $1/N_{exp}^{op}$). Dashed blue curve: open-circuit measurement with the usual demagnetizing field correction (slope: 1/N). Green solid curve: raw open-circuit measurement corrected to be parallel to the closed-circuit one (slope: 1/N'). Red solid curve: closed-circuit measurement (slope: $1/N_{exp}^{cl}$). Short dotted lines: tangents at H=H_c for the closed-circuit measurement and for the open-circuit measurement corrected with N'. Inset: complete hysteresis loop for sample S1. (b) Same data for the sample S2 of thickness 4 mm. (c) Same data for the sample S3 of thickness 5 mm. [124]

The experimental magnetic characteristics determined from the above hysteresis loops are collected in Table 23. M_S is the spontaneous magnetization taken as the magnetization measured under 6 T in open-circuit. H_c^{cl} and H_c^{op} are the closed- and open-circuit measured coercive fields, respectively. $\Delta H_c^{t.a.}$ is the difference in coercivity between the closed- and open-circuit measurements due to thermal activation effects [59]. $H_c'^{cl}$ represents the closed-circuit coercive field corrected for thermal activation effects (taking open-circuit measurements as reference). ΔH_c^{exp} is the difference between the closed- and open-circuit coercive fields after thermal activation correction. N_{exp}^{op} and N_{exp}^{cl} are the inverse of the experimental slope determined at H = H_c for the open- and closed-circuit measurement, respectively.

Sample	t (mm)	M_S (kA/m)	H_c^{cl} (kA/m)	H_c^{op} (kA/m)	$\Delta H_c^{t.a.}$ (kA/m)	$H_c'^{cl}$ (kA/m)	$\Delta H_c^{exp} = H_c'^{cl} - H_c^{op}$ (kA/m)	N_{exp}^{op}	N_{exp}^{cl}
S1	3	1151 (1)	692 (1)	650 (1)	20	672	22 (2)	0.42 (1)	0.015 (1)
S2	4	1165 (1)	638 (1)	599 (2)	20	618	19 (3)	0.35 (1)	0.014 (1)
S3	5	1154 (1)	650 (2)	591 (3)	20	630	39 (3)	0.30 (1)	0.015 (1)

Table 23: Experimental magnetic characteristics of samples S1, S2 and S3 (same diameter ϕ = 6 mm).

The lower coercivity of sample S2 (as measured in closed-circuit) comes from the fact that S2 was cut from a magnet made in a different run than S1 and S3. This difference in coercivity has no impact on the current analysis since the differences between open- and closed-circuit measurements on a given magnet are studied here.

For all three magnets, the coercive field at which magnetization vanishes is smaller in open-circuit measurements than in closed-circuit ones. However, a fully quantitative comparison between coercive field values is not possible, due to the different contributions of thermal activation to the measured coercivity in both conditions. For instance, assuming that the magnetic viscosity coefficient S_v is constant, two loops measured at two different characteristic times t_1 and t_2 are shifted in field by $S_v Ln(t_1/t_2)$. For Nd-Fe-B magnets with a coercive field around 1 T, the magnetic viscosity coefficient is estimated to 4 kA/m [59]. For closed-circuit measurements with the hysteresigraph, the characteristic time is $t_1 \approx 1$ s and for open-circuit measurements, it amounts to $t_2 \approx 100$ s. As a result, the hysteresis loops measured in closed-circuit are shifted towards higher fields with respect to those measured in open-circuit, by approximatively 20 kA/m (corresponding to $\Delta H_c^{t.a.}$ in Table 23). For the purpose of comparing demagnetizing field effects during open- and closed-circuit measurements, this field is subtracted from the closed-circuit coercive field and gives $H_c'^{cl}$, as shown in Table 23. After thermal activation correction, the experimental difference in coercivity ΔH_c^{exp} between closed- and open-circuit measurements reaches up to 6.6 %.

Moreover, the inverse of the open-circuit experimental slope N_{exp}^{op} is systematically smaller than the demagnetizing factor N (calculated from [125], see Table 24). This leads to the overcorrection (also referred as overskewing in literature) observed on all demagnetization curves when applying the 1/N usual demagnetizing field correction (dashed blue curves). It again highlights the fact that the usual correction is not applicable to the case of hard magnets.

III.2.3. Analysis and model improvement

The calculated magnetic characteristics determined from the above hysteresis loops are given in Table 24. N is the open-circuit calculated demagnetizing factor. $N_{exp}^{op} - N_{exp}^{cl}$ is the difference between the inverse of the experimental slope determined at $H=H_c$ for the open-circuit measurement and the one determined for the closed-circuit measurement. α_{exp}^{op} represents the contribution of collective reversal during open-circuit measurements. β^{col} is a phenomenological parameter for collective reversal and is taken as 0.5. ΔH_c^{calc} is the calculated difference between the closed- and the open-circuit coercive fields.

Sample	N	$N_{exp}^{op} - N_{exp}^{cl}$	α_{exp}^{op}	β^{col}	ΔH_c^{calc} (kA/m)
S1	0.46	0.40 (1)	0.82	0.5	34.5
S2	0.40	0.34 (1)	0.82	0.5	35.0
S3	0.35	0.29 (1)	0.82	0.5	34.6

Table 24: Calculated magnetic characteristics of samples S1, S2 and S3.

The above experimental results illustrate the fact that differences in demagnetizing field effects must be considered when comparing closed- to open-circuit measurements. Remembering that H_D^{surf} favors homogeneous reversal whereas H_D^{cav} favors collective reversal, the closed-circuit configuration should exhibit a fully collective reversal since H_D^{surf} = 0 in this condition. Under this hypothesis, the closed-circuit demagnetizing field slope $1/N_{exp}^{cl}$ should be infinite. This slope represents the distribution in coercive field values of individual grains. This intrinsic distribution should also affect the slope $1/N_{exp}^{op}$ that characterizes the open-circuit measurement. It is eliminated in the difference $N_{exp}^{op} - N_{exp}^{cl} = \Delta N'_{exp}$. This corresponds to the green curves in Fig. 49 obtained by applying a slope correction ($1/\Delta N'_{exp}$) to open-circuit curves, so that they become parallel to the respective closed-circuit curves. From [Eq. 33], it can be derived:

$$-\Delta N'_{exp}.M = -NM - \Delta\alpha.\beta^{hom}.N_g M \quad \text{[Eq. 35]}$$

Assuming that N_g = 1/3, β^{hom} = 1 and $\Delta\alpha = \alpha_{exp}^{op} - \alpha_{exp}^{cl}$, with α_{exp}^{cl} = 1 (closed-circuit is supposed to present a fully collective reversal), the parameter α_{exp}^{op} can be obtained. For all three magnets, it is of the order of 0.82. The absence of significant differences in the contribution of collective effects to reversal for the three samples may be attributed to the fact that their shape factors lie in a restricted range of values (see III.3.3.2).

Experimentally, it has been observed that the coercive field is higher in closed-circuit than in open-circuit. From [Eq. 34], the calculated reduction in coercivity in open-circuit with respect to closed-circuit is expressed as:

$$\Delta H_c^{calc} = (\alpha_{exp}^{op} - \alpha_{exp}^{cl})\beta^{col} N_g M_s \approx (\alpha_{exp}^{op} - 1)\beta^{col} N_g M_s \qquad \text{[Eq. 36]}$$

The above expression shows that the reduction in coercivity in open-circuit is related to a difference in the collective character of reversal (that is more important during closed-circuit measurements). ΔH_c^{calc} is proportional to β^{col} and the best agreement between the experimental and calculated coercive field differences is obtained by taking $\beta^{col} \approx 0.5$. This value can be interpreted in this way: in the case of collective reversal, just before its magnetization reverses, a grain is close to the boundary between two regions, one having a magnetization $+M_S$ and the other $-M_S$. The cavity field, which is determined by two contributions of opposite signs, explains the reduced value of β^{col} compared to β^{hom} (≈ 1).

To conclude, the above experimental work shows that differences in various contributions to the demagnetizing field must be considered when comparing hysteresis loops of hard magnets measured in open- and closed-circuit conditions. First, the slope of the magnetization variation in open-circuit is different from that due to usually considered demagnetizing effects. It has been demonstrated that this usual demagnetizing field correction is not applicable to the case of hard magnets. Furthermore, a reduction in the open-circuit coercive field value compared to the closed-circuit one is found, which is of the order of 25 kA/m for the magnets studied here. This comes from the fact that the reversal process is affected by how the measurement is made: *i.e*. reversal has less collective character in open-

circuit than in closed-circuit. Due to the long-range nature of magnetostatic interactions, this first discussion is limited to a semi-quantitative understanding of demagnetizing field effects. A more quantitative evaluation of their strength and link with the reversal patterns requires numerical modeling. This constitutes the work described in the following sections.

III.3. Study of collective magnetostatic effects: numerical approach

The polycrystalline FE model depicted in Section II.5.2.1 aims at yielding a quantitative assessment of the previous formalism for the demagnetizing field that takes into account the collective effects. In this frame, both open- and closed-circuit configurations are simulated and the patterns of grain reversal are compared and discussed in the following section.

III.3.1. Closed-circuit configuration simulation

III.3.1.1. Model parameters

The magnet taken as the reference for the following simulation belongs to the previous set of samples (S1) and has an aspect ratio (h/D) of 0.5. Three parameters have to be known for the simulation run: (i) the remanence of the grains, taken here as the value of the whole magnet remanence (1.3 T), (ii) the mean value of the grain coercivity $<H_c>$ and (iii) the standard deviation σ_{Hc}. These last two values have been selected in order to fit the experimental demagnetizing curve obtained with the hysteresigraph system (closed-circuit measurement).

A numerical sample made of n_x=10 x n_y=10 x n_z=5 cubic grains (corresponding to 1/8 of the whole sample due to symmetries) has been considered. Fig. 50 shows the repartition of the grain coercivity that is randomly generated at the beginning of the simulation by a gaussian realization.

A few trials with varied values of $<H_c>$ and σ_{Hc} have been necessary to obtain the results reported in Fig. 51. The experimental and simulated demagnetizing curves are found to be consistent with the following values: $<\mu_0 H_c>$ = 1.08 T (860 kA/m) and σ_{Hc} = 0.1 T. It is worth noting that the distribution curve of the grain coercivity is shifted toward higher values of the applied field compared to the simulated demagnetizing curve: the value of the coercive field is about 700 kA/m, *i.e.* 160 kA/m lower than the value of $<\mu_0 H_c>$ which can be explained considering the grain reversal pattern.

III.3.1.2. Analysis of the grain reversal pattern

In the 3D array, demagnetization starts from the least coercive grain located in this case at the top. This is pointed out in Fig. 52 where first reversed grains are colored in dark grey in two consecutive demagnetized states. Once demagnetization starts, it rapidly propagates in the grain array by cascade resulting from strong magnetostatic coupling between neighboring grains. These cascades form, once the coercive field is reached (J = 0), large clusters of reversed grains (see Fig. 52). These effects become more important as the applied field approaches coercivity and generate the increasing large steps noticeable in the simulated demagnetizing curve (see the left pattern in Fig. 52 that depicts the first cascade while the right pattern details the final cascade that lead to coercivity). The cascades are the consequence of the local increase in the demagnetizing field felt by non-reversed grains when they are surrounded by top and/or bottom grains that are already reversed (see Fig. 53). In that case, the magnetostatic field produced by the reversed grains add in magnitude to the external applied field.

Since this local rise in H occurs when the values of the applied field are close to the local coercive field (depending on coercivity distribution), it becomes more and more efficient to induce the reversal of the neighboring grains. The local increase in H acts only at a distance of the order of the grain size and is more important in the direction of the applied field.

These considerations explain the development of large and axial stripes, or clusters, observable on the grain reversal patterns. They also account for the fact that the demagnetizing curve is more “rectangular” than a curve simply drawn from the grain coercivity distribution and that would describe the demagnetization of the grain array without magnetostatic coupling between grains (ideal curve plotted in blue solid line in Fig. 51).

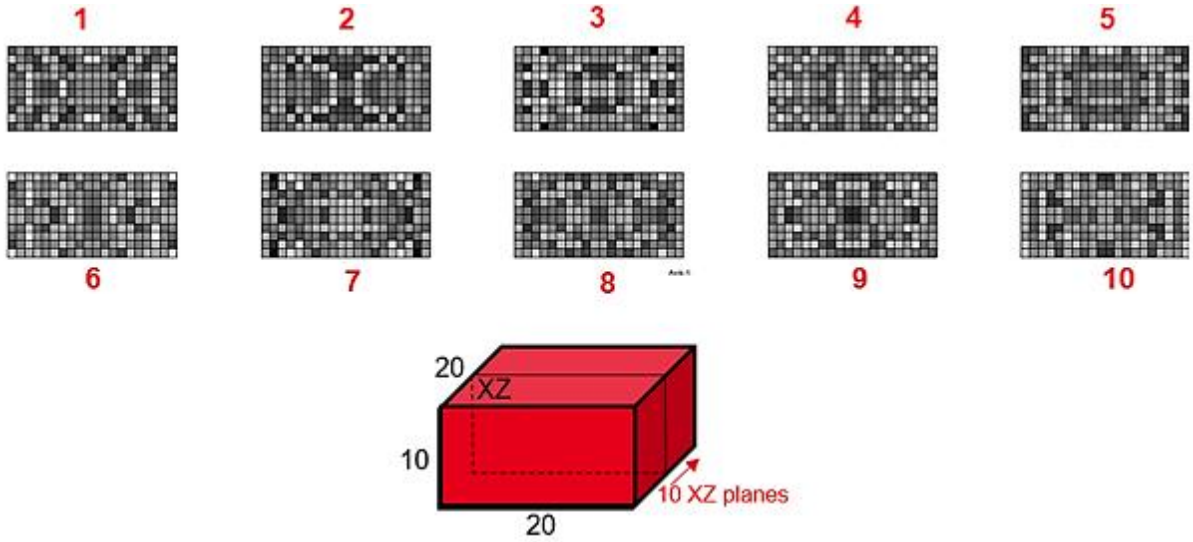


Fig. 50: Repartition of the grain coercivity in gray scale in the numerical sample used for the simulation of the closed-circuit configuration (arbitrary units: black = lower value, white = higher value), the 2D maps are given for each XZ plane starting from the mid-plane of the complete grain array (the numbers indicate the position of the XZ plane starting from the mid-plane towards the back).

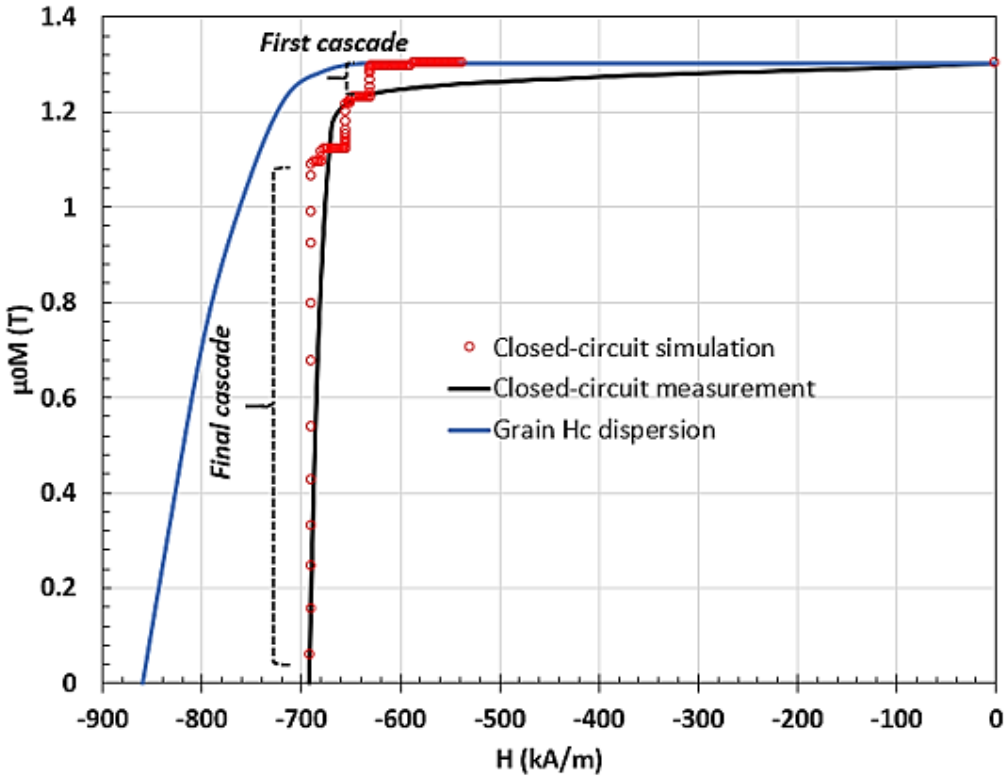


Fig. 51: Experimental (black solid line) and simulated (red dots) demagnetization curves in the closed-circuit configuration compared to the grain coercivity distribution (blue solid line).

J/J_s First cascade	Grain reversal in plane XZ #7
0.996	
0.992	
0.988	
0.984	
0.972	
0.96	
0.952	
0.944	

J/J_s Final cascade	Grain reversal in plane XZ #1
0.832	
0.812	
0.757	
0.705	
0.609	
0.518	
0.410	
0.326	

Fig. 52 : (Left) Grain reversal patterns for the first reversal cascade indexed in Fig. 51 (XZ plane labelled #7 in Fig. 50), the filled and non-filled squares in the grids refer to reversed and non-reversed grains, respectively. (Right) Grain reversal patterns for the final reversal cascade indexed in Fig. 51 (XZ plane labelled #1 in Fig. 50).

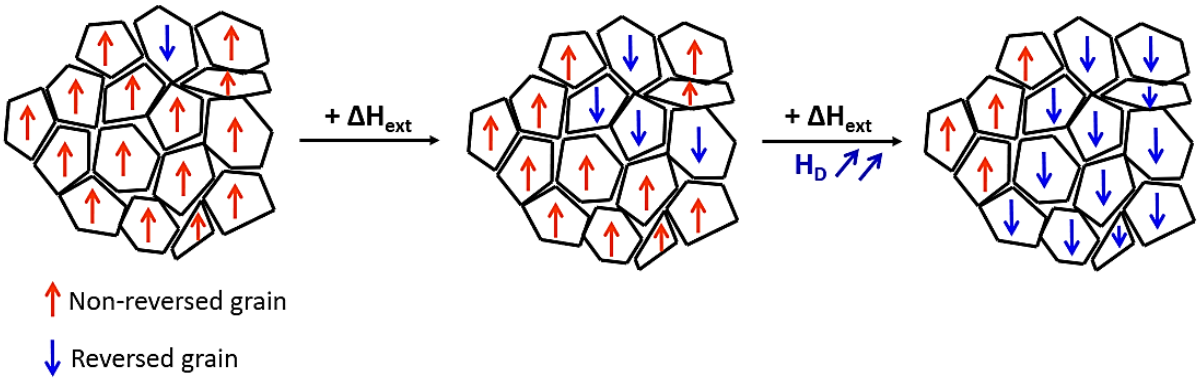


Fig. 53: Schematic representation of the cascade grain reversal in closed-circuit.

The experimental J-H curve obtained with the hysteresigraph compares well with the simulated one even if the first one is smoother. Our interpretation lies in the fact that the real magnet is constituted by a very large number of grains. When the reversal cascades occur, they should concern each time a small fraction of grains and the combination of a lot of separate events should lead to the smooth J-H curve. Thus, the polycrystalline model implemented with a limited number of grains (about 1000) tends to give an ideal representation of the J-H curve for which each individual grain reversal has a weight larger than in the real case. It is also worth underlying that cascades of grain reversal are a full 3D process that implies more than one axial layer introduced in the simulation. Actually, a quasi-2D system simulated by an array made of one layer of cubic grains (n_x x n_y and n_z=1) leads to a J-H curve that follows the curve deduced from the grain coercivity distribution (blue solid line in Fig. 51).

III.3.2. Open-circuit configuration simulation

III.3.2.1. Shape of the J-H curve

The numerical sample has also been simulated in open-circuit with the same grain coercivity realization. It allows avoiding a statistical bias that would occur when comparing simulations made with consecutive realizations, due to the limited number of grains in the model (500). In this case, reversal begins in the grains for which the cumulative effect of low coercivity and high local demagnetization field is critical, *i.e.* for which the amount $[H_c/M_s - N_z]$ is the lowest (see mapping in Fig. 54). In this last term, N_z stands for the local demagnetization factor calculated for each grain at the first step when $H_{ext} = 0$. N_z depends on the shape ratio of the magnet but is not uniform in the magnet, as previously reported for rectangular samples [126]. In this particular run, the first reversed grain is the same for the open- and closed-circuit simulations. The experimental and simulated curves are shown in Fig. 55 and the grain reversal patterns are reported in Fig. 56 for some selected field values. The open-circuit simulation exhibits different characteristics compared to the closed-circuit one.

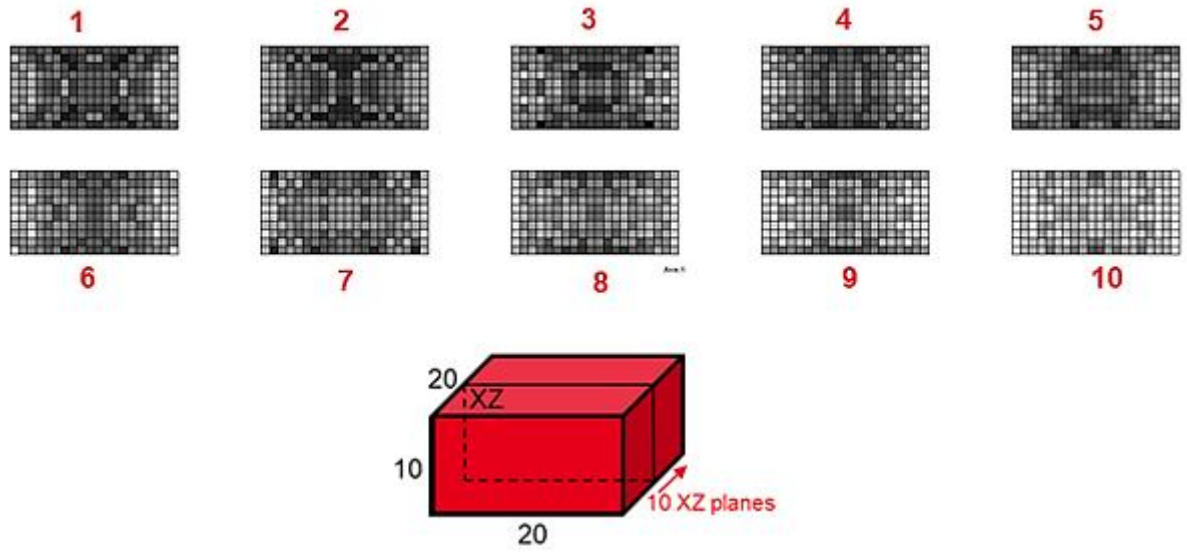


Fig. 54: Repartition of the reduced grain coercivity $[H_c/M_s - N_z]$ in gray scale in the numerical sample used for the simulation in the open-circuit configuration (arbitrary units: black = lower value, white = higher value), the 2D maps are given for each XZ plane starting from the mid-plane of the complete grain array (the numbers indicate the position of the XZ plane starting from the mid-plane towards the back).

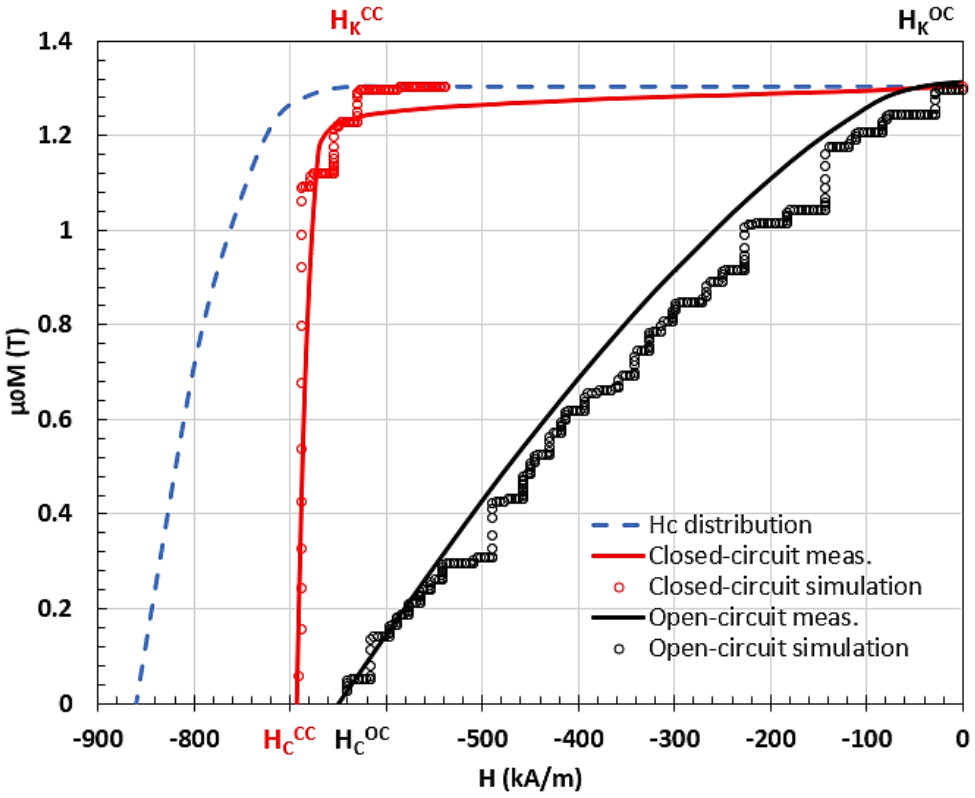


Fig. 55: Experimental (solid lines) and simulated (dots) demagnetization curves in the closed-circuit (red) and open-circuit (black) configurations, grain coercivity distribution (dotted blue line), the magnetic fields at the curve knees and at the coercive field are indicated on each curve as labels for the maps plotted in Fig. 56.

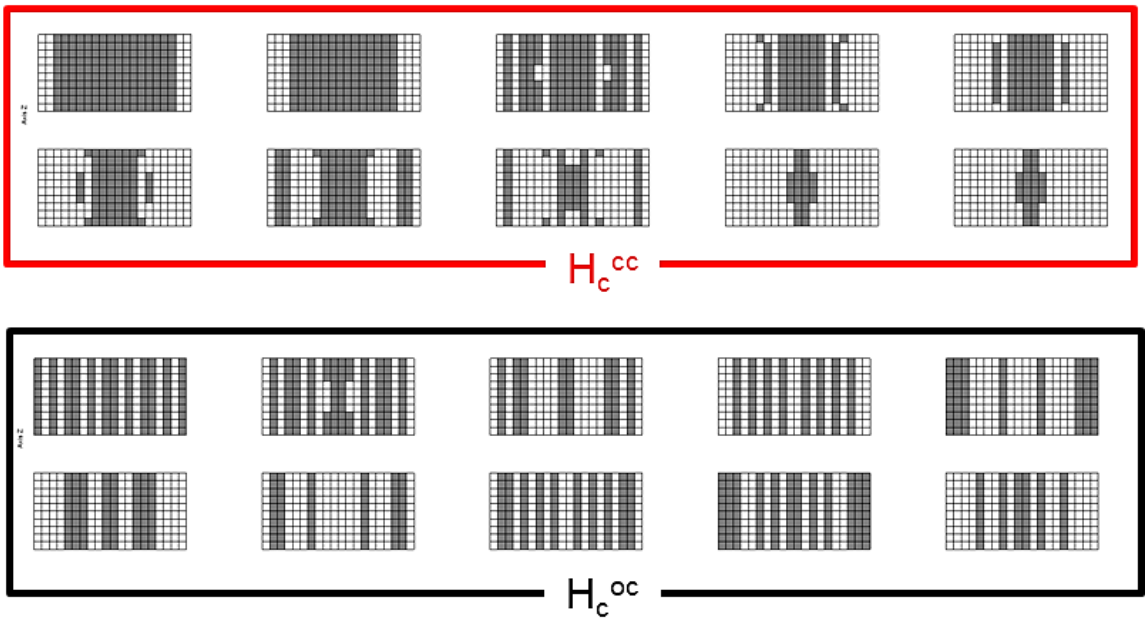


Fig. 56: Grain reversal patterns for selected field values indicated in Fig. 55: the filled and non-filled squares in the grids refer to reversed and non-reversed grains, respectively (XZ planes ranked from the y=0 to higher y positions incremented from left to right). Simulation of a 10x10x5 grains array (symmetry duplicated) with σ_{Hc} = 0.1 T. Patterns at coercive field in closed-circuit (red border) and patterns at coercive field in open-circuit (black border).

III.3.2.2. Analysis of grain reversal pattern

The open-circuit demagnetization curve evolves almost linearly with few cascade phases. The pattern of grain reversal is radically different compared to the closed-circuit simulation and exhibits quasi-regularly spaced columns of reversed grains aligned along the z-axis (see Fig. 56). This behavior is explained by the fact that, in the open-circuit configuration, the demagnetizing field acting on non-reversed grains comprises the important contribution coming from the whole sample polarization. This self-demagnetizing field acts strongly at low fields since it depends on the average polarization M. Although being important in the open-circuit case, this contribution vanishes in the closed-circuit. This difference accounts for the quasi-linear evolution of the curve in open-circuit. This artefact can be removed to extract a representative magnet behavior under external field with the demagnetization field corrections described in Section III.2.1.

The pattern of grain reversal corresponds in both cases to the minimization of the magnetostatic energy. In open-circuit, as expected, the simulation naturally leads to a pattern made of alternate columns with opposite polarization since this configuration tends to minimize the magnetostatic energy.

It has to be pointed out that the simulated curves J(H) follows the experimental ones without any parameter adjustment (apart from the coercivity distribution of the grains). More interesting is the fact that the difference in coercivity obtained numerically between open- and closed-circuit configurations (≈20 kA/m) is very close to the experimental value (≈25 kA/m) reported in Section III.2.2.

III.3.3. Discussion about collective effects

III.3.3.1. Relation between grain reversal pattern and collective effects

The cavity field, introduced in the previous section to describe the demagnetizing field, reflects the magnetostatic interactions felt by each grain (not yet reversed) from the surrounding grains. In this formalism, the cavity field can be seen as a combination of a “homogeneous” term, proportional to the average polarization M, and a “collective” term proportional to M_S that accounts for the effect of the adjacent and non-reversed grains.

$$H_D^{cav} = (1-\alpha)\beta^{hom} N_g M + \alpha\beta^{col} N_g M_S \qquad \text{[Eq. 31]}$$

The parameter α gives the weight of collective effects in the cavity field. Its value was found from experimental data to be larger in the closed-circuit configuration, for which collective effects are maximal ($\alpha^{cl} = 1$), than in the open-circuit case for which these effects were found to be lower ($\alpha^{op} = 0.82$). In this formalism, a pronounced collective character means that the cavity field experienced by a non-reversed grain is mostly a fraction of + $N_g M_S$. The simulation in the closed-circuit condition clearly shows that when reversed grains form large clusters, the second term of the cavity field (see [Eq. 31]) is dominant since on average non-reversed grains are surrounded by non-reversed ones, except at the interface with clusters. This is a strong argument supporting the previous formalism that assumed the role of collective effects.

The parameter β^{hom} was previously inferred to be close to unity while the last term β^{col} was assumed to be equal to 0.5 considering that, before its reversal, a grain is close to a boundary between two regions with opposite magnetization directions**.** This is again consistent with the grain reversal patterns exhibiting large clusters oriented along the axial axis.

It has to be pointed out that this unique fitting parameter α^{op} accounts both for the slope of the M(H) curve in open-circuit and for the coercivity difference between open- and closed-circuit measurements that is given by:

$$\Delta H_c = (\alpha^{op} - 1)\beta^{col} N_g M_s \qquad \text{[Eq. 37]}$$

While this parameter value was fitted on experimental results in the previous section, an identical value (α^{op} = 0.82) is obtained with the polycrystalline model without making any other assumption than the grain coercive field dispersion (σ_{Hc} = 0.1 T).

III.3.3.2. Effect of sample aspect ratio

The influence of the sample aspect ratio on collective effects has been analyzed by the finite element simulation. Table 25 below reports the different cases studied in this parametric study. The second and third cases correspond to the extreme values of the h/D values used in the experimental approach (h/D = 0.5 and h/D = 1). Two other geometries have also been modeled: the case 1 is a thin sample with h/D = 0.2 and the last case is an elongated one with h/D = 2. Fig. 57 compares the experimental demagnetization curves in open-circuit with the numerical ones for the two cases with median values of h/D. The difference in the slope of the curve is mainly due to the evolution of the self-demagnetization factor that depends on the sample aspect ratio. This is confirmed by Table 25 in which the values of the parameter α that accounts for the weight of collective effects have been extracted from the four computed demagnetization curves. For each case, the value of α is deduced from the slope of the J-H curve (N' corrected by the grain coercivity dispersion according to [Eq. 33]). The values of N_g = 0.33 and β^{hom} = 0.5 have been kept constant. This data shows that the weight of collective effects, evaluated by the coefficient α, remains nearly constant (α = 0.82) within the range of shape ratio values used in the experimental study, confirming the previous analysis. For flat samples (h/D = 0.2), the model predicts that collective effects should decrease (α = 0.62), whereas they should become more important for elongated samples (α = 0.90). The grain reversal patterns plotted for J=0 confirm this trend, exhibiting more clusters as h/D increases (see the pattern at the mid plane for h/D=2, *i.e.* for the lowest local self-demagnetization factor $<N_z>$). Finally, it can be inferred that the behavior of an infinite elongated sample measured in open-circuit tends slowly to the case of a finite length sample tested in closed-circuit.

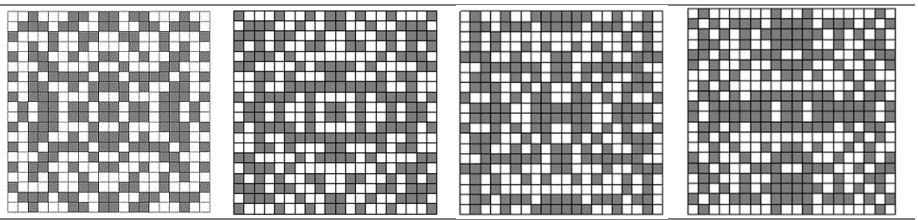
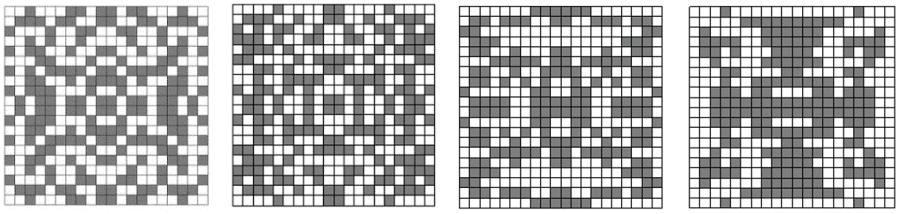
Aspect ratio	h/D = 0.2	h/D = 0.5	h/D = 1	h/D = 2
Size of the model (n_x x n_y x n_z)	10 x 10 x 2	10 x 10 x 5	10 x 10 x 10	10 x 10 x 20
Apparent slope N' of J-H curve	0.59	0.44	0.28	0.16
Weight of collective effects α	0.62	0.82	0.82	0.90
Grain reversal pattern at J=0 (coercivity) in the top XY plane of the sample				
Grain reversal pattern at J=0 (coercivity) in the mid XY plane of the sample				

Table 25: Influence of the sample aspect ratio on collective effects.

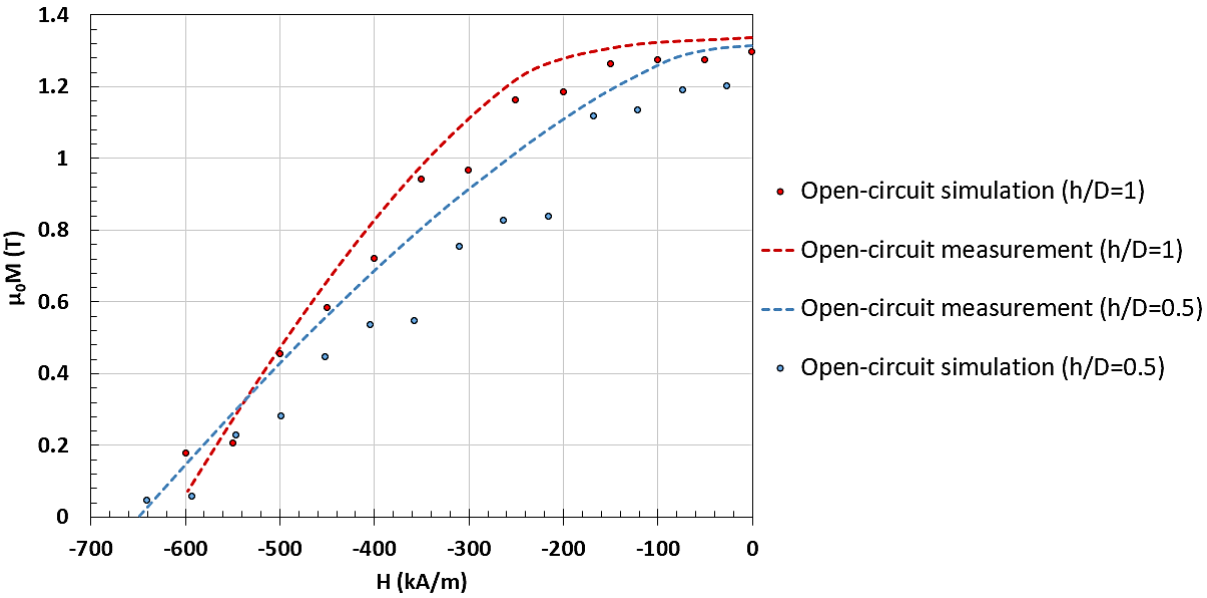


Fig. 57: Comparison of simulated and experimentally measured demagnetization curves in open-circuit for two different aspect ratios (h/D = 0.5 and 1).

III.3.3.3. Influence of the grain coercive dispersion on collective effects

With this low standard deviation value, α^{op} is found to be close to unity which is correlated to a reversal grain structure that does not form a fully homogeneous pattern, even in open-circuit. Actually, reversed grains tend to be aligned and form one-grain-wide columns axially oriented. It is worth noting that when the standard deviation is raised from 0.1 T to 0.2 T, the parameter α^{op} deduced with the polycrystalline model becomes lower (= 0.6), meaning a reduction of the weight of collective effects. The simulation also shows a larger difference between coercivity values in open- and closed-circuit and a less inhomogeneous pattern of grain reversal is found in open-circuit (see Fig. 58).

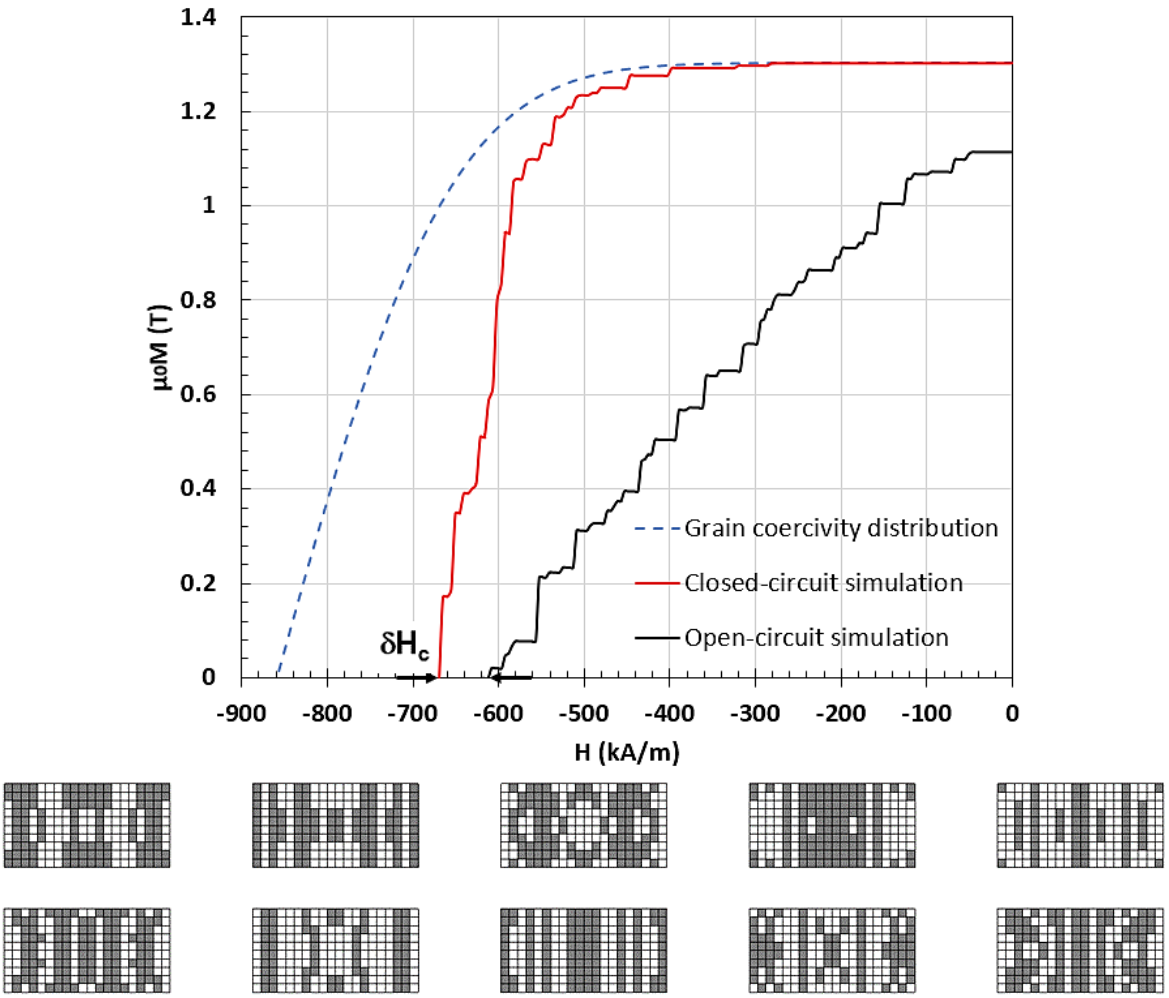


Fig. 58: (Top) Demagnetizing curves in the closed-circuit (red solid line) and open-circuit (black solid line) configurations obtained by simulation of 10x10x5 grains array and σ_{Hc} = 0.2 T. (Bottom) Grain reversed patterns at the coercive field in open-circuit, the filled and non-filled squares in the grids refer to reversed and non-reversed grains, respectively (XZ planes ranked from the y=0 to higher y positions incremented from left to right, duplicated symmetries).

III.3.4. Experimental validation

While the simulation of demagnetization in closed-circuit predicts large clusters of reversed grains with a size that exceeds largely the grain size, the open-circuit configuration tends to induce finer reversed zones with a length scale of the order of the grain dimension. An experimental approach has been implemented in order to determine if this difference in reversal pattern could be observed. For this purpose, a polarization mapping of the magnet has been performed on partially demagnetized samples. A Hall probe mounted on a three axes displacement fixture, and able to measure the three components of the induction field over a sample, has been used (SENIS device). The distance of the sensor to the sample surface is 400 µm and the displacement step is 100 µm. With these characteristics, only clusters of the same dimension (> 0.1 mm) can be reasonably observed.

The test consists in comparing the induction field maps measured over the same magnet sample in the following conditions: (i) in the remanent state that follows magnetic saturation performed with a field of 7 T using a Bitter coil (ii) after demagnetization of the sample performed by the hysteresigraph (closed-circuit) up to the coercive field and (iii) after the complete sample demagnetization obtained

in an open-circuit condition via the Bitter coil operating in a mode where gradually decreasing hysteresis loops are followed up to the full demagnetization state.

The maps of the induction field obtained in those three states are reported in Fig. 59 and in Fig. 60. The upper face of the cylindrical sample (10 mm diameter in that case) has been scanned and the axial component B_z is plotted. As expected, the mapping reveals only field variations with extensions larger than 0.1 mm. Over the saturated sample (Fig. 59), the magnetic field is very homogeneous, especially in the central part. No defect in the sample polarization is visible. The decrease in the B_z values observed near the circular edge is consistent with the axisymmetric tilt on the field direction expected in the free space close to a uniformly polarized sample.

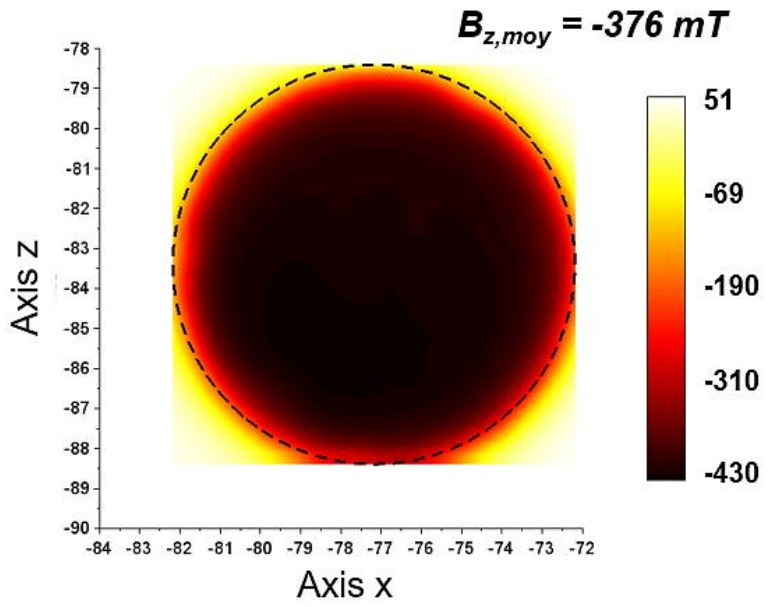


Fig. 59: Induction field map (B_Z component, scale in mT) measured with the Hall probe over the sample in the remanent state after saturation. The value of B_Z indicated in the insert is the spatially averaged value performed inside a 10 mm circle (dotted line) corresponding to the sample dimension. The values on axes correspond to the scanning position in mm.

Maps of induction recorded over the sample demagnetized in the closed- and in the open-circuit configurations are compared in Fig. 60. In the first case, very large field heterogeneities are revealed with several adjacent and distinct zones having opposite polarization directions. In the second case, the induction field is homogeneous in the central part and keeps only small (negative) values in the rim region (with the same sign than the induction measured in the initial saturated state). This last feature results from the fact that, in open-circuit, reversal is easier to initiate at the center part of the sample due to a higher self-demagnetizing field factor in this zone. In Fig. 60 are also plotted the grain reversal patterns computed on the top XY plane of the sample, showing the appearance of large clusters in closed-circuit while the grain reversal pattern is more diffuse in open-circuit.

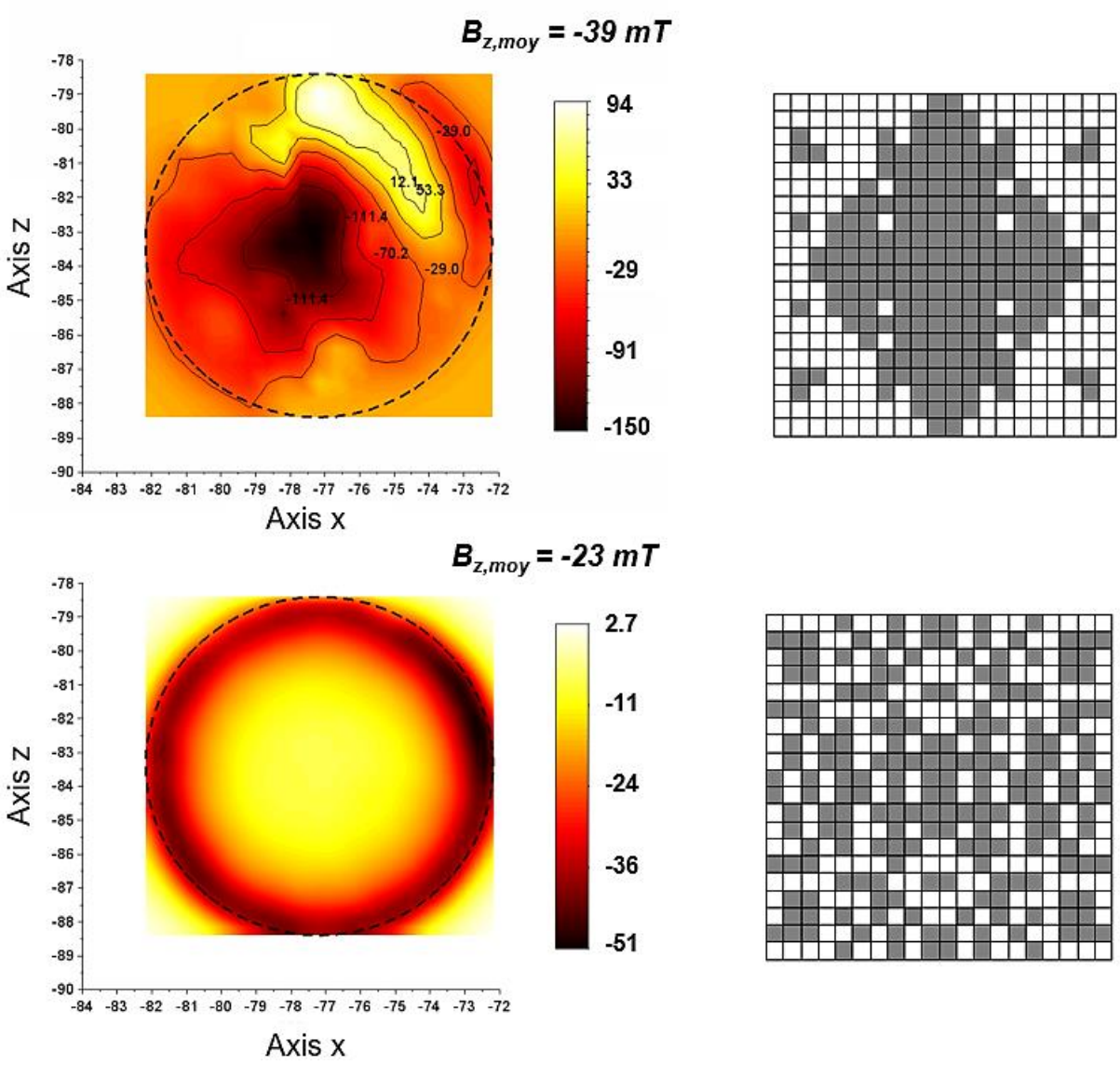


Fig. 60: (Left) Residual induction field maps (B_Z component, scale in mT) measured with the Hall probe over the sample in the demagnetized state achieved in closed-circuit (top) and in open-circuit via the Bitter coil (down). The values of B_Z indicated in the insert are the spatially averaged values performed inside a 10 mm circle (dotted line) corresponding to the sample dimension. The values on axes correspond to the scanning position in mm. (Right) Grids correspond to the grain reversal patterns simulated on the highest XY plane at J=0.

The observation of large heterogeneities with the Hall probe has been reproduced with the same sample submitted to repeated cycles and also checked with other samples. Furthermore, the induction field map measured over a sample (of diameter 6 mm) after its demagnetization performed by the extraction magnetometer (open-circuit) up to the coercive field is reported in Fig. 61 and compared to the corresponding map after demagnetization in closed-circuit. In terms of homogeneity of the induction field, the maps in Fig. 61 are consistent with those in Fig. 60.

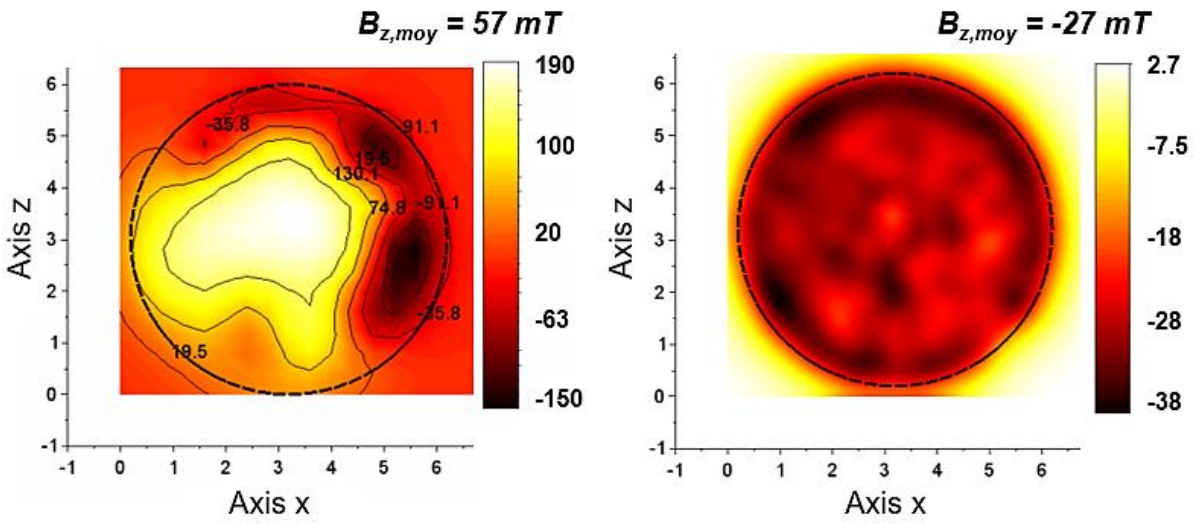


Fig. 61: (Left) Residual induction field maps (B_Z component, scale in mT) measured with the Hall probe over the sample in the demagnetized state achieved in closed-circuit. (Right) Same measurement in open-circuit using the extraction magnetometer. The values of B_Z indicated in the insert are the spatially averaged values performed inside a 6 mm circle (dotted line) corresponding to the sample dimension. The values on axes correspond to the scanning position in mm.

Our interpretation is that such measurement reveals large clusters in the reversal pattern that could be consistent with the polycrystalline model prediction. In open-circuit, field variations predicted by the model occur at the scale of grains and cannot be observed with this protocol.

III.4. Magnetostatic coupling in heterogeneous magnets

The previous results established the role of cascade effects on the shape of the demagnetizing curve measured in closed-circuit. Actually, the polycrystalline model predicts that demagnetization is triggered by the first reversed grains and that the J-H curve should feature high "squareness" in the case of a narrow dispersion of the grain coercivity. In this paragraph, two cases are considered in order to analyze how the J-H curve squareness can be affected by some heterogeneities in the magnet. The objective is to supply some interpretation elements of the experimental results obtained on specific samples which will be detailed in Chapter IV and V.

III.4.1. J-H curve of a two-grain-population magnet

III.4.1.1. Model parameters

In this first case, the polycrystalline model is applied to a sample made of two populations of grains with different mean coercivity values randomly distributed in the array (10x10x5). The first population, with the lower coercive field, represents here a very small fraction of the total population of grains (fixed at 3 %) and can be considered as defects. These low coercivity grains ($<\mu_0 H_c>$ = 1.1 T, σ_{Hc} = 0.1T) are rather isolated and surrounded by high coercive grains ($<\mu_0 H_c>$ = 1.6 T, σ_{Hc} = 0.1T) as shown by the coercivity distribution map plotted in Fig. 62 (low coercive grains are filled in black).

III.4.1.2. Analysis of grain reversal pattern

The simulated J-H curve of this two-grain-population sample is shown in Fig. 63. The reversal of the high coercivity grains that are highly majoritarian (97%) is found to be anticipated. This is pointed out by the shift between the curve expected from the coercivity distribution and the simulated curve (gap

larger than 100 kA/m). The low content of defect grains (3%) has a limited impact on the first statistical curve but a strong one on the resulting J-H curve.

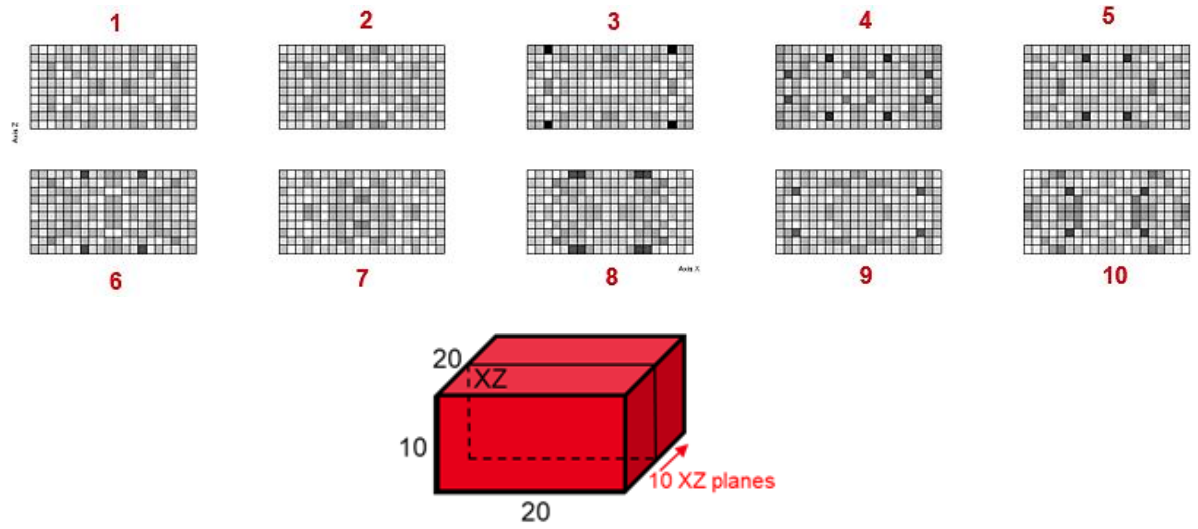


Fig. 62: Repartition of the grain coercivity in gray scale in the numerical sample used for the simulation of the bimodal grain population magnet (arbitrary units: black = lower value, white = higher value), the 2D maps are drawn for each XZ plane starting from the mid-plane of the complete grain array (the numbers indicate the position of the XZ plane starting from the mid-plane towards the back).

The grain reversal patterns help understanding the degradation of the J-H curve squareness (see Fig. 64). As expected, all low coercive grains firstly reverse (point #15) and in turn, they induce cascade reversals (forming axial stripes seen in points #17 and #19) that affect the surrounding high coercivity grains. When the sample coercive field is close (point #22), the reversal patterns again form large clusters as in the homogeneous grain array. The simulated curve compares to an experimental one obtained on a sintered sample after thermal annealing that exhibits poor squareness (see IV.1.1). Since the distribution of low coercivity grains corresponds to the grain characteristics obtained after sintering, it is believed that a few grains may remain not fully affected by the annealing and keep their low initial coercivity after the thermal treatment. This assumption should be validated by a more accurate characterization of the microstructure but it is interesting to keep in mind that the polycrystalline model accounts for a significant loss of the J-H curve squareness induced by a low content of defect grains (3%).

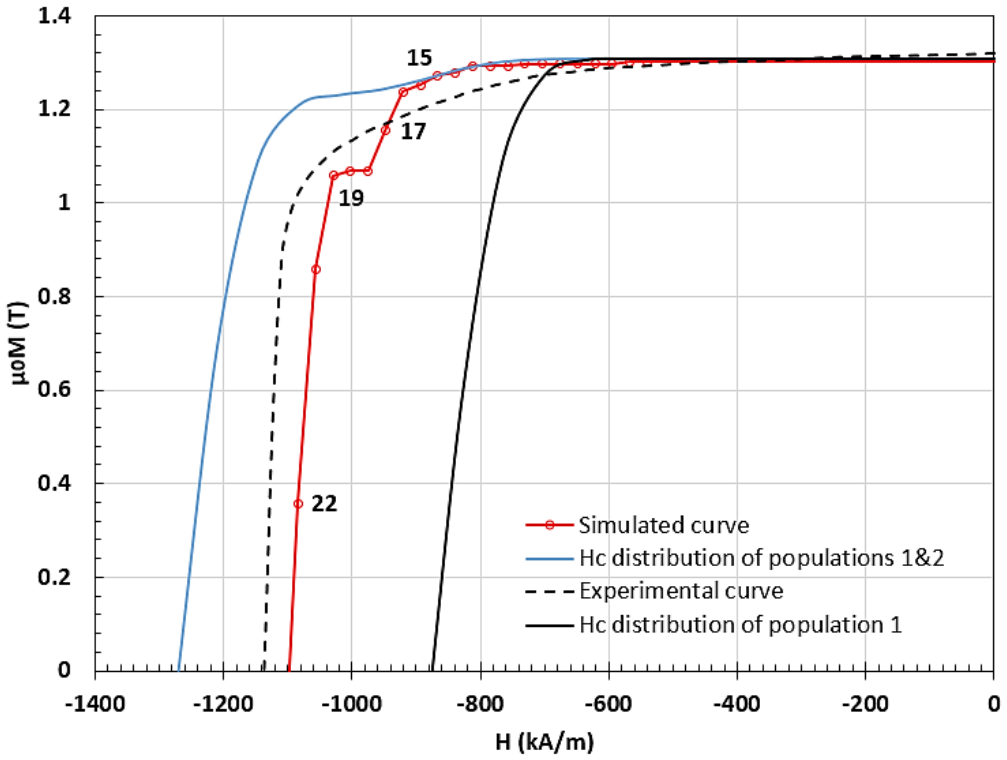


Fig. 63: Simulated demagnetization curve of the bimodal grain population magnet (red open symbols with following inputs for low coercive grains: $<\mu_0 H_c> = 1.1$ T, $\sigma_{Hc} = 0.1$ T and for high coercive grains: $<\mu_0 H_c> = 1.6$ T, $\sigma_{Hc} = 0.1$ T). The coercivity distribution is indicated by the blue solid line for the whole magnet and by the black solid line for the population 1 alone. The dotted line corresponds to the experimental curve of an annealed sample chosen as reference.

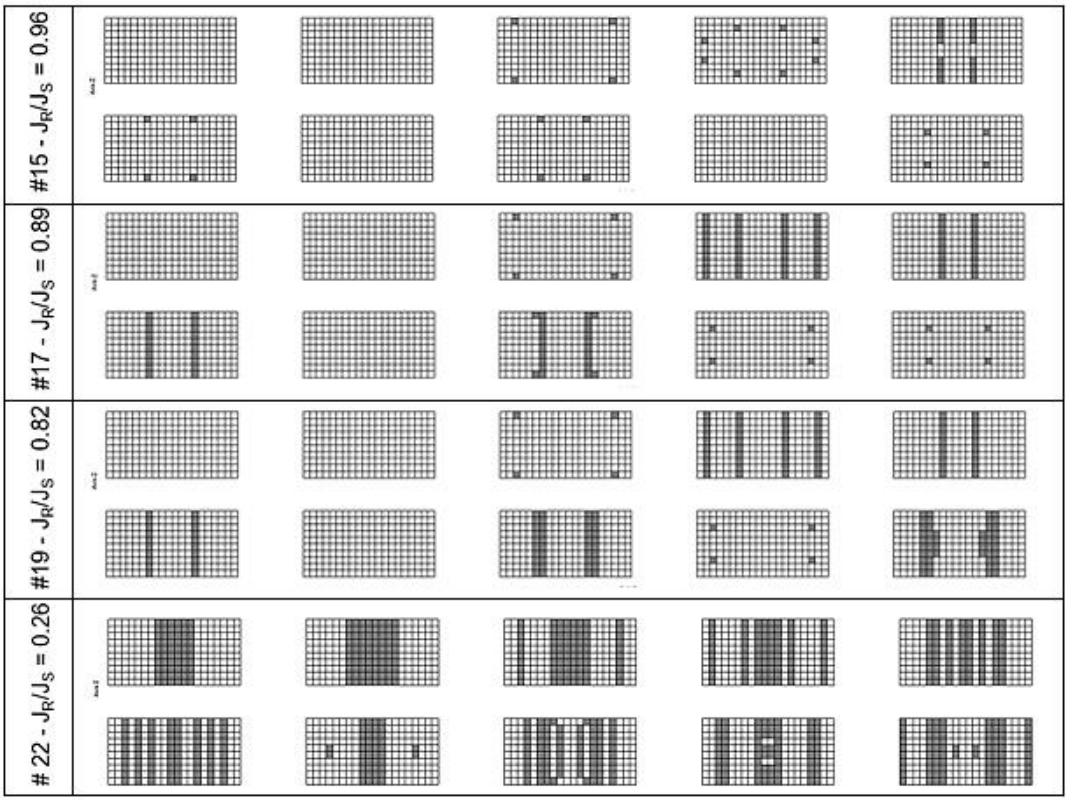


Fig. 64: Grain reversal patterns for the four selected field values indicated in Fig. 63.

III.4.2. J-H curve of duplex magnets

III.4.2.1. Model parameters

A second configuration has been investigated to shed light on magnetostatic coupling effects. It consists in a duplex magnet made of a low coercivity Nd-Fe-B magnet (H_C = 1140 kA/m, 10 mm diameter and 5 mm height) sandwiched between two symmetrical highly coercive Nd-Fe-B magnets (H_C = 1700 kA/m, 10 mm diameter and 10 mm height). Both regions have the same remanence (1.3 T) and the coercivity distribution obtained with $<\mu_0 H_C>$ = 1.6 T and σ_{Hc} = 0.2T for the low coercive grains, and $<\mu_0 H_C>$ = 2.35 T and σ_{Hc} = 0.1T for the high coercive grains is plotted in Fig. 65.

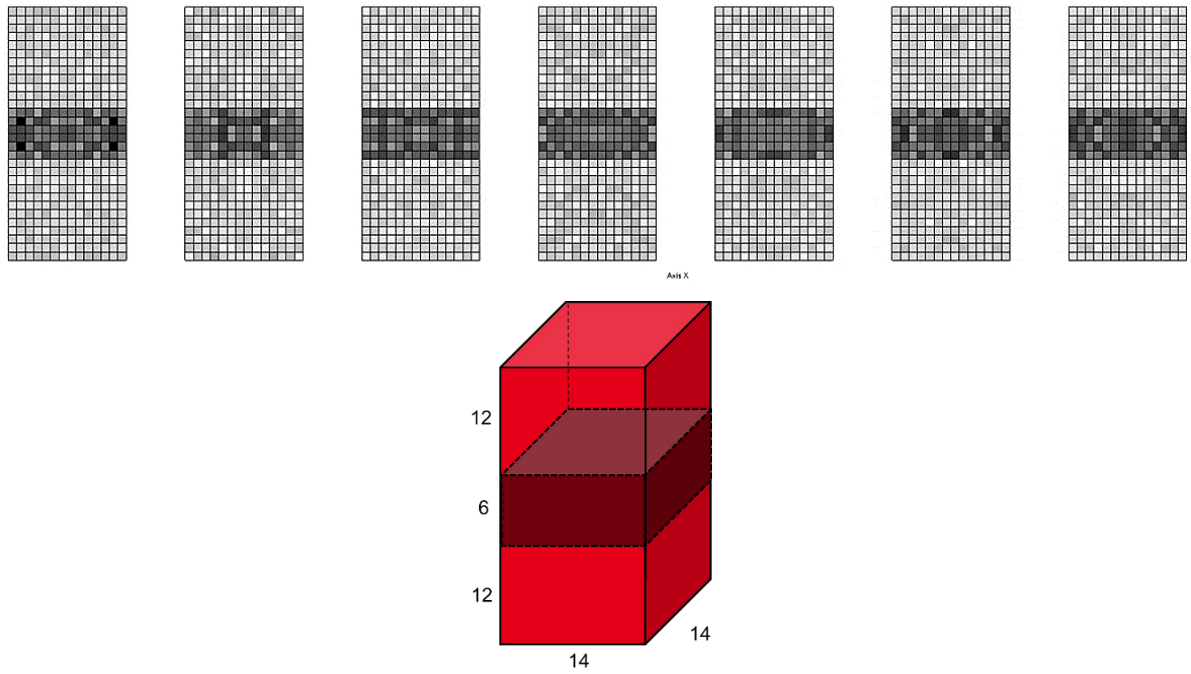


Fig. 65: Repartition of the grain coercivity in gray scale in the numerical sample used for the simulation of the duplex magnet (arbitrary units: black = lower value, white = higher value). The 2D maps are drawn for each XZ plane starting from the mid-plane of the complete grain array.

III.4.2.2. Analysis of grain reversal pattern

This stack is simulated in the closed-circuit testing condition using arrays with the same shape ratio as the individual magnets. The experimental and simulated demagnetization curves are plotted in Fig. 66 and show three main stages: (i) a plateau that extends up to the H_K value resulting from the linear combination of the curves of individual magnets, (ii) a quasi-linear decrease in magnetization and (iii) an abrupt loss of magnetization leading to the “duplex magnet” coercivity. The simulated curve obtained with values of M and H extracted at the mid-plane, which corresponds to the position of the measuring coil, is in good agreement with the experimental one, contrary to the case for which the simulated curve is plotted with the averaged values of M and H.

The grain reversal patterns at selected field values (A-F) reported in Fig. 67 indicate that the second stage (ii) can in turn be decomposed into two steps. In a first step (A-D), reversal is located in the less coercive central magnet, its extension shows few cascades and the demagnetizing curve is found to be broader than the experimental curve of the individual magnet. Then, in the second step (E-F), reversal enters the high coercive region where grain switching occurs for field values lower than expected from the coercivity distribution. At the end of the second stage, cascade effects occur in the more coercive

magnets (F) and finally, the overall coercivity of the sample is 100 kA/m lower than the value that would be obtained by a simple linear combination of the respective demagnetizing curves.

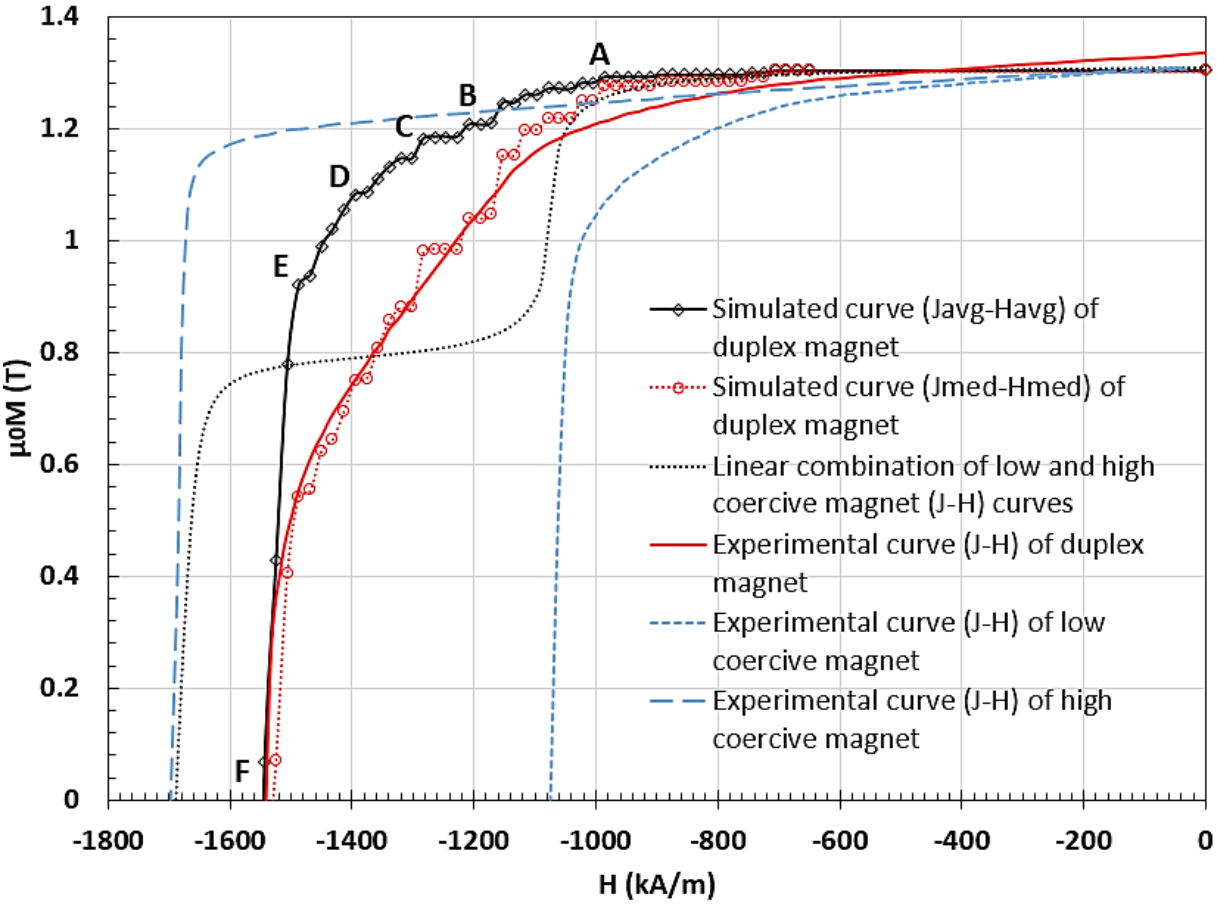


Fig. 66: Simulated demagnetizing curve of the duplex magnet (in red open symbols, low coercive grains: $<\mu_0 H_C> = 1.6$ T and $\sigma_{Hc} = 0.2$ T, high coercive grains: $<\mu_0 H_C> = 2.35$ T and $\sigma_{Hc} = 0.1$ T). The grain coercivity distribution in the duplex magnet is indicated by the black dotted line. The blue dotted lines correspond to the experimental curve of each magnet measured separately.

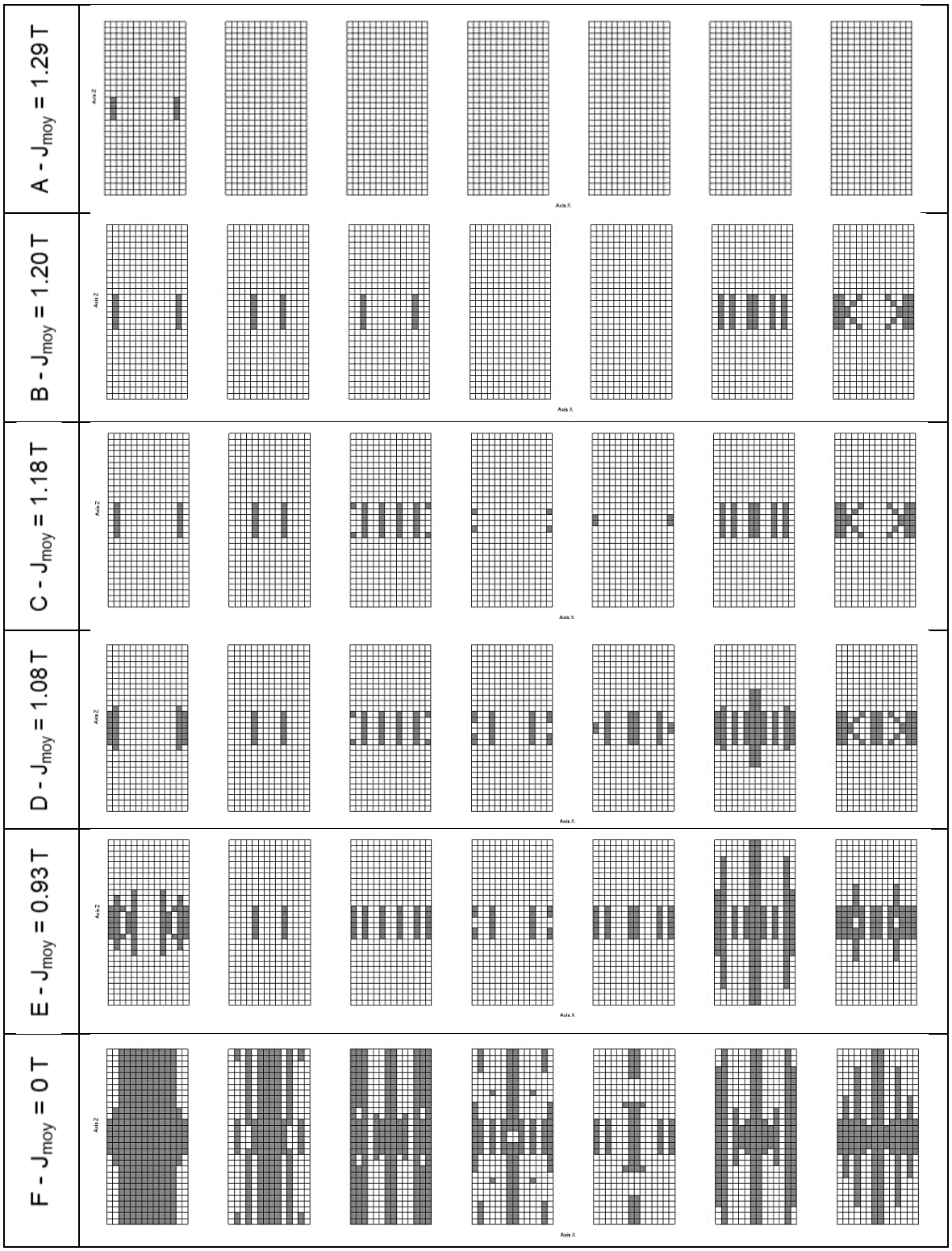


Fig. 67: Grain reversal patterns for the 6 selected field values indicated in Fig. 66 (A-F): the filled and non-filled squares in the grids refer to reversed and non-reversed grains, respectively (XZ planes ranked from the y=0 to higher y positions incremented from left to right).

III.4.2.3. Influence of the axial position of the pick-up coil

The grain reversal pattern depicted in the previous section is not homogeneous along the magnet stack height especially between the points A and E indexed on the J-H curve. Actually, in the second quadrant of the hysteresis loop, grain reversal seems logically more developed in the central magnet. This model

prediction has been checked by the measurement of the residual induction performed with the Hall probe device over the central magnet after a demagnetization run interrupted firstly near point D and then at the coercive field (point F). The corresponding induction maps are presented in Fig. 68. On the one hand, at point D, the central magnet in found to be quasi fully demagnetized (average residual induction is low = -63 mT) and again, large zones with opposite directions of residual magnetization are observed. On the other hand, at point F, the "re-magnetization" of the low coercivity magnet is homogeneous and well advanced (the sign of the average induction is reversed as the polarization would be in the third quadrant, if the magnets were measured separately).

Different J-H experimental curves have been successively measured after increasing the axial position of the coil sensor (with respect to the duplex magnet) by a step of 1.5 mm and starting from a configuration where the sensor is located at the mid plane. As can be noticed in Fig. 69, the shape of the J-H curve evolves with the coil height, featuring decreasing slopes (within the range representative for the magnet interaction) as the scanned zone is shifted from the mid plane. This result confirms the fact that the polarization is actually graded along the stack, being more advanced in the low coercivity magnet than in the high coercivity one. However, it has to be pointed out that, even at the highest coil position, the J-H curve remains still influenced by the central magnet. The measuring coil has a thickness of 2.5 mm leading to values of J and H that should be considered as averaged values over this height. With a height of 7.5 mm from the mid plane of the stack, the highest curve covers values of J and H that could be reasonably considered as inherent to the high coercivity magnet. Invalidating this assumption, the J-H curve recorded at this position exhibits poor squareness compared to the intrinsic curve of the high coercive magnet. This again supports the effect of magnetostatic interactions upon demagnetization of heterogeneous magnets.

The shift of the experimental curve as a function of the sensor position has also been simulated with the polycrystalline model and the results, plotted in Fig. 70, are consistent with the experimental findings. Finally, it has to be kept in mind that the duplex magnet case chosen for the study has a strong property gradient (larger than the one expected in Dy-diffused magnets). Even for this extreme case, the shift on J-H curves observed by sweeping the pick-up coil remains limited, the coercivity being moved of 20-30 kA/m (≈ 2%).

The main finding of the study made on heterogeneous magnets is that magnetostatic coupling between grains gives rise to intricate J-H curves. More precisely, the loss in squareness observed in the curves can be correlated to the presence of low coercivity grains. The early reversal of the weak grains tends to trigger grain reversal over the whole magnet. However, the J-H curve obtained with the hysteresigraph method, even if it is affected by the heterogeneities, would not give alone quantitative information about the amount and the precise repartition of the defective grains. In Chapter V, taking into account this remark, the polycrystalline model will be implemented and combined to advanced magnetic measurements to supply quantitative data about the axial profile of coercivity in Dy-diffused magnets.

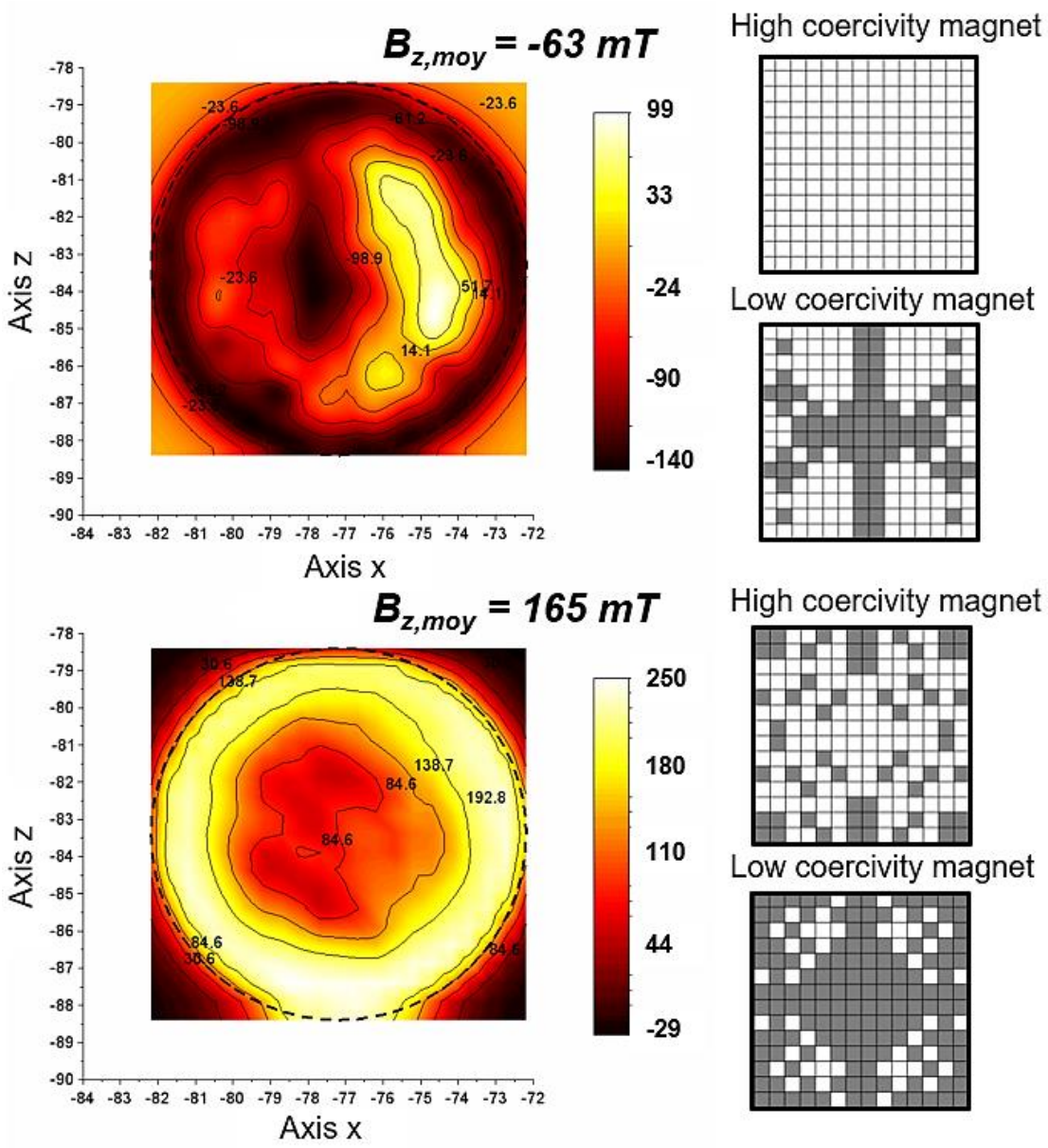


Fig. 68: (Left) Residual induction field maps (B_Z component, scale in mT) measured with the Hall probe over the low coercivity sample of the duplex magnet taken in two demagnetized states achieved in closed-circuit (hysteresigraph) corresponding to the points D (up) and F (down) indexed on the J-H curve plotted in Fig. 66. The values of B_Z indicated are the spatially averaged values measured in the 10 mm circle (dotted line) corresponding to the sample dimension. The values on the axes correspond to the scanning position in mm. (Right) Grids correspond to the grain reversal patterns in the XY plane located at the top of the high coercivity magnet and at the top of the low coercivity magnet.

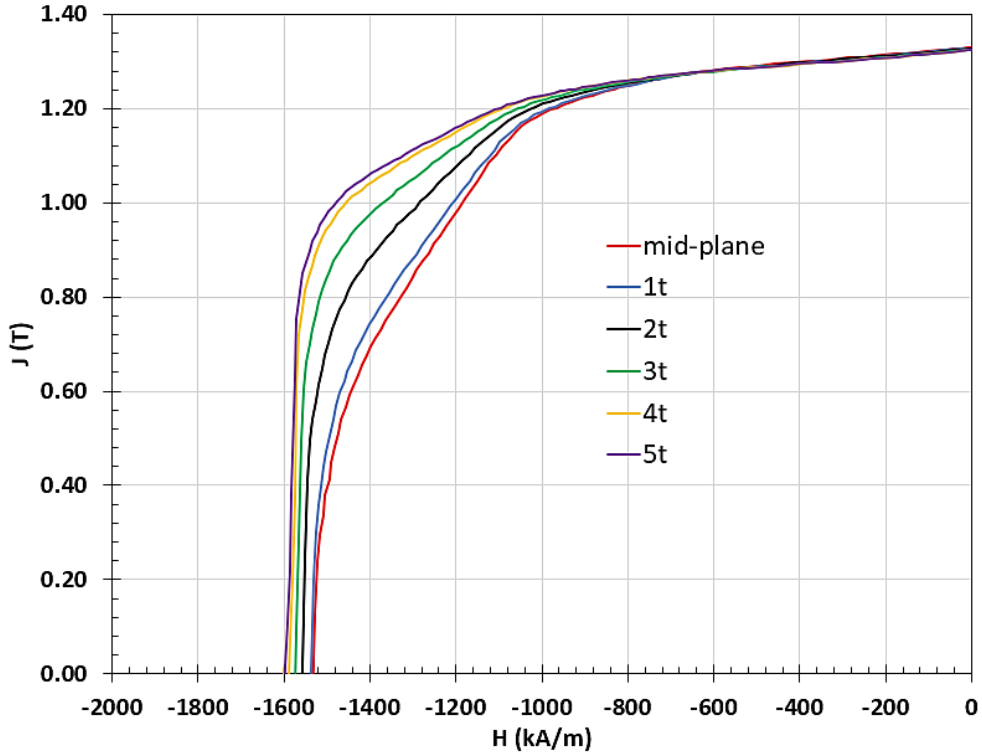


Fig. 69: Experimental J-H curves measured on the duplex magnet (central low coercivity magnet with h=5mm, high coercive magnets with h=10mm, diameter 10 mm). The measuring coil is positioned in the middle plane (solid red curve) and then shifted upward by regular steps (t=1.5 mm).

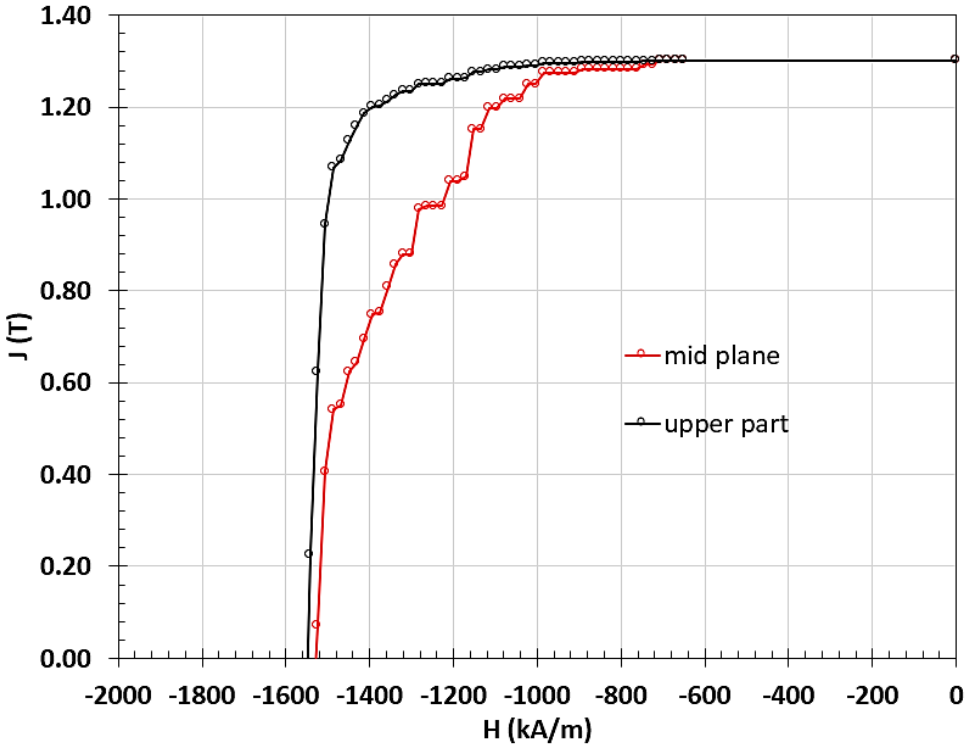


Fig. 70: Simulation of the influence of the shift of the measuring coil obtained with the polycrystalline model applied to the duplex magnet configuration. J and H values are averaged over a height equivalent to half of the thickness of the central magnet. Sensors are located at the mid-plane (open red circles) and at the top end of the stack (open black circles).

III.5. Conclusions

Demagnetizing field effects have been studied on hysteresis loops of hard magnets measured in both open- and closed-circuit conditions. Experimentally, it has been observed that the slope of the magnetization variation in open-circuit is different from that due to usually considered demagnetizing effects. Furthermore, a reduction in coercivity in open-circuit compared to closed-circuit is found. Magnetization reversal is found to depend on the measurement type. The cavity field model developed here to better describe the demagnetizing field effects in hard magnets predicts that magnetization reversal has less collective character in open-circuit than in closed-circuit. In addition, to assess the demagnetizing field effects, a polycrystalline model has been implemented. The simulated difference in coercivity between both configuration types is in good agreement with the experimental one. Moreover, the simulated reversal patterns are consistent with the respective collective characters predicted by the cavity field model. For instance, reversal patterns in the closed-circuit condition show large clusters of reversed grains (fully collective process) whereas those in the open-circuit configuration are mainly made of alternate columns of opposite polarization (less collective character). Finally, the numerical polycrystalline model can reproduce and explain the shape of experimental demagnetization curves obtained for duplex magnets. The deterioration of squareness observed for these magnets can be correlated to the presence of low coercivity grains.

The work presented in this chapter deals with two complementary and original approaches useful for the analysis of the demagnetizing curves obtained in open- and closed-circuit configurations. The formalism that accounts for collective effects and the polycrystalline finite element simulation developed in the frame of this thesis are supported by several experimental results. The methodology is implemented in the following chapters for the interpretation of the J-H curves of magnets with coercivity gradient. However, the approach remains of general interest in the domain of permanent magnet characterization. Actually, closed- and open-circuit techniques are widely used for determining hard magnet performance and the work could be completed in the future to supply some guidelines for experimenters. This work brings a quantitative understanding of the J-H curve shapes and also paves the way for a more detailed study of the influence of some microstructural evolutions during magnet manufacturing. For instance, polycrystalline magnets made of non-cubic grains (involving differences in the local demagnetizing factor), with size and/or alignment dispersion, as well as the effect of soft magnetic phases, could be investigated in a future work.

IV. Experimental and computational study of magnetization reversal in Dy-Co diffused Nd-Fe-B sintered magnets

This chapter describes the experimental parametric study carried out about Grain Boundary Diffusion Process (GBDP) using Dy-Co diffusion alloys in Nd-Fe-B sintered magnets. The influence of diffusion time and temperature, and of annealing before and after GBDP on magnetic properties is reported. Moreover, microstructural observations and further magnetic measurements are performed to characterize the core-shell microstructure and the diffusion profile of the GBDP magnets. Finally, micromagnetic simulations using the FEMME software are also presented to describe magnetization reversal at nanoscale in a grain represented by core-shell model and to determine the influence of some microstructural features on the resulting magnetic properties.

IV.1. Magnetic properties in the as-sintered state and after post-sinter annealing (PSA)

IV.1.1. Experimental results

In this work, sintered magnets with the following composition $(Nd,Pr,Dy)_{31}Fe_{67.1}B_1Al_{0.3}Co_{0.5}Cu_{0.1}$ (wt.%) are used as base magnets (Dy content = 0.5 wt.%). The latter are cylindrical with a diameter of about 10 mm and a thickness of about 5 mm. The average magnetic properties measured on 20 samples after sintering at 1032°C for 4 h are given in Table 26. Note that all magnetic properties presented in this chapter are measured at room temperature using the hysteresigraph system (*i.e.* closed-circuit configuration).

Value	J_R (T)	H_{cj} (kA/m)	H_{knee} (kA/m)	H_{knee}/H_{cj}	$(BH)_{max}$ (kJ/m^3)
Average	1.34	832 (1.05 T)	777 (0.98 T)	0.93	335
Standard deviation	± 0.01	± 6	± 7	± 0.01	± 7

Table 26: Magnetic properties of base magnets in the as-sintered state.

The magnets then undergo post-sinter annealing (PSA) at different temperatures for 2 h. Different annealing temperatures can be tested on the same magnet owing to the coercivity reversibility (see Table 27 for the example of successive PSA at 530°C). In fact, a heat treatment around 900-920°C after PSA enables the recovery of a coercivity that is equivalent to that of the as-sintered state. As reported in Table 27, the remanence remains unchanged after the consecutive heat treatments.

Heat treatment	J_R (T)	H_{cj} (kA/m)
Sintering 1032°C (4h)	1.36	824 (1.04 T)
+ PSA 530°C (2h)	1.36	1086 (1.36 T)
+ 920°C (3h)	1.36	816 (1.03 T)
+ PSA 530°C (2h)	1.36	1087 (1.36 T)

Table 27: Coercivity reversibility for successive PSA at 530°C.

This is similar to the study of Woodcock *et al.* [127] that also concerned the reversible and repeatable increase in coercivity after successive heat treatments performed on Nd-Fe-B sintered magnets. Post-

sinter annealing at 500°C for 1h resulted in an increase in coercivity of about 30 % and a subsequent heat treatment at 1050°C for 1 h led to a decrease in the coercive field with a similar magnitude. The process was repeated several times and coercivity changed by 30 % each time. This relative gain in coercivity is in good agreement with the one reported for our work in Table 27 (≈32%). Furthermore, the remanence remained also unchanged in [127] after the successive heat treatments. With the help of scanning and transmission electron microscopy, these results were attributed to differences in the distribution of the Nd-rich phases between the low and high coercivity states. For instance, the heat treatment at 1050°C is far above the eutectic temperatures of Nd-Cu (520°C) and the Nd-rich phase (655-665°C) and at this temperature, the edges of $Nd_2Fe_{14}B$ grains melt. During quenching, the re-solidification of the edges of the $Nd_2Fe_{14}B$ grains is assumed to reject the Nd-rich phases from GBs to the triple junctions, resulting in a poor distribution of the Nd-rich phases and thus in a low coercivity state. In the case of annealing at 500°C, the Nd-rich phases at triple junctions melt via eutectic reactions but no partial melting of $Nd_2Fe_{14}B$ grains happens. The Nd-rich liquid then flows along the GBs by capillary forces, leading to an optimized distribution of the Nd-rich phases and to a high coercivity state.

The demagnetization curves of the samples annealed at different temperatures (470, 500, 530, 550 and 600°C) are shown in Fig. 71, together with a demagnetization curve of a sample in the as-sintered state.

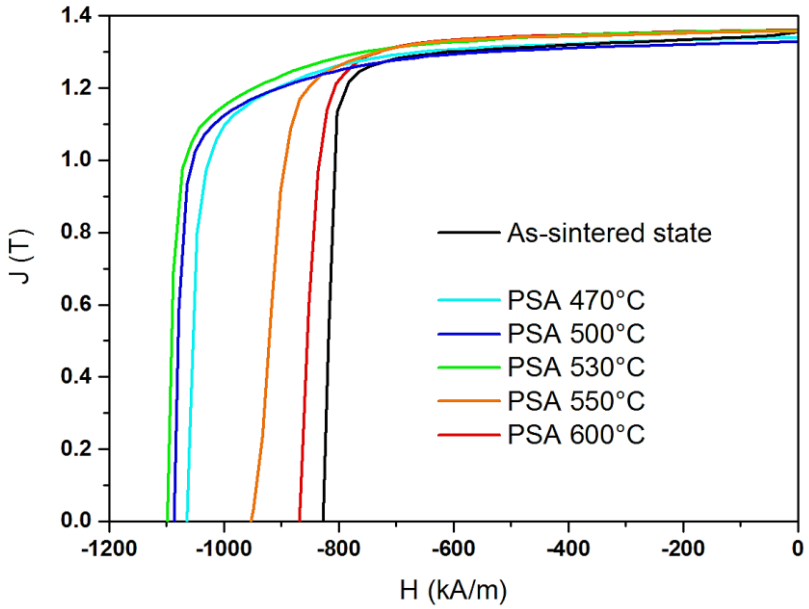


Fig. 71: Demagnetization curves measured after PSA at 470, 500, 530, 550 and 600°C. The black curve represents the demagnetization curve of the as-sintered state.

The corresponding average magnetic properties are given in Table 28. The annealing heat treatments at 470, 500, 550 and 600°C are each tested on 4 different samples and the heat treatment at 530°C is performed on 8 different magnets.

PSA temperature (°C)	J_R (T)	H_{cj} (kA/m)	H_{knee} (kA/m)	H_{knee}/H_{cj}	$(BH)_{max}$ (kJ/m³)
470	1.34 (± 0.003)	1052 (1.32 T) (± 13)	899 (1.13 T) (± 1)	0.86 (± 0.01)	346 (± 2)
500	1.33 (± 0.002)	1092 (1.37 T) (± 6)	915 (1.15 T) (± 3)	0.84 (± 0.002)	339 (± 1)
530	1.35 (± 0.01)	1105 (1.39 T) (± 15)	918 (1.15 T) (± 10)	0.83 (± 0.01)	351 (± 7)
550	1.35 (± 0.01)	961 (1.21 T) (± 39)	828 (1.04 T) (± 16)	0.86 (± 0.02)	348 (± 5)
600	1.36 (± 0.002)	862 (1.08 T) (± 7)	796 (1.00 T) (± 2)	0.92 (± 0.01)	355 (± 2)

Table 28: Magnetic properties after PSA at 470, 500, 530, 550 and 600°C. The ± values between parentheses correspond to the standard deviation.

After PSA, remanence remains almost unchanged but coercivity shows remarkable improvement compared to that of the as-sintered state. The $(BH)_{max}$ figure of merit is also increased compared to that of the as-sintered state but does not vary too much between the different PSA (since $(BH)_{max}$ depends on the square of remanence if $\mu_0 H_{C,J} > J_R/2$). However, the rectangularity of the demagnetization curves is systematically lowered after PSA (except for PSA at 600°C). By plotting the evolution of coercivity with the PSA temperature (see Fig. 72), it can be observed that an optimum of coercivity exists for a specific annealing temperature:

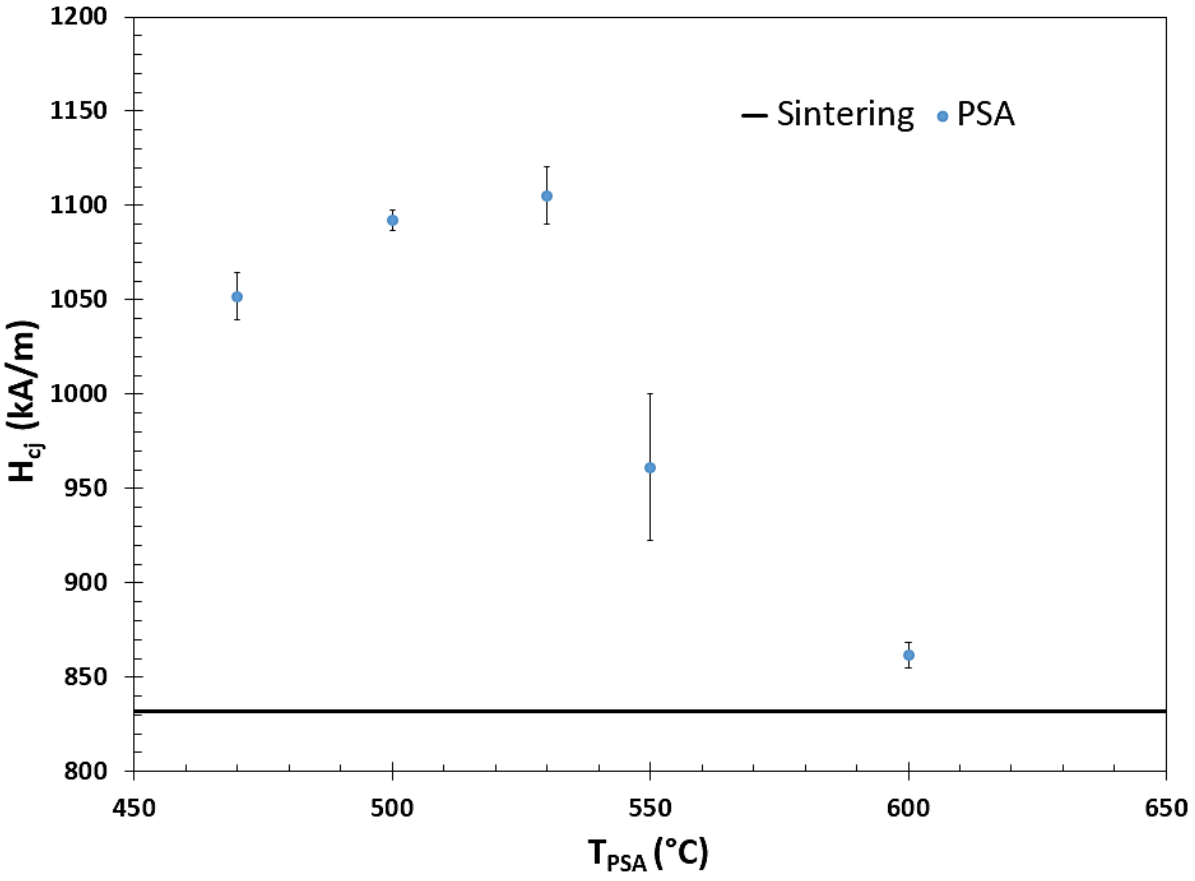


Fig. 72: Evolution of coercivity with the PSA temperature. The black solid line represents the average coercivity of the as-sintered state.

For the studied base composition, coercivity is the highest after PSA performed at 530°C (gain of 33 % in H_{cj} with respect to the as-sintered state). Nevertheless, coercivity also shows high sensitivity to the chosen PSA temperature. For instance, a huge drop in the coercive field (of about 150 kA/m ≈ 14 %) is observed between the optimal temperature of 530°C and 550°C. This is problematic for industrial processes since the perfect control of the temperature inside industrial furnaces is challenging.

Below the optimal temperature (from 470°C to 530°C), coercivity increases steadily. This behavior is triggered by the Cu addition in the magnet base composition (0.1 wt.%) and is attributed to the gradual formation of Nd-Cu or Nd-Fe-Cu eutectic phases during PSA via the following reactions: L ↔ Nd + NdCu at ≈ 500°C and L ↔ Nd + NdCu + $Nd_6Fe_{13}Cu$ at ≈ 480°C [128], [129] identified in the pseudo-binary phase diagram (see Fig. 73). Moreover, Cu is known to improve the wettability of the Nd-rich phase at GBs by reducing the melting temperature of this phase [39]. Coercivity after PSA increases with the better wettability of the Nd-rich phase.

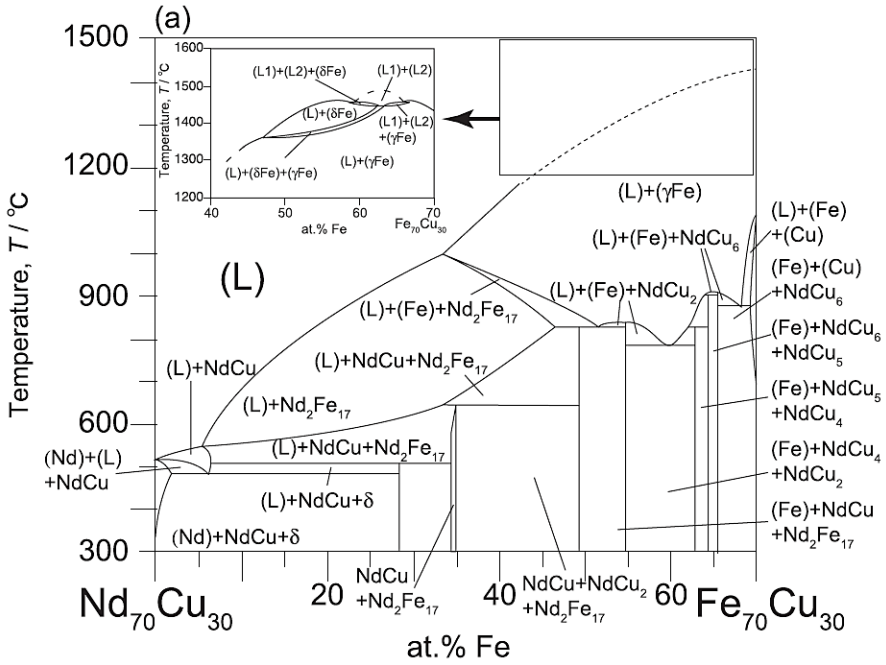


Fig. 73: Pseudo-binary phase diagram (30 at.% Cu) extracted from the ternary Nd-Cu-Fe phase diagram (δ denotes $Nd_6Fe_{13}Cu$ phase). [129]

The early works of Sagawa *et al.* [130] attributed the sudden drop in coercivity above the optimal temperature to a lower efficiency of the eutectic reaction (between Nd and $Nd_2Fe_{14}B$ phases in this case) to remove nanoscale defects by the phase separation process. It is worth noting that the optimal annealing temperature in the present study is very close to the temperature of the deep eutectic reaction found in the Nd-Cu binary phase diagram (520°C). Similar results have been obtained for the same magnet composition in the thesis of B. Hugonnet [131].

Several investigations on annealing have been performed by TEM on magnets with similar compositions. Vial *et al.* [7] showed that a thin interphase with a complex chemistry forms at grain boundaries and that this phase could be non-magnetic. Finally, the general mechanism accounting for the increase in coercivity is attributed to the two following processes: (i) grain exchange decoupling thanks to the efficient wettability of the Nd-rich phase and (ii) curing of defects due to the eutectic reaction and the subsequent phase separation.

IV.1.2. FEMME simulations: sintering vs PSA

The shape of the J-H curves reported in Fig. 71 suggests that two kinds of defects could be effective on the studied magnets after sintering: (i) a majority of nanoscale defects located at grain boundaries and that can be partially removed during annealing and (ii) some dispersed and more extended defects that could hardly be cured by thermal treatment. The presence of these two defect populations could explain the poor squareness of the J-H curves since demagnetization always starts from the stronger defects. The objective of the micromagnetic simulation is to compare the harmfulness of such a defect in exchange-coupled and -decoupled grains.

IV.1.2.1. Description of the model

Preliminary micromagnetic simulations are performed with the FEMME software package to simulate magnetization reversal in a simple model depicted in Fig. 74. The model is composed of 8 cubic $Nd_2Fe_{14}B$ hard magnetic grains of dimensions 60 x 60 x 60 nm^3. Furthermore, the grains are separated by a 2-nm-thick GB phase of various nature. A defect (pure Fe) of dimensions 60 x 4 x 4 nm^3 is localized in one of the grains to act as the nucleation zone for magnetization reversal (*i.e.* so that reversal always starts in the grain that contains the defect). This is original compared to the case of a $Nd_2Fe_{14}B$ grain with near zero anisotropy that is more often used in literature for nucleation [48], [106]. In Fig. 74, only 2 grains are represented for simplification reasons.

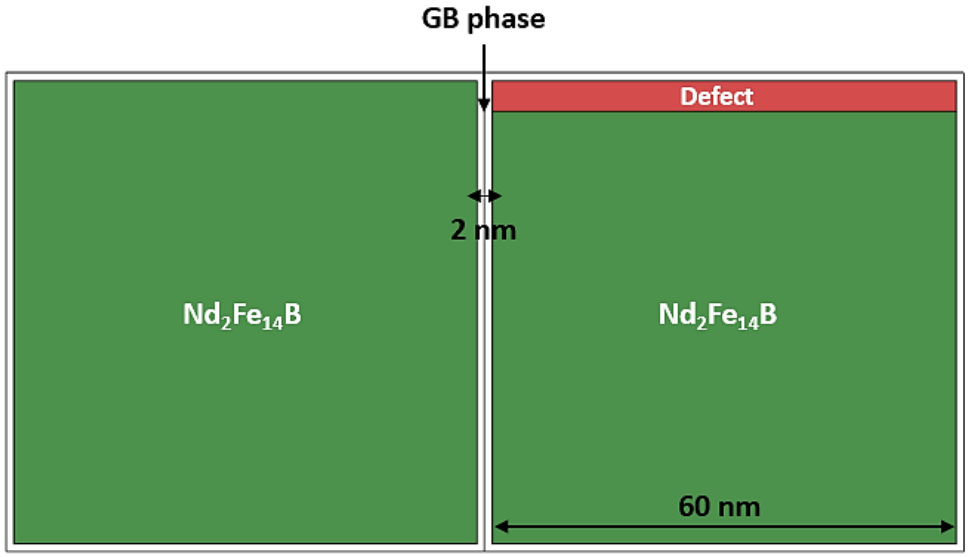


Fig. 74: Cubic model used for preliminary FEMME simulations.

The input parameters for the $Nd_2Fe_{14}B$ grains, the GB phase and the defect are summarized in Table 29, with the respective exchange lengths.

Phase	K_1 (MJ/m^3)	J_S (T)	A (pJ/m)	L_{ex} (nm)
$Nd_2Fe_{14}B$ **[81]**	4.3	1.61	7.7	≈ 3
Non-magnetic GB phase **[132]**	0	0.001	0.077	≈ 440
Soft ferromagnetic GB phase **[132]**	0	0.75	2.5	≈ 3
Defect (pure Fe) **[133]**	0	2	20.7	≈ 4

Table 29: Intrinsic magnetic properties at 300 K of the different phases of the model.

As mentioned in Chapter II, the mesh size of the finite element model has to be of the order of the exchange length of the simulated material. In this work, tetrahedral meshes with a size between 2 nm (edges of $Nd_2Fe_{14}B$ grains, GB phase and defect) and 10 nm (center of $Nd_2Fe_{14}B$ grains) are used.

IV.1.2.2. Simulated demagnetization curves: sintering vs PSA

Two different cases are simulated, depending on the nature of the GB phase: soft ferromagnetic or non-magnetic. The simulated demagnetization curves are shown in Fig. 75.

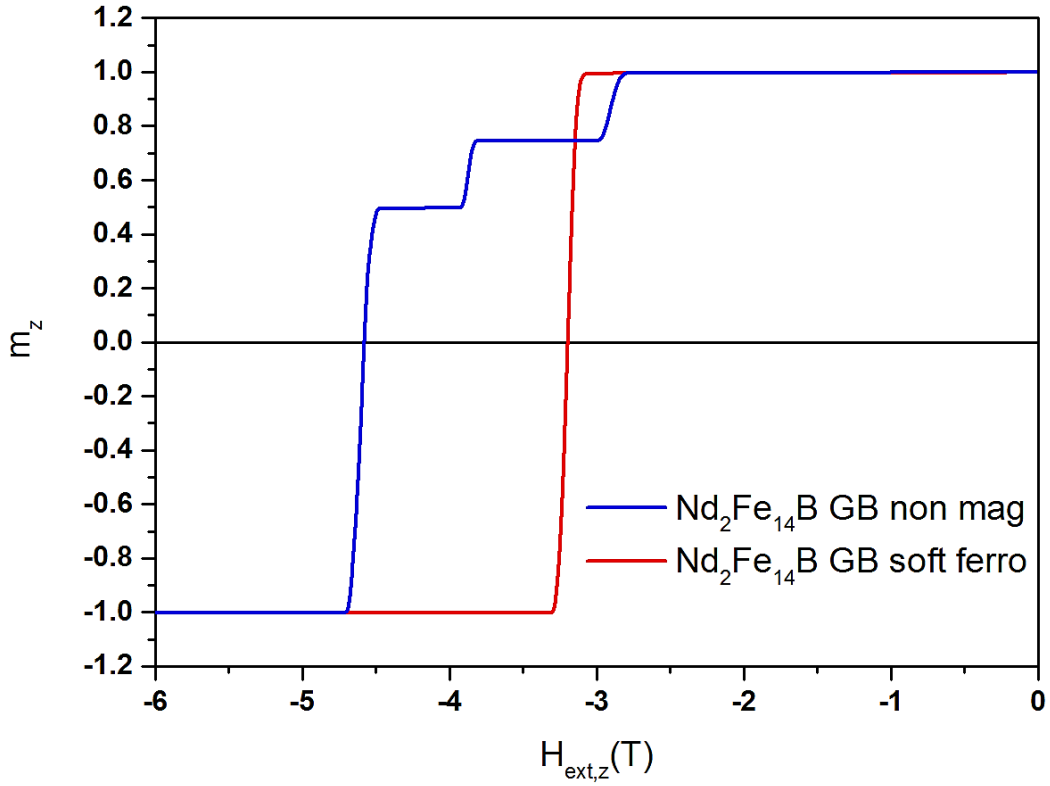


Fig. 75: Simulated demagnetization curves corresponding to a soft ferromagnetic (solid red curve) and to a non-magnetic (solid blue curve) GB phase.

The case with a soft ferromagnetic GB phase is equivalent to the as-sintered state (discontinuous GB phase ≡ exchange-coupled grains) whereas the case with a non-magnetic GB phase is similar to the microstructural state after optimal post-sinter annealing (continuous GB phase ≡ exchange-decoupled grains). The defect involved in the reversal nucleation is kept effective in both cases. As observed in Fig. 75, for a soft-ferromagnetic GB phase, magnetization reversal occurs in one step while for a non-magnetic GB phase, it proceeds in several steps. It can also be observed that magnetization reversal starts later for a soft-ferromagnetic GB phase, which is unexpected. This can be inferred from the fact that the GB phase has a thickness of 2 nm, which is lower than the exchange length, and so that magnetic domains remain pinned at the GB phase (as reported in [47]). Moreover, the shape of the simulated demagnetization curves is in good agreement with the experimental ones: rectangularity is close to unity when the GB phase is soft ferromagnetic and is deteriorated when the GB phase is non-magnetic (step reversal). The shapes of the simulated demagnetization curves are consistent with the ones computed in [47] and [48] for which extremely sharp and highly squared demagnetization curve is obtained for a standard sintered magnet (exchange coupling) while round shape curve is simulated for a Ga-doped magnet (exchange decoupling).

Furthermore, the gain in coercivity is about 44 % for the case with a non-magnetic GB phase with respect to the case with a soft-ferromagnetic GB phase. The simulated gain in coercivity is higher than the experimental one (33 %) because of the smaller volume proportion of defects in the simulation model. The same reason also explains the higher values found for the simulated coercivities.

IV.2. Magnetic properties after GBDP and post-diffusion annealing (PDA)

IV.2.1. GBDP using intermetallic compound vs eutectic alloy

After PSA, GBDP is performed on Nd-Fe-B sintered magnets using the $Dy_{66}Co_{34}$ eutectic alloy and the $Dy_{63}Co_{37}$ intermetallic compound (see Fig. 30). Diffusion is done along the easy axis direction and at 920°C for 3h (see Section II.3.1). Afterwards, the diffused magnets undergo a post-diffusion annealing (PDA) at 530°C for 2h. This PDA is crucial since it has been shown that a heat treatment around 900°C leads to a coercivity (microstructural state) that is equivalent to that of the as-sintered state (see Table 27). Moreover, Kim *et al.* [96] reached a coercivity of about 3 T by subsequent PDA on Dy-containing (7.5 wt.%) magnets and claimed that this PDA was required because of the discontinuity of the Nd-rich phase (characterized by HAADF-STEM) after GBDP using Dy vapor.

The demagnetization curves corresponding to the four thermal treatments are shown for both diffusion sources in Fig. 76:

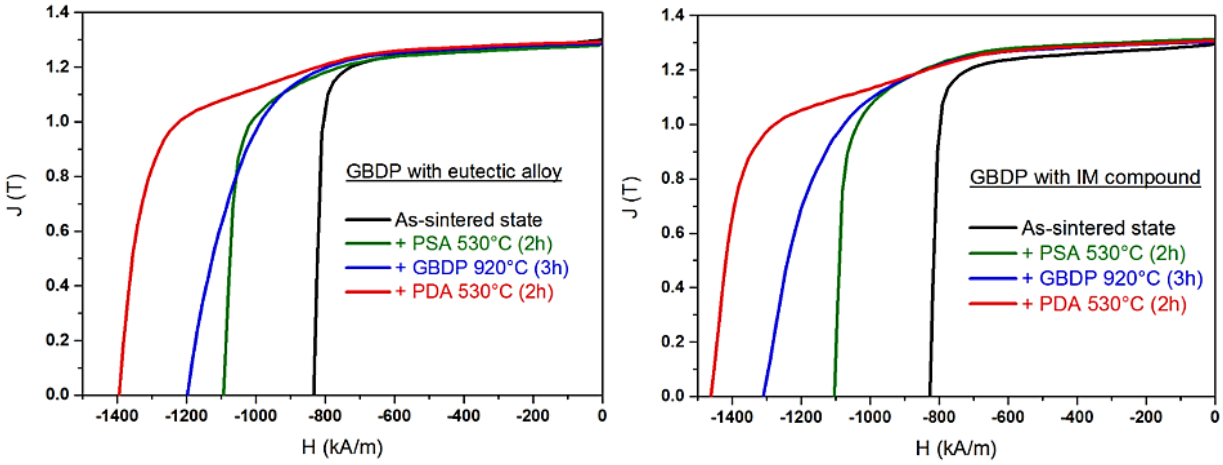


Fig. 76: (Left) Demagnetization curves measured for the magnet diffused with the eutectic alloy: after sintering (black solid curve), after optimal PSA (green solid curve), after GBDP (blue solid curve) and after PDA (red solid curve). (Right) Same measurements for the magnet diffused with the intermetallic compound.

The coercive fields measured after each fabrication step are given in Table 30:

Magnet	Fabrication step	H_{cj} (kA/m)
Diffused with the eutectic alloy $Dy_{66}Co_{34}$ (at.%)	As-sintered	833 (1.05 T)
	+ PSA 530°C (2h)	1093 (1.37 T)
	+ GBDP 920°C (3h)	1197 (1.50 T)
	+ PDA 530°C (2h)	1394 (1.75 T)
Diffused with the intermetallic compound $Dy_{63}Co_{37}$ (at.%)	As-sintered	826 (1.04 T)
	+ PSA 530°C (2h)	1103 (1.39 T)
	+ GBDP 920°C (3h)	1309 (1.64 T)
	+ PDA 530°C (2h)	1461 (1.84 T)

Table 30: Coercivity measured after each fabrication step for the magnets diffused with the eutectic alloy and the intermetallic compound.

In the following, the coercivity after optimal PSA is taken as reference. For the eutectic alloy, Dy-Co diffusion leads to an increase in coercivity of about 10 %, while Dy-Co diffusion combined with PDA raises the coercive field by about 28 %. In the case of the intermetallic compound, Dy-Co diffusion leads to an increase in coercivity of around 19 %, while combined with PDA, it raises the coercive field by almost 33 %. The more important gain in coercivity for GBDP with the intermetallic compound can be attributed to its easier grinding, compared to the eutectic alloy, leading to a more homogeneous deposition of the powder at the magnet surfaces (see Fig. 77) and to a more efficient diffusion process. The next results will therefore concern GBDP performed with the intermetallic compound $Dy_{63}Co_{37}$.



Fig. 77: (Left) Image of the surface state of a magnet diffused with the eutectic alloy $Dy_{66}Co_{34}$. (Right) Same for a magnet diffused with the intermetallic compound $Dy_{63}Co_{37}$.

IV.2.2. Influence of diffusion time on magnetic properties

A parametric study has been carried out to analyze the influence of some experimental features on magnetic properties. The first studied parameter is the diffusion time. For that, GBDP at 920°C for 3 h and for 12 h has been performed on different Nd-Fe-B sintered magnets. Afterwards, these latter undergo the same PDA at 530°C for 2 h. The demagnetization curves of the magnets diffused for different times are shown in Fig. 78. The normalized polarization is plotted as a function of the applied field to focus the discussion on the coercivity changes.

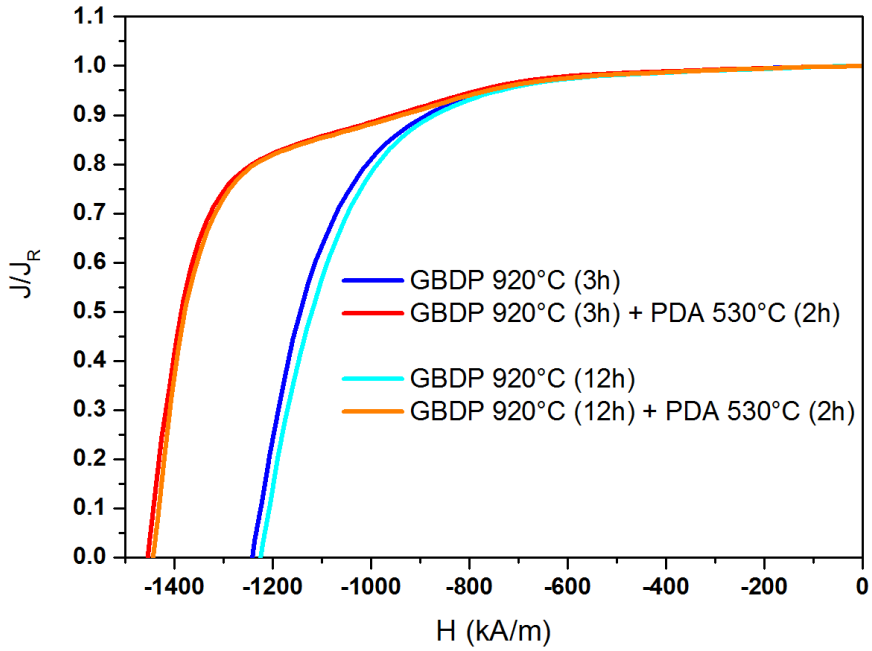


Fig. 78: Influence of diffusion time on coercivity for GBDP using $Dy_{63}Co_{37}$ intermetallic compound.

The corresponding magnetic properties are given in Table 31:

Fabrication step	J_R (T)	H_{cj} (kA/m)	H_{knee}/H_{cj}	$(BH)_{max}$ (kJ/m^3)
GBDP 920°C (3h)	1.33	1241 (1.56 T)	0.72	338
+ PDA 530°C (2h)	1.34	1454 (1.83 T)	0.66	345
GBDP 920°C (12h)	1.30	1224 (1.54 T)	0.72	322
+ PDA 530°C (2h)	1.30	1443 (1.81 T)	0.65	326

Table 31: Magnetic properties after GBDP at 920°C for 3 and 12 h, and after PDA at 530°C for 2h.

Compared to GBDP for 3 h, the remanence is smaller after GBDP for 12 h because Dy penetrates more into the hard magnetic grains and antiferromagnetic coupling is therefore more important. Moreover, no coercivity enhancement is measured after 12-hour-diffusion, coming from a saturation effect of Dy in $Nd_2Fe_{14}B$ grains. The rectangularity is also decreased after GBDP (with respect to the rectangularity after optimal PSA) and further deteriorated after PDA.

IV.2.3. Influence of diffusion temperature on magnetic properties

The second studied parameter is the diffusion temperature. GBDP at 870°C for 3 h is compared to GBDP at 920°C for 3h. Again, the magnets undergo the same PDA at 530°C for 2 h. The demagnetization curves for the magnets diffused at different temperatures are shown in Fig. 79:

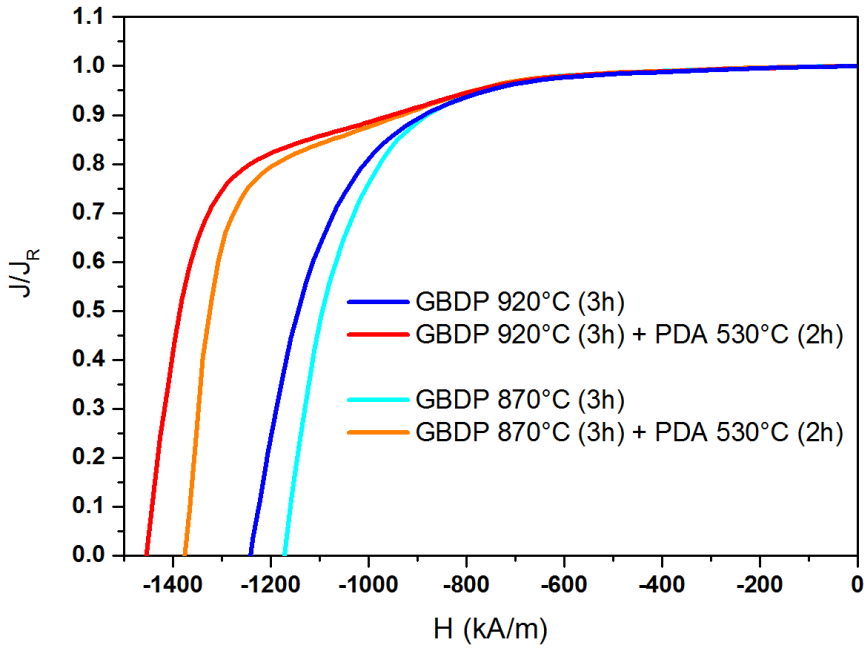


Fig. 79: Influence of diffusion temperature on coercivity for GBDP using $Dy_{63}Co_{37}$ intermetallic compound.

The corresponding magnetic properties are given in Table 32:

Fabrication step	J_R (T)	H_{cj} (kA/m)	H_{knee}/H_{cj}	$(BH)_{max}$ (kJ/m³)
GBDP 870°C (3h)	1.33	1172 (1.47 T)	0.75	339
+ PDA 530°C (2h)	1.34	1375 (1.73 T)	0.68	347
GBDP 920°C (3h)	1.33	1241 (1.56 T)	0.72	338
+ PDA 530°C (2h)	1.34	1454 (1.83 T)	0.66	345

Table 32: Magnetic properties after GBDP at 870°C and 920°C for 3 h, and after PDA at 530°C for 2h.

Compared to GBDP at 920°C, the remanence remains unchanged after GBDP at 870°C. Higher coercivity is measured after diffusion at 920°C than at 870°C owing to the more efficient diffusion process and thus the improved distribution of Dy in the magnet microstructure.

IV.2.4. Influence of PDA on magnetic properties

The last studied parameter is the PDA temperature. As shown before, the optimal annealing temperature prior to Dy-Co diffusion depends strongly on the magnet composition and is therefore expected to change after Dy-Co diffusion. For these experiments, GBDP at 920°C for 3 h is performed. Afterwards, different PDA at 500, 530, 550 and 600°C for 2 h are carried out. For each PDA, the corresponding magnetic properties are given in Table 33:

Fabrication step	J_R (T)	H_{cj} (kA/m)	H_{knee}/H_{cj}	$(BH)_{max}$ (kJ/m³)
PDA 500°C (2h)	1.34	1457 (1.83 T)	0.68	344
PDA 530°C (2h)	1.34	1454 (1.83 T)	0.66	345
PDA 550°C (2h)	1.33	1455 (1.83 T)	0.69	341
PDA 600°C (2h)	1.32	1280 (1.61 T)	0.76	337

Table 33: Magnetic properties after PDA at 500, 530, 550 and 600°C for 2h.

The evolution of coercivity with the PDA temperature can be directly compared to the one with the PSA temperature in Fig. 80:

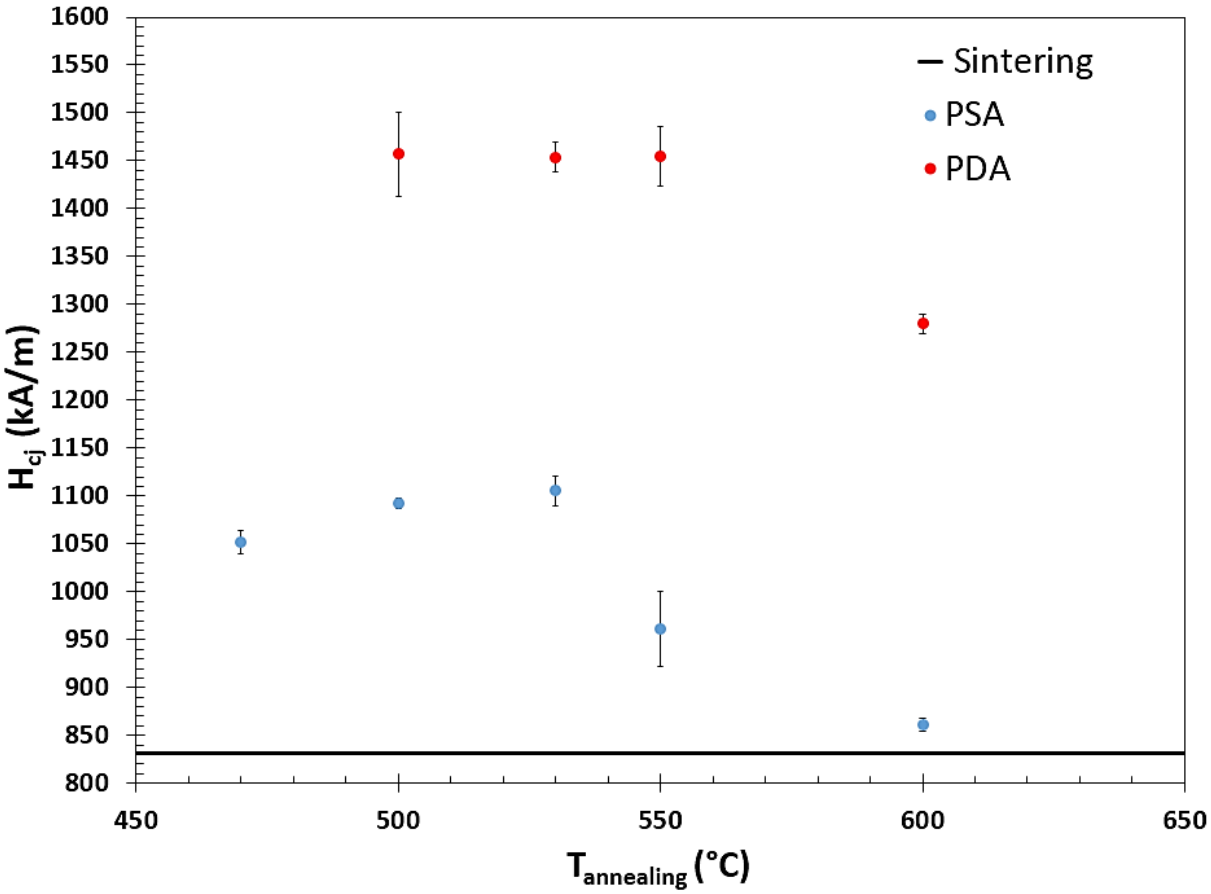


Fig. 80: Evolution of coercivity with the PDA temperature (compared to the one with the PSA temperature).

The optimum of coercivity can be reached after PDA at a temperature ranging between 500 and 550°C. Compared to non-diffused samples, coercivity shows less sensitivity to the annealing temperature after GBDP, which is interesting for industrial processes.

The particular microstructural changes at GBs during thermal annealing in Dy-diffused samples reported by Sepehri-Amin *et al.* [80] help understanding this behavior. Actually, the authors noticed that the Nd atoms of the hard magnetic phase replaced by Dy atoms are rejected to GBs and form a continuous Nd-rich layer of width 4 nm that enhances exchange decoupling between grains. Kim *et al.* [96] showed that this layer continues to form during PDA and accounts for a coercivity enhancement that is less sensitive to the wetting process involving Cu.

The demagnetization curves measured after GBDP and after PDA (red curves in Fig. 78 and Fig. 79) exhibit deteriorated rectangularity (0.68 after optimal PDA), which is detrimental for potential applications. Generally, the appearance of microstructural heterogeneities, and more particularly grain size dispersion, explains these degraded J-H curves with low squareness [134], [135]. For instance, Bittner *et al.* [135] studied the grain size reduction in sintered magnets by the He jet-mill process and measured J-H curves with poor rectangularity. In this case, they reported abnormal grain growth leading to two grain populations with large and low coercivity grains (10 µm-sized) distributed between high coercivity grains (less than 2 µm). Even if the shape of the J-H curves is very similar to the J-H curves obtained here after Dy diffusion, the involved heterogeneity is different since abnormal grain growth can be excluded in our case. Indeed, a reference sample undergoing the same diffusion heat treatment but without Dy-Co coating exhibits a non-degraded J-H curve. The shape of the

experimentally measured demagnetization curves will be explained in the following sections with the help of microstructural characterization and numerical simulations.

IV.2.5. M(T) measurements

As mentioned in II.3.1, Co substitutes to Fe of the hard magnetic phase in Nd-Fe-B sintered magnets and increases the Curie temperature. Measurements of the magnetization evolution with temperature (see II.4.1.3) under an applied field of 1 T have been performed to indirectly evaluate the penetration of Co in the hard magnetic grains. The measured magnets have been diffused in the three above experimental conditions (870°C-3h, 920°C-3h and 920°C-12h) and further annealed at 530°C for 2 h. The measurement of a magnet in the optimal PSA state is taken as a reference. The Curie temperature of each sample can be determined by plotting the evolution of the second derivative of magnetization (with respect to temperature) with temperature (see Fig. 81). The corresponding M(T) measurements are also given in Fig. 81.

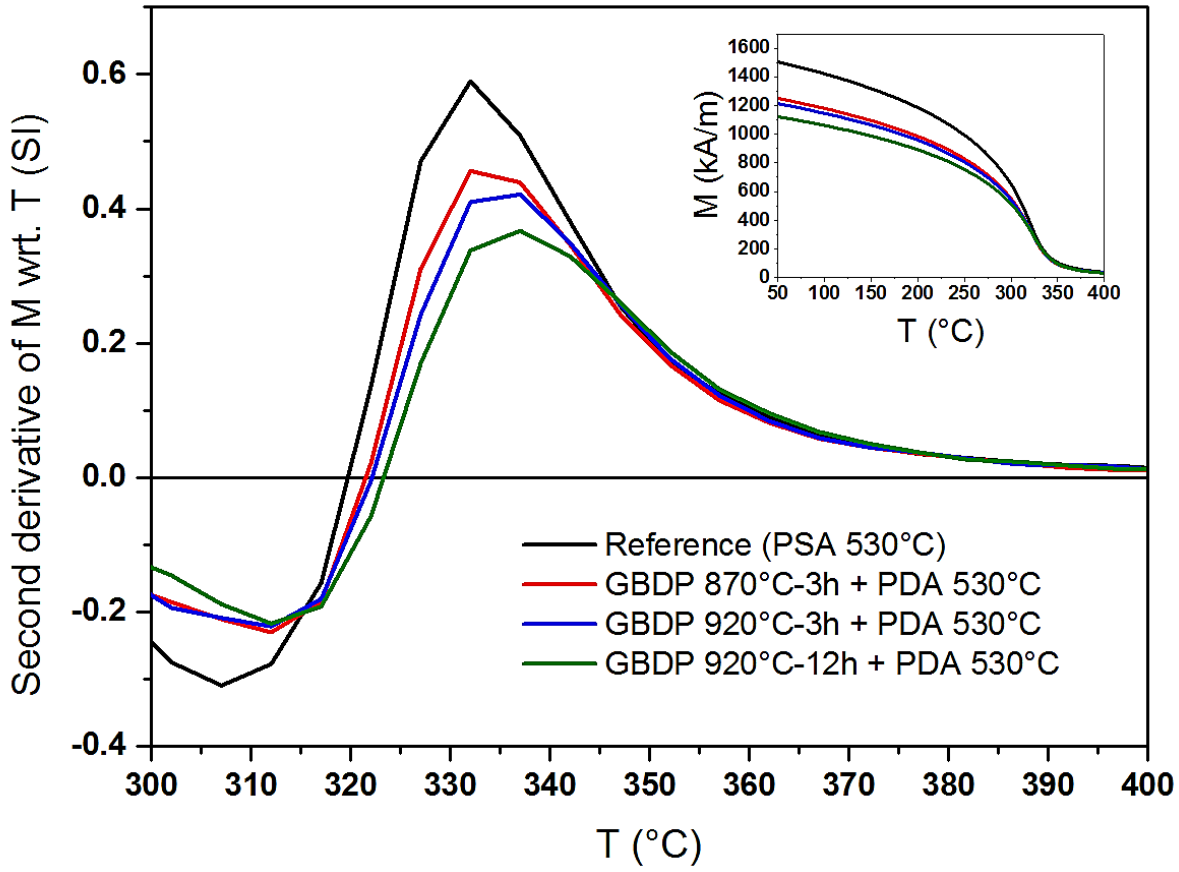


Fig. 81: Evolution of the second derivative of magnetization (with respect to temperature) with temperature for the magnets diffused in three different experimental conditions and for a reference magnet. (Inset) Corresponding evolution of magnetization with temperature.

The Curie temperature is defined here as the x-coordinate of the maximum point of the second derivative of M. The Curie temperatures of the magnets after GBDP (332, 336 and 337°C for 870°C-3h, 920°C-3h and 920°C-12h, respectively) are slightly higher than that of the reference magnet (330°C). Zhang *et al.* [136] reported a Curie temperature around 310°C for Nd-Fe-B sintered magnets undergoing the intergranular addition of the intermetallic compound $Dy_{82.3}Co_{17.7}$ (wt.%). In addition, Chen *et al.* [101] performed GBDP on Nd-Fe-B sintered magnets using the $Dy_{60}Co_{40}$ (at.%) alloy and observed a Curie temperature of about 320°C. The increase of the Curie temperature after GBDP in

[101], [136] (+ 2-8°C with respect to the reference magnet) is in good agreement with the one in this work (+ 2-7°C).

Because the Curie temperature of $Dy_2Fe_{14}B$ is only 13°C higher than that of $Nd_2Fe_{14}B$, the observed increase of the Curie temperature essentially results from the diffusion of Co into the hard magnetic phase. In this work, the addition of Co in the magnet microstructure during GBDP is very small (*i.e.* about 0.2 wt.%), explaining the very small increase of the Curie temperature. This is also consistent with the results reported in V.1.4. and obtained using a diffusion model for Co.

IV.2.6. Characterization of microstructure and coercivity profiles

IV.2.6.1. Microstructural characterization: SEM-EDX

Microstructural characterization is carried out on magnets diffused at 870°C-3h, 920°C-3h, 920°C-12h and further annealed at 530°C-2h. The SEM images using backscattered electron contrast shown in Fig. 82 are taken at various distances from the coated surface: 100, 200, 800 et 2000 µm. The observations are performed along the easy axis direction and with the following features: accelerating voltage of 5 kV, working distance of about 10 mm and 5000 x magnification.

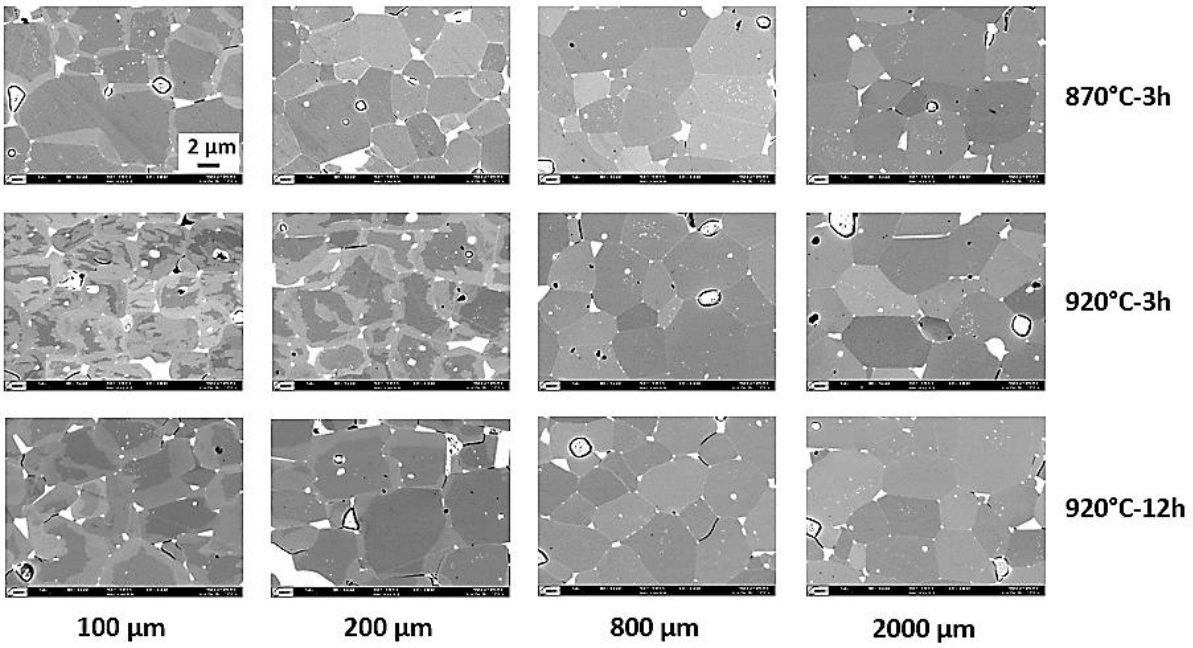


Fig. 82: BSE-SEM images taken at various distances from the coated surface for the magnets diffused in three different conditions.

The grains located in the vicinity of the coated surface (*i.e.* in the first 50 µm, not shown in Fig. 82) appear brighter than the grains further away, indicating a higher atomic weight due to Dy. After this zone (from 100 µm for all samples), the typical core-shell microstructure of the $(Nd,Dy)_2Fe_{14}B$ grains is observed. The average grain size and thickness of the Dy-enriched shells determined by image analysis (intercept method) are given in Table 34 for each BSE-SEM image.

		100 µm	200 µm	800 µm	2000 µm
870°C-3h	Average grain size (µm)	5.2 ± 0.9	4 ± 0.6	4.2 ± 1.6	4.4 ± 0.6
	Average thickness of Dy shell (µm)	1 ± 0.3	0.3 ± 0.2	/	/
920°C-3h	Average grain size (µm)	4.5 ± 0.6*	4.4 ± 0.8	4.4 ± 0.7	4.8 ± 1.6
	Average thickness of Dy shell (µm)	1.2 ± 0.3*	1 ± 0.3	/	/
920°C-12h	Average grain size (µm)	4.7 ± 0.9	5.8 ± 1.5	4.1 ± 1.1	4.4 ± 0.8
	Average thickness of Dy shell (µm)	1.6 ± 0.3	1.3 ± 0.4	/	/

Table 34: Average grain size and thickness of the Dy-rich shells determined from Fig. 82 by image analysis.

*The intercept method has only been performed on certain grains *i.e.* on those exhibiting a clear core-shell structure.

In addition, EDX maps of Dy are shown in Fig. 83 for all samples at a distance of 50, 100, 200, 400, 800 and 2000 µm from the coated surface.

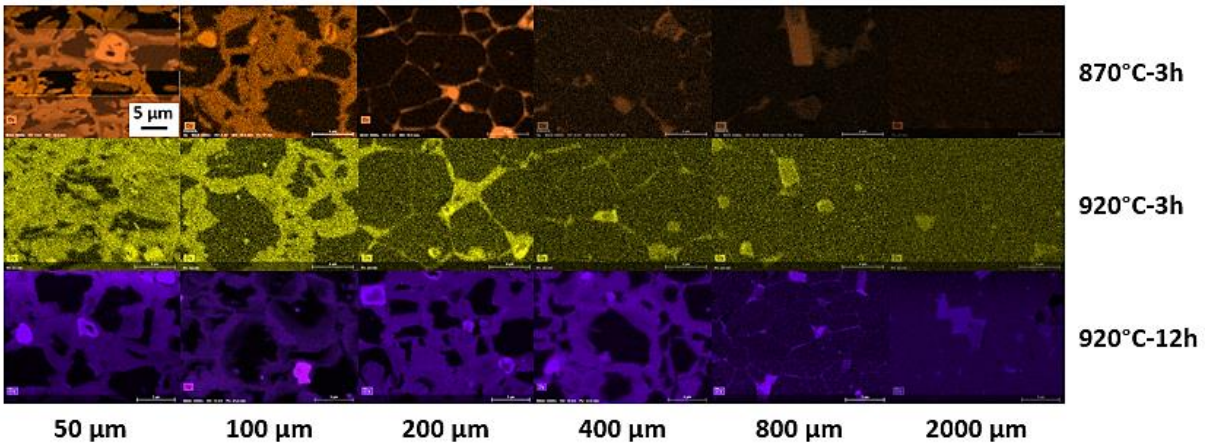


Fig. 83: EDX maps of Dy at various distances of the coated surface for all samples.

For the 870°C-3h diffused magnet, the thickness of the Dy-enriched shells rapidly decreases for a distance between 100 and 200 µm from the coated surface (see Fig. 82 and Fig. 83) and these structures are no longer observed after 200 µm. For the 920°C-3h diffused magnet, the Dy-enriched shells are still µm-thick after 200 µm from the coated surface and disappear after 400 µm. For the 920°C-12h diffused magnets, the thickness of the Dy-shells is more important than the two former magnets in the near surface region (100-200 µm) and according to Fig. 83, the core-shell structure is still observed at 400 µm with µm-thick Dy shells. These latter are observable until 600 µm from the coated surface (not shown here) and at 800 µm, Dy is only present at grain boundaries. According to Fig. 83, the 870°C-3h-200 µm, 920°C-3h-400 µm and 920°C-12h-800 µm EDX maps of Dy show a similar microstructural state. The concentration profiles of these three maps will be more detailed in the following.

The EDX maps of Dy and Nd at a distance of 100 µm are given with their respective concentration profiles along a line in Fig. 84 for each sample. The line starts from a $Nd_2Fe_{14}B$ grain and crosses a Dy-

enriched shell until reaching the neighboring $Nd_2Fe_{14}B$ grain. The normalized weight percentages are given for Dy and Nd (the wt.% of Fe is not reported in Fig. 84 since it is predominant).

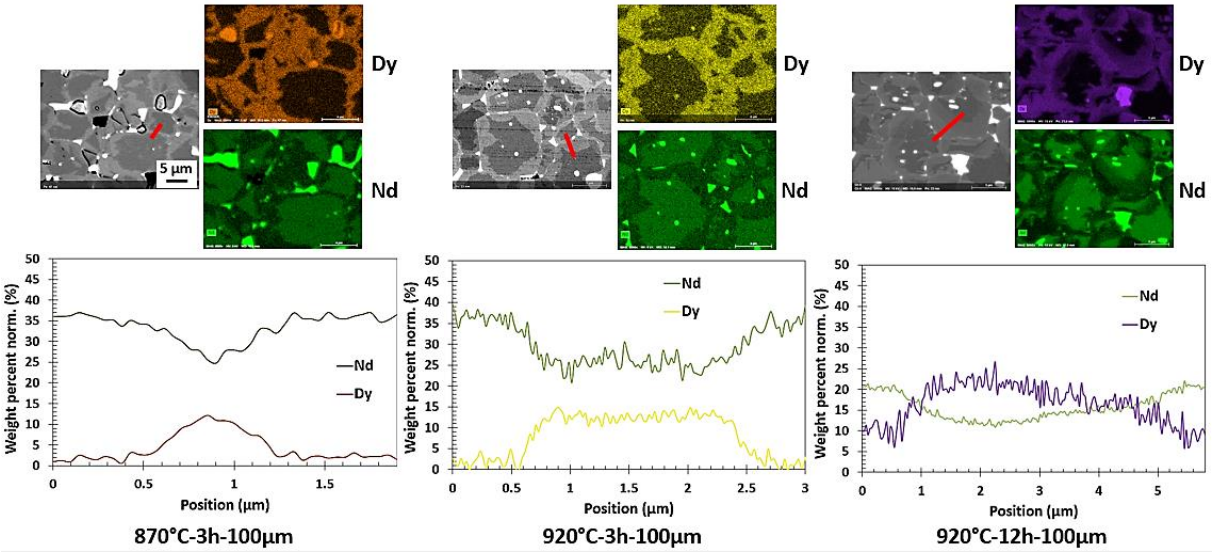


Fig. 84: EDX maps of Dy and Nd at a distance of 100 µm for each sample with the corresponding BSE-SEM image and concentration profiles along a line.

According to Fig. 84, the elemental maps of Nd and Dy reveal that the formation of the $(Nd,Dy)_2Fe_{14}B$ shells is attributed to the replacement of Nd by Dy in the outer regions of the $Nd_2Fe_{14}B$ grains. The amount of Dy relatively close to the coated surface in each sample can be directly compared. As shown by the concentration profiles, it is equivalent in the $Nd_2Fe_{14}B$ grains and the Dy-enriched shells (10-15 wt.%) for the 870°C-3h and the 920°C-3h diffused magnets. The amount of Dy is smaller than the one of Nd for these two magnets. However, for the 920°C-12h diffused magnet, the amount of Dy becomes more important in the Dy-enriched shell (> 20 wt.%) than the one of Nd. It is also particularly higher in the $Nd_2Fe_{14}B$ cores (≈ 10 wt.%). This comes from the saturation effect mentioned in IV.2.2. The penetration of Dy into the hard magnetic grains is the most pronounced for the 920°C-12h diffused magnet.

Moreover, the EDX maps of Dy and Nd are shown in Fig. 85 at various distances from the coated surface, but for a microstructural state that is similar between all diffused magnets (*i.e.* for which Dy is only found at grain boundaries).

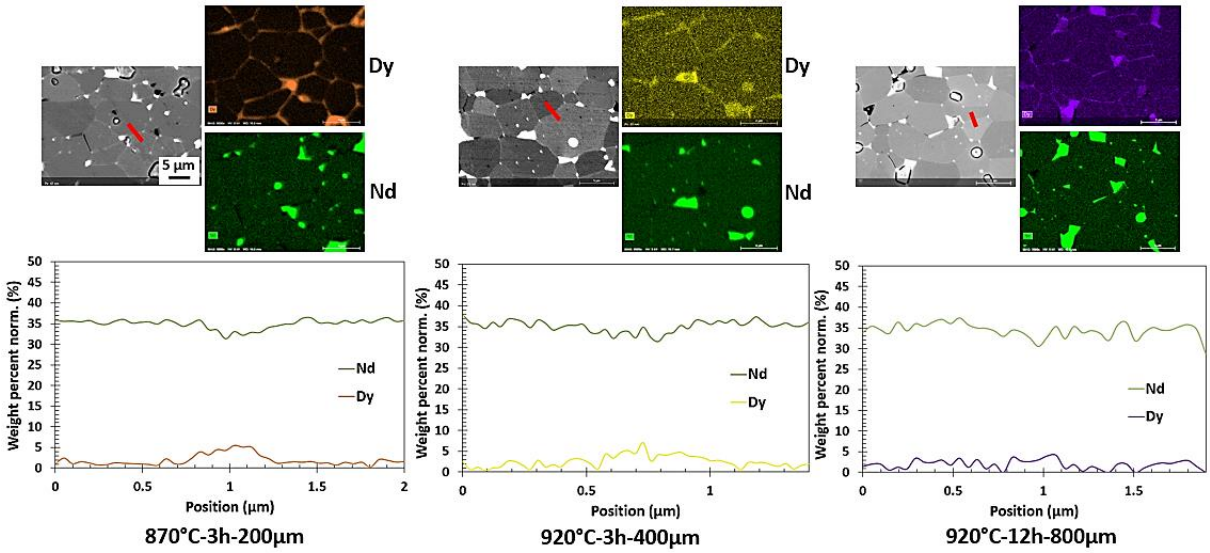


Fig. 85: EDX maps of Dy and Nd at various distances for a similar microstructural state between all diffused magnets, with the corresponding BSE-SEM image and concentration profiles along a line.

The concentration profiles of Dy in Fig. 85 show that it is present at equivalent weight percentages (≈ 5 wt.%) in the Dy-enriched regions for the 870°C-3h, 920°C-3h and 920°C-12h at a distance of 200, 400 and 800 µm from the coated surface, respectively. This shows again that the Dy diffusion is the most important for the 920°C-12h magnet.

The gains in coercivity obtained in this thesis are compared to the ones from the work of Kim *et al.* [96] to discuss the role of PDA in the coercivity enhancement (see Fig. 86). The coercivity increases in Fig. 86 are those reported for GBDP performed at 920°C for 3h using the intermetallic Dy-Co compound (see IV.2.1). In [96], the reported gains in coercivity were about 75 % and 19 % after PDA at 520°C for 1h (with respect to annealing before GBDP) for Dy-free and Dy-containing Nd-Fe-B sintered magnets, respectively. For Dy-containing magnets, the amount of Dy in the microstructure in [96] (base Dy composition + Dy diffusion) was much higher than the one reported in this thesis (≈ 8 wt.% vs ≈ 1.3 wt.%), partially explaining the very high coercivity in the as-sintered state and after PDA. For Dy-free magnets, it was still higher (≈ 2.8 wt.% vs ≈ 1.3 wt.%) but the coercivity improvements measured after each fabrication step are in good agreement with ours.

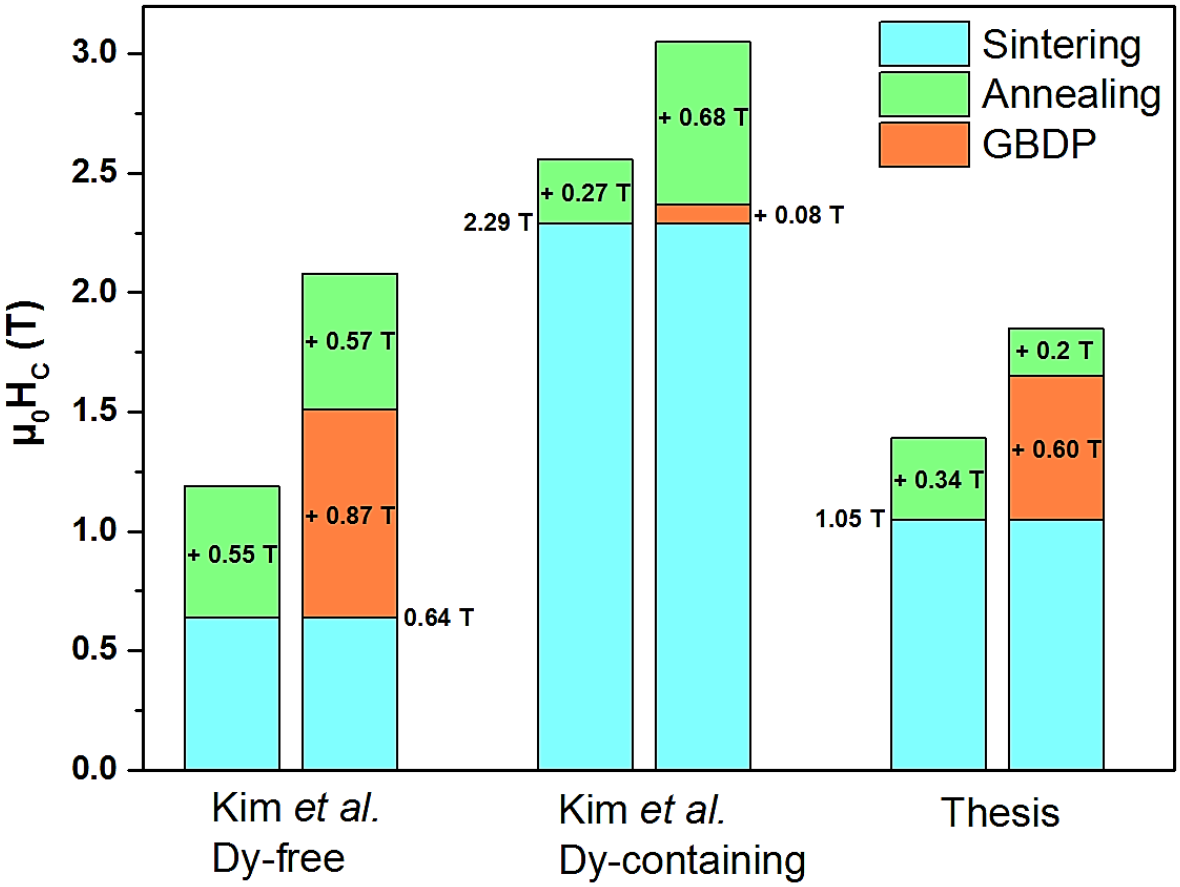


Fig. 86: Coercivity improvements after GBDP performed at 920°C for 3h and after PDA compared to the ones from the work of Kim et al. [96].

The microstructure changes responsible for the coercivity enhancement after PDA were also detailed in [96] (see Fig. 87). The very high coercivity of 3 T achieved for Dy-containing magnets was explained by the formation of Nd-rich phases with higher Nd content and by a higher Dy concentration achieved at the interface between the Nd-rich phases and the formed secondary Dy-rich shell (compared to Dy-free magnets). Moreover, the GB phase is thicker in the case of Dy-containing magnets after PDA because of the more important rejection of Nd to GBs by the substantial increase in Dy substitution.

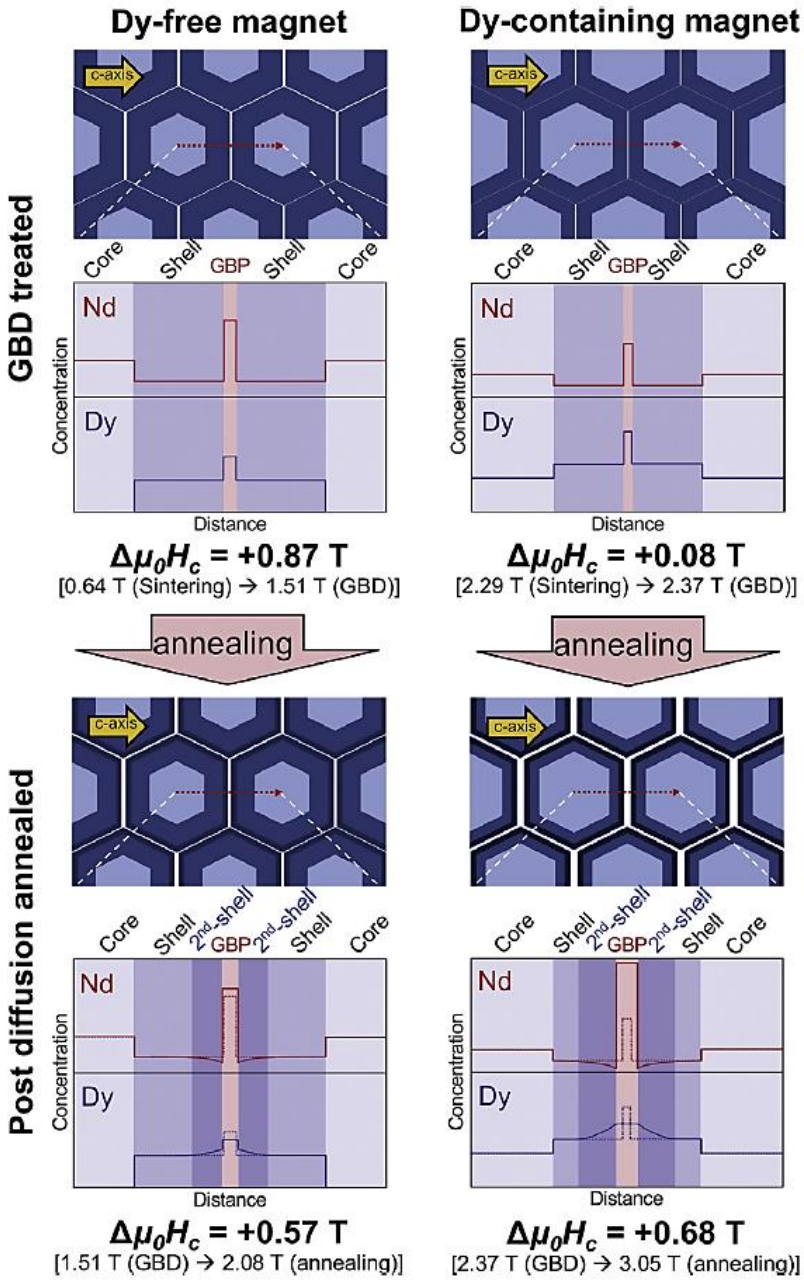


Fig. 87: Schematic illustration of the microstructures changes after PDA performed on Dy-free and Dy-containing Nd-Fe-B sintered magnets. [96]

IV.2.6.2. Coercivity profile of diffused magnets

In addition to microstructural observation for the diffusion profile of Dy, further magnetic measurements are carried out on the 920°C-3h and 920°C-12h diffused magnets. These latter are polished to remove different thicknesses of the material and coercivity is measured after each polishing step. This gives information about the coercivity profile of those magnets that will be later discussed with the help of the above EDX maps of Dy.

From the practical point of view, the polishing steps consist in the removal of 200, 400, 750 and 1250 µm on each side of the diffused magnet. Polishing is performed with a SiC #240 disk at a velocity of 40-50 rpm.

Prior to the measurements on the diffused magnets, a measurement is done on a reference magnet (in the optimal PSA state) to check the influence of the polishing on the shape of the demagnetization curve. The measurement is performed after removal of 250 µm on each side of the reference magnet and is shown in Fig. 88:

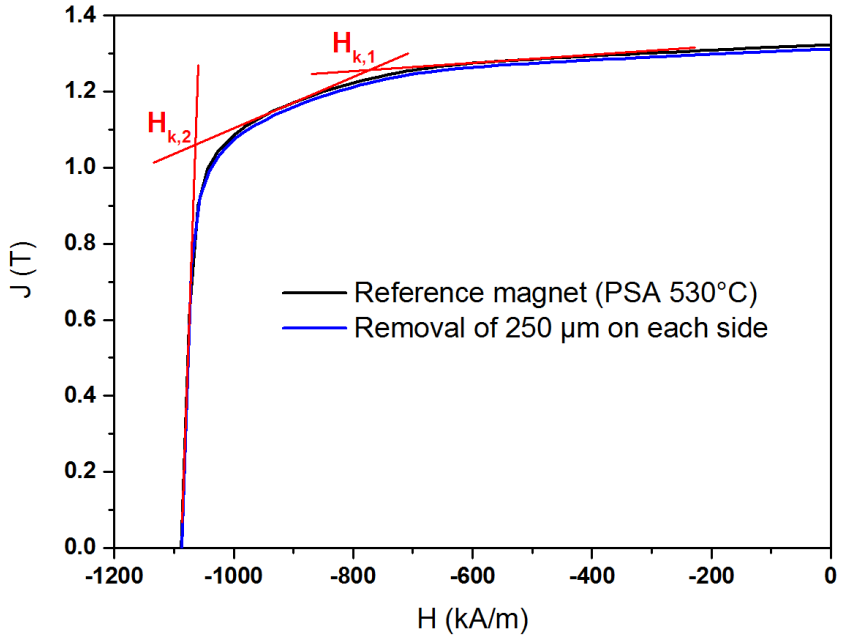


Fig. 88: Measurement of the demagnetization curve after polishing on a reference magnet.

The removal of 250 µm on each side of the magnet has no major influence on its remanence or coercivity, as well as the shape of the demagnetization curve. As a result, the same measurements can be applied to the case of diffused magnets. The demagnetization curves obtained after successive polishing on the 920°C-3h diffused magnet are shown in Fig. 89. Note that the normalized polarization is again plotted as a function of the applied field to focus on the coercivity changes.

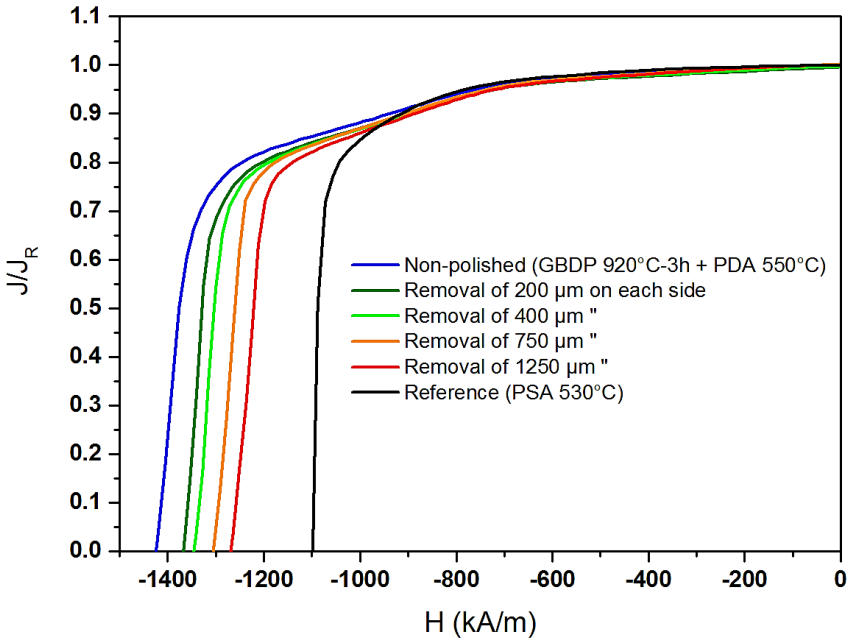


Fig. 89: Measurements of the demagnetization curve after successive polishing on the 920°C-3h diffused magnet.

From Fig. 89, the values of coercivity after each polishing step for the 920°C-3h diffused magnet are reported in Table 35. The values of $H_{k,1}$ and $H_{k,2}$ reported for each demagnetization curve are determined with the help of tangents, as shown in Fig. 88.

As pointed out in the previous section, the gap between $H_{k,1}$ and $H_{k,2}$ values reflects the level of heterogeneity in the microstructure. It is worth noting that this gap is already high (≈ 330 kA/m) for the base magnet (before Dy diffusion). The gap between $H_{k,1}$ and $H_{k,2}$ gradually increases as the thickness of the removed layer decreases to finally reach a maximal value of 650 kA/m. It is also interesting that the value of $H_{k,1}$ which refers to the first knee of the J-H curves remains nearly constant whatever the thickness of the removed layer. It could be assumed that $H_{k,1}$ corresponds to defects already present in the magnet before GBDP and that are not fully removed during PDA.

Magnet	Removed thickness on each side (µm)	$H_{k,1}$ (kA/m)	$H_{k,2}$ (kA/m)	H_{cj} (kA/m)
GBDP 920°C-3h + PDA 550°C	0	700	1349	1424 (1.79 T)
	200	677	1309	1367 (1.72 T)
	400	670	1278	1346 (1.69 T)
	750	703	1235	1305 (1.64 T)
	1250	690	1197	1269 (1.59 T)
PSA 530°C	0	752	1081	1099 (1.38 T)

Table 35: Values of $H_{k,1}$, $H_{k,2}$ and coercivity after each polishing step for the 920°C-3h diffused and reference magnets.

For the 920°C-3h diffused magnet, the loss in coercivity is the highest for the removal of the first 200 µm on each side (≈ - 4 %), then decreases between 200 and 400 µm (≈ - 1.5 %) and remains constant (≈ - 3 %) after 400 µm.

The demagnetization curves obtained after successive polishing on the 920°C-12h diffused magnet are shown in Fig. 90.

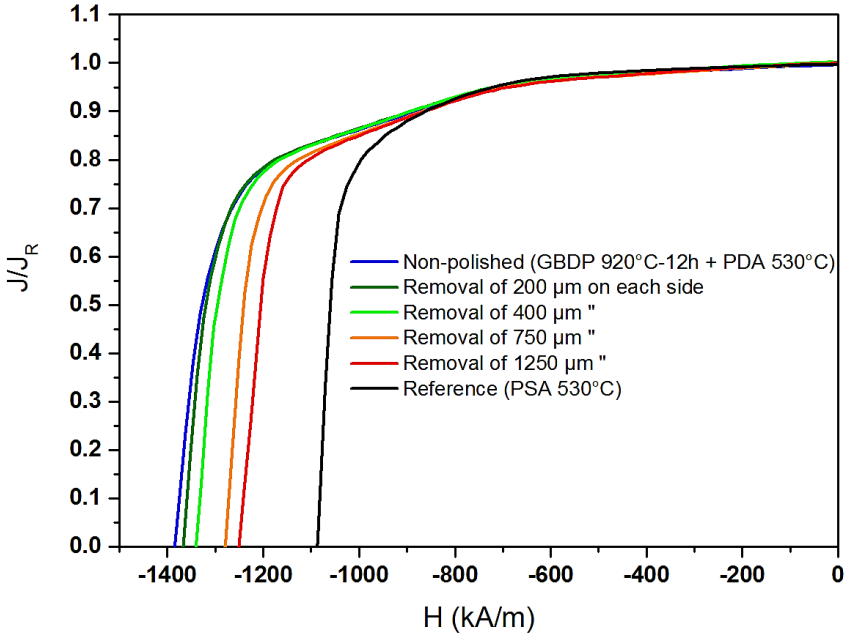


Fig. 90: Measurements of the demagnetization curve after successive polishing on the 920°C-12h diffused magnet.

The corresponding values of coercivity after each polishing step for the 920°C-12h diffused magnet are reported in Table 36.

Magnet	Removed thickness on each side (µm)	$H_{k,1}$ (kA/m)	$H_{k,2}$ (kA/m)	H_{cj} (kA/m)
GBDP 920°C-12h + PDA 530°C	0	690	1304	1385 (1.74 T)
	200	693	1304	1367 (1.72 T)
	400	692	1276	1340 (1.68 T)
	750	695	1220	1280 (1.61 T)
	1250	697	1177	1251 (1.57 T)
PSA 530°C	0	724	1040	1087 (1.37 T)

Table 36: Values of $H_{k,1}$, $H_{k,2}$ and coercivity after each polishing step for the 920°C-12h diffused and reference magnets.

For the 920°C-12h diffused magnet, a small reduction in coercivity is observed after the removal of the first 200 µm on each side (≈ - 1.3 %). It increases between 200 and 400 µm (≈ - 2 %), reaches a maximum between 400 and 750 µm (≈ - 4.5 %) and then decreases to ≈ - 2.3 % after 750 µm.

In the following, the coercivity of the non-polished diffused magnet $H_{cj,0}$ is taken as reference (= 1424 kA/m for the 920°C-3h diffused magnet, = 1385 kA/m for the 920°C-12h diffused magnet). The evolution of the ratio $H_{cj}/H_{cj,0}$ with the removed thickness on each side is plotted in Fig. 91 for both diffused magnets. Furthermore, the EDX mappings of Dy are also shown in Fig. 91 to shed light on the link between microstructural characterization and the coercivity measurement.

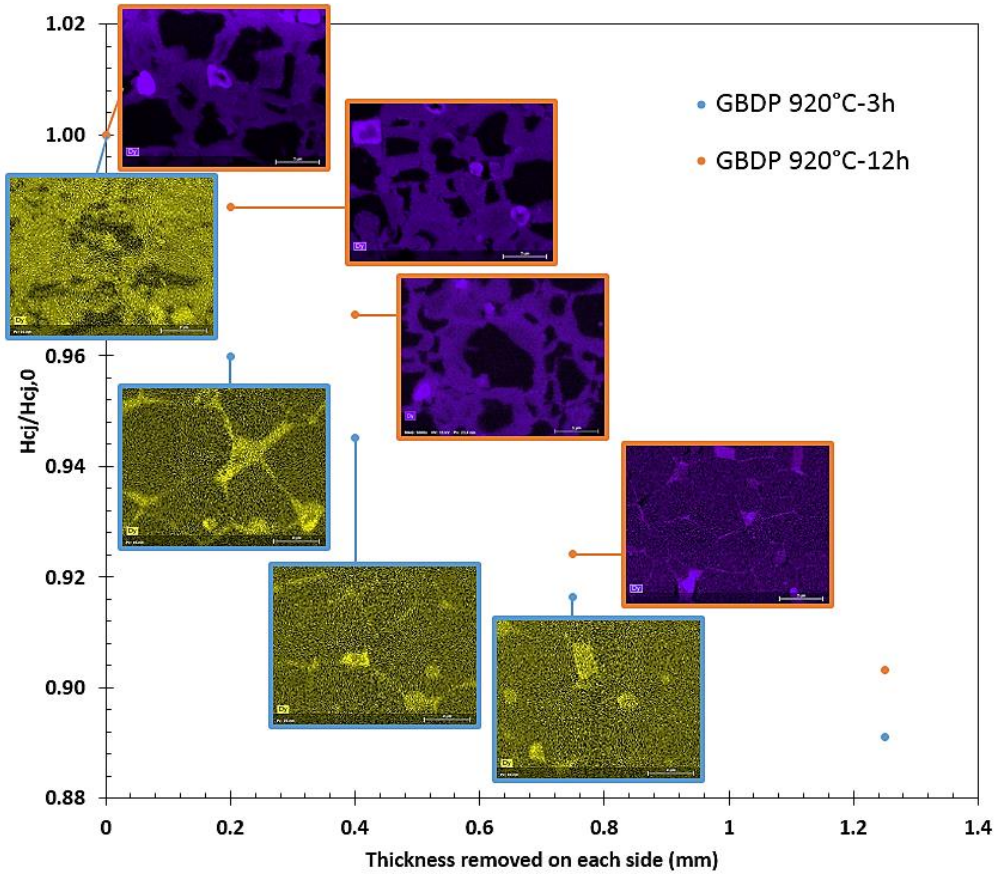


Fig. 91: Evolution of the ratio $H_{cj}/H_{cj,0}$ with the removed thickness for the 920°C-3h and 920°C-12h diffused magnets and respective EDX maps of Dy.

The losses in coercivity reported in Table 35 and Table 36 can be explained with the help of Fig. 91 by correlation with the EDX mappings of Dy. As shown before, the highest loss in coercivity is observed for the first 200 µm in the case of the 920°C-3h diffused magnet. For instance, the EDX map of Dy corresponding to the non-polished magnet reveals saturation in Dy at/near the coated surface and the EDX map at 200 µm from the coated surface shows the reduced localization of Dy at grain boundaries. The same conclusion can be drawn for the 920°C-12h diffused magnet for the polishing between 400 and 750 µm on each side (from clear core-shell structures to reduced localization at grain boundaries).

Micromagnetic simulations are here required to understand the link between the local composition and the macroscopic coercivity measurement. This can be studied at the grain scale by calculations performed on a simple model that is representative of the core-shell structure experimentally found in Dy-diffused Nd-Fe-B sintered magnets, but at a smaller scale due to computational limits. Numerical modelling is also a helpful tool to explain the shape of the experimental demagnetization curves of Dy-diffused magnets, *i.e.* to explain the deterioration of rectangularity.

IV.2.7. FEMME simulations: core-shell model

IV.2.7.1. Scope of the numerical simulation

Micromagnetic simulations are performed at the grain scale on a core-shell model using the FEMME software. The objective is to determine the role of a non-magnetic GB phase and of the Dy-rich shell (thickness and concentration of Dy) on coercivity in such structures.

IV.2.7.2. Description of the model

To simulate magnetization reversal in a core-shell structure, the model (see Fig. 92) is based on the one described in IV.1.2.1. It is composed of 8 cubic grains, each one consisting of a $Nd_2Fe_{14}B$ hard magnetic core surrounded by a $(Nd,Dy)_2Fe_{14}B$ shell of various thickness (5-10 nm). The grains are again separated by a 2-nm-thick GB phase of various nature. The defect is still localized in one of the grains to act as the nucleation zone for magnetization reversal.

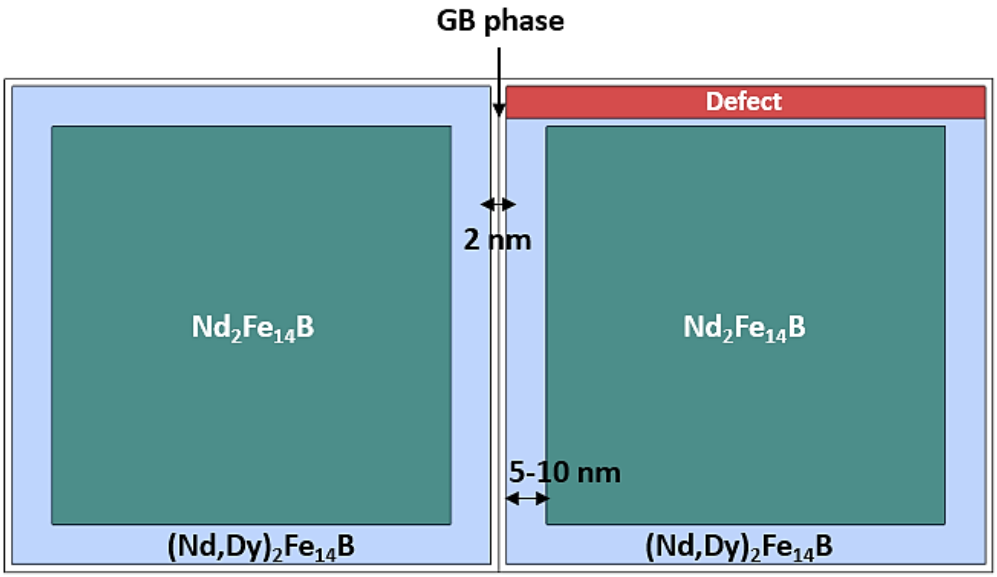


Fig. 92: Cubic model representative of a core-shell structure.

The input parameters for the $Nd_2Fe_{14}B$ grains, the GB phase and the defect are the same as in Table 29. The intrinsic magnetic properties for the different Dy-rich shells considered in the simulations are given in Table 37. The parameters at 300 K for the $(Nd_{53}Dy_{47})_2Fe_{14}B$ phase are taken from [81]. The K_1

and J_S parameters at 300 K for the $(Nd_{90}Dy_{10})_2Fe_{14}B$ and $(Nd_{76.5}Dy_{23.5})_2Fe_{14}B$ phases are calculated by linear interpolations between the values for $Nd_2Fe_{14}B$ and $(Nd_{53}Dy_{47})_2Fe_{14}B$ phases, according to [82], [106]. The A parameter is also determined by linear interpolation, which can be questionable. However, the exchange stiffness of the Dy-rich shell has no major influence on the simulated demagnetization curve and it also lies in a restricted range of values. In addition, the chosen $(Nd_{53}Dy_{47})_2Fe_{14}B$ composition for the Dy shell can be justified by the EDX analyses in IV.2.6.1 (crossing of the Dy and Nd concentration profiles in the shell region). The $(Nd_{90}Dy_{10})_2Fe_{14}B$ and $(Nd_{76.5}Dy_{23.5})_2Fe_{14}B$ compositions correspond to a very local anisotropy enhancement and to the intermediate case, respectively.

Phase	K_1 (MJ/m^3)	J_S (T)	A (pJ/m)	L_{ex} (nm)
$(Nd_{53}Dy_{47})_2Fe_{14}B$ **[81]**	5.17	1.15	8.7	≈ 4
$(Nd_{90}Dy_{10})_2Fe_{14}B$	4.5	1.51	7.9	≈ 3
$(Nd_{76.5}Dy_{23.5})_2Fe_{14}B$	4.7	1.38	8.2	≈ 3

Table 37: Intrinsic magnetic properties at 300 K of the Dy-rich shells.

Tetrahedral meshes are used with the same size as in IV.1.2.1 for the $Nd_2Fe_{14}B$ grains, the GB phase and the defect. For the Dy-rich shells, meshes with a size of 2 nm are also used.

In the following, the impact of some model parameters on magnetization reversal is reported: the thickness and content in Dy of the Dy-rich shell and the nature of the GB phase.

IV.2.7.3. Influence of thickness/content in Dy of Dy-rich shell on magnetization reversal

The first studied parameter is the thickness of the Dy-rich shell. In the following simulations, the GB phase is set to be non-magnetic (see Table 29 for parameters), so that the $Nd_2Fe_{14}B$ grains are exchange-decoupled. Two different thicknesses are tested for the Dy-rich shell: 5 and 10 nm. Furthermore, the impact of the content in Dy of the Dy-rich shell is also reported. For that, simulations with different compositions for the Dy-rich shell are carried out: 10, 23.5 and 47 at.% of Dy. The simulated demagnetization curves are shown in Fig. 93.

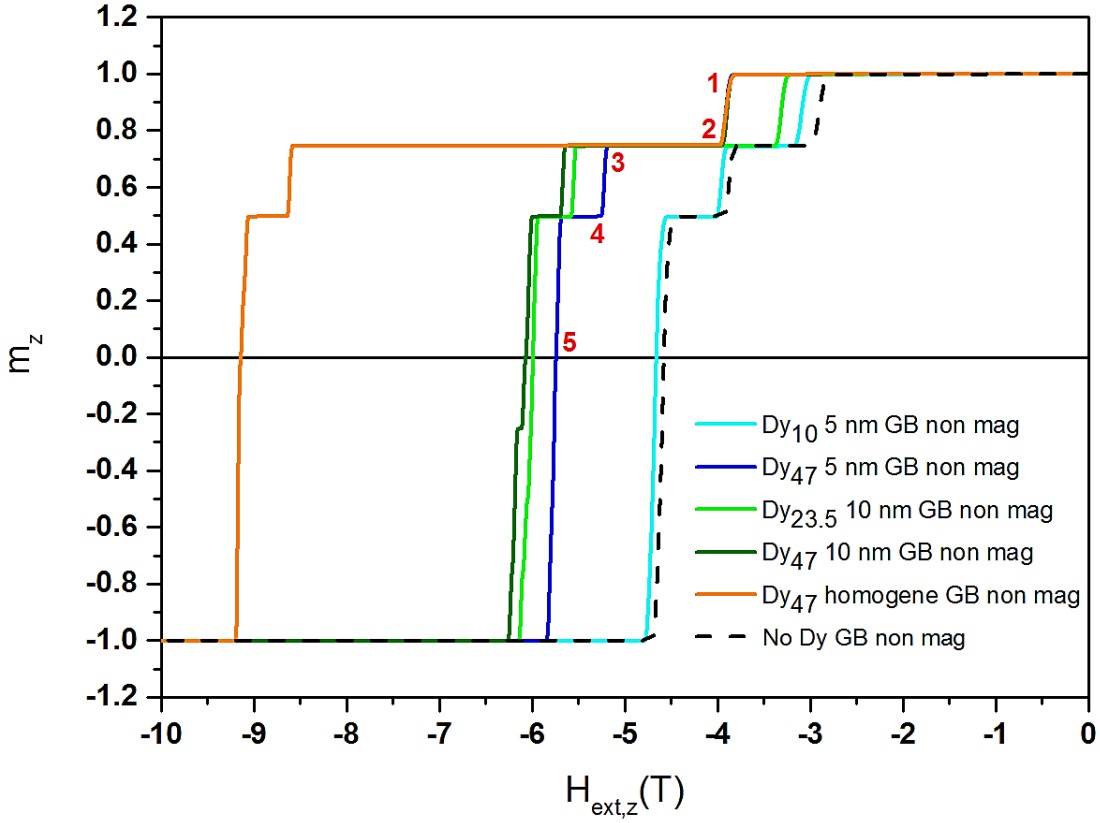


Fig. 93: Simulated demagnetization curves showing the influence of the Dy-rich shell thickness and content in Dy on magnetization reversal. The red numbers correspond to the screenshots in Fig. 94.

In Fig. 93, all simulated demagnetization curves exhibit a stepwise behavior for magnetization reversal. Neither thickness nor content in Dy of the Dy-rich shell have an influence on this stepwise behavior. However, this latter can be attributed to the presence of the non-magnetic GB phase in the model. For instance, some images of the magnetization direction distribution are represented at different field values in Fig. 94 for the reference case with a $(Nd_{53}Dy_{47})_2Fe_{14}B$ shell of thickness 5 nm.



Fig. 94: Magnetization configuration during reversal for the case with a $(Nd_{53}Dy_{47})_2Fe_{14}B$ shell of thickness 5 nm and a non-magnetic GB phase (dark blue solid curve in Fig. 93).

From Fig. 94, magnetization reversal starts from the defect and propagates in the rest of the grain that contains the defect (1st step: images 1 and 2). Owing to its non-magnetic nature, reversed domains are pinned at the GB phase and a higher applied field is required for depinning. Then, reversed domains propagate in the above neighboring grain and 2 grains are thus completely reversed (2nd step: images 3 and 4). After further pinning and depinning processes, reversal of all the remaining grains happens (3rd step). The image 5 corresponds to the magnetization distribution at the coercive field, for which equipartition of blue and red domains is observed. This discrete switching of individual grains in the case of a non-magnetic GB phase is in good agreement with the idea developed in the work of Dobrynin *et al.* [120].

Compared to the simulated case with no Dy shell (dashed black curve in Fig. 93), the above simulations show that the $(Nd,Dy)_2Fe_{14}B$ shell efficiently hinders nucleation of reversed domains from the defect (when the content in Dy of the Dy-rich shell is higher than 10 at.%). For instance, the simulated case with a Dy_{10} shell of thickness 5 nm shows very small improvement in coercivity, since its thickness is of the same order of magnitude than the one of the defect (4 nm) and because of its low content in Dy. The Dy-rich shell also delays the reversal propagation from the first grain to neighboring grains, which leads to coercivity enhancement. In fact, the gain in coercivity for the simulated cases with a Dy shell of thickness 10 nm is about 30 % and is in good agreement with the experimental one reported in IV.2.1 after GBDP using the intermetallic compound and further PDA (+ 33%).

According to Fig. 93, the reversal of the first grain (that contains the defect) essentially depends on the content of Dy in the Dy shell. The propagation (2^{nd} and 3^{rd}) steps are in addition determined by the thickness of the Dy shell. Indeed, the curves in Fig. 93 with a thicker Dy shell exhibit higher coercivity, even if the content in Dy of the Dy shell is smaller (*i.e.* $Dy_{23.5}$ 10 nm case shows higher coercivity than Dy_{47} 5 nm case).

IV.2.7.4. Influence of GB phase nature on magnetization reversal

The above section has already given some information about the impact of a non-magnetic GB phase on magnetization reversal of the studied core-shell model. An additional case with a soft ferromagnetic GB phase is simulated and is compared to the reference case of Fig. 93 (Dy_{47} 5 nm GB non-magnetic). For this computation, the considered Dy shell is therefore the $(Nd_{53}Dy_{47})_2Fe_{14}B$ phase with a thickness of 5 nm. The simulated demagnetization curve for a soft ferromagnetic GB phase is given in Fig. 95. This case corresponds to GBDP without further annealing, which is still efficient for coercivity enhancement, as experimentally observed.

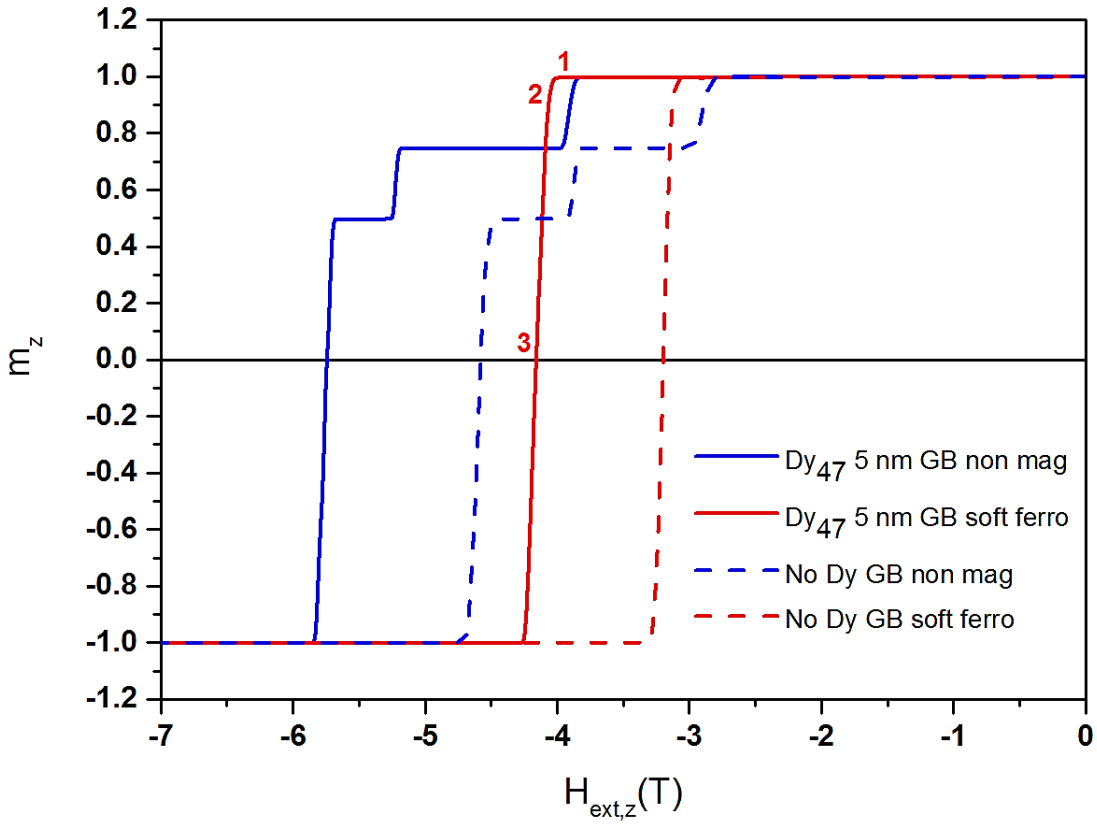


Fig. 95: Simulated demagnetization curves showing the influence of the GB phase nature on magnetization reversal. The red numbers correspond to the screenshots in Fig. 96.

The simulation highlights the fact that the stepwise behavior of magnetization reversal essentially depends on the nature of the GB phase. Indeed, the model with a soft-ferromagnetic GB phase exhibits magnetization reversal in one step. The screenshots of the magnetization configuration during reversal for the case with a soft ferromagnetic GB phase are shown in Fig. 96:

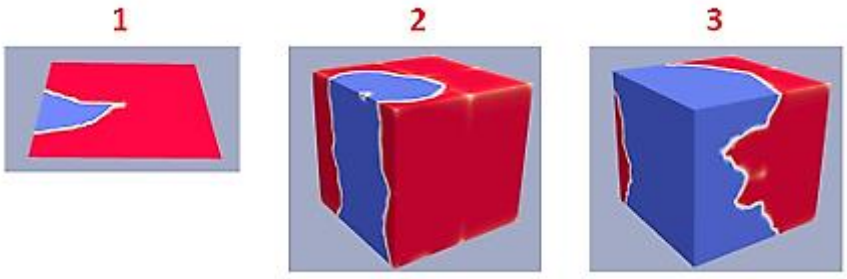


Fig. 96: Magnetization configuration during reversal for the case with a $(Nd_{53}Dy_{47})_2Fe_{14}B$ shell of thickness 5 nm and a soft ferromagnetic GB phase (red solid curve in Fig. 95).

From Fig. 96, magnetization reversal starts again from the defect zone but propagates in several grains at the same time (images 1 to 3). Meanwhile propagation, nucleation of additional reversed domains occurs at the corners of grains (white domains on image 2). Coercivity therefore decreases a lot when the GB phase is soft-ferromagnetic (- 26% with respect to the case with a non-magnetic GB phase).

IV.3. Conclusions

Core-shell microstructures have been obtained by GBDP on Nd-Fe-B sintered magnets using a Dy-Co intermetallic compound. An experimental parametric study has been done to determine the influence of diffusion time, temperature and of post-diffusion annealing on coercivity. Diffusion performed at higher temperatures (920°C vs 870°C) leads to a better distribution of Dy in the microstructure and hence to better coercivity. Diffusion for a longer duration (12 h vs 3 h) doesn't result in an improvement of coercivity because of a saturation effect in Dy. In addition, a post-diffusion annealing enables further coercivity enhancement and lower sensitivity to the annealing temperature (compared to the coercivity dependence with annealing before GBDP). Microstructural observations in complement to magnetic measurements were performed to characterize the diffusion and coercivity profiles and to establish the link between the local composition and the measured coercive field. Furthermore, micromagnetic simulations have been carried out at the grain scale on a simple core-shell model. By introducing a defect in the model, its impact on the reversal of exchange-coupled and decoupled grains has been studied. Microstructural features such as the content in Dy and thickness of the Dy shell, as well as the nature of the GB phase, have a major influence on the simulated demagnetization curves. On the one hand, nucleation of magnetization reversal from the defect zone essentially depends on the content in Dy of the Dy shell (hindered with the increase of Dy content) while the increase of the Dy shell thickness delays the propagation of reversal, leading to coercivity enhancement. On the other hand, the nature of the GB phase determines the stepwise behavior/shape of the demagnetization curves. These first computations reproduce well the shape of the experimentally measured demagnetization curves (*i.e.* the deterioration of rectangularity after annealing and GBDP). For instance, the decreased rectangularity can be explained by the presence of a non-magnetic GB phase that results in exchange decoupling between grains (= stepwise reversal). The simulations are also in good agreement with the experimental gains in coercivity.

The next chapter deals with the analysis of the Dy distributions with the help of a diffusion model. The purpose is to correlate the local Dy content to specific values of coercive fields that will be used as input parameters for simulations performed with the previously described polycrystalline model.

Magnetization reversal will therefore be simulated on multigrain systems representative of magnets with coercivity gradient to further compare the simulated and experimental demagnetization curves obtained for the 870°C-3h, 920°C-3h and 920°C-12h diffused magnets.

V. Discussion: coercivity of graded magnets

The objective of this chapter is to propose a discussion on the coercivity of polycrystalline Nd-Fe-B sintered magnets covering the different scales that have been investigated. Actually, it has been shown that the magnet coercivity can be seen as a combination of several physical processes, which justifies considering this property as extrinsic. Schematically, the triggering of magnetization reversal starts near grain boundaries at the nanoscale and affects an activation volume of several nm^3. Then, reversal propagates into the grain volume, leading to a complete grain switching for a critical value of the applied field. Finally, magnetostatic interactions between grains generate specific grain reversal patterns in the sintered parts. These patterns are governed by the demagnetizing field and lead to second quadrant J-H curves with shapes depending on the measurement conditions. Consequently, the experimental coercive field value (H_{ext} for J=0) obtained by hysteresigraph measurement needs further assessment and interpretation.

In the previous chapter, the influence of thermal treatments (annealing, GBDP of Dy) on the triggering of reversal and the switching field has been described via magnetic measurements and numerical modelling at the nanoscale. This chapter enlarges the analysis to the effect of large grain heterogeneities, as observed after Dy diffusion and unavoidable for magnets with a thickness larger than 2-3 mm. In the first part, the Dy distributions are analyzed via a diffusion model in order to estimate the Dy concentration in grains and at different depths. Then, after ascribing to the grains some critical values for the switching field that are related to the local Dy content, the polycrystalline model is implemented for the simulation of J-H curves in closed-circuit. The simulation allows understanding the large local values of switching fields that are relevant at the grain scale, compared to the coercive field measured on the magnet.

V.1. Modelling of diffusion profiles

The diffusion of Dy and Co from the surface coating into the volume of sintered magnets is expected to occur preferentially along grain boundaries (GBs) since, at the temperature of the diffusion treatment (> 850°C), the Nd-rich phase located at GBs is in the liquid state. Actually, diffusion in a liquid phase is generally considered as a faster process than solid-state transport [137].

This assumption is consistent with the chemical element mapping (see Fig. 84 and Fig. 85 in Chapter IV) showing that the large Nd-rich precipitates, clearly visible at triple junctions after sintering, become also Dy-rich after diffusion, revealing a preferential path for the heavy rare-earth elements. However, the Dy element diffuses also from GBs into the volume of $Nd_2Fe_{14}B$ grains. The competition between grain boundary diffusion and volume diffusion results in the previously described core-shell structure. Both mechanisms are controlled by specific values of diffusion coefficients. Since the diffusivities could be different between the two mechanisms, the diffusion fronts (and their evolution with temperature and time) could be complex. They could strongly differ from the well-known concentration profile resulting from a single diffusion process that occurs in a semi-infinite and homogeneous body.

V.1.1. Diffusion model hypothesis

V.1.1.1. Diffusion in a bi-crystal

Different models have been proposed in literature to account for the combination of grain boundary and volume diffusion mechanisms. The first model has been introduced by Fisher [138] who considered a simple geometrical representation of the grain boundary consisting in two semi-infinite planar crystals separated by a thin horizontal layer (located at x=0, see Fig. 97). Diffusion occurs from the top

line (located at y=0) of the bi-crystal and is assumed to follow Fick's law in each medium (low diffusivity D_v in grains and high diffusivity D_j in GBs). At the initial state, the concentration is ascribed to be equal to 1 at the top line (y=0) and is zero in the volume. Fisher obtained the following analytical expression for the concentration profile:

$$c(\xi,\eta,\beta) = erfc\left(\frac{\xi}{2}\right) \times exp\left(-\frac{\eta}{\pi^{1/4}\beta^{1/2}}\right) \qquad \text{[Eq. 38]}$$

The reduced coordinates are expressed as (with *a* being the half width of the grain boundary):

$$\xi = \frac{x-a}{\sqrt{D_v t}} \qquad \text{[Eq. 39]}$$

$$\eta = \frac{y}{\sqrt{D_v t}} \qquad \text{[Eq. 40]}$$

$$\beta = \frac{D_j}{D_v}\frac{a}{\sqrt{D_v t}} \qquad \text{[Eq. 41]}$$

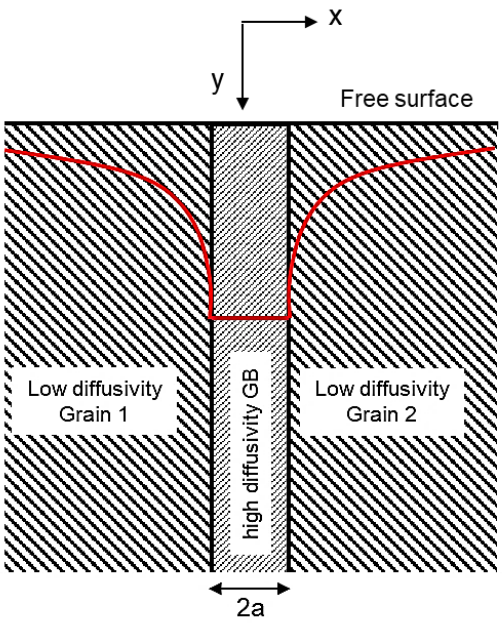


Fig. 97: Bi-crystal model for the calculation of the Dy profile in a polycrystalline sample by mixed diffusion (volume/grain boundary) of elements from the surface. The red line illustrates the shape of iso-concentration lines (from [138]).

The concentration is given in [Eq. 38] as a product of two distinct terms. The first one (error function) depicts the lateral profile in grains with respect to the x-coordinate and represents therefore the consumption by the grains of the diffused species. The second term takes into account diffusion along the grain boundary (*i.e.* along the y-axis). The attenuation of the penetration profile is described with the exponential function (*i.e.* the factor β). When the factor β is small, the iso-concentration lines tend to be flat, diffusion being controlled by volume diffusion and limited to a thin layer under the sample surface. On the contrary, when the factor β is high, the diffusion along GBs is predominant and the iso-concentration lines become very steep (sharp) near GBs. This last regime is preferred for optimizing the Dy diffusion.

The Fisher approximation stands when the concentration profile remains flat along the thickness of the grain boundary (along the x-axis) and for an infinite source of Dy available at the sample surface. Whipple [139] improved the model for large GBs (non-flat profile) and Suzuoka [140] gave a solution

taking into account the consumption of the diffused element. However, these last two formalisms are more complicated and the solutions require numerical evaluation. As a first approach, the Fisher approximation has been implemented in this study in order to establish some main trends.

V.1.1.2. Application to the diffusion of Dy in sintered magnets

In sintered magnets, diffusion annealing is carried out within a range of temperature for which a liquid phase forms at GBs via the eutectic reaction between the Nd-rich phases localized at GBs and the $Nd_2Fe_{14}B$ grains. The eutectic reaction occurs at 677°C [130] and the resulting liquid phase tends to wet the GBs before the onset of the precursor melting ($T_M(Dy_{63}Co_{37})$ = 734°C). For this reason, the diffusion process of Dy in magnets can hardly be modeled by the penetration of a liquid alloy formed at the top surface and penetrating into the bulk along GBs. The process differs also from the case of an element diffusing in the solid state and preferentially at GBs. In the first case, the diffusion process is controlled by the wetting of GBs by the precursor alloy and is driven by the surface energy balance [141], [142]. In the second situation, solid state diffusion occurs along very thin GBs (2a = 0.5 nm) and the activation energy of GBDP is about half that of the volume diffusion [143].

The values of diffusion coefficients D_v and D_j are the key parameters in this model. For the volume diffusion of Dy in $Nd_2Fe_{14}B$ grains, the following expression has been proposed by Campos et al. [144] for the coefficient D_v:

$$D_v[m^2.s^{-1}] = 8.10^{-4} exp\left(-\frac{315\,000}{R.T[K]}\right) \quad \text{[Eq. 42]}$$

The diffusion coefficient D_j has been evaluated by Loewe *et al.* [94] for some rare-earth elements (Dy, Tb…) at 900°C from coercivity profiles (D_j = 1.1 10^{-10} $m^2.s^{-1}$, *i.e.* $D_j/D_v \approx 10^7$). In the following, it has been assumed that the value of D_j evolves from the "pivot" temperature of 900°C, according to an Arrhenius law, with an activation energy Q_j of 315 kJ/mol equivalent to the bulk diffusion. The exact activation energy is still unknown but the following trends are not drastically changed with another values of Q_j due to the narrow range of temperature studied (50 °C).

Some other geometrical parameters required for the calculation of the Dy volumetric concentration and the ratio between Nd and Dy atoms are given in Table 38. It has to be noticed that the width of the grain boundary has been taken here as 2a=20 nm, which is a large value regarding the grain boundary thickness revealed by TEM analysis [80]. Since the grains are partially melted at 900°C at their surface and form channels for Dy diffusion, a larger value for the grain boundary thickness can be reasonably assumed during the diffusion heat treatment. This value also corresponds to an estimation made from the STEM-EDX lines performed on GBs by Loewe *et al.* [94].

Parameters	Numerical value
Mass of $Dy_{63}Co_{37}$ alloy deposited on the top surface of the magnet	20 mg
Diameter of the sample	10 mm
Estimated thickness of the $Dy_{63}Co_{37}$ alloy layer deposited on the surface	200 µm
Molar concentration of Dy in the deposited layer	6.47 (x 10^{-3} mol.cm^{-3})
Molar concentration of Nd in the $Nd_2Fe_{14}B$ phase	13.9 (x 10^{-3} mol.cm^{-3})
Grain size	5 µm
Grain boundary thickness for the GB diffusion path (2a)	20 nm
Factor β in [Eq. 38] (920°C / 3h)	4.10^5

Table 38: Geometrical data for the computation of the Dy concentration profile with the Fisher model.

V.1.2. Results

V.1.2.1. Lateral concentration profile in grains

The lateral Dy concentration profiles (along the x-axis) obtained with the Fisher model are representative of the Dy penetration in grains. The profiles are plotted in Fig. 98 at different depths (100, 200, 400 and 800 µm) for the three experimental diffusion conditions (870°C-3h, 920°C-3h and 920°C-12h).

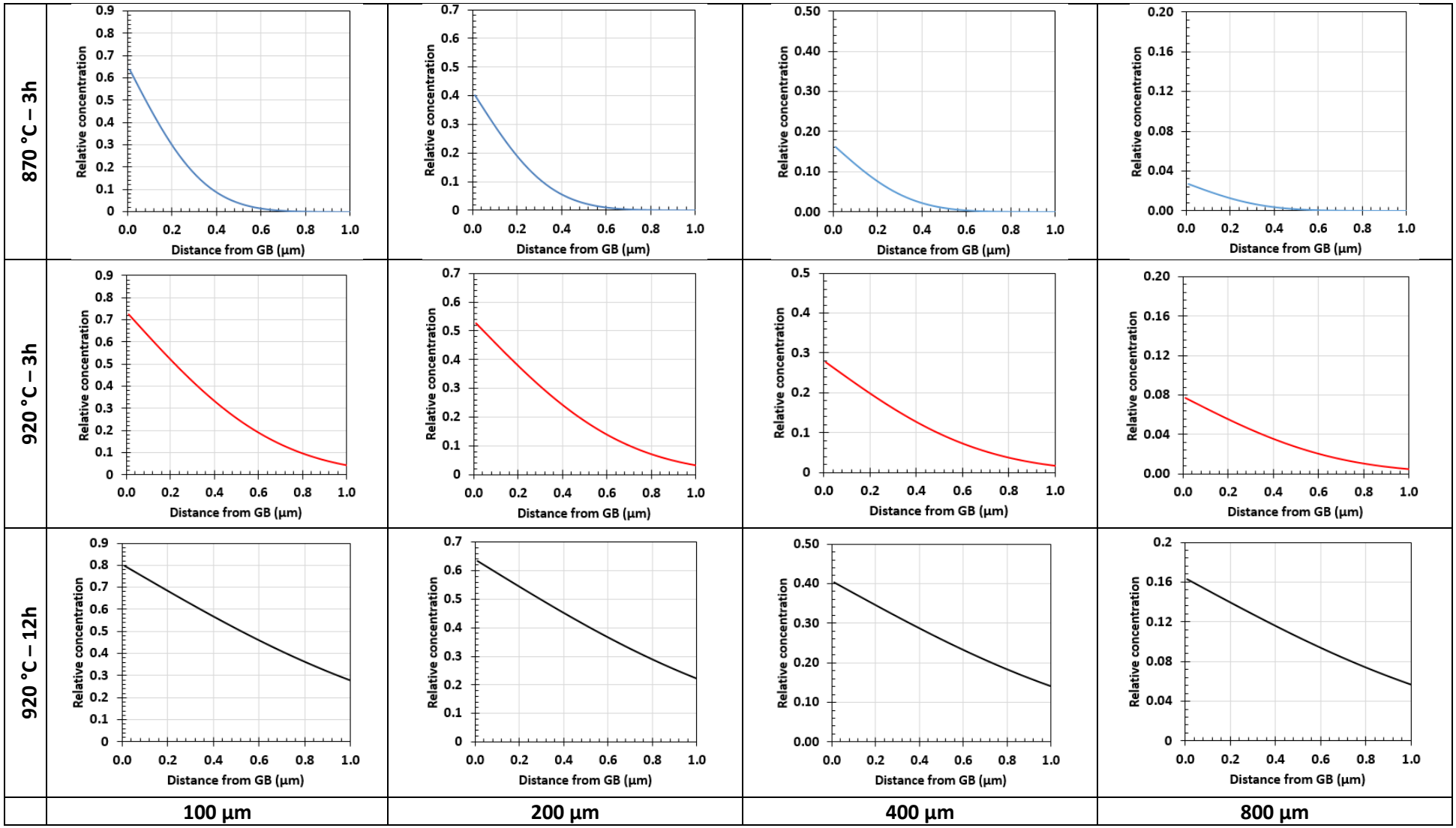


Fig. 98: Dy concentration profile (relative to the surface) obtained with the Fisher model for the three experimental diffusion conditions.

From these curves, the values of the Dy concentration, averaged over a shell of width 1 µm located at the grain rim, have been calculated and reported in Table 39. Three color coded groups have been distinguished among the previous 12 cases: (i) high concentration shells ($C_{Dy} > 0.25$), (ii) medium ($0.10 < C_{Dy} < 0.25$) and (iii) low diffused shells ($C_{Dy} \approx 0.10$). Table 39 regroups the computed data that are superposed to the corresponding EDX maps of Dy given as guidelines.

	100 µm	200 µm	400 µm	800 µm
870°C-3h	0.14	0.09	0.04	0.01
920°C-3h	0.30	0.22	0.12	0.03
920°C-12h	0.52	0.42	0.26	0.11

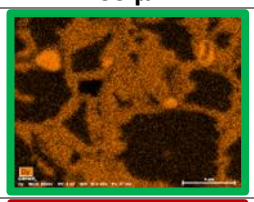
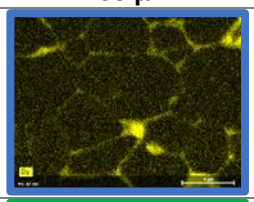
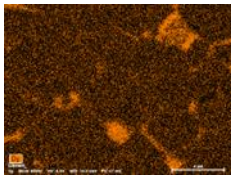
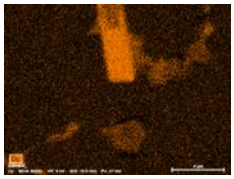
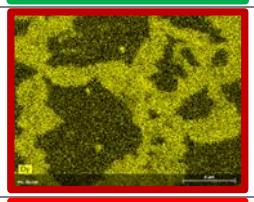
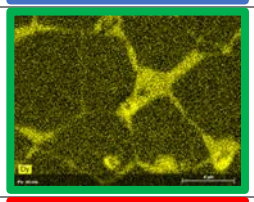
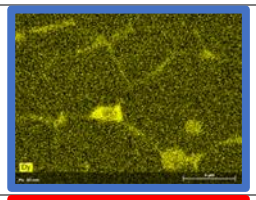
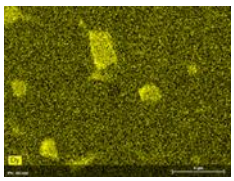
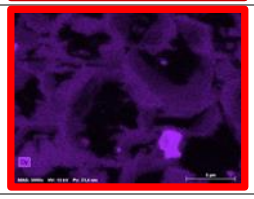
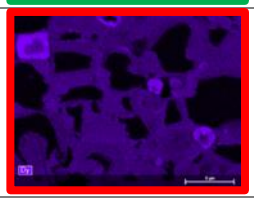
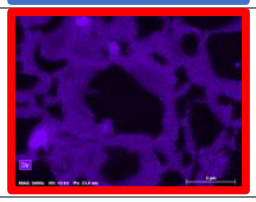
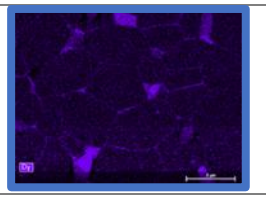
	100 µm	200 µm	400 µm	800 µm
870 °C – 3h				
920°C – 3h				
920°C – 12h				

Table 39: Dy volumetric concentration (normalized to Dy surface concentration) averaged over 1-µm-thick shell from the Fisher model. Corresponding Dy elemental maps obtained by SEM-EDX.

It is worth noting that the different positions (from the sample surface) of the high Dy concentration shells predicted by the model correspond well with most of the SEM-EDX mappings showing enriched and contrasted Dy shells. The trend is the same for intermediate and low Dy concentration shells. The width of the Dy-rich shell is also well depicted by the model, as illustrated by the threshold values reported in Table 40.

	100 µm	200 µm	400 µm	800 µm
870°C-3h	0.26 µm	0.2 µm	0.18 µm	/
920°C-3h	0.6 µm	0.44 µm	0.2 µm	/
920°C-12h	> 1 µm	> 1 µm	0.75 µm	/

Table 40: Distance from the grain boundary in µm below which the Dy/Nd-init ratio exceeds the threshold value of 0.1 considered as an indicator of the width of the Dy-rich shell visible on SEM-EDX elemental maps.

V.1.2.2. Comparison with SEM-EDX quantitative analyses

Fig. 100, Fig. 101 and Fig. 102 compare the Dy/Nd profiles measured by SEM-EDX to the depletion calculated for the three diffusion conditions in the grain volume. For each condition, two cases have been selected: (i) the grain concentration profile near the surface (100 µm) and (ii) the profile at a

depth corresponding to the intermediate averaged Dy content (c ≈ 0.1) previously identified in Table 39. At 920°C, the experimental profile in grains near the surface exhibits a large plateau followed by a rapid decrease in the Dy content (see Fig. 100 (up)). This profile shape differs strongly from the calculated depletion line and reveals a different mechanism for the Dy penetration into the grain, as already inferred by several authors. Near the sample surface, as the Dy concentration is high, a large amount of Nd is rejected to the GB phase and forms a thick liquid phase as the eutectic reaction proceeds (see (b) in Fig. 99). During cooling, the liquid phase solidifies and tends to transform into large and stepped shells with quasi homogeneous Dy content (see (c) in Fig. 99). [98]

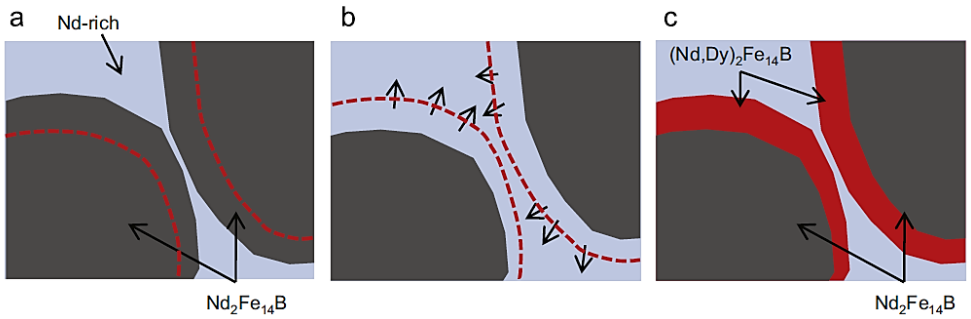


Fig. 99: Schematic representation of the possible mechanism for the replacement of Nd by Dy. [98]

The effect is more pronounced after 12 h (see Fig. 102 up)) at 920°C. However, the discrepancy tends to decrease for lower Dy content, *i.e.* for the profiles measured at 400 and 800 µm from the surface for 920°C-3h and 920°C-12 h, respectively, and for the profiles measured at 100 and 200 µm for 870°C-3h. For all these cases, the agreement between the model and the quantitative SEM-EDX analyses for Dy and Nd is quite good.

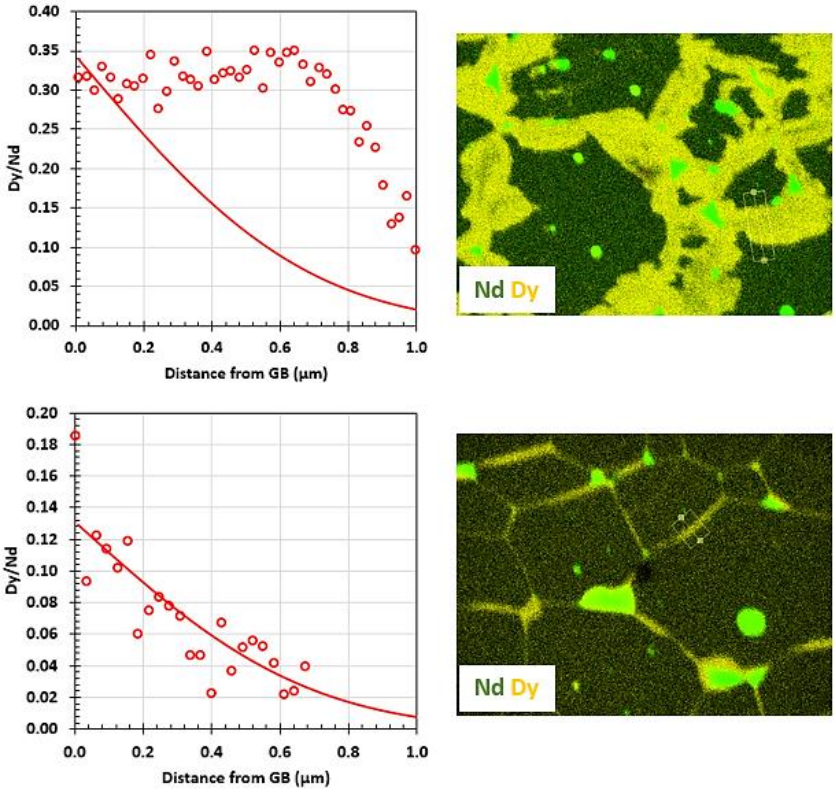


Fig. 100: Dy/Nd depletion in grain volume at 100 µm and 400 µm for the sample diffused at 920°C-3h. (Left) Measured (open symbols) and calculated (solid line) concentration profiles. (Right) SEM-EDX maps of Nd and Dy with the localization of the profile line.

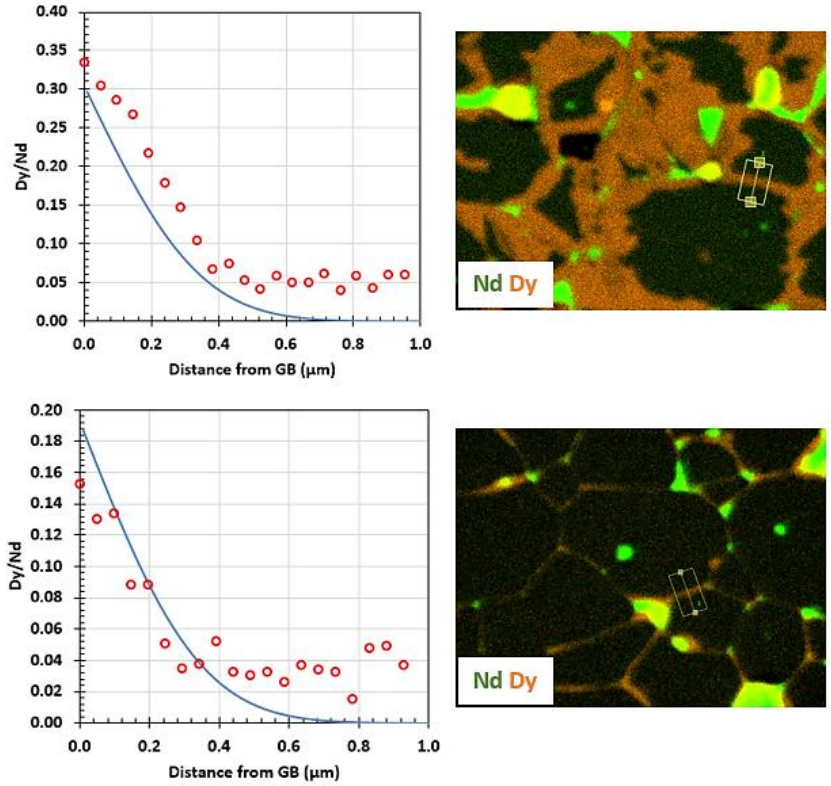


Fig. 101: Dy/Nd depletion in grain volume at 100 µm and 200 µm for the sample diffused at 870°C-3h. (Left) Measured (open symbols) and calculated (solid line) concentration profiles. (Right) SEM-EDX maps of Nd and Dy with the localization of the profile line.

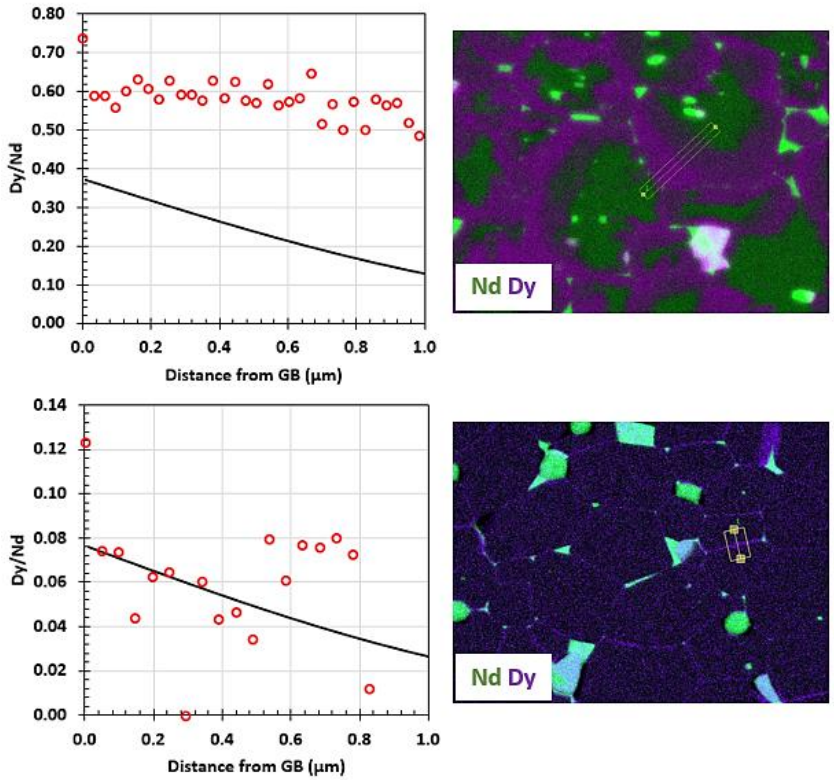


Fig. 102: Dy/Nd depletion in grain volume at 100 µm and 800 µm for the sample diffused at 920°C-12h. (Left) Measured (open symbols) and calculated (solid line) concentration profiles. (Right) SEM-EDX maps of Nd and Dy with the localization of the profile line.

V.1.3. Impact on coercivity profile

In the previous sections, the diffusion model has been implemented to estimate the Dy content in grains as a function of depth and diffusion conditions. Table 41 provides the ratio of Dy atoms over the initial Nd atoms calculated in the 1-µm-wide grain shells. The values are deduced from data of Table 39. Since the grain coercivity enhancement depends mostly on the Dy/Nd ratio, Table 41 supplies a first overview of the distribution of the coercivity improvement that could be expected in the magnet after GBDP. For instance, Loewe *et al.* [79] found that the local switching field is enhanced by 250 kA/m (≈0.31 T) with a ratio Dy/Nd equal to 0.12 in the shell (averaged over 1-µm-depth). It is worth noting that this last value is obtained for similar diffusion conditions (900°C-6h-100µm).

	100 µm	**200 µm**	**400 µm**	**800 µm**
870°C-3h	0.07 (+ 0.18 T)	0.04 (+ 0.10 T)	0.02 (+ 0.05 T)	0.00
920°C-3h	0.14 (+ 0.36 T)	0.10 (+ 0.26 T)	0.05 (+ 0.13 T)	0.01
920°C-12h	0.24 (+ 0.62 T)	0.19 (+ 0.49 T)	0.12 (+ 0.31 T)	0.05 (+ 0.13 T)

Table 41: Dy/Nd-init ratio averaged over 1-µm-thick grain shell of Dy diffused sample estimated with the Fisher model. The values between parentheses reflect the estimation of the coercivity increase due to the local Dy enrichment.

The core-shell structures disappear in the SEM analyses at a depth larger than 800 µm. Considering a Dy enrichment effective only until 800 µm, as suggested by the data of Table 41, it would tend to minimize the actual depth of the magnet for which coercivity is enhanced. Actually, several authors [79], [96] observed a local coercivity enhancement up to 2.5-3 mm from the surface in diffused samples, *i.e.* at a distance from the surface for which the Dy enrichment is not visible by SEM due to the resolution limitation. However, using STEM-EDX analysis, Loewe *et al.* [79] reported a local Dy concentration of 0.4 at.% at 10 nm from GBs located at 1.5 mm from the sample surface. This corresponds to an atomic ratio Dy/Nd-init equal to 0.03 (Nd-init corresponds to the atomic content of Nd in the $Nd_2Fe_{14}B$ phase before diffusion and is mentioned since Dy substitutes to Nd in the diffused region while the Nd in excess is rejected to GBs [80]). With this low Dy content, the coercivity enhancement is still significant (150 kA/m ≈ 0.19 T). From this data, it has been assumed here that the threshold for a grain coercivity enhancement corresponds to a minimum penetration of 10 nm in the grain with a ratio Dy/Nd-init ≈ 0.01.

Fig. 103 plots the evolution of the Dy/Nd ratio at 10 nm from the GB with the depth for the three diffusion conditions calculated with the Fisher model. According to the curves, the critical depths for coercivity enhancement are estimated to be 1, 1.5 and 2 mm for the 870°C-3h, 920°C-3h and 920°C-12h diffusion conditions, respectively.

Kim *et al.* [96] showed that Dy can still penetrate the magnet beyond this limit. Up to a depth of 3.25 mm, Dy is detected at GBs by STEM-EDX. A fine shell of 2 nm width with a content of Dy = 0.1 at.% is also formed during PDA performed at 520°C. However, as noticed in Chapter IV thanks to micromagnetic modelling, such a fine Dy shell should not be efficient enough to improve (or restore) the grain coercivity when a defect (*i.e.* a phase with low magnetocrystalline anisotropy) of 4 nm width is introduced. It has been inferred that the behavior of the magnets investigated in this study could be explained by a two-population distribution of defects affecting their coercivity. The influence of the smaller defects could be alleviated by the heat treatments while the larger ones remain harmful. Even if the larger defects have not been directly observed, this assumption is consistent with previous findings [131]. As pointed out in Chapter III, the shape of the experimental J-H curves after annealing (and without Dy diffusion) could be accounted with a low content of defective grains (< 3 %).

For this reason, it has been assumed that the inner part of thick diffused magnets (depth = 2.5 mm) studied here keeps the same coercivity as the base magnet, even if a small amount of Dy can penetrate up to the center of the samples. These elements have been considered in Table 41 that provides the basis for the demagnetization simulations exposed in the next section.

Finally, the total amount of Dy atoms that penetrate into the magnet by diffusion during the experiment has been extracted from the calculated profiles and compared to the amount of Dy initially available at the free surface. The results are indicated in Table 42 and show that, for the last diffusion condition (920°C-12h), all Dy atoms have been consumed and the initial amount is even not sufficient to lead to the theoretical profile plotted in Fig. 103. As a consequence, the coercivity enhancement predicted by the Fisher model should be overestimated for this sample.

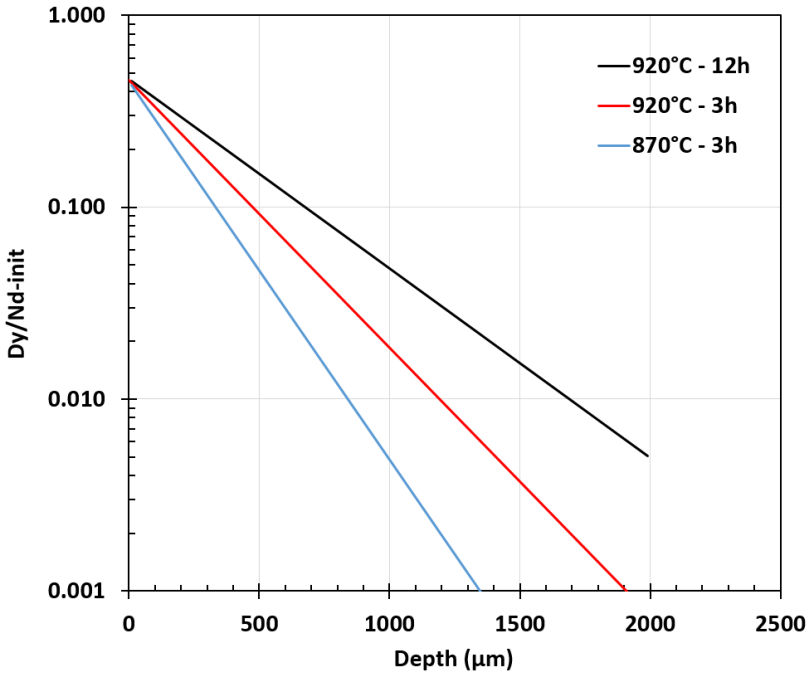


Fig. 103: Evolution of the Dy enrichment calculated at 10 nm from the grain boundary with the distance from the sample surface with the Fisher model for the three diffusion conditions.

	0-100 µm	100-200 µm	200-400 µm	400-800 µm	Total
870°C-3h	0.11	0.07	0.04	0.01	0.23
920°C-3h	0.21	0.16	0.20	0.18	0.75
920°C-12h	0.35	0.28	0.41	0.44	1.48

Table 42: Fraction of the total Dy atoms initially available at the free surface and diffused in successive slices distributed from the sample surface.

V.1.4. Diffusion of Co

Cook *et al.* [145] reported that the diffusion coefficient of Co in $Nd_2Fe_{14}B$ is two orders of magnitude higher than the diffusion coefficient of Dy at 950°C. The Fisher model has therefore been used with values of D_v and D_j 100 times higher than the values used for Dy in order to estimate the impact on the concentration profiles. The results are plotted in Fig. 104. Unlike for Dy, the concentration profile of Co is very flat and the Co/Fe ratio is low (around 1 %). Furthermore, this result highly overestimates the Co content since the calculation shows that all the available Co atoms, deposited at the free surface, should be rapidly consumed (after a few minutes at 920°C). These elements confirm that Co

should be very difficult to be detected by SEM-EDX in the diffused samples and should be quasi-homogeneously distributed into the magnet. Moreover, the influence on the Curie temperature is very low ($\Delta T_C \approx 9°C$ for Co/Fe = 1% [130]).

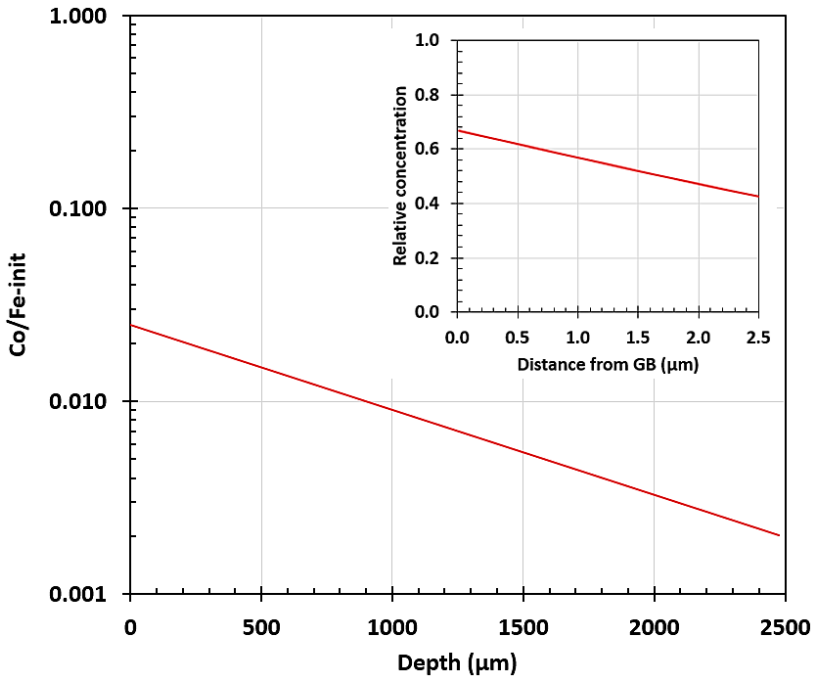


Fig. 104: Evolution of the Co enrichment calculated at 2.5 µm from the grain boundary (grain center) with the distance from the sample surface with the Fisher model for the 920°C-3h diffusion condition. (Insert) Grain concentration profile at 400 µm.

V.2. Polycrystalline model applied to Dy-diffused thick magnets

V.2.1. Description of the geometrical model

The polycrystalline finite element model is implemented in this section to quantitatively analyze the magnetic properties of Dy-diffused samples. In the following simulation cases, different arrays of cubic grains made of stacks of grain layers are considered, each grain layer exhibiting its own coercivity distribution (function of $<H_C>$ and σ_{Hc}). At the mid-plane of a given array, the first layer is assumed to have the same properties as the non-diffused material. Then, the coercivity values of the upper layers of the array are ascribed to be higher, reflecting the coercivity profile of the Dy-diffused sample. The model is assessed on its ability to describe the shape of J-H curves measured by the hysteresigraph system.

V.2.1.1. 3D-array models with graded properties

As mentioned in Chapter II (see II.5.2.4), only several thousands of grains can be described with the finite element model. Moreover, the aspect ratio of the sample (height = 5 mm, diameter = 10 mm) has to be kept in the geometrical model in order to correctly reflect the demagnetizing field effects. Considering these constraints, the model cannot reproduce simultaneously the distance along which the property profile is observed (2.5 mm) and the grain size (5 µm).

As pointed out previously, the grain size is not a relevant parameter of the model as long as the objective of the model is to deal with dipolar interactions. With a reduced number of grains compared to actual samples, the model is thus able to take into account magnetostatic interactions in a layered

sample as long as the geometrical aspect ratio remains representative of the real sample. These considerations lead to the selection of the two following polycrystalline model configurations described in Table 43:

Layer	Number of grains in layer n_x x n_y = 10 x 10 Configuration #1	Number of grains in layer n_x x n_y = 20 x 20 Configuration #2	Grain coercivity distribution parameters
1	2	4	$<\mu_0 H_c>$ = 1.6 T - σ_{Hc}= 0.2 T
2	1	2	$<\mu_0 H_c>$ = 2.0 T - σ_{Hc}= 0.1 T
3	1	2	$<\mu_0 H_c>$ = 2.2 T - σ_{Hc}= 0.1 T
4	1	2	$<\mu_0 H_c>$ = 2.4 T - σ_{Hc}= 0.1 T

Table 43: Polycrystalline model configurations for simulated magnetization reversal in Dy-diffused samples.

These 3D arrays are scaled by the number of grains (n_x x n_y in Table 43 denotes the number of grains in the 2D grid of each layer and represents a quarter of the full grid thanks to in-plane symmetries). In configuration #1, the first layer which represents the half-height of the central zone (unaffected by the Dy diffusion) consists of two sub-layers of grains of the same type. Then, each upper layer affected by the Dy diffusion is made of a one-grain-high array. This leads to a total number of grains equal to 500 for configuration #1. However, with only one grain in the layer thickness, the cascade effects are poorly described. In configuration #2, there are twice as many layers in order to improve the grain reversal pattern, leading to a total number of grains of 4000 and to a significant rise in the computation time (see Fig. 105).

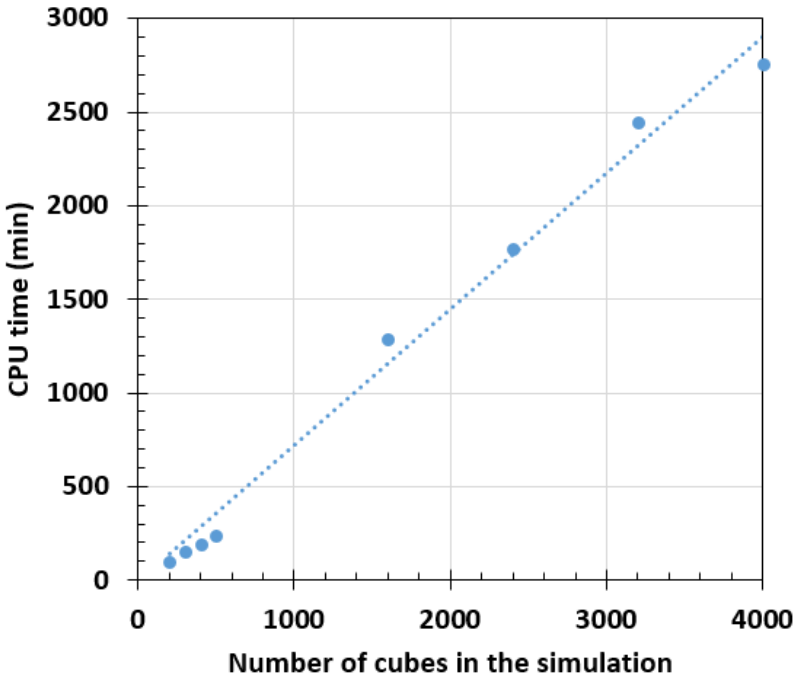


Fig. 105: Computation time as a function of the number of grains considered in the simulation.

V.2.1.2. Evolution of the geometrical model by layer removal

The simulation of the demagnetization is performed in closed-circuit and involves different runs starting from the calculation of the J-H curve of the first isolated layer (stack #1), followed by the computation of the J-H curve with the stacking of layers #1 and #2 (stack #2) and so on until the computation of the complete stack (stack #4). The Gaussian realization is performed once at the

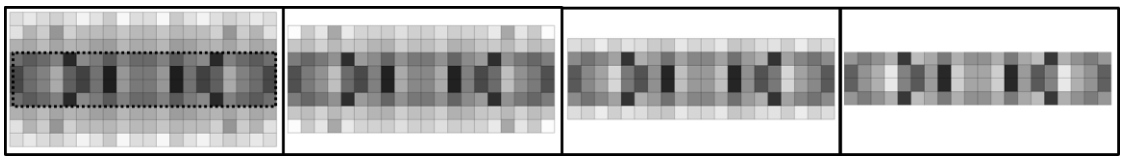
beginning of the simulation in order to ascribe the same grain coercivity distribution to a given layer during the whole sequence. This approach allows the description of the effect of a layer removal from the whole sample and the results could be compared to the magnetic measurements performed after consecutive sample polishing (see IV.2.6.2). For instance, the stack #3 simulation is representative of the magnetic measurement performed after the first polishing (up to a depth corresponding to the external layer) while the non-polished sample is described by the stack #4.

V.2.2. Results: grain reversal patterns in a graded sample

V.2.2.1. Demagnetization curves

Fig. 106 shows the grain coercivity in the graded numerical sample for configuration #1 (model with 500 grains, n_x = 10 x n_y = 10 x n_z = 5) and the evolution of the J-H curves obtained for the four stacks. It can be noticed that the J-H curves are highly stepped because of the small number of grains used in the model. More striking is the fact that the steps (*i.e.* the sudden drops in the polarization curve followed by a plateau), already observed during the demagnetization of the first stack (central zone), seem to translate to other J-H curves with an enlargement of the step width. This result reveals that the grain reversal, once initiated in the central part, tends to extend upwards to the higher coercive layers. The grain reversal in the low coercive region is however triggered with a "delay" (*i.e.* the first reversal occurs for higher fields) compared to the situation occurring in the non-diffused magnet.

This situation is emphasized by the evolution of the grain reversal pattern simulated for the whole magnet (stack #4). Four points (A-D) are selected on the J-H curve (see Fig. 107) to highlight some important stages in the demagnetization process of the graded sample. The first grains that reverse at point A are the lowest coercivity grains located in the central zone (see Fig. 108). Until point B, grain switching happens mainly in this layer with a delaying effect due to the magnetostatic "shielding" of the upper layers. After this "pivot" point B, reversal propagates easily towards the ends of the magnet (point C) and coercivity (point D) is obtained at a field much lower ($\Delta H \approx 200$ kA/m) than the one expected from the grain coercivity distribution (represented by the dashed line in Fig. 107).



stack #4 **stack #3** **stack #2** **stack #1**

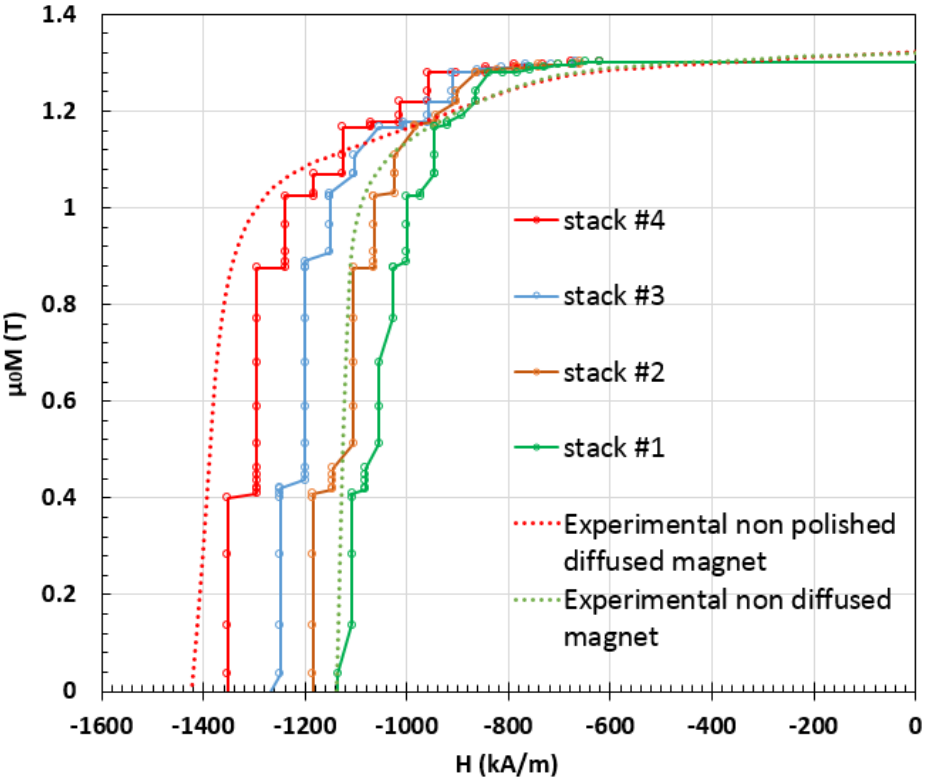


Fig. 106: Demagnetization curves simulated for the four stacks with magnetic properties given in Table 43 (configuration #1). The distribution of grain coercivity is illustrated by the XZ patterns in gray scale (black = lower values, white = higher values) for each stack.

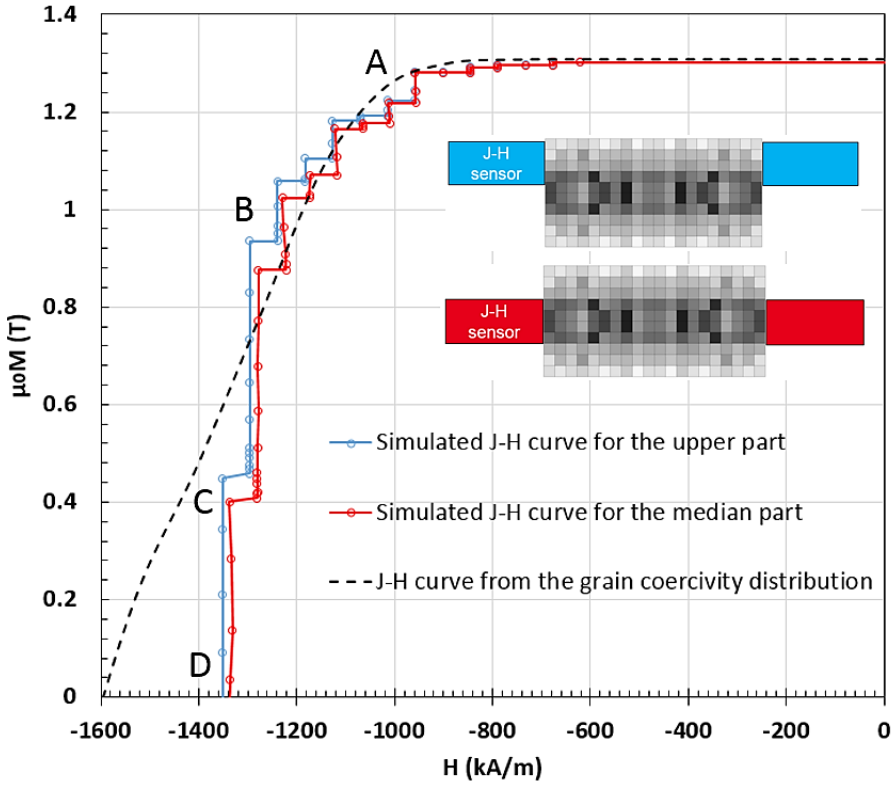


Fig. 107: Demagnetization curves simulated for stack #4 with magnetics properties given in Table 43 and for two positions of the pick-up coil relative to the sample. The dashed line represents the expected J-H curve with no magnetostatic interactions.

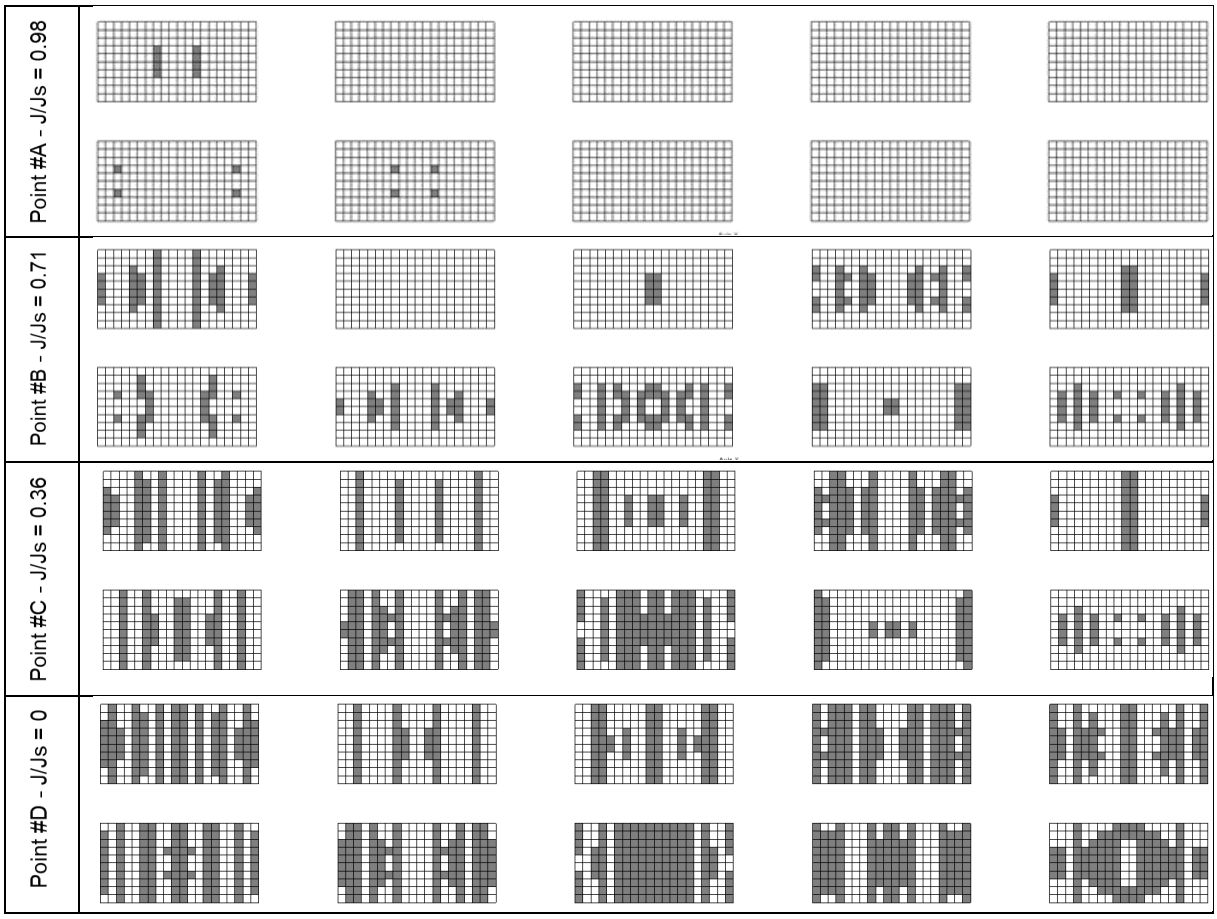


Fig. 108: Grain reversal patterns for the four selected points of the J-H curve labelled in Fig. 107.

This behavior is very similar to the case of the duplex magnet described in Chapter III that constituted a simple model of graded magnets. However, in the present case, the J-H curves that have been recorded along the sample height (simulated for stack #4) do not exhibit a significant shift (see Fig. 107). This comes from the large size of the sensor used for the J-H recording, especially the height along which the fields are integrated, which is equal to the half of the sample thickness (as in the real situation). The values of J and H plotted on the curves are thus smoothed along the axial direction. This fact is confirmed by direct magnetic measurements performed with the hysteresigraph system on the diffused samples. Actually, the pick-up coil has been displaced axially along the magnet axis without observing an evolution of the experimental J-H curve shape.

The calculation with more grains per layer allows checking that the results obtained with configuration #1 are not affected by some numerical artefacts due to the lower number of grains per layer. The results for configuration #2 are plotted in Fig. 109 and confirm the previous trend, *i.e.* the pronounced influence of the lowest coercive layer on the shape of the whole sample J-H curve.

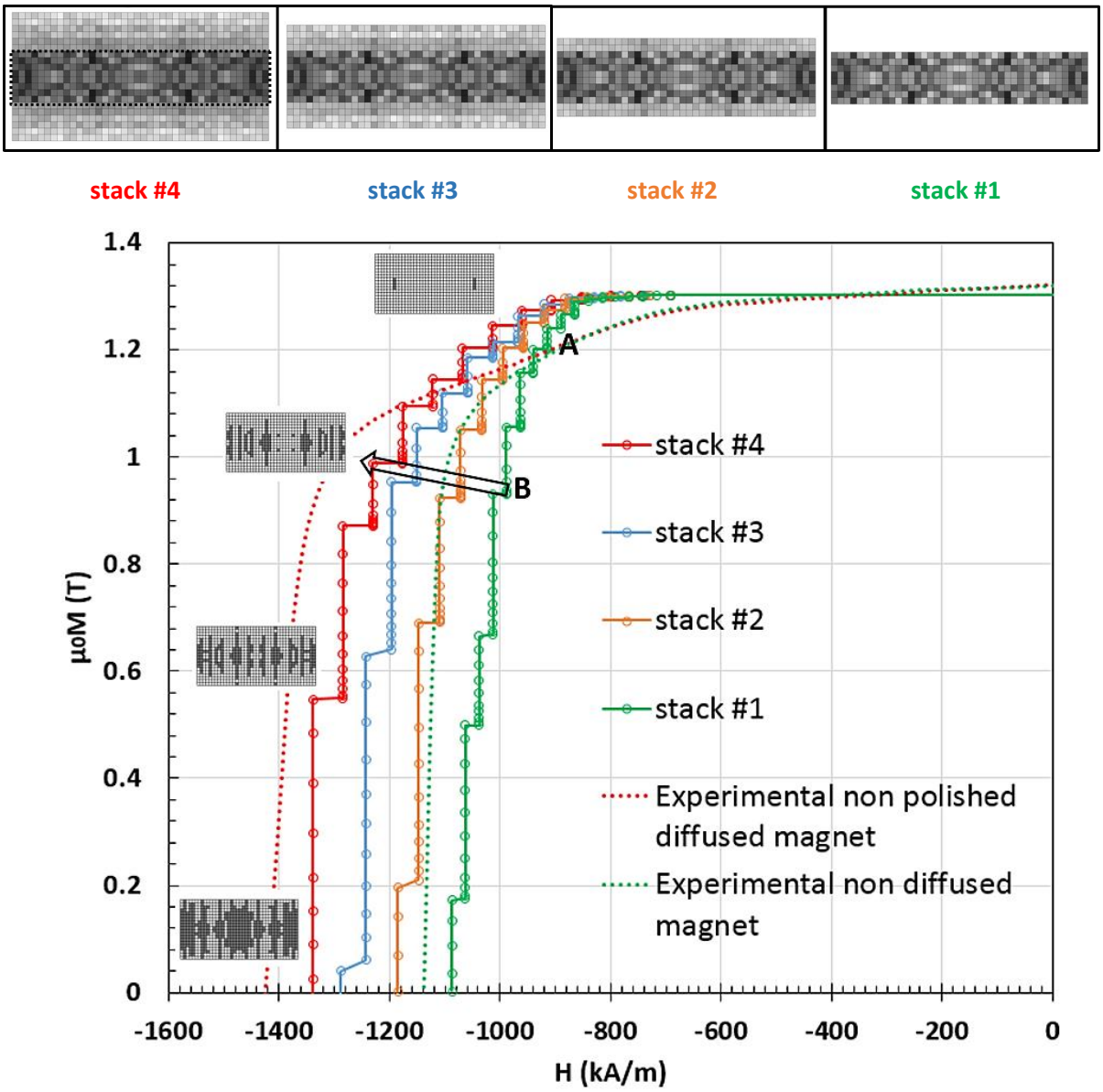


Fig. 109: Demagnetization curves simulated for the four stacks with magnetics properties given in Table 43 (configuration #2). The distribution of grain coercivity is illustrated by the XZ patterns in gray scale (black = lower values, white = higher values). The grain reversal patterns at selected points of the J-H curve are also given.

V.2.2.1. Comparison with results obtained for 920°C-3h diffusion

The simulation of the J-H curve for stack #4 compares well with the experimental data obtained on the whole magnet sample diffused at 920°C for 3h. Fig. 109 reports the experimental demagnetization curves measured for the non-polished sample after GBDP and the base sample measured before GBDP. These two extreme curves are actually the upper and lower bounds for the set of J-H curves measured after successive polishing runs. Even if the curves do not superpose perfectly with the simulation (since no fitting of grain coercivity distribution parameters has been performed), the main features of the experimental curves are reasonably well reproduced by the model. First, the total increment in the magnet coercive field after diffusion is correctly accounted for by the simulation. Then, the shape of the experimental curve after GBDP is also well reproduced, especially the decomposition of the J-H curve into three quasi-linear regions characterized by increasing slopes (flat region 1 from 0 to 800 kA/m, region 2 with slow linear decrease in J followed region 3 with a rapid drop of J). Regarding the

intermediate region, the simulation reproduces the shift towards higher field values of the connection point between regions 2 and 3, as observed experimentally on the polished sample.

This last result is better illustrated by the arrow drawn in Fig. 109 showing the evolution of point B. This latter is representative of the transition from the stage for which grain reversal in the central magnet is delayed to the stage for which cascade reversal propagates to upper layers. The slope in this transition region evolves between the base magnet and the diffused thick magnet curve as a combination of the following features:

- The transition between regions 1 and 2, labelled by the point A, occurs at the same field value whatever the stack. The critical field values depend on low coercive grains in the central magnet.
- The transition between regions 2 and 3 shifts towards higher field values as a result of the delaying effect.
- The height of the polarization drops occurring in region 2 tends to decrease as the weight of the central region is reduced (*i.e.* as the sample becomes thicker).

In the simulations, this combination leads to a J-H curve for stack #4 that exhibits a poor squareness ratio, as the one measured for the whole magnet sample.

V.2.2.2. Correlation with the experimental residual induction map

Residual induction mapping has been performed on the sample after GBDP (without polishing) with the Hall probe in three different states: (i) the remanent state after saturation, (ii) a partial demagnetization state obtained before the second knee of the J-H curve and (iii) the state achieved at the coercive field. The top face of the sample has been scanned and the results are given in Fig. 110. Before reaching the second knee (point 2 for which $J/J_S = 0.82$), the residual induction at the top surface ($B_{z,moy}$ = -356 mT) is very close to the one obtained at the remanent state (point 1 for which $B_{z,moy}$ = -366 mT), confirming that demagnetization occurs mainly in the magnet core. The recoil curve performed for this intermediate value clearly shows that an irreversible demagnetization has occurred in the magnet for this applied field value (≈ 1100 kA/m), although this cannot be observed on the residual induction map.

When the coercive field is reached (point 3 for which $J/J_S=0$), mapping reveals large heterogeneities in the sample magnetization that are consistent with the appearance of clusters. The simulated grain reversal patterns in two particular XY planes (*i.e.* the top plane and the plane located at the limit of the enhanced coercivity zone) are plotted in Fig. 111 for comparison. The correlation of the model prediction with the experimental data confirms that the simulation correctly describes the main features of the demagnetization curve of Dy-diffused magnets.

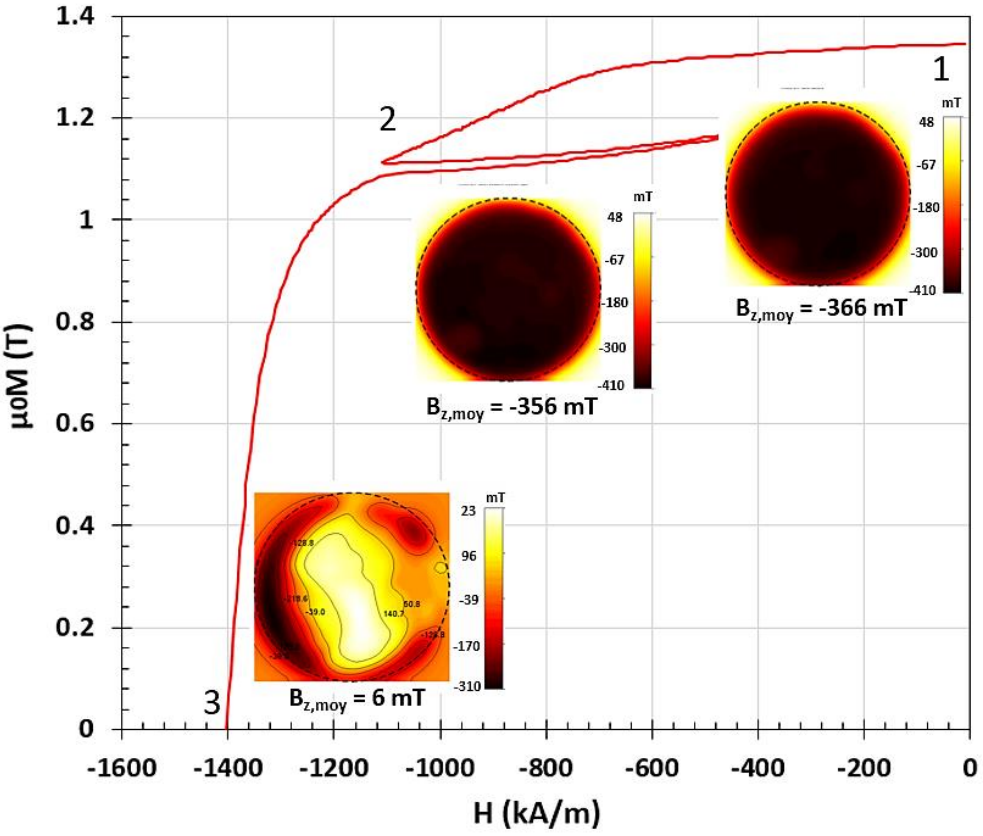


Fig. 110: Residual induction map at the top of a Dy-diffused sample at three selected stages (1-remanent state, 2-partial demagnetization before recoil, 3-coercivity state) .$B_{z,moy}$ denotes the averaged value of the residual induction measured in the scanned plane (400 µm over the sample).

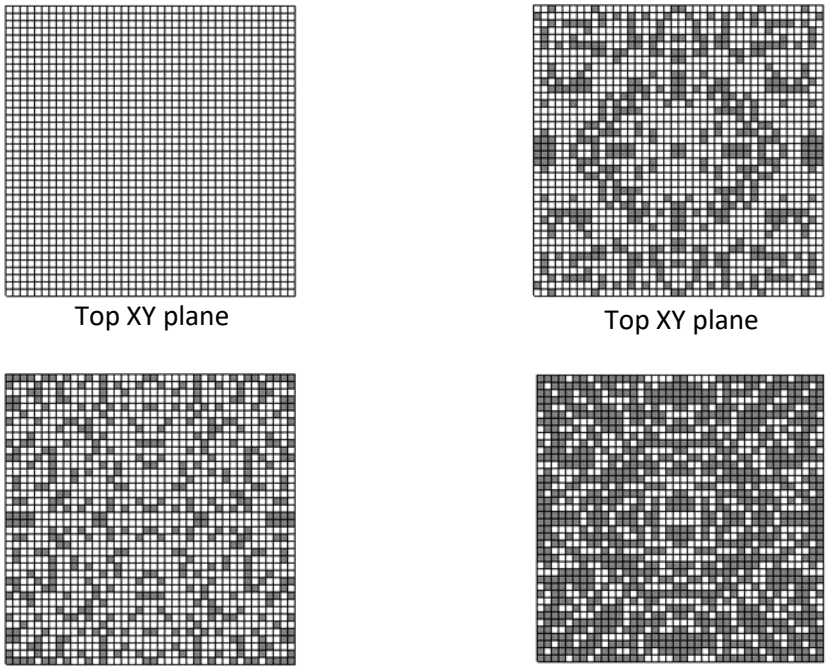


Fig. 111: Grain reversal patterns simulated for stack #4 and for two selected points of the J-H curve from Fig. 110 (XY planes at the top surface and at the interface with the non-enhanced coercivity zone).

V.2.2.3. Comparison with magnetic property gradient obtained after polishing

The measurements of the J-H curves after successive polishing runs, performed on the same diffused sample, give a valuable insight into the coercivity profile resulting from Dy diffusion and provide a basis to establish some correlations with microstructural observations. The question arises about the agreement between the coercivity value measured after material removal (on thin samples) and the local coercivity value (*i.e.* the coercivity of the top plane after polishing). Since this latter data cannot be directly determined, this section aims at inferring the gradient of coercive field that would be consistent with the magnetic properties measured on polished samples.

The first line of Table 44 gives the coercive field values of each layer considered separately, *i.e.* the mean grain coercivity $<\mu_0 H_c>$ used as an input data for the simulation. Then, the coercive field values calculated from the contribution of each layer considering their respective coercive field distribution weighted according to their volume are listed. This pondered value would stand for the coercive field of the corresponding stack without any magnetostatic interactions (between grains of the same layer and between layers). Finally, the values obtained by simulation for each stack taking into account magnetostatic interactions are reported. The experimental values are also mentioned in Table 44, but they should be considered as indicative values, since no fitting procedure has been performed. Furthermore, since the layer thickness ratios do not coincide perfectly with the simulation, the reported values in the last line in Table 44 have been obtained by interpolation of experimental data.

Stack	Stack #1	Stack #2	Stack #3	Stack #4
Coercivity of the external layer of the stack (kA/m)	1273 (1.60 T)	1591 (2.00 T)	1750 (2.20 T)	1910 (2.40 T)
Coercivity of the stack without magnetostatic interactions (kA/m)	1273 (1.60 T)	1380 (1.73 T)	1500 (1.88 T)	1591 (2.00 T)
Coercivity of the stack with magnetostatic interactions for configuration #1 (kA/m)	1115 (1.40 T)	1186 (1.49 T)	1248 (1.57 T)	1351 (1.70 T)
Coercivity of the stack with magnetostatic interactions for configuration #2 (kA/m)	1087 (1.37 T)	1185 (1.49 T)	1288 (1.62 T)	1335 (1.68 T)
Coercivity measured for the polished sample (kA/m)	1137 (1.43 T)	1280 (1.61 T)	1340 (1.68 T)	1435 (1.80 T)

Table 44: Coercivity values for the different stacks.

Table 44 highlights the fact that the values of the local coercivity at a given height, estimated by the value of the grain coercivity ascribed to this layer, is much higher than the coercivity of the stack considered as a whole. Logically, the difference rises with the spread of magnetic properties along the stack and reaches a maximum of about 500 kA/m for stack #4. The weight combination of layers accounts for 50-60 % of this difference whereas 40-50 % comes from magnetostatic interactions.

Finally, it can be reasonably assumed that the coercive field of the material located beneath the surface of the Dy-diffused sample, until a depth of 1 mm (difference between stack #4 and stack #3), should be much higher than the apparent value measured on the whole sample, the difference being predicted by the model to be of the order of 300-400 kA/m.

V.2.3. Results for other diffusion conditions

According to the discussion about the Dy concentration profile after GBDP and its influence on the local coercivity, the following set of input data has been established for the simulation runs. The sample geometry and slicing remain the same for the three diffusion conditions. The only variation concerns the coercivity ascribed to the different layers as indicated in Table 45.

Layer	Grain coercivity distribution parameters 920°C-3h	Grain coercivity distribution parameters 920°C-12h	Grain coercivity distribution parameters 870°C-3h
1 (2)	$<\mu_0 H_c>$ = 1.6 T - σ_{Hc}= 0.2 T	$<\mu_0 H_c>$ = 1.6 T - σ_{Hc}= 0.2 T	$<\mu_0 H_c>$ = 1.6 T - σ_{Hc}= 0.2 T
2 (1)	$<\mu_0 H_c>$ = 2.0 T - σ_{Hc}= 0.1 T	$<\mu_0 H_c>$ = 2.2 T - σ_{Hc}= 0.1 T	$<\mu_0 H_c>$ = 1.6 T - σ_{Hc}= 0.1 T
3 (1)	$<\mu_0 H_c>$ = 2.2 T - σ_{Hc}= 0.1 T	$<\mu_0 H_c>$ = 2.4 T - σ_{Hc}= 0.1 T	$<\mu_0 H_c>$ = 2.0 T - σ_{Hc}= 0.1 T
4 (1)	$<\mu_0 H_c>$ = 2.4 T - σ_{Hc}= 0.1 T	$<\mu_0 H_c>$ = 2.6 T - σ_{Hc}= 0.1 T	$<\mu_0 H_c>$ = 2.2 T - σ_{Hc}= 0.1 T

Table 45: Polycrystalline model configurations for simulated magnetization reversal in Dy-diffused samples corresponding to the three experimental diffusion conditions (n_x x n_y = 10 x 10).

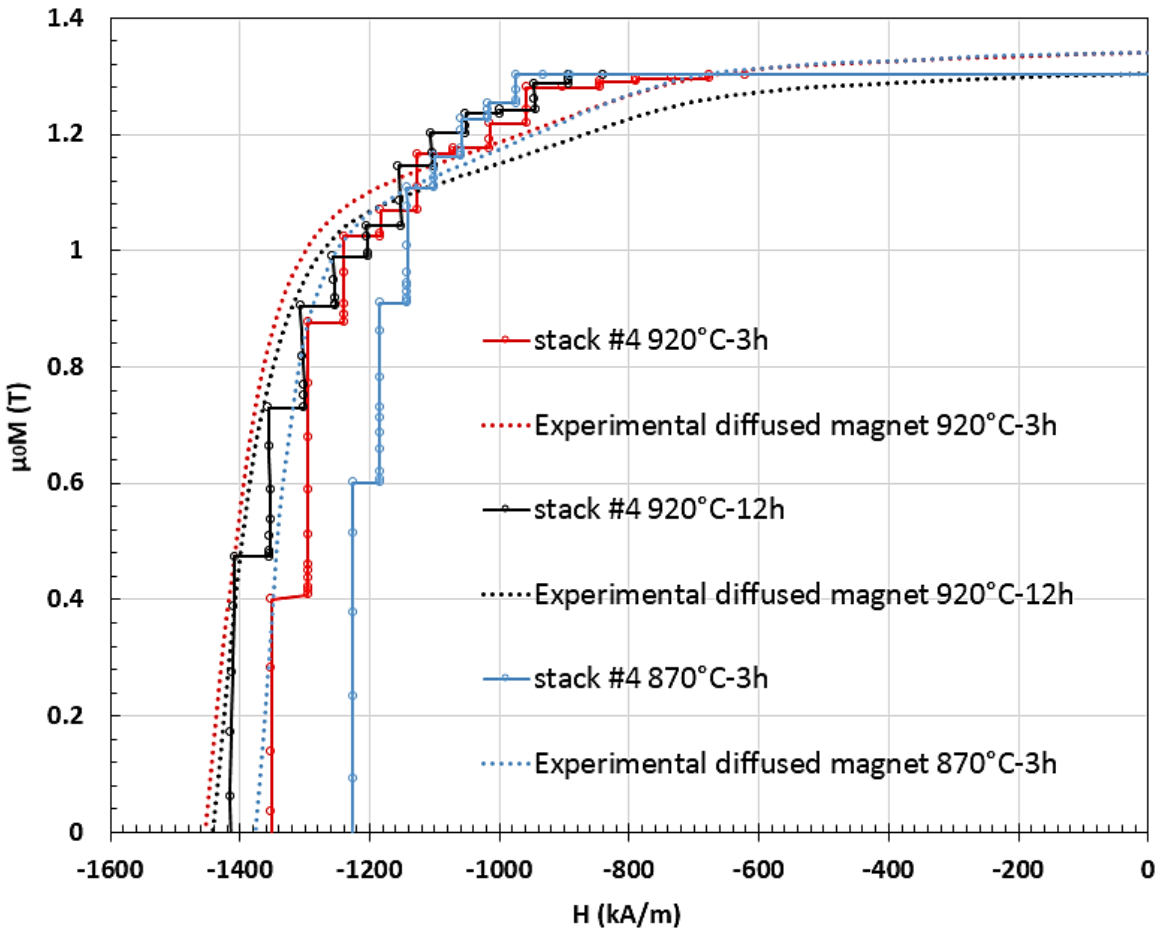


Fig. 112: Demagnetization curves obtained by simulation for the input data reported in Table 45.

The simulated demagnetization curves are plotted in Fig. 112. The J-H curves for 920°C-3h and 12h are found to be close exhibiting a quasi-superposition until the point B and a small difference in the coercive field values (≈60 kA/m). This gap is more important than for the experimental curves (see dotted lines in Fig. 112 taken from IV.2.2). This can be explained by the fact that the simulation poorly takes into account the Dy saturation effect. Actually, it has been estimated that all the available Dy should penetrate the sample after only 5 h of diffusion treatment at 920°C. This limitation could explain why the experimental J-H curves for the 920°C-3h and 920°C-12h cases are very close. The simulated J-H curve for 870°C-3h is as expected shifted towards lower field values and the difference with the result at 920°C ($\Delta H \approx 100$ kA/m) is consistent with the experimental results ($\Delta H \approx 70$ kA/m, see IV.2.3).

V.3. Conclusions

GBDP performed with Dy-Co alloy improves coercivity only over a few millimeters. The limitation comes from the consumption of the heavy rare-earth elements in the grain volume. Actually, at 920°C more than 75 % of the available Dy atoms diffuse in a thin layer (800-µm-thick) localized beneath the surface where the diffusion alloy is deposited. The increase of diffusion time at 920°C leads to a Dy saturation effect without any observed improvement in coercivity. The reduction of the diffusion temperature by 50°C decreases the penetration depth and requires longer diffusion time to complete the thermal treatment. Finally, it can be stated that the optimal diffusion temperature is around 900-920°C, confirming the previous study of Loewe [94] performed with different precursor alloys.

The ideal case for Dy diffusion would be achieved with a deep penetration of the diffusing species along GBs, combined with a small consumption of Dy by grains, so that Dy remains localized in thin shells of 10 to 100 nm width at the grain rim. This will ensure that the Dy feeding could be low (0.8 % wt.) and efficient for coercivity enhancement, even for thick magnets. The close examination of [Eq. 38] shows that this optimal case corresponds to large values of the factor β. Ascribing the lateral diffusion inside grains to be of the order of the GB thickness (a = 10 nm), this involves fulfillment of the following condition: $\sqrt{D_v t} \approx a$. Then, the Dy concentration near GBs would be homogeneous over large depths (d > 1 mm) if the argument of the exponential term of [Eq. 38] remained lower than 1, *i.e.* if the ratio of the diffusion coefficients satisfied: $D_j/D_v > [d/a]^2$. With the selected target, this ratio should be $D_j/D_v > 10^{10}$. The values of D_j and D_v considered in the Fisher model, and consistent with the experimental results, lead to a ratio three orders of magnitude lower than the ideal value, explaining the poor efficiency of GBDP applied to very thick magnets.

Several authors showed that the enrichment of GBs by Nd atoms rejected from the matrix after Dy substitution is also an efficient way to improve the grain coercivity. Besides the anisotropy increase in the shells coming from the Dy atoms, the Nd layer formed at GBs tends to enhance grain decoupling. The chemistry of the GB phases after Dy diffusion and its evolution during post-diffusion annealing should be investigated in more detail. This could be helpful for the selection of alloying elements and for defining new strategies to improve diffusion at GBs.

The heterogeneous distribution of Dy in the microstructure has a deleterious impact on the resistance to demagnetization of the magnet. The polycrystalline model provides a better understanding of the grain reversal sequence, starting in graded magnets from the less coercive grains and propagating towards upper layers via magnetostatic interactions. When the coercivity gradient is large, as in the 5-mm-thick magnets studied in this work, the coercivity of the whole magnet, measured in closed-circuit, is 100-200 kA/m lower than the value expected without considering magnetostatic interactions. This result means that a specific dimensioning approach is required when using thick Dy-diffused magnets in electrical devices [146].

Conclusions and prospects

The objective of this thesis was to gain a better understanding of coercivity in Nd-Fe-B sintered magnets by coupling experimental and numerical approaches.

It is widely accepted that $Nd_2Fe_{14}B$ gains are mostly exchange-decoupled and that magnetization reversal occurs via discrete switching. However, magnetostatic interactions between grains also play an important role in the demagnetization process of such materials. The first part of the work was focused on the study of demagnetizing field effects in Nd-Fe-B sintered magnets. Two different experimental configurations (open- and closed-circuit) used for coercivity measurement have been compared experimentally and numerically. First of all, it has been shown that the usual demagnetizing field correction required for open-circuit measurements is not applicable to hard magnets. A new expression for the demagnetization field has been established with the help of the cavity field model. Experimentally, the hysteresis loops measured in open-circuit showed a coercivity reduction compared to those measured in closed-circuit. According to the cavity field model, it has been predicted that magnetization reversal in closed-circuit has a higher collective character than in open-circuit. The demagnetization process is strongly affected by the measurement type. Moreover, a finite element polycrystalline model has been implemented to assess the differences in the demagnetizing field effects for both configurations. The simulated difference in coercivity was in good agreement with the experimental one. Furthermore, the simulated reversal patterns were also consistent with the previous experimental findings: they showed large clusters of reversed grains in the closed-circuit condition whereas columns of reversed grains were found in open-circuit.

The occurrence of collective effects during demagnetization of Nd-Fe-B sintered magnets has been predicted by the cavity field model. However, further experimental characterization of these effects is required to complete the study. The SENIS Hall probe used in this work enabled the indirect observation of these collective effects (clusters of reversed grains) but a direct evaluation could be performed using other techniques. For example, magnetic force microscopy (MFM) and magneto-optical Kerr effect (MOKE) microscopy are powerful tools that may serve in the better understanding of magnetization reversal. The greater importance of collective effects during reversal in closed-circuit compared to open-circuit could be quantitatively assessed using these imaging techniques. Moreover, computations with FEMME and Flux3D software could be coupled to consider both exchange and magnetostatic interactions and thus further improve the accuracy of the developed polycrystalline model. These suggested improvements would enable the definition of guidelines for experimenters in the comparison of the coercive field values measured in open- and closed-circuit conditions.

The second part of the work concerned the experimental and computational study of magnetization reversal in Dy-Co diffused Nd-Fe-B sintered magnets. The main purpose here was to understand the shape of the demagnetization curves measured after Dy diffusion that showed deteriorated rectangularity. Experimentally, it has been observed that the intermetallic compound $Dy_{63}Co_{37}$ is easier to grind and leads to more efficient diffusion compared to the eutectic alloy $Dy_{66}Co_{34}$. An experimental parametric study has been carried out to determine the influence of diffusion time, temperature and of post-diffusion annealing on coercivity. The latter has shown lower sensitivity to the post-diffusion annealing temperature compared to the post-sintering annealing one. The typical core-shell microstructure developed in diffusion treated magnets was characterized by SEM-EDX for three different diffusion conditions and at several depths. Complementary magnetic measurements were also performed to establish the corresponding coercivity profiles. In addition, micromagnetic simulations helped in determining the influence of some microstructural features on magnetization reversal, in a simple core-shell model. A defect has been introduced in the model to study its impact

on grain reversal. The Dy shell enables coercivity enhancement since it delays magnetization reversal from a grain to its neighbors. The nature of the grain boundary phase determines the shape of the simulated demagnetization curves. For instance, the decreased rectangularity after Dy diffusion and after subsequent annealing has been explained by the presence of a non-magnetic grain boundary phase that decouples grains and leads to the observed step-like reversal. Consequently, the simulations reproduced well the shape of the experimentally measured demagnetization curves, but also the experimental gains in coercivity. Finally, magnetization reversal has been simulated in the case of magnets with coercivity gradient (*i.e.* diffused in the three different conditions) using the polycrystalline model. The Fisher diffusion model along with the SEM-EDX analyses provided the switching field values ascribed to each layer in the model. The simulated demagnetization curves were also in good agreement with the experimental ones and their shape was explained by the pronounced influence of the layer with lowest coercivity.

The grain boundary phase controls coercive properties of Nd-Fe-B sintered magnets. Further fine and structural characterization such as transmission electron microscopy and 3D atom probe tomography could be used to study the evolution of the chemical composition at grain boundaries after each fabrication step (particularly after post-diffusion annealing). The interactions between the additional elements (Cu, Al and Co) and Dy could be further investigated. This could help in the improvement of diffusion along grain boundaries, rather than in the volume of $Nd_2Fe_{14}B$ grains. In addition, the impact of Co on the corrosion resistance of Dy-Co diffused magnets could be assessed. Concerning simulations, further calculations could be performed using the polycrystalline model with some microstructural heterogeneities (abnormal grain growth, soft phases). Furthermore, the grain boundary diffusion process performed on 5-mm-thick Nd-Fe-B sintered magnets led to high coercivity gradients within the microstructure and this heterogeneous distribution of Dy had a bad impact on the magnet's coercivity. The same study could therefore be performed on thinner magnets with a homogeneous distribution of Dy to compare the shape of demagnetization curves. Alternatively, the powder blending method with Dy-Co and Nd-Fe-B powders is also of interest but requires an excellent and simultaneous control of the sintering and diffusion heat treatments.

References

[1] M. Sagawa, S. Fujimura, N. Togawa, H. Yamamoto, and Y. Matsuura, "New material for permanent magnets on a base of Nd and Fe," *J. Appl. Phys.*, vol. 55, no. 6, pp. 2083–2087, Mar. 1984.

[2] J. J. Croat, J. F. Herbst, R. W. Lee, and F. E. Pinkerton, "High-energy product Nd-Fe-B permanent magnets," *Appl. Phys. Lett.*, vol. 44, no. 1, pp. 148–149, Jan. 1984.

[3] J. J. Croat, J. F. Herbst, R. W. Lee, and F. E. Pinkerton, "Pr-Fe and Nd-Fe-based materials: A new class of high-performance permanent magnets (invited)," *J. Appl. Phys.*, vol. 55, no. 6, pp. 2078–2082, Mar. 1984.

[4] O. Gutfleisch, M. A. Willard, E. Brück, C. H. Chen, S. G. Sankar, and J. P. Liu, "Magnetic materials and devices for the 21st century: stronger, lighter, and more energy efficient," *Adv. Mater.*, vol. 23, no. 7, pp. 821–842, Feb. 2011.

[5] H. Sepehri-Amin, S. Hirosawa, and K. Hono, "Advances in Nd-Fe-B Based Permanent Magnets," in *Handbook of Magnetic Materials*, vol. 27, Elsevier, 2018, pp. 269–372.

[6] T. G. Woodcock *et al.*, "Understanding the microstructure and coercivity of high performance NdFeB-based magnets," *Scr. Mater.*, vol. 67, no. 6, pp. 536–541, Sep. 2012.

[7] F. Vial, F. Joly, E. Nevalainen, M. Sagawa, K. Hiraga, and K. T. Park, "Improvement of coercivity of sintered NdFeB permanent magnets by heat treatment," *J. Magn. Magn. Mater.*, vol. 242, pp. 1329–1334, 2002.

[8] Y. Shinba, T. J. Konno, K. Ishikawa, K. Hiraga, and M. Sagawa, "Transmission electron microscopy study on Nd-rich phase and grain boundary structure of Nd–Fe–B sintered magnets," *J. Appl. Phys.*, vol. 97, no. 5, p. 053504, Mar. 2005.

[9] K. T. Park and M. Sagawa, "Effect of metal-coating and consecutive heat treatment on coercivity of thin Nd-Fe-B sintered magnets," *16th Int Workshop Rare-Earth Magn. Their Appl.*, 2000.

[10] J. M. D. Coey, *Rare-earth iron permanent magnets*. Clarendon Press, 1996.

[11] S. Sugimoto, "Current status and recent topics of rare-earth permanent magnets," *J. Phys. Appl. Phys.*, vol. 44, no. 6, p. 064001, Feb. 2011.

[12] F. Jimenez-Villacorta and L. H. Lewis, *Nanomagnetism*. One Central Press Manchester, UK, 2014.

[13] O. Fruchart, "Lecture notes on Nanomagnetism," Ecole Doctorale de Physique de Grenoble, 2017.

[14] S. Chikazumi, C. D. Graham, and S. Chikazumi, *Physics of ferromagnetism*, 2nd ed. Oxford ; New York: Oxford University Press, 2009.

[15] J. M. D. Coey, "Hard magnetic materials: A perspective," *IEEE Trans. Magn.*, vol. 47, no. 12, pp. 4671–4681, 2011.

[16] S. Constantinides, "The demand for rare earth materials in permanent magnets," in *51st Annual Conference of Metallurgists*, 2012, vol. 7546.

[17] E. C. Stoner and E. P. Wohlfarth, "A mechanism of magnetic hysteresis in heterogeneous alloys," *Philos. Trans. R. Soc. Lond. Math. Phys. Eng. Sci.*, vol. 240, no. 826, pp. 599–642, May 1948.

[18] G. Ciuta, "Une étude expérimentale de la coercivité des aimants NdFeB," Université de Grenoble, 2013.

[19] W. F. Brown Jr, "Virtues and weaknesses of the domain concept," *Rev. Mod. Phys.*, vol. 17, no. 1, p. 15, 1945.

[20] K. Hono and H. Sepehri-Amin, "Strategy for high-coercivity Nd–Fe–B magnets," *Scr. Mater.*, vol. 67, no. 6, pp. 530–535, Sep. 2012.

[21] J. F. Herbst, "R2-Fe14-B materials: intrinsic properties and technological aspects," *Rev. Mod. Phys.*, vol. 63, no. 4, p. 819, 1991.

[22] D. Givord, H. S. Li, J. M. Moreau, R. P. De La Bâthie, and E. D. T. De Lacheisserie, "Structural and magnetic properties in R2Fe14B compounds," *Phys. B C*, vol. 130, no. 1–3, pp. 323–326, 1985.

[23] M. Fähnle, K. Hummler, M. Liebs, and T. Beuerle, "Ab initio electron theory for hard-magnetic rare-earth-transition-metal intermetallics," *Appl. Phys. A*, vol. 57, no. 1, pp. 67–76, 1993.

[24] J. M. . Coey, *Magnetism and magnetic materials*. Cambridge: Cambridge University Press, 2010.
[25] W. Mo, L. Zhang, Q. Liu, A. Shan, J. Wu, and M. Komuro, “Dependence of the crystal structure of the Nd-rich phase on oxygen content in an Nd–Fe–B sintered magnet,” *Scr. Mater.*, vol. 59, no. 2, pp. 179–182, Jul. 2008.
[26] T. G. Woodcock and O. Gutfleisch, “Multi-phase EBSD mapping and local texture analysis in NdFeB sintered magnets,” *Acta Mater.*, vol. 59, no. 3, pp. 1026–1036, Feb. 2011.
[27] H. Sepehri-Amin, T. Ohkubo, T. Shima, and K. Hono, “Grain boundary and interface chemistry of an Nd–Fe–B-based sintered magnet,” *Acta Mater.*, vol. 60, no. 3, pp. 819–830, Feb. 2012.
[28] O. Gutfleisch, “Controlling the properties of high energy density permanent magnetic materials by different processing routes,” *J. Phys. Appl. Phys.*, vol. 33, no. 17, p. R157, 2000.
[29] G. Hrkac *et al.*, “The role of local anisotropy profiles at grain boundaries on the coercivity of Nd2Fe14B magnets,” *Appl. Phys. Lett.*, vol. 97, no. 23, p. 232511, Dec. 2010.
[30] G. Hrkac *et al.*, “Impact of different Nd-rich crystal-phases on the coercivity of Nd–Fe–B grain ensembles,” *Scr. Mater.*, vol. 70, pp. 35–38, Jan. 2014.
[31] T. T. Sasaki, T. Ohkubo, and K. Hono, “Structure and chemical compositions of the grain boundary phase in Nd-Fe-B sintered magnets,” *Acta Mater.*, vol. 115, pp. 269–277, Aug. 2016.
[32] G. A. Zickler, J. Fidler, J. Bernardi, T. Schrefl, and A. Asali, “A combined TEM/STEM and micromagnetic study of the anisotropic nature of grain boundaries and coercivity in Nd-Fe-B magnets,” *Adv. Mater. Sci. Eng.*, vol. 2017, pp. 1–12, 2017.
[33] H. Sepehri-Amin, Y. Une, T. Ohkubo, K. Hono, and M. Sagawa, “Microstructure of fine-grained Nd–Fe–B sintered magnets with high coercivity,” *Scr. Mater.*, vol. 65, no. 5, pp. 396–399, Sep. 2011.
[34] M. Sagawa, S. Hayashi, and K. Isogai, “The ultimate production technology of Nd-Fe-B sintered magnets,” presented at the REPM 2016, Darmstadt, 2016.
[35] R. Ramesh and K. Srikrishna, “Magnetization reversal in nucleation controlled magnets. I. Theory,” *J. Appl. Phys.*, vol. 64, no. 11, pp. 6406–6415, Dec. 1988.
[36] S. Bance *et al.*, “Grain-size dependent demagnetizing factors in permanent magnets,” *J. Appl. Phys.*, vol. 116, no. 23, p. 233903, Dec. 2014.
[37] H. Okamoto, “Supplemental Literature Review of Binary Phase Diagrams: Al-Mg, Bi-Sr, Ce-Cu, Co-Nd, Cu-Nd, Dy-Pb, Fe-Nb, Nd-Pb, Pb-Pr, Pb-Tb, Pd-Sb, and Si-W,” *J. Phase Equilibria Diffus.*, vol. 36, no. 2, pp. 183–195, 2015.
[38] W. F. Li, T. Ohkubo, T. Akiya, H. Kato, and K. Hono, “The role of Cu addition in the coercivity enhancement of sintered Nd-Fe-B permanent magnets,” *J. Mater. Res.*, vol. 24, no. 02, pp. 413–420, Feb. 2009.
[39] S. Nishio, S. Sugimoto, R. Goto, M. Matsuura, and N. Tezuka, “Effect of Cu Addition on the Phase Equilibria in Nd-Fe-B Sintered Magnets,” *Mater. Trans.*, vol. 50, no. 4, pp. 723–726, 2009.
[40] T.-H. Kim, S.-R. Lee, S. Namkumg, and T.-S. Jang, “A study on the Nd-rich phase evolution in the Nd–Fe–B sintered magnet and its mechanism during post-sintering annealing,” *J. Alloys Compd.*, vol. 537, pp. 261–268, Oct. 2012.
[41] J. Strzeszewski, G. C. Hadjipanayis, and A. S. Kim, “The effect of Al substitution on the coercivity of Nd-Fe-B magnets,” *J. Appl. Phys.*, vol. 64, no. 10, pp. 5568–5570, Nov. 1988.
[42] K. G. Knoch, G. Schneider, J. Fidler, E. T. Henig, and H. Kronmuller, “Al-doped Nd-Fe-B permanent magnets: wetting and microstructural investigations,” *IEEE Trans. Magn.*, vol. 25, no. 5, pp. 3426–3428, Sep. 1989.
[43] R. . Mottram, A. . Williams, and I. . Harris, “Blending additions of aluminium and cobalt to Nd16Fe76B8 milled powder to produce sintered magnets,” *J. Magn. Magn. Mater.*, vol. 222, no. 3, pp. 305–313, Dec. 2000.
[44] G. Sadullahoğlu, B. Altuncevahir, and A. Okan Addemir, “Effect of intergranular phase segregation on magnetic properties of NdFeB magnet,” *Electron. Mater. Lett.*, vol. 10, no. 1, pp. 153–157, Jan. 2014.

[45] R. . Mottram, A. . Williams, and I. . Harris, “Blending additions of cobalt to Nd16Fe76B8 milled powder to produce sintered magnets,” *J. Magn. Magn. Mater.*, vol. 217, no. 1–3, pp. 27–34, Jul. 2000.
[46] T. T. Sasaki *et al.*, “Formation of non-ferromagnetic grain boundary phase in a Ga-doped Nd-rich Nd–Fe–B sintered magnet,” *Scr. Mater.*, vol. 113, pp. 218–221, Mar. 2016.
[47] M. Soderžnik *et al.*, “Magnetization reversal of exchange-coupled and exchange-decoupled Nd-Fe-B magnets observed by magneto-optical Kerr effect microscopy,” *Acta Mater.*, vol. 135, pp. 68–76, Aug. 2017.
[48] X. D. Xu *et al.*, “Microstructure of a Dy-free Nd-Fe-B sintered magnet with 2 T coercivity,” *Acta Mater.*, vol. 156, pp. 146–157, Sep. 2018.
[49] J. Fujisaki *et al.*, “Micromagnetic simulation of the orientation dependence of grain boundary properties on the coercivity of Nd-Fe-B sintered magnets,” *AIP Adv.*, vol. 6, no. 5, 2016.
[50] H. Sepehri-Amin, T. Ohkubo, and K. Hono, “Micromagnetic simulations of magnetization reversals in Nd-Fe-B based permanent magnets,” *Mater. Trans.*, vol. 57, no. 8, pp. 1221–1229, 2016.
[51] C. Abraham and A. Aharoni, “Linear decrease in the magnetocrystalline anisotropy,” *Phys. Rev.*, vol. 120, no. 5, pp. 1576–1579, 1960.
[52] A. Aharoni, “Reduction in coercive force caused by a certain type of imperfection,” *Phys. Rev.*, vol. 119, no. 1, pp. 127–131, 1960.
[53] H. Kronmüller, “Theory of nucleation fields in inhomogeneous ferromagnets,” *Phys. Status Solidi B*, vol. 144, no. 1, pp. 385–396, Nov. 1987.
[54] H. Kronmüller, K.-D. Durst, and G. Martinek, “Angular dependence of the coercive field in sintered Fe77Nd15B8 magnets,” *J. Magn. Magn. Mater.*, vol. 69, no. 2, pp. 149–157, Oct. 1987.
[55] H. Kronmüller, K.-D. Durst, S. Hock, and G. Martinek, “Micromagnetic analysis of the magnetic hardening mechanisms in RE-Fe-B magnets,” *J. Phys. Colloq.*, vol. 49, no. C8, pp. C8-623-C8-628, Dec. 1988.
[56] D. Givord, P. Tenaud, and T. Viadieu, “Coercivity mechanisms in ferrite and rare earth transition metal sintered magnets (SmCo5, Nd-Fe-B),” *IEEE Trans. Magn.*, vol. 24, no. 2, pp. 1921–1923, 1988.
[57] H. Kronmüller, K.-D. Durst, and M. Sagawa, “Analysis of the magnetic hardening mechanism in RE-FeB permanent magnets,” *J. Magn. Magn. Mater.*, vol. 74, no. 3, pp. 291–302, 1988.
[58] H. Fukunaga and T. Fukuda, “Effect of magnetic inhomogeneity on magnetization reversal in sintered Nd-Fe-B magnet – Numerical approach,” *Jpn. J. Appl. Phys.*, vol. 29, no. 9R, p. 1711, Sep. 1990.
[59] D. W. Taylor *et al.*, “Coercivity analysis in R17Fe83-xBx magnets,” *J. Magn. Magn. Mater.*, vol. 130, no. 1–3, pp. 225–236, 1994.
[60] V. Villas-Boas, J. M. Gonzalez, F. Cebollada, M. F. Rossignol, D. W. Taylor, and D. Givord, “Coercivity and magnetic viscosity of NdDyFeB mechanically alloyed magnets,” *IEEE Trans. Magn.*, vol. 31, no. 6, pp. 3647–3649, 1995.
[61] D. Givord, A. Lienard, P. Tenaud, and T. Viadieu, “Magnetic viscosity in Nd-Fe-B sintered magnets,” *J. Magn. Magn. Mater.*, vol. 67, no. 3, pp. L281–L285, Jul. 1987.
[62] V. Villas-Boas, F. Missell, G. Schneider, Q. Lu, and D. Givord, “Coercivity and magnetic viscosity in Nd80Fe15B5,” *Solid State Commun.*, vol. 74, no. 7, pp. 683–686, May 1990.
[63] D. Givord, M. Rossignol, and V. M. Barthem, “The physics of coercivity,” *J. Magn. Magn. Mater.*, vol. 258, pp. 1–5, 2003.
[64] S. Bance *et al.*, “Influence of defect thickness on the angular dependence of coercivity in rare-earth permanent magnets,” *Appl. Phys. Lett.*, vol. 104, no. 18, p. 182408, May 2014.
[65] T. Schrefl, D. Suess, W. Scholz, H. Forster, V. Tsiantos, and J. Fidler, “Finite Element Micromagnetics,” in *Computational Electromagnetics*, vol. 28, P. Monk, C. Carstensen, S. Funken, W. Hackbusch, and R. H. W. Hoppe, Eds. Berlin, Heidelberg: Springer Berlin Heidelberg, 2003, pp. 165–181.

[66] T. Schrefl, H. F. Schmidts, J. Fidler, and H. Kronmuller, “Nucleation fields and grain boundaries in hard magnetic materials,” *IEEE Trans. Magn.*, vol. 29, no. 6, pp. 2878–2880, 1993.
[67] H. Kronmüller, R. Fischer, R. Hertel, and T. Leineweber, “Micromagnetism and the microstructure in nanocrystalline materials,” *J. Magn. Magn. Mater.*, vol. 175, no. 1–2, pp. 177–192, 1997.
[68] H. Sepehri-Amin, T. Ohkubo, M. Gruber, T. Schrefl, and K. Hono, “Micromagnetic simulations on the grain size dependence of coercivity in anisotropic Nd–Fe–B sintered magnets,” *Scr. Mater.*, vol. 89, pp. 29–32, Oct. 2014.
[69] M. Sagawa, S. Fujimura, H. Yamamoto, Y. Matsuura, and S. Hirosawa, “Magnetic properties of rare-earth-iron-boron permanent magnet materials,” *J. Appl. Phys.*, vol. 57, no. 8, pp. 4094–4096, Apr. 1985.
[70] J. Liu *et al.*, “Grain size dependence of coercivity of hot-deformed Nd–Fe–B anisotropic magnets,” *Acta Mater.*, vol. 82, pp. 336–343, Jan. 2015.
[71] H. Forster, N. Bertram, X. Wang, R. Dittrich, and T. Schrefl, “Energy barrier and effective thermal reversal volume in columnar grains,” *J. Magn. Magn. Mater.*, vol. 267, no. 1, pp. 69–79, Nov. 2003.
[72] T. Fukada *et al.*, “Evaluation of the microstructural contribution to the coercivity of fine-grained Nd–Fe–B sintered magnets,” *Mater. Trans.*, vol. 53, no. 11, pp. 1967–1971, 2012.
[73] S. Bance, J. Fischbacher, T. Schrefl, I. Zins, G. Rieger, and C. Cassignol, “Micromagnetics of shape anisotropy based permanent magnets,” *J. Magn. Magn. Mater.*, vol. 363, pp. 121–124, Aug. 2014.
[74] M. Yi, O. Gutfleisch, and B.-X. Xu, “Micromagnetic simulations on the grain shape effect in Nd-Fe-B magnets,” *J. Appl. Phys.*, vol. 120, no. 3, p. 033903, Jul. 2016.
[75] J. Fujisaki *et al.*, “Micromagnetic simulations of magnetization reversal in misaligned multigrain magnets with various grain boundary properties using large-scale parallel computing,” *IEEE Trans. Magn.*, vol. 50, no. 11, pp. 1–4, Nov. 2014.
[76] J. Liu *et al.*, “Effect of Nd content on the microstructure and coercivity of hot-deformed Nd–Fe–B permanent magnets,” *Acta Mater.*, vol. 61, no. 14, pp. 5387–5399, Aug. 2013.
[77] H. Sepehri-Amin *et al.*, “High-coercivity ultrafine-grained anisotropic Nd–Fe–B magnets processed by hot deformation and the Nd–Cu grain boundary diffusion process,” *Acta Mater.*, vol. 61, no. 17, pp. 6622–6634, Oct. 2013.
[78] H. Sepehri-Amin, T. Ohkubo, and K. Hono, “The mechanism of coercivity enhancement by the grain boundary diffusion process of Nd–Fe–B sintered magnets,” *Acta Mater.*, vol. 61, no. 6, pp. 1982–1990, Apr. 2013.
[79] K. Löewe, C. Brombacher, M. Katter, and O. Gutfleisch, “Temperature-dependent Dy diffusion processes in Nd–Fe–B permanent magnets,” *Acta Mater.*, vol. 83, pp. 248–255, Jan. 2015.
[80] H. Sepehri-Amin, T. Ohkubo, and K. Hono, “Grain boundary structure and chemistry of Dy-diffusion processed Nd–Fe–B sintered magnets,” *J. Appl. Phys.*, vol. 107, no. 9, p. 09A745, May 2010.
[81] S. Bance, J. Fischbacher, and T. Schrefl, “Thermally activated coercivity in core-shell permanent magnets,” *J. Appl. Phys.*, vol. 117, no. 17, p. 17A733, May 2015.
[82] T. Helbig, K. Loewe, S. Sawatzki, M. Yi, B.-X. Xu, and O. Gutfleisch, “Experimental and computational analysis of magnetization reversal in (Nd,Dy)-Fe-B core shell sintered magnets,” *Acta Mater.*, vol. 127, pp. 498–504, Apr. 2017.
[83] N. Watanabe, M. Itakura, and M. Nishida, “Microstructure of high coercivity Nd–Fe–Co–Ga–B hot-deformed magnet improved by the Dy diffusion treatment,” *J. Alloys Compd.*, vol. 557, pp. 1–4, Apr. 2013.
[84] S. Sawatzki, A. Dirks, B. Frincu, K. Löwe, and O. Gutfleisch, “Coercivity enhancement in hot-pressed Nd-Fe-B permanent magnets with low melting eutectics,” *J. Appl. Phys.*, vol. 115, no. 17, p. 17A705, May 2014.
[85] J. Li *et al.*, “Coercivity and its thermal stability of Nd Fe B hot-deformed magnets enhanced by the eutectic grain boundary diffusion process,” *Acta Mater.*, vol. 161, pp. 171–181, Dec. 2018.

[86] X. Zhu *et al.*, “Direct observation of magnetization reversal of hot-deformed Nd-Fe-B magnet,” *AIP Adv.*, vol. 8, no. 1, p. 015227, Jan. 2018.
[87] S. Kim, D.-S. Ko, H.-S. Lee, D. Kim, J. W. Roh, and W. Lee, “Enhancing the coercivity of Nd-Fe-B sintered magnets by consecutive heat treatment–induced formation of Tb-diffused microstructures,” *J. Alloys Compd.*, vol. 780, pp. 574–580, Apr. 2019.
[88] H. Nakamura, K. Hirota, T. Ohashi, and T. Minowa, “Coercivity distributions in Nd–Fe–B sintered magnets produced by the grain boundary diffusion process,” *J. Phys. Appl. Phys.*, vol. 44, no. 6, p. 064003, Feb. 2011.
[89] M. Soderžnik, M. Korent, K. Žagar Soderžnik, M. Katter, K. Üstüner, and S. Kobe, “High-coercivity Nd-Fe-B magnets obtained with the electrophoretic deposition of submicron TbF3 followed by the grain-boundary diffusion process,” *Acta Mater.*, vol. 115, pp. 278–284, Aug. 2016.
[90] Z. Samardžija, P. McGuiness, M. Soderžnik, S. Kobe, and M. Sagawa, “Microstructural and compositional characterization of terbium-doped Nd–Fe–B sintered magnets,” *Mater. Charact.*, vol. 67, pp. 27–33, May 2012.
[91] K.-H. Bae, T.-H. Kim, S.-R. Lee, H.-J. Kim, M.-W. Lee, and T.-S. Jang, “Magnetic and microstructural characteristics of DyF3/DyHx dip-coated Nd–Fe–B sintered magnets,” *J. Alloys Compd.*, vol. 612, pp. 183–188, Nov. 2014.
[92] T. Ma, X. Wang, X. Liu, C. Wu, and M. Yan, “Coercivity enhancements of Nd–Fe–B sintered magnets by diffusing DyH along different axes,” *J. Phys. Appl. Phys.*, vol. 48, no. 21, p. 215001, Jun. 2015.
[93] T.-H. Kim *et al.*, “Anisotropic diffusion mechanism in grain boundary diffusion processed Nd–Fe–B sintered magnet,” *Acta Mater.*, vol. 112, pp. 59–66, Jun. 2016.
[94] K. Loewe, D. Benke, C. Kübel, T. Lienig, K. P. Skokov, and O. Gutfleisch, “Grain boundary diffusion of different rare earth elements in Nd-Fe-B sintered magnets by experiment and FEM simulation,” *Acta Mater.*, vol. 124, pp. 421–429, Feb. 2017.
[95] N. Watanabe, M. Itakura, N. Kuwano, D. Li, S. Suzuki, and K. Machida, “Microstructure analysis of sintered Nd-Fe-B magnets improved by Tb-vapor sorption,” *Mater. Trans.*, vol. 48, no. 5, pp. 915–918, 2007.
[96] T.-H. Kim *et al.*, “Microstructure and coercivity of grain boundary diffusion processed Dy-free and Dy-containing Nd Fe B sintered magnets,” *Acta Mater.*, vol. 172, pp. 139–149, Jun. 2019.
[97] K. Lu *et al.*, “Boundary optimization and coercivity enhancement of high (BH) max Nd-Fe-B magnet by diffusing Pr-Tb-Cu-Al alloys,” *Scr. Mater.*, vol. 138, pp. 83–87, Sep. 2017.
[98] N. Oono, M. Sagawa, R. Kasada, H. Matsui, and A. Kimura, “Production of thick high-performance sintered neodymium magnets by grain boundary diffusion treatment with dysprosium–nickel–aluminum alloy,” *J. Magn. Magn. Mater.*, vol. 323, no. 3–4, pp. 297–300, Feb. 2011.
[99] M. Tang *et al.*, “Microstructure modification and coercivity enhancement of Nd-Ce-Fe-B sintered magnets by grain boundary diffusing Nd-Dy-Al alloy,” *J. Magn. Magn. Mater.*, vol. 442, pp. 338–342, Nov. 2017.
[100] K. Lu, X. Bao, M. Tang, L. Sun, J. Li, and X. Gao, “Influence of annealing on microstructural and magnetic properties of Nd-Fe-B magnets by grain boundary diffusion with Pr-Cu and Dy-Cu alloys,” *J. Magn. Magn. Mater.*, vol. 441, pp. 517–522, Nov. 2017.
[101] F. Chen, L. Zhang, Y. Jin, and Y. Cheng, “Simultaneous enhancement of the coercivity and remanence at high temperatures in a sintered Nd-Fe-B magnet after grain boundary diffusion with Dy60Co40 alloy,” *Mater. Charact.*, vol. 144, pp. 547–553, Oct. 2018.
[102] M.-W. Lee, K.-H. Bae, S.-R. Lee, H.-J. Kim, and T.-S. Jang, “Microstructure and magnetic properties of NdFeB sintered magnets diffusion-treated with Cu/Al mixed DyCo alloy-powder,” *Arch. Metall. Mater.*, vol. 62, no. 2, pp. 1263–1266, Jun. 2017.
[103] F. Chen, T. Zhang, W. Zhang, L. Zhang, and Y. Jin, “Dependence of the demagnetization behavior on the direction of grain boundary diffusion in sintered Nd-Fe-B magnets,” *J. Magn. Magn. Mater.*, vol. 465, pp. 392–398, Nov. 2018.

[104] “OOMMF Project at NIST.” [Online]. Available: https://math.nist.gov/oommf/. [Accessed: 16-May-2019].
[105] G. A. Zickler, P. Toson, A. Asali, and J. Fidler, “Nanoanalytical TEM studies and micromagnetic modelling of Nd-Fe-B magnets,” *Phys. Procedia*, vol. 75, pp. 1442–1449, 2015.
[106] T. Oikawa, H. Yokota, T. Ohkubo, and K. Hono, “Large-scale micromagnetic simulation of Nd-Fe-B sintered magnets with Dy-rich shell structures,” *AIP Adv.*, vol. 6, no. 5, p. 056006, May 2016.
[107] W. Li, Q. Zhou, L. Z. Zhao, Q. X. Wang, X. C. Zhong, and Z. W. Liu, “Micromagnetic simulation of anisotropic grain boundary diffusion for sintered Nd-Fe-B magnets,” *J. Magn. Magn. Mater.*, vol. 451, pp. 704–709, Apr. 2018.
[108] K. Yamamoto, M. Matsuura, and S. Sugimoto, “Microstructure Formation in Strip-Cast RE-Fe-B Alloys for Magnets,” *Metall. Mater. Trans. A*, vol. 48, no. 7, pp. 3482–3489, Jul. 2017.
[109] J. Bernardi, J. Fidler, M. Sagawa, and Y. Hirose, “Microstructural analysis of strip cast Nd–Fe–B alloys for high (BH)max magnets,” *J. Appl. Phys.*, vol. 83, no. 11, pp. 6396–6398, Jun. 1998.
[110] K. Oesterreicher and H. Oesterreicher, “Structure and Magnetic Properties of Nd2Fe14BH2.7,” *Phys. Status Solidi A*, vol. 85, no. 1, pp. K61–K64, Sep. 1984.
[111] T. Hattori *et al.*, “Microstructural evaluation of Nd-Fe-B jet-milled powders,” *Mater. Trans.*, vol. 50, no. 10, pp. 2347–2350, 2009.
[112] M. Tokunaga, H. Kogure, M. Endoh, and H. Harada, “Improvement of thermal stability of Nd-Dy-Fe-Co-B sintered magnets by additions of Al, Nd and Ga,” *IEEE Trans. Magn.*, vol. 23, no. 5, pp. 2287–2289, Sep. 1987.
[113] Y. Matsuura, S. Hirosawa, H. Yamamoto, S. Fujimura, and M. Sagawa, “Magnetic properties of the Nd2(Fe1−xCox)14B system,” *Appl. Phys. Lett.*, vol. 46, no. 3, pp. 308–310, Feb. 1985.
[114] K. Löwe, “Grain boundary engineering in sintered Nd-Fe-B permanent magnets for efficient utilization of heavy rare earth elements,” Technische Universität Darmstadt, 2016.
[115] C. H. Chen, C. D. Graham, R. M. Strnat, B. K. Pugh, A. Wangler, and A. K. Higgins, “Verification by finite element modeling for the origin of the apparent image effect in closed-circuit magnetic measurements,” *J. Magn. Magn. Mater.*, vol. 323, no. 1, pp. 108–114, Jan. 2011.
[116] J. Goldstein *et al.*, *Scanning Electron Microscopy and X-Ray Microanalysis: Third Edition*, 3rd ed. Springer US, 2003.
[117] V. Astapenko, *Polarization bremsstrahlung on atoms, plasmas, nanostructures and solids*. New York: Springer, 2013.
[118] “SALOME Platform.” [Online]. Available: https://salome-platform.org/. [Accessed: 06-Aug-2019].
[119] G. A. Zickler, P. Toson, A. Asali, and J. Fidler, “Nanoanalytical TEM studies and micromagnetic modelling of Nd-Fe-B magnets,” *Phys. Procedia*, vol. 75, pp. 1442–1449, 2015.
[120] A. N. Dobrynin, V. M. T. S. Barthem, and D. Givord, “Revisiting magnetization processes in granular hard magnetic materials,” *Appl. Phys. Lett.*, vol. 95, no. 5, p. 052511, Aug. 2009.
[121] A. N. Dobrynin, V. M. T. S. Barthem, F. Ingwiller, and D. Givord, “Influence of dipolar collective effects on coercivity and demagnetizing factors in hard magnetic materials,” *Phys. Rev. B*, vol. 81, no. 17, May 2010.
[122] A. N. Dobrynin, T. R. Gao, N. M. Dempsey, and D. Givord, “Experimental determination of the magnetization dependent part of the demagnetizing field in hard magnetic materials,” *Appl. Phys. Lett.*, vol. 97, no. 19, p. 192506, Nov. 2010.
[123] A. Aharoni, “Demagnetizing factors for rectangular ferromagnetic prisms,” *J. Appl. Phys.*, vol. 83, no. 6, pp. 3432–3434, Mar. 1998.
[124] J. Fliegans, G. Delette, A. N. Dobrynin, N. M. Dempsey, and D. Givord, “Closed-Circuit Versus Open-Circuit Characterization of Hard Magnets,” *IEEE Trans. Magn.*, vol. 55, no. 2, pp. 1–5, Feb. 2019.
[125] D.-X. Chen, J. A. Brug, and R. B. Goldfarb, “Demagnetizing factors for cylinders,” *IEEE Trans. Magn.*, vol. 27, no. 4, pp. 3601–3619, 1991.
[126] D.-X. Chen, E. Pardo, and A. Sanchez, “Demagnetizing factors of rectangular prisms and ellipsoids,” *IEEE Trans. Magn.*, vol. 38, no. 4, pp. 1742–1752, 2002.

[127] T. G. Woodcock, F. Bittner, T. Mix, K.-H. Müller, S. Sawatzki, and O. Gutfleisch, “On the reversible and fully repeatable increase in coercive field of sintered Nd–Fe–B magnets following post sinter annealing,” *J. Magn. Magn. Mater.*, vol. 360, pp. 157–164, Jun. 2014.
[128] T.-H. Kim *et al.*, “Dependence of magnetic, phase-transformation and microstructural characteristics on the Cu content of Nd–Fe–B sintered magnet,” *Acta Mater.*, vol. 66, pp. 12–21, Mar. 2014.
[129] M. Saeki, Y. Horino, L. Jinya, M. Enoki, and H. Ohtani, “Thermodynamic Analysis of Phase Equilibria in the Nd-Fe-Cu Ternary System,” *J. Jpn. Inst. Met.*, vol. 81, no. 1, pp. 32–42, 2017.
[130] M. Sagawa, S. Fujimura, H. Yamamoto, Y. Matsuura, and K. Hiraga, “Permanent magnet materials based on the rare earth-iron-boron tetragonal compounds,” *IEEE Trans. Magn.*, vol. 20, no. 5, pp. 1584–1589, Sep. 1984.
[131] B. Hugonnet, “Frittage et évolution de la microstructure au cours des traitements thermiques d’aimants NdFeB: influence sur les propriétés magnétiques,” Université Grenoble Alpes, 2016.
[132] P. Toson, G. A. Zickler, and J. Fidler, “Do micromagnetic simulations correctly predict hard magnetic hysteresis properties?,” *Phys. B Condens. Matter*, vol. 486, pp. 142–150, Apr. 2016.
[133] H. Kronmüller and M. Fähnle, *Micromagnetism and the microstructure of ferromagnetic solids*. New York: Cambridge University Press, 2003.
[134] E. A. Perigo, H. Takiishi, C. C. Motta, and R. N. Faria, “On the Squareness Factor Behavior of RE-FeB (RE = Nd or Pr) Magnets Above Room Temperature,” *IEEE Trans. Magn.*, vol. 45, no. 10, pp. 4431–4434, Oct. 2009.
[135] F. Bittner *et al.*, “Normal and abnormal grain growth in fine-grained Nd-Fe-B sintered magnets prepared from He jet milled powders,” *J. Magn. Magn. Mater.*, vol. 426, pp. 698–707, Mar. 2017.
[136] X. Zhang *et al.*, “Improvement of the thermal stability of sintered Nd-Fe-B magnets by intergranular addition of Dy 82.3Co 17.7,” *J. Appl. Phys.*, vol. 115, no. 17, p. 17A757, May 2014.
[137] J. Philibert, *Diffusion et transport de matière dans les solides*. Les Ulis, France: Editions de Physique, 1985.
[138] J. C. Fisher, “Calculation of Diffusion Penetration Curves for Surface and Grain Boundary Diffusion,” *J. Appl. Phys.*, vol. 22, no. 1, pp. 74–77, 1951.
[139] R. T. P. Whipple, “CXXXVIII. Concentration contours in grain boundary diffusion,” *Lond. Edinb. Dublin Philos. Mag. J. Sci.*, vol. 45, no. 371, pp. 1225–1236, 1954.
[140] T. Suzuoka, “Exact Solutions of Two Ideal Cases in Grain Boundary Diffusion Problem and the Application to Sectioning Method,” *J. Phys. Soc. Jpn.*, vol. 19, no. 6, pp. 839–851, 1964.
[141] B. B. Straumal and B. Baretzky, “Influence of the Grain Boundary Phase Transitions on the Diffusion-Related Properties,” *Defect Diffus. Forum*, vol. 216–217, pp. 53–64, Feb. 2003.
[142] B. B. Straumal *et al.*, “Grain boundary phenomena in NdFeB-based hard magnetic alloys,” *Rev. Adv. Mater. Sci.*, vol. 38, no. 1, 2014.
[143] C. Herzig and Y. Mishin, “Grain Boundary Diffusion in Metals,” in *Diffusion in Condensed Matter*, P. Heitjans and J. Kärger, Eds. Berlin/Heidelberg: Springer-Verlag, 2005, pp. 337–366.
[144] M. F. De Campos and J. A. De Castro, “Optimizing the Heat Treatment of Rare Earth-Transition Metal Sintered Magnets,” in *Materials Science Forum*, 2010, vol. 660, pp. 290–295.
[145] B. A. Cook, J. L. Harringa, F. C. Laabs, K. W. Dennis, A. M. Russell, and R. W. McCallum, “Diffusion of Fe, Co, Nd, and Dy in R2(Fe1- xCox) 14B where R= Nd or Dy,” *J. Magn. Magn. Mater.*, vol. 233, no. 3, pp. 136–141, 2001.
[146] M. P. Thompson *et al.*, “Grain-Boundary-Diffused Magnets: The challenges in obtaining reliable and representative BH curves for electromagnetic motor design,” *IEEE Electrification Mag.*, vol. 5, no. 1, pp. 19–27, Mar. 2017.

Abstract - Résumé

Nd-Fe-B permanent magnets are the most powerful among all commercially available magnets. They play a significant role in energy applications, such as motors of electric vehicles and generators of windmills. Their outstanding properties come from the excellent intrinsic magnetic properties of the $Nd_2Fe_{14}B$ phase and from their microstructure. However, electrical machines operate at about 120-180°C and extrinsic magnetic properties such as coercivity and remanence decrease rapidly with temperature. One way of improving coercivity of Nd-Fe-B sintered magnets is to substitute Nd with a heavy rare earth such as Dy, so as to increase the magnetocrystalline anisotropy. However, Dy is a strategic element and a major objective of the research community is therefore to develop Nd-Fe-B magnets that possess excellent extrinsic magnetic properties with a reduced content of Dy. This requires a better understanding of the link between microstructure and coercivity. The key point is the control of the grain size and the distribution of secondary phases at grain boundaries to prevent magnetization reversal and magnetic coupling. The first part of this thesis concerns a comparison of open-circuit and closed-circuit magnetization measurements carried out on Nd-Fe-B sintered magnets. The observed differences in coercivity values are discussed in terms of magnetic viscosity and demagnetizing field effects. The second part deals with the grain boundary diffusion process performed on Nd-Fe-B sintered magnets using Dy-Co alloys. Microstructural observations and magnetic measurements have been carried out to characterize the diffusion and coercivity profiles and to establish the link between local variations in composition and coercivity. Moreover, micromagnetic simulations have been performed to describe magnetization reversal at the nanoscale in a simple core-shell model. The last part constitutes a discussion about coercivity in graded magnets via a diffusion model and further simulations on a polycrystalline model.

Keywords: Nd-Fe-B, coercivity, microstructure, demagnetizing field, micromagnetism, grain boundary diffusion process

Les aimants permanents Nd-Fe-B sont actuellement les plus puissants du marché. Ils sont indispensables pour des applications telles que les moteurs des véhicules électriques ou les générateurs des éoliennes. Leurs propriétés exceptionnelles viennent des propriétés magnétiques intrinsèques de la phase $Nd_2Fe_{14}B$ et de leur microstructure. Cependant, les machines électriques fonctionnent entre 120 et 180°C et les propriétés magnétiques extrinsèques telles que la coercitivité et la rémanence diminuent avec la température. Un moyen d'améliorer la coercitivité des aimants frittés Nd-Fe-B est la substitution du Nd par des terres rares lourdes comme le Dy, afin d'augmenter l'anisotropie magnétocristalline. Néanmoins, le Dy est un matériau critique et un objectif majeur de la recherche est actuellement de développer des aimants possédant d'excellentes propriétés magnétiques extrinsèques et contenant peu de Dy. Cela nécessite une meilleure compréhension du lien entre microstructure et coercitivité. Dans les aimants frittés Nd-Fe-B, un des points-clés est le contrôle de la taille de grain et de la répartition des phases secondaires aux joints de grains de façon à limiter la nucléation du retournement de l'aimantation et à garantir un bon découplage magnétique des grains. La première partie de la thèse est une étude comparative des caractérisations magnétiques en circuit ouvert et fermé réalisées sur des aimants frittés Nd-Fe-B. Les différences de coercitivité observées sont expliquées par les phénomènes de viscosité magnétique et d'effets de champ démagnétisant. La deuxième partie traite du procédé de diffusion aux joints de grains appliqué aux aimants frittés Nd-Fe-B et utilisant des alliages Dy-Co. Des caractérisations microstructurales ont été réalisées en complément de mesures magnétiques afin de déterminer les profils de diffusion et de coercitivité, et ainsi d'établir le lien entre les variations locales de composition chimique et le champ coercitif. De plus, des simulations micromagnétiques ont permis de décrire le retournement de l'aimantation à l'échelle nanométrique dans un modèle simplifié cœur-coquille. Enfin, la dernière partie de la thèse constitue une discussion sur la coercitivité des aimants diffusés au Dy-Co (à gradient de champ coercitif) à l'aide d'un modèle de diffusion et de simulations sur un modèle polycristallin.

Mots-clés : Nd-Fe-B, coercitivité, microstructure, champ démagnétisant, micromagnétisme, diffusion aux joints de grain